ANELASTIC BEHAVIOR AND DIFFRACTION MODELING OF SILICON CARBIDE WHISKER REINFORCED ALUMINA

ANELASTIC BEHAVIOR AND DIFFRACTION MODELING OF SILICON CARBIDE WHISKER REINFORCED ALUMINA

By

JUAN KONG, B. Eng., M. Eng.

A Thesis

Submitted to the School of Graduate Studies

In Partial Fulfillment of the Requirements

For the Degree

Doctor of Philosophy

McMaster University

DOCTOR OF PHILOSOPHY (2012) McMaster University
(Materials Science and Engineering) Hamilton, Ontario

TITLE: Anelastic Behavior and Diffraction Modelling of Silicon Carbide Whisker Reinforced Aumina

AUTHOR: Juan Kong,
B.Eng. (Beijing Univ. of Aero.&Astro.- P.R.China),
M.Eng. (Beijing Univ. of Aero.&Astro.- P.R.China)

SUPERVISORS: Professor David S. Wilkinson
Professor Nikolas Provatas

NUMBER OF PAGES: xx, 209

ABSTRACT

The superior high-temperature elastic-plastic properties coupled with greater damage tolerance when compared with monolithic ceramics make ceramic matrix composites, CMCs, promising candidates for challenging applications such as engine components, rocket nozzles, cutting tools and nuclear energy reactor core components. Anelastic recovery is the time-dependent back strain observed upon the load removal following creep. In whisker-reinforced CMCs this can be a factor limiting operating conditions. Plastic strain misfit between two phases is thought to be the main driver in terms of the interactions within a percolating network. However, the network deformation mechanisms are still unclear and a previous neutron diffraction study showed an unexpected decrease of peak width after creep contradicting the theoretical predictions.

In this contribution, the finite element method (FEM) is applied to a representative volume element (RVE) with proper boundary conditions in order to simulate the creep deformation and hot pressing processes. Three geometries have been generated and studied: a 3D randomly-oriented short-fiber unit cell without fiber to fiber contact, generated by a random sequential adsorption algorithm; 3D regularly aligned single fiber unit cells; and 2D regularly aligned percolating unit cells. Deformation mechanism has been studied from an energy point of view and compared with a modified analytical model. Then a virtual diffraction model has been developed providing a framework to transfer information between the FEM simulations (strain fields) and the diffraction pattern in terms of the peak width (full width at half maximum: ***FWHM***) and peak position as a measure of stress distribution and mean stress state respectively. Furthermore, the coupling effects of external stress, deformation mode, and thermal stress on the diffraction patterns have been studied.

The critical importance of a percolating whisker network for the anelastic recovery is demonstrated based on the 3D multi-whisker random unit cell. Whisker bending is shown to

be the dominant mechanism over contact effects during the creep deformation of a composite containing a well aligned percolating whisker network based on the 2D unit cell model. Good qualitative agreement was found between our FEM simulations and the analytical model of Wilkinson and Pompe with regards to the maximum recoverable strain and the characteristic relaxation time. The analytical model captures all the critical factors characterizing the strain recovery, e.g., the effect of creep pre-exponent constant, whisker Young's modulus and aspect ratio. Furthermore, it is found that the deformation from an initial stress-free state inevitably introduces peak broadening of whiskers inside the matrix. Several factors determine the peak-width and -shift, i.e., creep strain, applied stress, aspect ratio and geometry. However, thermal stress from the cooling stages following creep and hot pressing processes shelters this broadening effect and complicates the trends. Wide-ranging peak-width changes from narrowing to broadening are predicted depending on the geometry and applied stress. The peak position is shifted to a lower angle due to this thermal effect. This clearly explains the contradicting phenomena motivating this work and leads to that recommendation that a diffraction source with high angular resolution is needed to detect the subtle change of peak profile during creep.

ACKNOWLEDGEMENTS

Foremost, I would like to express my sincere gratitude to my supervisor Professor D. S. Wilkinson for the continuous support and patience throughout this entire journey. I really appreciate the freedom he gave me to pursue my research interest while guiding things on the right path. His way of explaining things in a simple language has a profound effect that I will carry wherever I go. I am indebted to my other supervisor Professor N. Provatas for providing a different perspective and thoughtful comments during my Ph.D study.

I am grateful for my supervisory committee member, Professor M. Jain for his ideas and suggestions. I would also like to thank Professor D. Embury for his help and useful discussions.

I wish to thank staffs of the Research & High Performance Computing Support: Shawn Long and Mark Hahn, for the support with ABAQUS on MMRI and SHARCNET. The help of and useful discussions with Dr. XinJian Duan and Dr. XiaoHua Hu are also appreciated. Furthermore, it is a pleasant stay in JHE A206 with all lovely friends.

Lastly, I would like to dedicate this dissertation to my parents, my baby Jerren, my husband Zhi. Their support and consideration make the whole thing coming true.

TABLE OF CONTENTS

ABSTRACT iii

ACKNOWLEDGEMENTS v

TABLE OF CONTENTS vi

LIST OF FIGURES x

LIST OF TABLES xx

1. INTRODUCTION 1

2. LITERATURE REVIEW 3

2.1. Introduction 3

2.2. Structure of Al_2O_3-SiC_w 3

2.2.1. Crystalline structure of alumina 3

2.2.2. Crystalline structure of SiC 6

2.2.3. Microstructure of Al_2O_3-SiC_w 8

2.3. Creep mechanisms of single phase Al_2O_3 10

2.3.1. Basic creep phenomena 10

2.3.2. Creep models for single phase ceramics 12

2.3.2.1. Nabarro-Herring creep 12

2.3.2.2. Coble creep 13

2.3.2.3. Grain-Boundary Sliding (GBS) accommodated by Diffusion Creep 14

2.3.2.4. Other mechanisms 15

2.3.3. Creep behavior of alumina 16

2.4. Creep mechanisms of Al_2O_3-SiC_w 18

2.4.1. Whisker volume fraction effect 19

2.4.2. Stress dependence *n* 20

2.4.3. Grain size dependence *p* 20

2.4.4. Activation energy *Q* 21

2.4.5. Microstructures after creep 21

2.4.6. Summary 22

2.5. Models for elastic and creep behavior of composites 23

2.5.1. Micromechanical composite models 23
2.5.1.1. Rule of mixtures 23
2.5.1.2. Shear lag model 24
2.5.1.3. Other models 27
2.5.2. Creep models for composite materials 28
2.5.2.1. Shear lag model 28
2.5.2.2. Creep mechanisms in multiphase ceramics (Wilkinson, 1998) 30
2.6. Anelastic creep recovery **37**
2.6.1. Kelvin-Voigt element 37
2.6.2. Experimental observations 39
2.6.3. Anelastic recovery mechanism in Al_2O_3-SiC_w 41
2.6.3.1. Dislocation evolution 42
2.6.3.2. Creep strain misfit (Wilkinson and Pompe's bending model, Hertzian contact model) 42
2.6.4. Summary 46
2.7. Assessment of the literature **47**
3. FINITE ELEMENT SIMULATIONS 49
3.1. Assumptions and material properties **49**
3.2. Finite element Method **50**
3.2.1. Basic theory of finite element method 51
3.2.2. Finite element method in creep analysis 55
3.3. Fundamentals of unit cell technique **57**
3.4. Unit cells used in current study **60**
3.4.1. 3D periodic random-oriented-short-fiber unit cell 61
3.4.2. 2D oriented percolating unit cells 63
3.4.3. 3D single whisker unit cells 66
3.5. Accuracy analysis and element selection **70**
3.5.1. Source of Errors 70
3.5.2. Element selection 71

3.5.3. Discretization with respect to space 72
3.5.4. Discretization with respect to time 74
4. VIRTUAL MODEL OF DIFFRACTION 76
4.1. Introduction **76**
4.2. Fundamentals of the diffraction theory **77**
4.3. Relation between diffraction and deformation in Al_2O_3-SiC_w **82**
4.4. Development of the diffraction model **83**
4.4.1. Model construction 83
4.4.2. Model implementation through ABAQUS 86
4.5. Verification of the diffraction model **86**
4.5.1. Diffraction model predictions 86
4.5.2. Analytical model predictions 88
4.5.3. **Summary** 90
5. ANELASTIC BEHAVIOR MODELING OF Al_2O_3-SiC_w 91
5.1. Introduction **91**
5.2. Percolation of the whisker network **91**
5.3. Deformation mechanism of the 2D percolating whiskers network **94**
5.3.1. Typical stress reduction-strain transient and relaxation curves 94
5.3.2. Relative contribution of bending and contact effects 96
5.3.3. Comparison of FEM results with the analytical model 100
5.3.3.1. Analytical model construction 100
5.3.3.2. Aspect ratio dependence 102
5.3.3.3. Material mechanical property dependencies 105
5.4. Extrapolation to the 3D percolating whiskers network **108**
5.4.1. Typical creep strain curves for plane strain condition 109
5.4.2. Deformation mechanisms for plane strain condition 111
5.4.3. Comparison of FEM results with the analytical model 118
5.4.3.1. Analytical model construction for plane strain condition 118
5.4.3.2. Aspect ratio dependence 120

5.4.3.3. Material mechanical property dependences 124
5.5. Conclusions **131**
6. CORRELATION BETWEEN DIFFRACTION AND DEFORMATION 132
6.1. Introduction **132**
6.2. Peak width and position due to deformation **133**
6.2.1. Effect of whisker network 133
6.2.2. Effect of applied stress 137
6.2.3. Effect of aspect ratio 143
6.2.3.1. 2D percolating geometry 143
6.2.3.2. 3D aligned whisker geometry 145
6.2.4. Summary 147
6.3. Peak width and position with thermal stress **148**
6.3.1. Effect of whisker network during cooling after creep 148
6.3.2. Effect of whisker network during cooling after hot pressing 151
6.3.3. Effect of applied stress during cooling after creep 154
6.3.4. Effect of aspect ratio with thermal stress 155
6.3.4.1. 2D percolating geometry 155
6.3.4.2. 3D aligned geometry 159
6.3.5. Net change of peak-width and -shift after creep 163
6.4. Discussion **166**
7. SUMMARY AND FUTURE WORK 170
7.1. Summary **170**
7.2. Future work **172**
REFERENCES 174
Appendix A 181
Appendix B 185
Appendix C 192

LIST OF FIGURES

Figure 2.1 Structure of α-Al_2O_3 (Chiang *et al.*, 1997): (a) Filling of two-third of the octahedral sites in the basal plane; (b) Filling of two-third of the octahedral sites along *C* axis; (c) Structural unit cell, showing only the cation sublattice, A_i's are the hexagonal basis vectors 5
Figure 2.2 Unit cell of the (a) Zincblende structure of β-SiC; (b)Wurtzite structure of 2*H* SiC (From Chiang, Birnie and Kingery, 1997).....7
Figure 2.3 TEM images of the as-received β-SiC whiskers: (a) section normal to the axis, showing partial dislocations in radial directions and cavities in core region; (b) Typical distributions of cavities in whiskers with diameters around 5 to 10 *nm*. (Nutt, 1984).....7
Figure 2.4 A SEM micrograph of Al_2O_3 composite containing 30vol% of SiC whiskers with sample surface perpendicular to Hot-Press-Axis (HPA). The surface was thermally etched at 1400℃ for 2 hours to expose the whiskers (Quan, 2004) 9
Figure 2.5 A SEM micrograph of Al_2O_3 composite containing 30vol% of SiC whiskers with sample surface parallel to Hot-Press-Axis (HPA) (Quan, 2004) 9
Figure 2.6 A schematic diagram showing the typical creep deformation curve for a monolithic ceramic material (From Kingery *et al.*, 1976).....11
Figure 2.7 Deformation map for MgO doped Al_2O_3 at 1500℃(Chiang *et al.*, 1997; Heuer *et al.*, 1980) 17
Figure 2.8 A schematic diagram showing the logarithm of creep rate vs logarithm of grain size for Al_2O_3. Solid lines show the creep rate dependence on grain size for each assumed species (Al or O) and path (lattice or grain boundary) controlling the rate. The dotted line traces the rate-controlling mechanism: the slower ion along its fastest path.(Chiang *et al.*, 1997; Coble *et al.*, 1978) 18
Figure 2.9 (a) Steady creep rate vs stress relationship for polycrystalline Al_2O_3 and Al_2O_3-SiC_w within temperature range of 1200-1400℃ from flexural experiments (Lin *et al.*, 1990); (b) Steady creep rate vs stress relationship for Al_2O_3-SiC_w with whisker up to 50vol% from flexural experiments (Lin *et al.*, 1991) 19
Figure 2.10 (a) cavitation at triple grain boundary (Nutt *et al.*, 1993); (b) cavitation at GBI (Nutt *et al.*, 1993); (c) cavity between two grains (O'Meara *et al.*, 1996); (d) macroscopic cracks (O'Meara *et al.*, 1996).....22
Figure 2.11 Schematic illustration of the shear lag model: (a) representative short fibre composite; (b) unit cell for analysis; (c) finite length *dx* and stresses around. 26

Figure 2.12 Predicted variations in fibre tensile stress (black lines) and interfacial shear stress (purple lines) along the length of a SiC whisker, R=0.5μm, V_f=10%, e=1x10^{-4}, E_f=600GPa, G_m=100GPa. 26
Figure 2.13 Effective shear modulus of particle composite vs volume fraction V_f, provided that the ratio of the fibre shear modulus to the matrix's was kept 100 (Mura, 1987). 28
Figure 2.14 Predicted variations in fibre tensile stress (McLean, 1972). 29
Figure 2.15 Schematic illustration of network development in multiphase ceramic materials: (a) point-contact percolation in a whisker- or platelet-reinforced ceramic; (b) facet-contact percolation with most of the particle interactions involve full facet contacts. Thin grain-boundary layers separate the facets (shown in the inset), and creep occurs by the squeezing of this material from between the facets under compression (Wilkinson, 1998). 31
Figure 2.16 Schematic illustration of the assumed geometry (Wilkinson and Pompe, 1998): (a) dilute distribution of whiskers that rotate under the far-field stress; (b) an idealized regular whisker network; (c) bending of whisker network after creep. 34
Figure 2.17 Normalized viscosity η/η_0 as a function of volume fraction (ϕ) and packing efficiency f for three mechanisms (Wilkinson and Pompe, 1998). 35
Figure 2.18 Normallized total viscosity (η/η_0) as a function of volume fraction (ϕ) and packing efficiency (f). The solid curve represents the viscosity due to viscoelastic creep when $f = f_{\min}$ (Wilkinson and Pompe, 1998). 36
Figure 2.19 Predicted creep mechanism map of a constrained oriented whisker network, e.g. Al_2O_3-SiC_w with $\theta = 10^0$: The boundary separates regions dominated by viscoelastic and viscoplastic creep, which is sensitive to aspect ratio λ, especially at high values of packing efficiency (Wilkinson and Pompe, 1998). 36
Figure 2.20 Kelvin-Voigt body: (a) spring and dashpot in parallel, (b) for an imposed stress, strain exponentially reaches its elastic value. 38
Figure 2.21 Strain vs. Time plot: (a) Flexural creep test on pure Al_2O_3 (Gu *et al.*, 1994); (b) Tensile creep test on Al_2O_3 composite with 10vol% of SiC whisker (Quan, 2004).....40
Figure 2.22 Strain vs. Time plot on composite with 15vol% SiC_w via flexural test (Gu *et al.*, 1995). 40
Figure 2.23 Recovered strain vs. Time plot (Gu *et al.*, 1995): (a) Al_2O_3-SiC_w composite with aspect ratio of 30; (b) Al_2O_3-SiC_w composite with aspect ratio of 10. 41
Figure 2.24 (111) SiC whisker peaks measured before and after creep (Quan, 2004). 44
Figure 2.25 Schematic illustrations of Hertzian contact phenomena between (a) spheres and (b) rods in contact (Quan, 2004). 46

Figure 3.1 Schematic illustration of FEM (a) a bar under uniaxial end load *f* in global coordinate systems with element discretization; (b) line elements in local coordinate systems. 52
Figure 3.2 Schematic illustration of periodic hexagonal array of circular inclusions in a matrix and 11 unit cells that can be used based on symmetries present (Böhm, 1998). 58
Figure 3.3 Sketch of periodicity (left), symmetry (center), and antisymmetry (right) boundary conditions as used with two-dimensional unit cells (Böhm, 1998). 58
Figure 3.4 Periodic multi-whisker unit cell with randomly oriented whiskers: (a) fibres, (b) fibre meshing, (c) matrix meshing. 62
Figure 3.5 (a) Idealized micro-geometry of aligned percolating whisker network, λ=5; (b) 2D percolating unit cell with meshes, λ=7; (c) magnified view (~ 20 times) of contact region shown in square box in (b). 64
Figure 3.6 2D aligned percolating unit cells with meshes, from top to bottom with aspect ratios of 3, 5, 7, 10, 15 and 20. Red lines delineate the whiskers inside. 66
Figure 3.7 (a)&(b) Idealized micro-geometry of aligned whisker network, λ=5, V_f =10%, *l/L = R/D*; (c)&(d) unit cell used in the simulation. 68
Figure 3.8 3D single whisker unit cells with meshes, from left to right with aspect ratios of 5, 7, 10, 15 and 20, red lines delineate the whiskers inside, element size is around 0.05. 69
Figure 3.9 Von Mises Stress for different element sizes with deformation scale factor of 1145, based on unit cell in Figure 3.6 with λ=5, $\sigma_{applied}$ = -60MPa. 73
Figure 3.10 Displacement along y direction (U2) versus loading time for different value of error tolerance (cetol) from 1×10^{-1} (cetol-1) to 1×10^{-7} (cetol-7) based on unit cell in Figure 3.6 with λ=5, $\sigma_{applied}$ = -60MPa, element size = 0.05 (μ*m*). 74
Figure 3.11 Error tolerance (cetol) versus CPU time and error tolerance versus U2 at time 264960 seconds, based on unit cell in Figure 3.6 with λ=5, $\sigma_{applied}$ = -60MPa, element size = 0.05 (μm). 75
Figure 4.1 Relations involved in the vector representation of the Bragg law. 78
Figure 4.2 Schematic illustration of the interference of two atoms in a unit cell. 79
Figure 4.3 A typical observed line profile (Klug *et al.*, 1974). 81
Figure 4.4 Schematic illustration of change in the shape and position of (111) peak due to lattice deformation: (a) without deformation (b) uniaxial compression and (c) bending. 82
Figure 4.5 Diffraction model verification: (a) schematic illustration of a simple supported beam with height of 0.5μ*m* and span of 9.9μ*m* under bending and tension; (b) normal strain (E_{11} or ε_{xx}) distribution obtained from FEM simulations with element size around 0.1μ*m*; (c) with element size around 0.05μ*m*. 87

Figure 5.1 Stress reduction-Strain transient curve for the random, three-dimensional multi-whisker unit cell without contact, $\sigma_{applied}$ =-60MPa, σ_{final} =-20MPa. 93
Figure 5.2 Stress reduction-Strain transient curve for 2-D percolating network, λ=5, $\sigma_{applied}$ = -75MPa, the solid line shows the asymptotic curve, the dotted line shows the behaviour while unloading at the strain of 5×10^{-3} with a final stress of -20MPa. 95
Figure 5.3 Plot of natural log of the fraction of recovered strain vs time, λ=5, σ_a = -75MPa. 96
Figure 5.4 S_{11} distribution within whisker network with invisible (white regions) matrix, λ=7, $\sigma_{applied}$ = -75MPa. 97
Figure 5.5 S_{22} distribution within whisker network with invisible matrix, λ=7, $\sigma_{applied}$ = -75MPa. 97
Figure 5.6 Deflection along the middle whisker, λ=7, $\sigma_{applied}$ = -75MPa. 98
Figure 5.7 Contribution of two deformation forms in terms of percentage versus aspect ratio. 99
Figure 5.8 Simplified 2D bending unit cell: *W*, *H* and *L* are the width, height and length of the unit cell, 2*d*=λ*2*r* is the length of whisker with radius of *r* and aspect ratio of λ. 101
Figure 5.9 Scaled maximum recoverable strain versus aspect ratio, finite element model (FEM): dotted trend lines with the fitting equations; analytical model (AM): solid line and the equation in red for comparison. 103
Figure 5.10 Characteristic relaxation time versus aspect ratio, finite element model (FEM): dotted trend lines with the fitting equations; analytical model (AM): solid line and the equation in red for comparison. 105
Figure 5.11 Maximum recoverable strain versus Young's modulus of the whisker, λ=5, $\sigma_{applied}$ = -100MPa. 106
Figure 5.12 Characteristic relaxation time versus Young's modulus of the whisker, λ=5, $\sigma_{applied}$ = -100MPa. 107
Figure 5.13 Plot of logarithm of characteristic relaxation time versus logarithm of creep constant, λ=5, $\sigma_{applied}$ = -100MPa. 108
Figure 5.14 Stress reduction-Strain transient curves for 2D percolating network with varied aspect ratio and plane strain condition, $\sigma_{applied}$ = -10MPa. 109
Figure 5.15 Plot of natural log of the fraction of recovered strain vs time for different aspect ratios: (a) with plane strain condition, $\sigma_{applied}$ = -10MPa; (b) with plane stress condition, $\sigma_{applied}$ = -75MPa, -75MPa, -10MPa, -5MPa and -1MPa for aspect ratios of 5, 7, 10, 15 and 20 respectively. 111
Figure 5.16 S_{11} distribution within whisker network with invisible (white regions) matrix for aspect ratio from 5 to 20 with plane strain condition, $\sigma_{applied}$ = -10MPa. 113

Figure 5.17 S_{22} distribution within whisker network with invisible (white regions) matrix for aspect ratio from 5 to 20 with plane strain condition, $\sigma_{applied}$ = -10MPa. 115
Figure 5.18 Deflection of the neutral line along the middle whisker, plane strain condition, $\sigma_{applied}$ = -10MPa. 116
Figure 5.19 Mean value of S_{11} within whiskers for plane stress and plane strain conditions respectively, $\sigma_{applied}$ = -10MPa. 117
Figure 5.20 Contribution of deformation forms in terms of percentage versus aspect ratio, plane strain condition, $\sigma_{applied}$ = -10MPa. 118
Figure 5.21 Scaled maximum recoverable strain versus aspect ratio for FEM with plane stress and plane strain ($\sigma_{applied}$ =-100MPa) conditions and for analytical model with plane strain condition. 120
Figure 5.22 Scaled maximum recoverable strain versus aspect ratio for plane strain condition with varied loading conditions for comparison. 121
Figure 5. 23 Maximum recoverable strain versus load with the fitting equations.....122
Figure 5.24 Plot of natural log of the fraction of recovered strain vs time with varied applied stress for different aspect ratio. 124
Figure 5.25 Maximum recoverable strain versus Young's modulus, plane strain condition, λ=10, $F_{applied}$ = -100N. 126
Figure 5.26 Deflection of the neutral line along the middle whisker for varied Young's modulus of the whisker, plane strain condition, λ=10, $F_{applied}$ = -100N.....126
Figure 5.27 Deflection of the neutral line along the middle whisker for varied Young's modulus of the matrix, plane strain condition, λ=10, $F_{applied}$ = -100N.....127
Figure 5.28 Maximum recoverable strain versus Poisson ratio, plane strain condition, λ=10, $F_{applied}$ = -100N. 127
Figure 5.29 Plot of natural log of the fraction of recovered strain vs time for varied Young's modulus of the whisker, plane strain condition, λ=10, $F_{applied}$ = -100N.....128
Figure 5.30 Plot of natural log of the fraction of recovered strain vs time for varied Young's modulus of the matrix, plane strain condition, λ=10, $F_{applied}$ = -100N.....129
Figure 5.31 Plot of natural log of the fraction of recovered strain vs time for varied Poisson ratio of the whisker, plane strain condition, λ=10, $F_{applied}$ = -100N. 129
Figure 5.32 Plot of natural log of the fraction of recovered strain vs time for varied Poisson ratio of the matrix, plane strain condition, λ=10, $F_{applied}$ = -100N. .130
Figure 5.33 Creep strain versus time for different creep constants *C*, plane strain condition, λ=10, $F_{applied}$ = -1N. 130

Figure 6.1 Creep strain versus time for three kinds of whisker networks: 3D random, 2D percolating and 3D aligned unit cells, λ=5, $\sigma_{applied}$ = 60MPa, T=1200℃. 134
Figure 6.2 FWHM versus creep strain for three kinds of whisker networks: 3D random, 2D percolating and 3D aligned unit cells, λ=5, $\sigma_{applied}$ = 60MPa, T=1200℃.....135
Figure 6.3 FWHM versus time for three kinds of whisker networks: 3D random, 2D percolating and 3D aligned unit cells, λ=5, $\sigma_{applied}$ = 60MPa, T=1200℃.....136
Figure 6.4 Peak shift versus creep strain for three kinds of whisker networks: 3D random, 2D percolating and 3D aligned unit cells, λ=5, $\sigma_{applied}$ = 60MPa, T=1200℃.....137
Figure 6.5 Creep strain versus time with different applied stresses for 3D aligned unit cell, λ=5, T=1400℃.....138
Figure 6.6 Creep strain versus time with different applied stresses for 2D percolating unit cell, λ=5, T=1400℃. 138
Figure 6.7 Creep strain versus time with different applied stresses for 3D random unit cell, λ=5, T=1400℃.....139
Figure 6.8 *FWHM* versus creep strain under different applied stresses for 2D percolating, 3D aligned and 3D random unit cells, λ=5, T=1400℃.....140
Figure 6.9 Enlarged view of *FWHM* versus creep strain for 2D percolating unit cell , λ=5, T=1400℃.....141
Figure 6.10 Peak shift versus creep strain under different applied stresses for 2D percolating, 3D aligned and 3D random unit cells, λ=5, T=1400℃.....142
Figure 6.11 Peak shift versus creep strain under different applied stresses for 2D percolating and 3D random unit cells, λ=5, T=1400℃. 142
Figure 6.12 *FWHM* versus aspect ratio for 2D percolating unit cells with λ=5, 7, 10, 15 and 20, T=1400℃, $\sigma_{applied}$ = -60MPa, -75MPa and -100MPa. 144
Figure 6.13 Peak shift versus aspect ratio for 2D percolating unit cells with λ=5, 7, 10, 15 and 20, T=1400℃, $\sigma_{applied}$ = -60MPa, -75MPa and -100MPa. 144
Figure 6.14 *FWHM* versus aspect ratio for 3D aligned unit cells with λ=5, 7, 10, 15 and 20, T=1400℃, $\sigma_{applied}$ = 60MPa, 75MPa and 100MPa. 146
Figure 6.15 Peak shift versus aspect ratio for 3D aligned unit cells with λ=5, 7, 10, 15 and 20, T=1400℃, $\sigma_{applied}$ = 60MPa, 75MPa and 100MPa. 147
Figure 6.16 Strain versus time for three whisker networks (3D random, 2D percolating and 3D aligned unit cells), with λ=5, $\sigma_{applied}$ = 60MPa, as they are deformed to a strain of 0.005 at 1400℃, then cooled to 20℃. 149
Figure 6.17 *FWHM* versus temperature for three whisker networks (3D random, 2D percolating and 3D aligned unit cells), with λ=5, $\sigma_{applied}$ = 60MPa, as they are deformed to a strain of 0.005 at 1400℃, then cooled to 20℃. 150

Figure 6.18 Peak-shift versus temperature for three whisker networks (3D random, 2D percolating and 3D aligned unit cells), with λ=5, $\sigma_{applied}$ = 60MPa, as they are deformed to a strain of 0.005 at 1400℃, then cooled to 20℃.....151
Figure 6.19 *FWHM* versus temperature after hot pressing for three kinds of whisker networks: 3D random, 2D percolating and 3D aligned unit cells, with λ=5, $\sigma_{applied}$ = - 50MPa. 152
Figure 6.20 Peak-shift versus temperature after hot pressing for three kinds of whisker networks: 3D random, 2D percolating and 3D aligned unit cells, with λ=5, $\sigma_{applied}$ = - 50MPa. 152
Figure 6.21 *FWHM* versus temperature under different applied stresses for 2D percolating, 3D aligned and 3D random unit cells, with λ=5, as they are deformed to a strain of 0.005 at 1400℃, then cooled to 20℃. 154
Figure 6.22 Peak-shift versus Temperature under different applied stresses for 2D percolating, 3D aligned and 3D random unit cells, with λ=5, as they are deformed to a strain of 0.005 at 1400℃, then cooled to 20℃ 155
Figure 6.23 *FWHM* versus aspect ratio for 2D percolating unit cells with λ=5, 7, 10, 15 and 20, deformed to a strain of 0.005 at 1400℃ then cooled to 20℃ with $\sigma_{applied}$ = 60MPa, ED: elastic deformation, CD: creep deformation, EU: elastic unloading. 156
Figure 6.24 Peak-shift versus aspect ratio for 2D percolating unit cells with λ=5, 7, 10, 15 and 20, deformed to a strain of 0.005 at 1400℃ then cooled to 20℃ with $\sigma_{applied}$ = 60MPa, ED: elastic deformation, CD: creep deformation, EU: elastic unloading. 157
Figure 6.25 *FWHM* versus temperature after hot pressing for 2D percolating unit cells with λ=5, 7, 10, 15 and 20, $\sigma_{applied}$ = - 50MPa. 158
Figure 6.26 Peak-shift versus temperature after hot pressing for 2D percolating unit cells with λ=5, 7, 10, 15 and 20, $\sigma_{applied}$ = - 50MPa. 158
Figure 6.27 *FWHM* versus aspect ratio for 3D aligned unit cells with λ=5, 7, 10, 15 and 20, deformed to a strain of 0.005 at 1400℃ then cooled to 20℃ with $\sigma_{applied}$ = 60MPa, ED: elastic deformation, CD: creep deformation, EU: elastic unloading. 160
Figure 6.28 Peak-shift versus aspect ratio for 3D aligned unit cells with λ=5, 7, 10, 15 and 20, deformed to a strain of 0.005 at 1400℃ then cooled to 20℃ with $\sigma_{applied}$ = 60MPa, ED: elastic deformation, CD: creep deformation, EU: elastic unloading. 161
Figure 6.29 *FWHM* versus temperature after hot pressing for 3D aligned unit cells with λ=5, 7, 10, 15 and 20, $\sigma_{applied}$ = - 50MPa. 162
Figure 6.30 Peak-shift versus temperature after hot pressing for 3D aligned unit cells with λ=5, 7, 10, 15 and 20, $\sigma_{applied}$ = - 50MPa. 162

Figure 6.31 Δ*FWHM* versus aspect ratio for 2D percolating unit cells with λ=5, 7, 10, 15 and 20, compared between samples before (hot pressed with $\sigma_{applied}$ = -50MPa) and after creep (deformed to a strain of 0.005 at 1400℃ then cooled to 20℃ with $\sigma_{applied}$ =-60MPa, -75MPa and -100MPa). 164
Figure 6.32 Peak-shift versus aspect ratio for 2D percolating unit cells with λ=5, 7, 10, 15 and 20, compared between samples before (hot pressed with $\sigma_{applied}$ = -50MPa) and after creep (deformed to a strain of 0.005 at 1400℃ then cooled to 20℃ with $\sigma_{applied}$ =-60MPa, -75MPa and -100MPa). 164
Figure 6.33 Δ*FWHM* versus aspect ratio for 3D aligned unit cells with λ=5, 7, 10, 15 and 20, compared between samples before (hot pressed with $\sigma_{applied}$ = -50MPa) and after creep (deformed to a strain of 0.005 at 1400℃ then cooled to 20℃ with $\sigma_{applied}$ =-60MPa, -75MPa and -100MPa). 165
Figure 6.34 Peak-shift versus aspect ratio for 3D aligned unit cells with λ=5, 7, 10, 15 and 20, compared between samples before (hot pressed with $\sigma_{applied}$ = -50MPa) and after creep (deformed to a strain of 0.005 at 1400℃ then cooled to 20℃ with $\sigma_{applied}$ =-60MPa, -75MPa and -100MPa). 165
Figure 6.35 *FWHM* and Peak-shift predictions (dark area) : (a) and (b) for three geometries without thermal stress, (c) and (d) for three geometries with thermal stress, (e) and (f) for all virtual tests with thermal stress, without thermal stress and experimental tests; virtual tests are with λ=5, 7, 10, 15 and 20, $\sigma_{applied}$ = 60MPa, 75MPa and 100MPa, as they are deformed to a strain of 0.005 at 1400℃, then cooled to 20℃ if thermal stress is considered. 168
Figure B-1 S_{11} distribution within whisker network without matrix for aspect ratio 5, 10 and 20 with plane strain condition. 186
Figure B-2 S_{22} distribution within whisker network without matrix for aspect ratio 5, 10 and 20 with plane strain condition. 187
Figure B-3 Von Mises stress distribution within whisker network without matrix for aspect ratio 5, 10 and 20 with plane strain condition. 188
Figure B-4 Maximum strain versus load with the fitting equations, plane strain condition. 190
Figure C-1 Creep strain versus time for 2D percolating unit cells with λ=5, 7, 10, 15 and 20, T=1400℃, $\sigma_{applied}$ = -60MPa. 192
Figure C-2 Creep strain versus time for 2D percolating unit cells with λ=5, 7, 10, 15 and 20, T=1400℃, $\sigma_{applied}$ = -75MPa. 193
Figure C-3 Creep strain versus time for 2D percolating unit cells with λ=5, 7, 10, 15 and 20, T=1400℃, $\sigma_{applied}$ = -100MPa. 193
Figure C-4 *FWHM* versus creep strain for 2D percolating unit cells with λ=5, 7, 10, 15 and 20, T=1400℃, $\sigma_{applied}$ = -60MPa. 194

Figure C-5 *FWHM* versus creep strain for 2D percolating unit cells with λ=5, 7, 10, 15 and 20, T=1400℃, $\sigma_{applied}$ = -75MPa.....194
Figure C-6 *FWHM* versus creep strain for 2D percolating unit cells with λ=5, 7, 10, 15 and 20, T=1400℃, $\sigma_{applied}$ = -100MPa.....195
Figure C-7 Peak shift versus creep strain for 2D percolating unit cells with λ=5, 7, 10, 15 and 20, T=1400℃, $\sigma_{applied}$ = -60MPa.....195
Figure C-8 Peak shift versus creep strain for 2D percolating unit cells with λ=5, 7, 10, 15 and 20, T=1400℃, $\sigma_{applied}$ = -75MPa.....196
Figure C-9 Peak shift versus creep strain for 2D percolating unit cells with λ=5, 7, 10, 15 and 20, T=1400℃, $\sigma_{applied}$ = -100MPa.....196
Figure C-10 Creep strain versus time for 3D aligned unit cells with λ=5, 7, 10, 15 and 20, T=1400℃, $\sigma_{applied}$ = 60MPa.....197
Figure C-11 Creep strain versus time for 3D aligned unit cells with λ=5, 7, 10, 15 and 20, T=1400℃, $\sigma_{applied}$ = 75MPa.....198
Figure C-12 Creep strain versus time for 3D aligned unit cells with λ=5, 7, 10, 15 and 20, T=1400℃, $\sigma_{applied}$ = 100MPa.....198
Figure C-13 *FWHM* versus creep strain for 3D aligned unit cells with λ=5, 7, 10, 15 and 20, T=1400℃, $\sigma_{applied}$ = 60MPa.....199
Figure C-14 *FWHM* versus creep strain for 3D aligned unit cells with λ=5, 7, 10, 15 and 20, T=1400℃, $\sigma_{applied}$ = 75MPa.....199
Figure C-15 *FWHM* versus creep strain for 3D aligned unit cells with λ=5, 7, 10, 15 and 20, T=1400℃, $\sigma_{applied}$ = 100MPa.....200
Figure C-16 Peak shift versus creep strain for 3D aligned unit cells with λ=5, 7, 10, 15 and 20, T=1400℃, $\sigma_{applied}$ = 60MPa.....200
Figure C-17 Peak shift versus creep strain for 3D aligned unit cells with λ=5, 7, 10, 15 and 20, T=1400℃, $\sigma_{applied}$ = 75MPa.....201
Figure C-18 Peak shift versus creep strain for 3D aligned unit cells with λ=5, 7, 10, 15 and 20, T=1400℃, $\sigma_{applied}$ = 100MPa.....201
Figure C-19 *FWHM* versus temperature for 2D percolating unit cells with λ=5, 7, 10, 15 and 20, $\sigma_{applied}$ = -60MPa, as they are deformed to a strain of 0.005 at 1400℃, then cooled to 20℃.....202
Figure C-20 *FWHM* versus temperature for 2D percolating unit cells with λ=5, 7, 10, 15 and 20, $\sigma_{applied}$ = -75MPa, as they are deformed to a strain of 0.005 at 1400℃, then cooled to 20℃.....203
Figure C-21 *FWHM* versus temperature for 2D percolating unit cells with λ=5, 7, 10, 15 and 20, $\sigma_{applied}$ = -100MPa, as they are deformed to a strain of 0.005 at 1400℃, then cooled to 20℃.....203

Figure C-22 Peak-shift versus temperature for 2D percolating unit cells with λ=5, 7, 10, 15 and 20, $\sigma_{applied}$ = -60MPa, as they are deformed to a strain of 0.005 at 1400℃, then cooled to 20℃.....204
Figure C-23 Peak-shift versus temperature for 2D percolating unit cells with λ=5, 7, 10, 15 and 20, $\sigma_{applied}$ = -75MPa, as they are deformed to a strain of 0.005 at 1400℃, then cooled to 20℃.....204
Figure C-24 Peak-shift versus temperature for 2D percolating unit cells with λ=5, 7, 10, 15 and 20, $\sigma_{applied}$ = -100MPa, as they are deformed to a strain of 0.005 at 1400℃ then cooled to 20℃.....205
Figure C-25 *FWHM* versus temperature for 3D aligned unit cells with λ=5, 7, 10, 15 and 20, $\sigma_{applied}$ =60MPa, as they are deformed to a strain of 0.005 at 1400 ℃, then cooled to 20℃. 206
Figure C-26 *FWHM* versus temperature for 3D aligned unit cells with λ=5, 7, 10, 15 and 20, $\sigma_{applied}$ = 75MPa, as they are deformed to a strain of 0.005 at 1400 ℃, then cooled to 20℃. 207
Figure C-27 *FWHM* versus temperature for 3D aligned unit cells with λ=5, 7, 10, 15 and 20, $\sigma_{applied}$ = 100MPa, as they are deformed to a strain of 0.005 at 1400℃, then cooled to 20℃. 207
Figure C-28 Peak-shift versus temperature for 3D aligned unit cells with λ=5, 7, 10, 15 and 20, $\sigma_{applied}$ = 60MPa, as they are deformed to a strain of 0.005 at 1400℃, then cooled to 20℃. 208
Figure C-29 Peak-shift versus temperature for 3D aligned unit cells with λ=5, 7, 10, 15 and 20, $\sigma_{applied}$ = 75MPa, as they are deformed to a strain of 0.005 at 1400℃, then cooled to 20℃. 208
Figure C-30 Peak-shift versus temperature for 3D aligned unit cells with λ=5, 7, 10, 15 and 20, $\sigma_{applied}$ = 100MPa, as they are deformed to a strain of 0.005 at 1400℃, then cooled to 20℃. 209

LIST OF TABLES

Table 2.1 Common processing routes and transition sequences toward the stable α-Al_2O_3 phase. Approximate packing of oxygen as HCP: α, χ and κ; FCC: γ, δ, θ, η (Levin and Brandon, 1998) 4
Table 2.2 Values of *n*, *p* and *Q* for creep mechanisms (Cannon *et al.*, 1983; Poirier, 1985) 16
Table 2.3 Lattice strains ($\times 10^{-3}$) measured at room temperature for SiC_w (Quan, 2004). Numbers in parenthesis are uncertainties. BC: before creep; AN: annealed; AC: after creep 45
Table 3.1 Material properties of Al_2O_3 (Munro, 1997) 50
Table 3.2 Material properties of SiC_w (Petrovic *et al.*, 1985; Wong *et al.*, 1997; Goldberg *et al.*, 2001) 50
Table 3.3 Two-dimensional percolating unit cell parameters 64
Table 3.4 Three-dimensional aligned single whisker unit cell parameters 68
Table 4.1 Comparisons of *FWHM* and $\Delta 2\theta$ for (111) peak between the diffraction model and analytical solution (in degree). (b): with element size around 0.1 μm (Figure 4.5 (b)), (c): with element size around 0.05 μm (Figure 4.5 (c)). 90
Table 5.1 Material properties of Al_2O_3 and SiC_w 91
Table 5.2 Maximum recoverable strain from FEM predictions (From Figure 5.24) and analytical model (AM) for 2D percolating whisker unit cells based on plane strain condition 122
Table 6.1 FWHM and Peak-shift (Δ2θ) range for three geometries without thermal stress 166
Table 6.2 FWHM and Peak-shift (Δ2θ) range for three geometries with thermal stress 167
Table B-1 FEM results and analytical model predictions (AM) for plane strain condition 190
Table B-2 Maximum strain from FEM predictions (Figure B-4) and analytical model (AM) for 2D percolating whisker unit cells without matrix based on plane strain condition 191

CHAPTER 1

INTRODUCTION

As compared to a monolithic alumina ceramic the addition of SiC whiskers into an Al_2O_3 matrix produces enhanced fracture toughness with up to 3 to 4 fold increase (Becher *et al.*, 1984, 1988), higher resistance to thermal shock (Tiegs *et al.*, 1987) and to room temperature slow crack growth (Becher *et al.*, 1990) and enhanced creep resistance by up to 2 orders of magnitude (Lin *et al.*, 1990, 1991). This composite material has been widely used for cutting tool inserts, valves, pump components and extrusion dies in the commercial market. Meanwhile, as a promising candidate for structural applications for more fuel-efficient energy conversion systems which require higher service temperatures and lighter weight, its creep resistance is perhaps the most critical high temperature property. The creep mechanisms of Al_2O_3-SiC_w composites must therefore be understood to enable a reliable employment.

However, the reinforcing effect of the SiC whisker for the creep property is not clear. Of particular importance is the phenomenon of anelastic recovery, which is the time-dependent back strain observed upon load removal in Al_2O_3-SiC_w during creep deformation. From an engineering perspective, anelastic recovery limits the operating range of CMCs. From a scientific perspective, anelastic recovery can be studied in order to develop a more fundamental understanding of the complex interactions of reinforcement network with the matrix. The mechanisms of this anelastic recovery are still under investigation. Generally, the mechanical performance of these composites is dependent on the individual properties of each of the constituents, the distribution and morphology of phases present and the properties of the interfaces between the phases.

Previous modeling suggests that whisker bending is the dominant deformation mechanism in an aligned percolating network (Wilkinson and Pompe, 1998). Experiments

were performed by Quan (2004) to verify this, using neutron diffraction peak-width (***FWHM***) as a measure of elastic whisker bending, and peak position to monitor average residual thermal stress. These experiments on crept alumina composites containing 20-30vol% of SiC whiskers showed an unexpected decrease of peak width for the <111> whisker peak which is parallel to the whisker axis. One must therefore consider competing mechanism. For example, Hertzian contact could also exist along with bending, as the deformation mechanism when the whiskers network is formed, and contribute to the elastic energy driving the back strain. However, both mechanisms lack of support from experimental data via diffraction.

The primary purpose of this work is to address the whisker network deformation inside a creeping matrix and provide correlations between the deformation and the diffraction characterization. Chapter 2 reviews the current understanding of creep properties of Al_2O_3-SiC_w, some composite theories related to elasticity and creep, and phenomena and mechanisms of anelasticity. In Chapter 3, finite element simulations used in this work are introduced. Chapter 4 illustrates the virtual diffraction model connecting the FEM simulations and diffraction patterns in terms of peak-width and position. Chapter 5 discusses the anelasticity modeling for the Al_2O_3-SiC_w composite. Chapter 6 presents the correlations between deformation and diffraction pattern. In chapter 7, we summarize the present work by highlighting the critical results obtained followed by a discussion on some ideas for future research.

CHAPTER 2

LITERATURE REVIEW

2.1. Introduction

This chapter reviews the background literature on fibre-reinforced composites related to the study in this thesis: section 2.2 introduces the structure of Al_2O_3-SiC_w composites; section 2.3 describes the basic creep theories of single phase alumina; section 2.4 discusses observations of creep properties of Al_2O_3-SiC_w composites; section 2.5 presents some theories of elastic and creep properties of composites in terms of micromechanical (rule of mixture, shear lag model and some mean field) theories and Wilkinson and Pompe's rheological theory (1998), respectively; section 2.6 gives detailed information of the anelastic recovery from experimental observations to the hypothesized mechanisms; and section 2.7 offers an overall assessment of the literature.

2.2. Structure of Al_2O_3-SiC_w

2.2.1. Crystalline structure of alumina

Alumina, the only solid oxide of metal aluminium, has the chemical formula of Al_2O_3 existing in many kinds of structures, namely α, γ, δ, θ, η, β, χ and κ aluminas, summarized thoroughly by Wefers and Misra (1987), then Levin and Brandon (1998). The most prevalent and thermodynamically stable form is α-Al_2O_3, referred to also as corundum, ruby or sapphire based on the occurring type and level of trace impurity, while other polymorphs are generally categorized as transition phases. Table 2.1 shows some commonly accepted processing routes and phase transition sequences toward the stable α-Al_2O_3 (Levin and Brandon, 1998). A theoretical explanation for the stability of the corundum structure is provided by Wilson *et al*. (1996), through calculating the energies of different solid phases of

Al_2O_3 using an *ab initio* pseudopotential method combining the density-functional theory with the local-density approximation for exchange and correlation.

Table 2.1 Common processing routes and transition sequences toward the stable α-Al_2O_3 phase. Approximate packing of oxygen as HCP: α, χ and κ; FCC: γ, δ, θ, η (Levin and Brandon, 1998)

hcp
α-AlOOH (diaspore) $\xrightarrow{700°–800°C}$ α-Al_2O_3
γ-$Al(OH)_3$(gibbsite) $\xrightarrow{150°–300°C}$ χ $\xrightarrow{650°–750°C}$ κ $\xrightarrow{1000°C}$ α-Al_2O_3
$5Al_2O_3 \cdot H_2O$ (tohdite) $\xrightarrow{700°–800°C}$ κ′ $\xrightarrow{750°C}$ κ $\xrightarrow{900°C}$ α-Al_2O_3
Vapor (CVD) → κ → α-Al_2O_3
fcc
γAlOOH (boehmite) $\xrightarrow{300°–500°C}$ γ $\xrightarrow{700°–800°C}$ δ $\xrightarrow{900°–1000°C}$ θ $\xrightarrow{1000°–1100°C}$ α-Al_2O_3
α-$Al(OH)_3$ (bayerite) $\xrightarrow{200°–300°C}$ η $\xrightarrow{600°–800°C}$ θ $\xrightarrow{1000°–1100°C}$ α-Al_2O_3
Amorphous (anodic film) → γ → δ → θ → α-Al_2O_3
Melt → γ → δ,θ → α-Al_2O_3

Corundum has a trigonal crystal structure with a space group of $R\bar{3}c$, number 167 in the International Tables for Crystallography, which contains two formula units per unit cell (Hübner, 1984). In ceramic science, anions with relatively big size are generally considered to form a close-packed sublattice, either face-centered cubic or hexagonal close packed, with the interstices filled by cations of relatively small size (Chiang *et al.*, 1997). The cation/anion radius ratio provides criteria that determine which interstitial sites will be occupied, either octahedral (0.414-0.732) or tetrahedral (0.225-0.414) sites for most common cases by far. According to this kind of ionic compound structure representation, for α-Al_2O_3, larger oxygen ions form an *HCP* sublattice and smaller aluminium ions occupy two-third of the octahedral

interstices maintaining charge neutrality in an ordered array, as shown in Figure 2.1 (Chiang *et al.*, 1997). A hexagonal array with the same spacing as the oxygen ions is formed by these octahedral sites. The columns of octahedral sites perpendicular to the (0001) or basal plane alternate in having every two sites occupied and one empty, as shown in Figure 2.1(a) and (b) with horizontal or vertical pattern respectively. The cation sublattice (Figure 2.1(c)) repeats after three layers. Taking into account the alternating placing of both the cation and anion layers, the structure repeats itself after six layers resulting in six formula units per hexagonal unit cell with *a* equal to 4.761Å and *c* equal to 12.991Å (Munro, 1997).

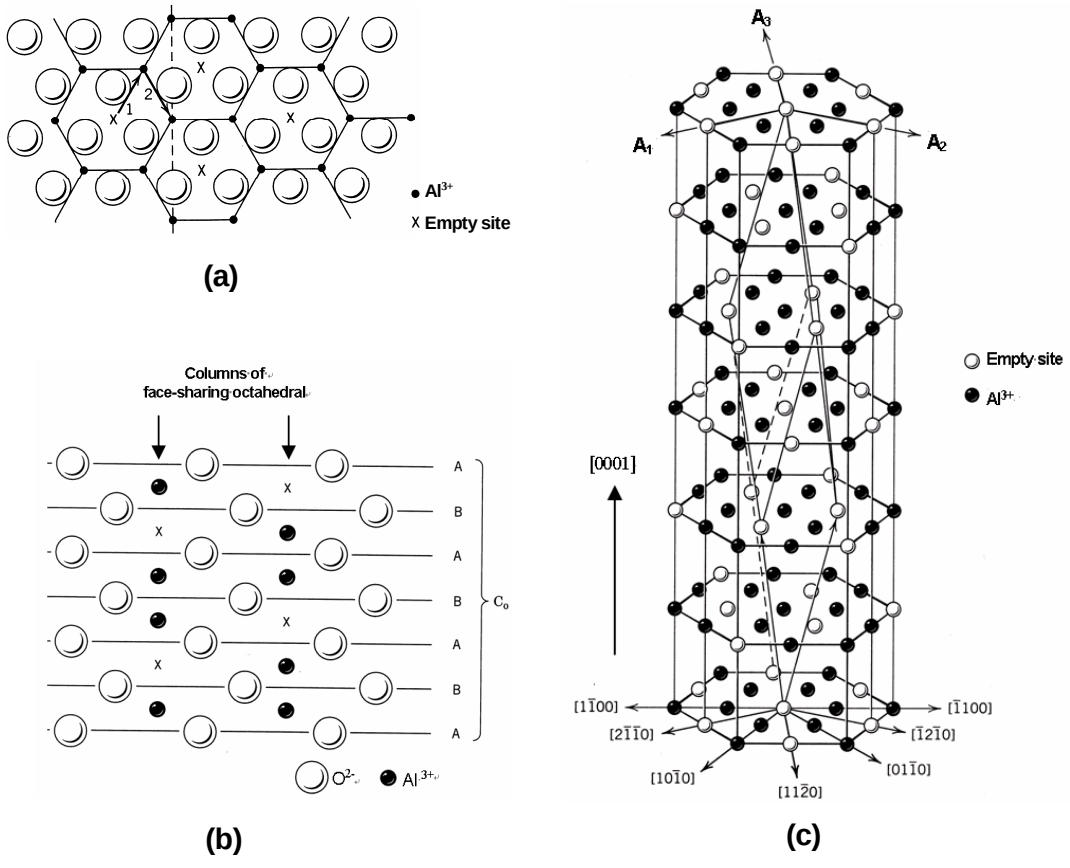

Figure 2.1 Structure of α-Al_2O_3 (Chiang *et al.*, 1997): (a) Filling of two-third of the octahedral sites in the basal plane; (b) Filling of two-third of the octahedral sites along *C* axis; (c) Structural unit cell, showing only the cation sublattice, A_i's are the hexagonal basis vectors

2.2.2. Crystalline structure of SiC

Silicon carbide, with chemical formula SiC, has more than 170 crystalline polytypes, among which 3C, 4H and 6H are the most extensively studied due to their electronic and structural applications (Levinshtein, Rumyantsev and Shur, 2001). The polytypes consist of identical close packed layers, referred to cubic (111) or hexagonal (0001) planes, but differ in the stacking sequences, e.g. *ABC* for 3*C*, *ABAB* for 2*H*, *ABCBA* for 4*H* and *ABCACB* for 6*H* (Park *et al*., 1994). Ramsdell notation (Ramsdell, 1947) is employed here, which consists of a number representing the number of close-packed double layers of silicon and carbon atoms in the unit cell, followed by a letter denoting the Bravais lattice type (*C* for cubic, *H* for hexagonal, *R* for rhombohedral). Therefore, for hexagonal phases, lattice constants vary with polytypes in terms of long axis *c* but have a similar value of *a*, e.g.: a=3.0730 Å, c=10.053 Å for 4H; a=3.0806 Å, c=15.1173 Å for 6H (Levinshtein *et al*., 2001). For comparison, the lattice constant *a* for cubic 3*C*-SiC is equal to 4.3596Å (Levinshtein *et al*., 2001). Generally, longer-period structures are based on combinations of the more commonly observed short-period polytypes, such as 3*C* and *2H*. For structural applications we generally classify the polytypes into β (cubic) and α (hexagonal or rhombohedral) phases. Figure 2.2 shows the unit cells of two typical structures, Zincblende and Wurtzite (Chiang, Birnie and Kingery, 1997), which represent the β-SiC (3*C*) and 2*H*-SiC polytypes respectively (Wyckoff, 1963). The bond between silicon and carbon is covalent resulting from the overlap of sp^3 hybridized orbitals with tetragonal directionality for all polytypes. Tetrahedral interstices with a coordination number of 4 are needed to satisfy this kind of geometry. Zincblende structure (β-SiC or 3*C*) consists of a *FCC* sublattice (silicon or carbon) with one-half of the tetrahedral sites filled through occupying the opposing positions. It is the same as diamond structure if all the atoms are the same. Wurtzite structure contains an *HCP* sublattice with one-half of the tetrahedral sites are filled.

β-SiC whiskers used to reinforce alumina composites are commercially fabricated through carbothermic reduction reactions of low-cost silica and carbon precursors, such as rice hulls (Lee and Cutler, 1975). They are rod-like single crystals with <111> crystallographic

direction parallel to the long axes, which could have an aspect ratio λ up to hundred. Besides the regular or irregular hexagonal cross-sections, Nutt (1984) also observed that SiC whiskers contain immobile partial dislocations, systematic stacking faults and core inclusions that are highly defective, shown in Figure 2.3.

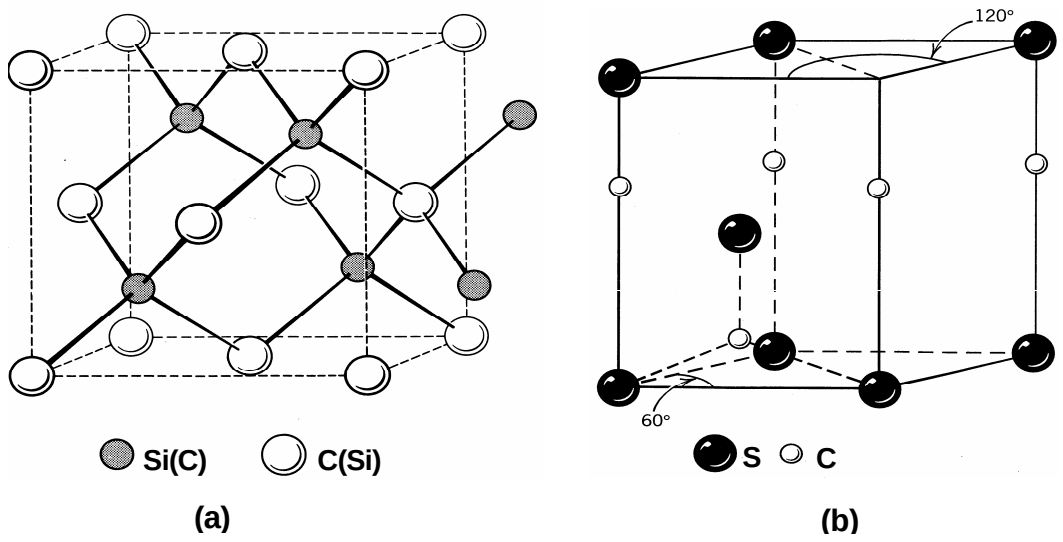

Figure 2.2 Unit cell of the (a) Zincblende structure of β-SiC; (b)Wurtzite structure of 2*H* SiC (From Chiang, Birnie and Kingery, 1997)

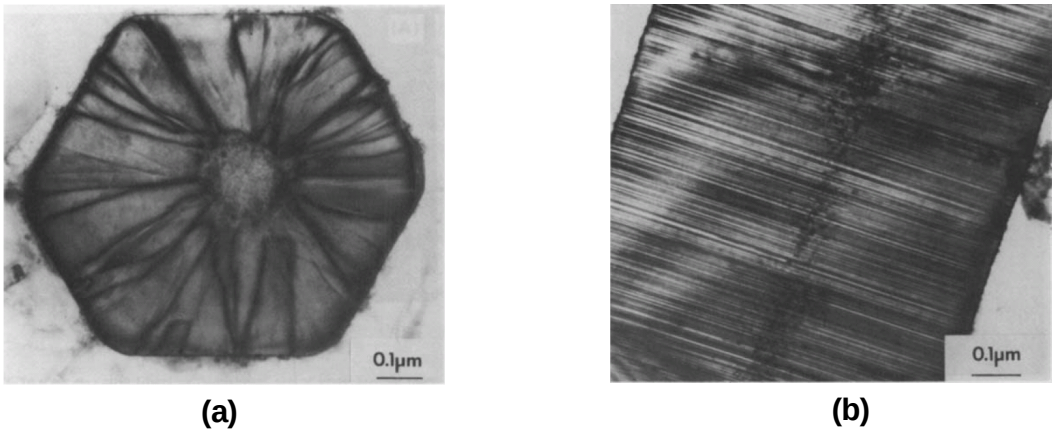

Figure 2.3 TEM images of the as-received β-SiC whiskers: (a) section normal to the axis, showing partial dislocations in radial directions and cavities in core region; (b) Typical distributions of cavities in whiskers with diameters around 5 to 10 *nm*. (Nutt, 1984)

2.2.3. Microstructure of Al_2O_3-SiC_w

Uniaxial hot pressing is commonly employed to fabricate alumina composites reinforced with SiC whiskers, which inevitably yields a whisker texture of preferred orientation with whisker axis normal to the hot-pressing-axis (HPA). Figures 2.4 and 2.5 show SEM micrographs of an Al_2O_3 composite containing 30vol% of SiC whiskers with sample surface perpendicular and parallel to the HPA respectively (Quan, 2004). The formation of a touching whisker network is observed which possesses a nearly plane-random distribution perpendicular to the HPA. Neutron diffraction experiments revealed an average out-of-plane angle of about 21° for this sample (Quan, 2004). A ball milling process is normally involved during fabrication, which significantly decreases the whisker aspect ratio. The regime of interest therefore deals with composites containing whiskers of an averaged diameter around 0.5-1 μm and an aspect ratio λ between 10 and 30 based on experimental data from the literature, e.g. (1) Quan (2004): **10** to **30**; (2) Gu, Porter and Langdon, (1994, 1995): as-fabricated SiC whiskers has averaged aspect ratio around **30**, and the value for whiskers after ball milling is around **10**; (3) Nutt *et al.* (1990, 1993): **5 to 10**; (4) Swan, Swain and Dunlop (*1992*): **10** to **20**; (5) Arellano-Lopez *et al.* (*1990, 1993,1998, 2001*): around **30, 20, 10** and **10**.

Matrix grain size is normally around 1 to 2 μm and sometimes up to 10 μm, depending on the whisker volume fraction and fabrication conditions (e.g. sintering aids, temperature and time). Generally, increasing whisker volume fraction has a counter effect on the grain size. Higher sintering temperature and longer sintering time yield a bigger grain size due to the enhanced diffusion process during sintering. It is well established that the creep strain rate is a function of grain size with an exponent of -2 or -3, depending on the deformation mechanism, whether through lattice or grain boundary diffusion. However, grain size is not of primary interest in the current research but rather the relationship between the reinforcing effect within a quasi-steady matrix microstructure and the externally measured macroscopic variables.

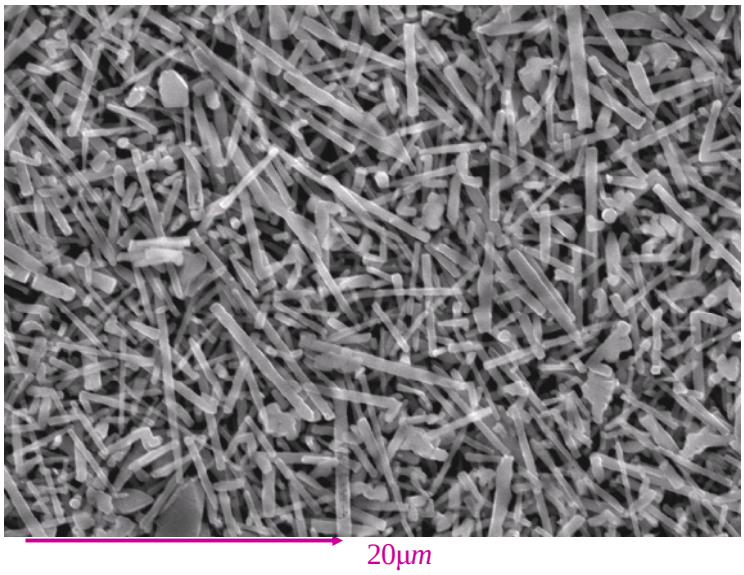

Figure 2.4 A SEM micrograph of Al_2O_3 composite containing 30vol% of SiC whiskers with sample surface perpendicular to Hot-Press-Axis (HPA). The surface was thermally etched at 1400℃ for 2 hours to expose the whiskers (Quan, 2004)

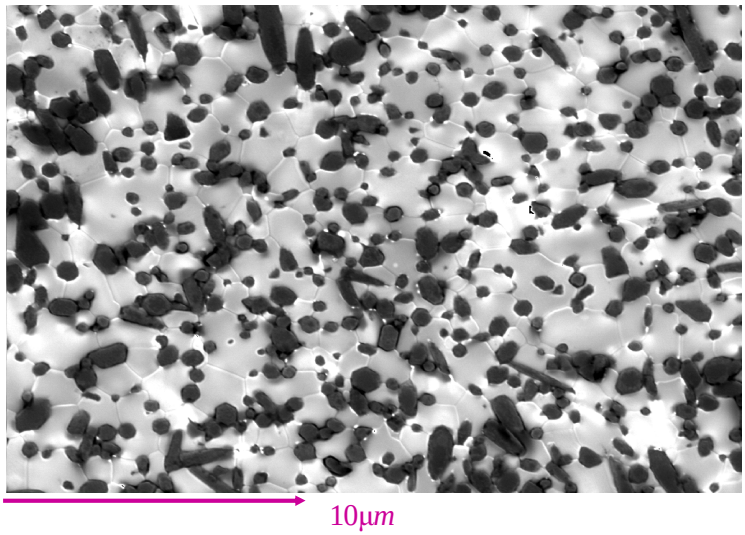

Figure 2.5 A SEM micrograph of Al_2O_3 composite containing 30vol% of SiC whiskers with sample surface parallel to Hot-Press-Axis (HPA) (Quan, 2004)

2.3. Creep mechanisms of single phase Al_2O_3

Reactions of a structural material to applied stresses are very important during engineering applications. Due to the nature of atomic bonding of ceramic materials, which comprise strong and directional covalent or ionic bonds, very limited plastic deformation is observed at room temperature before fracture since very high energy is needed to move dislocations in these structures. Nonetheless, as the temperature is raised, normally above half of the melting point, temperatures at which ceramics are often employed, for example in energy conversion systems, these materials can deform by way of creep. This is a process involving thermally activated dislocation movement or pure mass transport by diffusion through the lattice and/or grain boundary. Therefore, the creep rate at constant stress usually increases exponentially with the temperature showing Arrhenius behavior: $\dot{\varepsilon} \propto \exp(-\Delta G / RT)$, where ΔG is the activation energy, R is the Boltzmann Constant and T is the temperature. Similarly to room temperature plastic flow, creep is caused by the shear, or deviatoric part of the stress field σ_s. The dependence of the creep rate on the stress is generally a power-law relationship $\dot{\varepsilon} \propto \sigma_s^n$ with the stress exponent n determined by the creep controlling process. This section illustrates the creep deformation of single phase alumina, starting from a description of basic creep phenomena and models and then applied to alumina.

2.3.1. Basic creep phenomena

Typically, under constant load tests, creep can be divided into three regimes shown in Figure 2.6, namely: Primary creep, characterized by a decreasing creep strain rate; Secondary or Steady-State creep, characterized by a relatively constant creep strain rate (often referred to as the minimum strain rate); and Tertiary creep, characterized by an increasing strain rate and leading to the final fracture. However, a complete scenario does not always exist during experiments and sometimes a steady-state is not reached. Furthermore, especially for metals, depending on the extent to which the material is work hardened before creep, an increasing creep strain rate might be observed instead of a decreasing one during primary stage. Primary

creep and tertiary creep are also named transient creep in contrast to the steady-state creep, the latter being a state wherein the microstructure of the creeping material has attained a state of dynamic equilibrium.

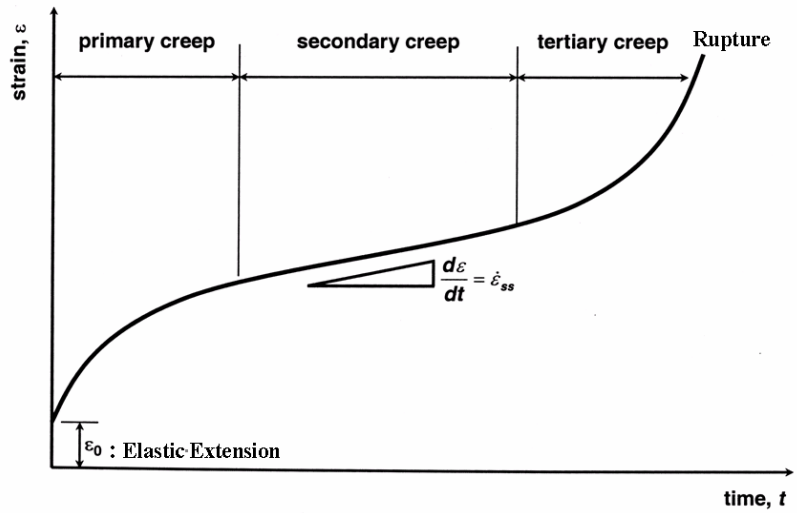

Figure 2.6 A schematic diagram showing the typical creep deformation curve for a monolithic ceramic material (From Kingery *et al.*, 1976)

The total creep strain can be expressed as (Beddoes *et al.*, 1995)

$$\varepsilon_{tot} = \varepsilon_0 + \varepsilon_P + \varepsilon_{SS} + \varepsilon_T = \varepsilon_0 + A\left(1 - \exp(-\frac{t}{\tau})\right) + \dot{\varepsilon}_{SS} \cdot t + B\left(\exp(\frac{t}{\tau}) - 1\right) \qquad (2.1)$$

where ε_{tot} is the total accumulated creep strain, ε_0 is the elastic strain, ε_P is the primary creep strain, ε_{ss} is the steady-state creep strain, ε_T is the tertiary creep strain, A and B are parameters related to strain hardening and softening respectively, τ is a rate constant, also called relaxation time for creep deformation, $\dot{\varepsilon}_{ss}$ is the steady-state creep strain rate, t is the loading time. Each term dominates during the corresponding regime. Generally, a curve fitting procedure is used to determine the parametric values of transient creep strains in Eq. (2.1). This is referred to as the "theta concept" (Wilshire and Evans, 1985) in some of the literature and is a phenomenological method since the theta concept parameters do not directly originate

from consideration of creep deformation physics. On the other hand, steady-state creep strain rate can be derived through physical models based on the creep controlling processes.

2.3.2. Creep models for single phase ceramics

From an engineering point of view, the steady-state creep region with the minimum strain rate is of particular importance since it determines the creep life of structural materials. Therefore, models dealing with creep mechanisms of ceramics within this regime will be illustrated below. The carriers for plastic flow are generally structural defects: point defects such as vacancies and interstitials, dislocations and grain boundaries. Unlike metals, for which the activities of dislocations in terms of climb or glide are responsible for creep deformation, characterized by a higher value of *n*, 3 to 5, diffusional creep is the main mode of deformation at elevated temperature for polycrystalline ceramics with the common value of *n* equal to 1 (Poirier, 1985). It is phenomenologically similar to Newtonian viscous flow ($\sigma = \eta\dot{\varepsilon}$, where η is viscosity) owing to the proportionality between strain rate and stress: $\dot{\varepsilon} \propto \sigma$ (Poirier, 1985). Grain boundaries act as defect sources and sinks under stress. Pure mass transport between grains results in a macroscopic deformation. Depending on the path of diffusion and the accommodation mode, Nabarro-Herring creep, Coble creep and grain boundary sliding (GBS) all contribute to creep strain and any one may be the rate controlling process.

2.3.2.1. Nabarro-Herring creep

A non-hydrostatic stress field could lead to different vacancy concentrations at grain boundaries experiencing different states of stress. A compressive stress results in a depletion of vacancies while a tensile stress results in an excess of vacancies. A diffusive flux of vacancies down the concentration gradient through the lattice causes an equal flux of atoms in the opposite direction. The grains then elongate in the direction of tensile stress and shrink in the direction of the compressive stress. Nabarro (1948) first proposed this mechanism and derived the corresponding macroscopic strain rate. Herring (1950) reached the same conclusion through the chemical potential gradient. The constitutive law is expressed as

$$\dot{\varepsilon}_{NH} = 40\frac{D_{sd}\sigma\Omega}{kTd^2} \quad (2.2)$$

where D_{sd} is the self-diffusion coefficient showing Arrhenius dependence on temperature, σ is the applied stress, Ω is the atomic volume, k is the Boltzmann's Constant, T is the absolute temperature, d is the grain size.

2.3.2.2. Coble creep

If the transport of matter occurs through the grain-boundary instead of the lattice, it is named Coble creep (Coble, 1963), and the constitutional law is expressed as

$$\dot{\varepsilon}_C = 141\frac{D_{gb}\delta\sigma\Omega}{kTd^3} \quad (2.3)$$

where D_{gb} is the grain boundary diffusion coefficient, δ is the grain-boundary thickness, and other parameters have their usual meanings as above.

The stress in equations 2.2 and 2.3 is shear stress. If engineering stress is employed, σ should be replaced by $\sigma/3$. The important difference between Nabarro-Herring and Coble creep lies in the fact that the former mechanism depends on grain size with an exponent of -2 and the latter mechanism with an exponent of -3. It is easy to understand this relationship since transport through the grain boundaries gives an effective diffusion coefficient that depends on δ/d, making the strain rate proportional to $1/d^3$. The two processes are independent or parallel-concurrent and both contribute to the total strain. The faster mechanism controls the creep behavior. The activation energy for lattice diffusion is higher than for grain-boundary diffusion. Therefore, in general, Nabarro-Herring creep can be the dominant mechanism of deformation at high temperatures with grain boundary diffusivity becoming dominant at lower temperatures.

2.3.2.3. Grain-Boundary Sliding (GBS) accommodated by Diffusion Creep

Herring and Coble calculated the diffusion creep rate based on identical spherical grain shape and didn't consider plastic incompatibility. Raj and Ashby (1971) later demonstrated that GBS is an integral part of diffusional creep and that diffusion and sliding are strongly coupled and mutually accommodating (as pointed out earlier by Lifshitz (1963) as one accommodating mode for GBS in addition to dislocation flow). The resulting deformation is correctly described either as diffusional creep or as grain boundary sliding with diffusional accommodation. The constitutive law is expressed as (Raj and Ashby, 1971):

$$\dot{\varepsilon}_{GBS} = 42\frac{D_{eff}\sigma\Omega}{kTd^2} \tag{2.4}$$

D_{eff} is an effective diffusion coefficient:

$$D_{eff} = D_{sd}\left(1+\frac{\pi\delta}{d}\frac{D_{gb}}{D_{sd}}\right) \tag{2.5}$$

Note that for lattice diffusion alone, equation 2.4 gives the same expression for creep-rate as the Nabarro-Herring theory and for grain-boundary diffusion alone is practically identical with the Coble expression. Still, the faster one is rate limiting. Generally, the diffusional process is ambipolar in ceramics which involves coupled transport of charged species through a common internal electric field in order to maintain the mass and charge balance of the stoichiometric ratio and avoid decomposition of the compound (Chiang *et al.*, 1997). While each ion can diffuse either through the lattice or grain boundary, the slowest ion in its fastest path controls the rate. For a pure binary compound M_xO_y, D_{eff} for use with Equation 2.4 becomes (Gordon, 1973)

$$D_{eff} = \frac{(x+y)\left(D_{sd}^{M}+\frac{\pi\delta D_{gb}^{M}}{d}\right)\left(D_{sd}^{O}+\frac{\pi\delta D_{gb}^{O}}{d}\right)}{y\left(D_{sd}^{M}+\frac{\pi\delta D_{gb}^{M}}{d}\right)+x\left(D_{sd}^{O}+\frac{\pi\delta D_{gb}^{O}}{d}\right)} \tag{2.6}$$

2.3.2.4. Other mechanisms

Diffusional creep dominates over a broad range of stress, grain size and temperature. However, grain boundaries do not always act as perfect sinks or sources of defects as assumed above. Sometimes, the interface reaction could be rate-controlling and display non-Newtonian behavior (n>1). One important thing to be mentioned is that the rate-controlling process does not necessarily contribute the majority of the strain, similarly as how dislocation glide provides the strain but the creep rate might be controlled by the dislocation climb through diffusion. Therefore, the activation energy of dislocation creep is normally the activation energy of self-diffusion. Besides interface-control, non-accommodated GBS at high stress also shifts the stress exponent from 1. While the kinetics of diffusion is not rapid enough, cavities then form and lead to the final fracture.

Furthermore, GBS, a major mode of deformation during high temperature creep, is in fact stochastic and history independent (Blanchard *et al.*, 1998). It is also the important mechanism for superplasticity, characterized by a stress exponent of 2, without elongation of grains. Large strain is achieved through a neighbour-switching event and the accommodating diffusion occurs over a shorter distance compared with diffusional creep. The models developed by Ashby and Verrall(1973) and Gifkins (1976, 1978) treat this process in detail. Table 2.2 summarizes some creep deformation mechanisms encountered frequently by ceramics with the emphasis on GBS.

Table 2.2 Values of *n, p* and *Q* for creep mechanisms (Cannon *et al.*, 1983; Poirier, 1985)

Mechanism	***n***	***P***	***Q***	Reference
(Ⅰ) Dislocation glide and climb:				
(a) controlled by climb	4.5		Q_l	Weertman
(b) controlled by glide	3		Q_{ci}	Weertman
(Ⅱ) Grain Boundary Sliding				
(1) Lifshitz sliding				
Sliding accommodated by diffusion:				
(a) through lattice	1	2	Q_l	Nabarro-Herring
(b) through boundary	1	3	Q_{gb}	Coble
(c) lattice + boundary	1	2 or 3		Raj&Ashby
(d) controlled by interface reaction	2	1	Q_l or Q_{gb}	
Sliding accommodated by intragranular flow across the grains	1	1	Q_{gb}	Crossman&Ashby
(2) Rachinger sliding				
With a continuous glassy phase at the boundary	1	1	Q_{ph}	Orowan
Without a glassy phase:				
(a) Sliding accommodated by formation of GB cavities	2	1	Q_l	Langdon
(b) Sliding accommodated by formation of triple-point folds	3.5	2	Q_l	Gifkins
(3) Superplasticity	2	2	Q_{gb}	Gifkins

** Power-law constitutive relationship: $\dot{\varepsilon} = C\sigma^n d^{-p} \exp(-Q/RT)$. In contrast to the Lifshitz sliding, Rachinger sliding occurs without concomitant grain elongation. Q_l, Q_{gb}, Q_{ci} and Q_{ph} are the activation energies for lattice self-diffusion, grain boundary diffusion, chemical inter-diffusion of solute atoms and the energy associated with the grain boundary liquid phase.

2.3.3. Creep behavior of alumina

Creep deformation of alumina has been extensively studied over the past several decades. It is well accepted that the main mechanism is diffusional creep over the range of interest. Work by Cannon *et al.* (1980) shows the observation of interface controlled diffusional creep at low σ which shifts *n* from 1 to 2. However, diffusional creep dominates

over a range of temperatures (1200 to 1750℃), stresses (1.4 to 310MPa) and grain sizes (1 to 15 μm). A threshold stress exists below which no creep occurs. This decreases more rapidly with increasing temperature (e.g. 23.4MPa at 1192℃ to 8.3MPa at 1418℃) than does the shear modulus. Furthermore, basal slip ($\sigma / G > 10^{-3}$) and non-accommodated GBS are also observed via TEM (Heuer *et al.*, 1980). A stress-grain size deformation map (Figure 2.7) is then constructed identifying the dominant deformation mechanisms (Heuer *et al.*, 1980).

The grain size exponent is between -2.7~ -2.9 suggesting that both lattice and grain boundary diffusion are important (Cannon *et al.*, 1980). Generally, for bulk diffusion, $D_l^{Al} \gg D_l^{O}$, for grain boundary diffusion $D_b^{O} \gg D_b^{Al}$ (Coble *et al.*, 1978). Each species/path combination might control in a specific grain size range, as shown in Figure 2.8 (Coble *et al.*, 1978). The diffusion of aluminum involves migration of charged *Al* defects, $Al_i^{\bullet\bullet\bullet}$ or $V_{Al}^{'''}$, while the oxygen diffusion in the bulk involves $V_O^{\bullet\bullet}$ and at grain boundaries is due to migration of neutral interstitial oxygen atoms $O_i^{\times}$ (Kröger, 1984).

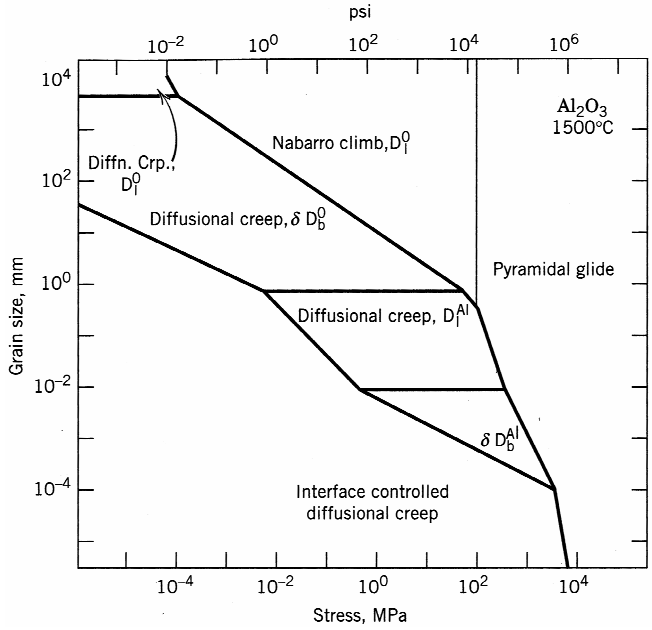

Figure 2.7 Deformation map for MgO doped Al_2O_3 at 1500℃(Chiang *et al.*, 1997; Heuer *et al.*, 1980)

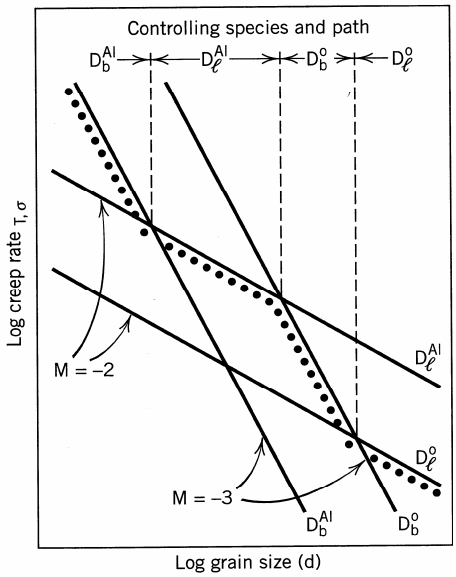

Figure 2.8 A schematic diagram showing the logarithm of creep rate vs logarithm of grain size for Al_2O_3. Solid lines show the creep rate dependence on grain size for each assumed species (Al or O) and path (lattice or grain boundary) controlling the rate. The dotted line traces the rate-controlling mechanism: the slower ion along its fastest path.(Chiang *et al.*, 1997; Coble *et al.*, 1978)

2.4. Creep mechanisms of Al_2O_3-SiC_w

Creep behavior of SiC whisker reinforced Al_2O_3 has been extensively studied by several groups (Lipetzky *et al.*, 1988, 1991; Lin *et al.*, 1990, 1991, 1996; Nutt *et al.*, 1990, 1993; Arellano-Lopez *et al.*, 1990, 1993, 1998, 2000, 2001; Swan *et al.*, *1992*; Gu *et al.*, 1994, 1995; Romero *et al.*, 1995; O'Meara *et al.*, 1996; Quan, 2004) since Chokshi and Porter (1985) published the first paper on the creep properties of this system. Due to the variations in processing routes, microstructures (the volume fraction of whiskers; the strength of the interfacial bond; grain size of the matrix; impurity; percent of glassy phases; oxidation susceptibility) and experimental methods (compressive, tensile and flexural), a direct comparison of the reported creep data is very difficult. Instead of exact values, this section summarizes some salient tendencies with an emphasis on whisker volume fraction effect, stress dependence, grain size dependence, activation energy and microstructures such as glassy phases and damage after creep.

2.4.1. Whisker volume fraction effect

Generally, the addition of SiC whiskers into an alumina matrix yields a lower creep rate provided that the microstructures are comparable (e.g., grain size and damage). For composites containing whiskers at less than 15vol%, the strain rates do not change by more than a factor of 4 compared with monolithic alumina. Above that, the creep rate of pure alumina could be reduced by up to 2 orders of magnitude using whisker additions (Figure 2.9(a)). The dependence of absolute creep rate on whisker concentration is complex (Figure 2.9(b)), as pointed out by Lin and Becher (1990, 1991). They found that creep resistance generally increases with increasing whisker loading until the volume fraction reaches about 30%. Then, due to the counter effect of grain size and the extensive formation of creep damage, no further increase is found. Furthermore, a smaller strain before fracture is observed.

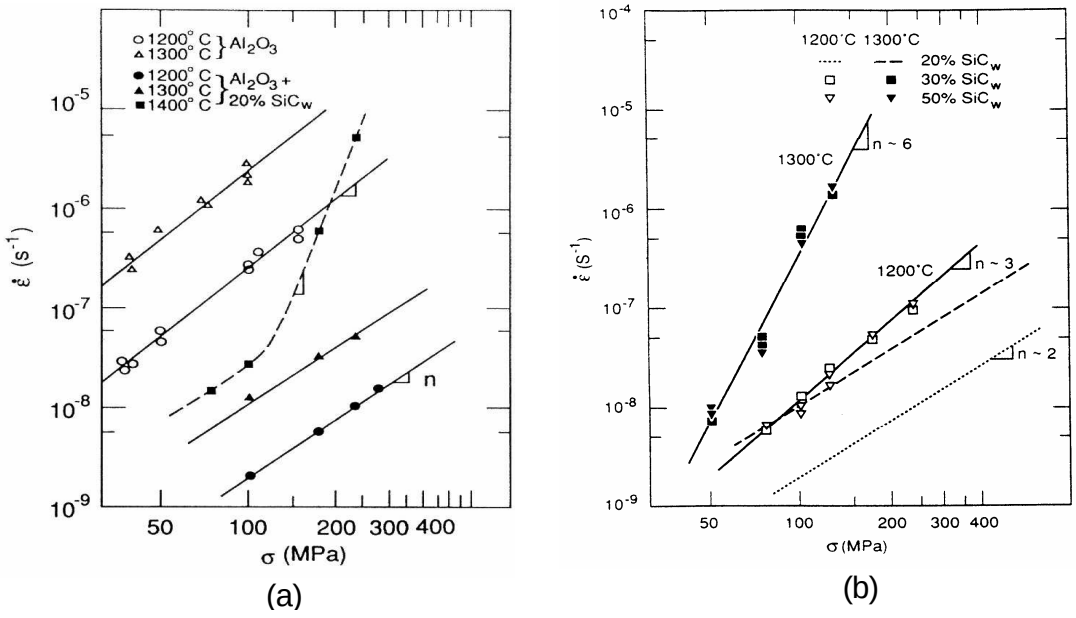

Figure 2.9 (a) Steady creep rate vs stress relationship for polycrystalline Al_2O_3 and Al_2O_3-SiC_w within temperature range of 1200-1400℃ from flexural experiments (Lin *et al.*, 1990); (b) Steady creep rate vs stress relationship for Al_2O_3-SiC_w with whisker up to 50vol% from flexural experiments (Lin *et al.*, 1991)

A longer primary stage is observed than in pure alumina (Lin *et al.*, 1990, 1996; Swan *et al.*, 1992; Romero *et al.*, 1995). This is interpreted as a long-range stress relaxation

process related to whisker network deformation (Wilkinson, 1998) since the primary stage is usually related to an internal stress distribution which decays with time (Frost and Ashby, 1982).

2.4.2. Stress dependence *n*

There are two distinct regimes of interest for the stress dependence. At moderate temperatures and stresses, the stress exponent tends to lie between 1 and 2, which is attributed to the diffusion-accommodated GBS, as with pure alumina. Above a critical stress, depending on the microstructure and testing environment, a value above 2 is obtained. From the microstructural observation, this is generally attributed to a damage accumulation process instead of dislocation creep (Lipetzky *et al.*, 1988, 1991; Lin *et al.*, 1990, 1991; Swan *et al.*, 1992; Romero *et al.*, 1995; O'Meara *et al.*, 1996). Bimodal behaviour is observed by several separate studies (Chokshi and Porter, 1985; Lipetzky *et al.*, 1988, 1991; Lin *et al*., 1990, 1991) with a pronounced stress exponent shift (Figure 2.9(a)) indicating the change of the dominant deformation mechanism. Generally, tensile and flexural creep tests result in a higher value of *n* than compressive tests due to more extensive damage; for example, Nutt *et al.* obtained 3 for compressive creep and 5 for flexural creep (1993), while Quan (2004) found a value as high as 11 for tensile creep tests.

2.4.3. Grain size dependence *p*

From the work by Lin and Becher (1996), Arellano-Lopez *et al.* (1990, 1993, 1998, 2000, 2001), creep rate generally decreases with increasing grain size provided the whisker loading is the same. However, no direct grain size dependence was observed without detailed information on the microstructure. For example, Lin *et al.* found a value of 1 at 1200℃ while at 1300℃ the creep rate was independent of matrix grain size. The latter case is attributed to the enhanced nucleation and coalescence of creep cavities and the development of macroscopic cracks. Instead, Arellano-Lopez *et al.* found that the effective grain size, and the distance between the whiskers, is more important than the nominal grain size when normalizing the creep rate by a grain size exponent of 3.

2.4.4. Activation energy *Q*

For micron grain size polycrystalline Al_2O_3, creep deformation is generally controlled by the diffusion of alumina through the lattice with Q=478*kJ*/*mol*, or grain boundary with Q=418*kJ*/*mol* (Cannon *et al.* 1980, Figure 2.7). However, for composites, activation energy shows a broader range between 210-966*kJ/mol* depending on the test mode, temperature range, stress range and microstructure, which might suggest more complicated deformation mechanisms for the composites.

2.4.5. Microstructures after creep

As specified in the stress dependence section, the higher value of n is attributed to creep damage. There are two categories of damage after creep: (1) nucleation and coalescence of submicron sized creep cavities at triple grain boundaries, grain-boundary-interfaces (GBI), and along grain boundary faces; (2) development of macroscopic cracks ($\geqslant$10μm). Figure 2.10 shows typical TEM observation for each of these. Creep damage contributes a significant portion of the creep strain. Generally, tensile creep (O'Meara *et al.*, 1996) results in more extensive damage than flexural (Lin *et al.*, 1991; Nutt *et al.*, 1993; Romero *et al.*, 1995) and compressive creep (Swan *et al.*, 1992). Whisker additions inhibit the GBS and act as stress concentration sites, resulting in creep damage. Furthermore, oxidation of SiC yields CaO-containing aluminosilicate glass that lubricates GBS and yields more cavities since diffusion is not fast enough to accommodate GBS (Lin *et al.*, 1991). Thus, creep in air normally results in a higher creep rate than in an inert atmosphere due to the severe oxidation and glassy phase (Lipetzky *et al.*, 1991; Nutt *et al.*, 1993). Unlike cavities, the macroscopic cracks generally originated from the surface, and the distribution, type, size and severity of the cracks varied with temperature and stress (O'Meara *et al.*, 1996). Creep damage promotes oxidation via providing diffusion paths for oxygen and oxidation promotes creep damage with the aid of glassy phase. Meanwhile, the thin film of glassy phase associated with the cavity also comes from the sintering additives (i.e. Y_2O_3, plus MgO) in addition to the oxidation of whiskers (Lin *et al.*, 1991).

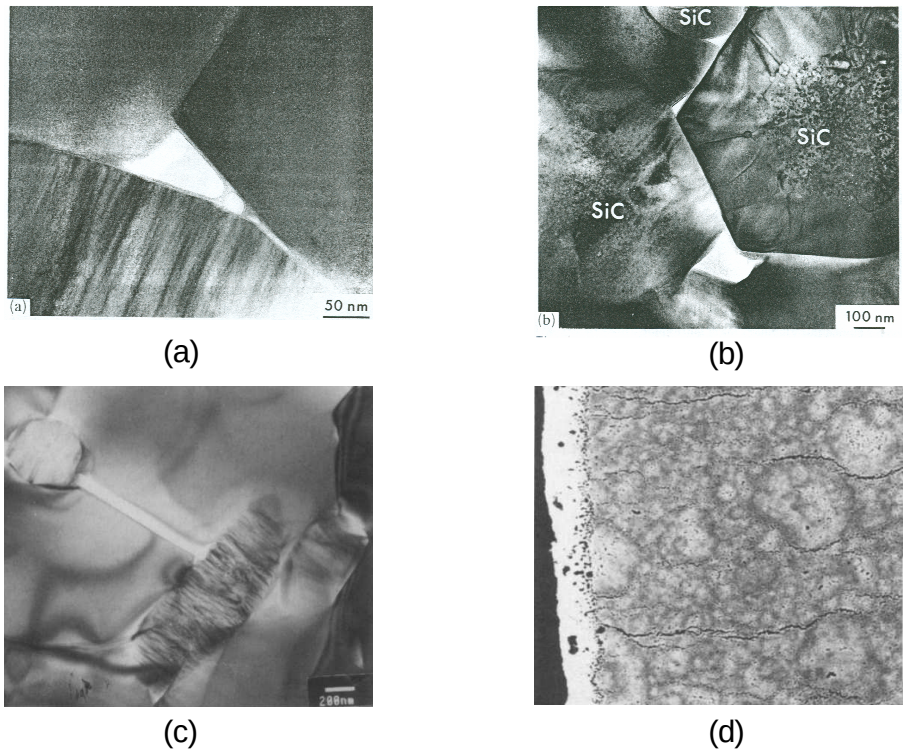

Figure 2.10 (a) cavitation at triple grain boundary (Nutt *et al.*, 1993); (b) cavitation at GBI (Nutt *et al.*, 1993); (c) cavity between two grains (O'Meara *et al.*, 1996); (d) macroscopic cracks (O'Meara *et al.*, 1996)

2.4.6. Summary

The creep behaviour of Al_2O_3-SiC_w is very complicated and the traditional analysis methodology used for a single phase ceramic such as diffusional creep and grain boundary sliding is not adequate. A more complete picture of creep in ceramic composites involves both the creep of ceramics and the reinforcing effect and load transfer within composites. Section 2.5 thus introduces the basic models developed for composites in a micro-continuum field such as rule of mixtures and the shear lag model. Following that the model dealing with two-phase ceramics developed by Wilkinson and Pompe (1998) will be described.

2.5. Models for elastic and creep behavior of composites

A composite is generally a mixture of at least two chemically distinct materials with a distinct interface between them. Composites are often characterized in the first instance by the matrix material (metal, ceramic or polymer) reinforcement type (particle, continuous fibre, short fibre or whisker) (Taya, 1989). From a design engineering point of view, predicting the overall behaviour (constitutive relationships for thermo-elasticity, plasticity/creep and heat conduction) of a composite by appropriate formulae from the already known thermo-mechanical behaviour of the individual constituents is critical to developing new composites with unique properties. This is a procedure generally referred to as homogenization. Mathematically, analytical models developed from a specific system are applicable to any composite systems, despite that the morphology, volume fraction and distribution of inclusions determine the application range and accuracy. Furthermore, the methodology is extendable from elastic to other properties. In this section, basic composite models for elastic behaviour are illustrated, followed by a discussion of the creep theories. No attempt is made to provide a complete summary of composite theories, rather the basic ones related to the topic of this research are noted.

2.5.1. Micromechanical composite models

2.5.1.1. Rule of mixtures

For a continuous aligned fibre reinforced composite with fibre volume fraction V_f, if loaded along the fibre axis direction, the strain in the matrix is equal to the strain in the fibres provided that there is no interfacial sliding. The axial Young's modulus is expressed as (Voigt, 1889)

$$E_c = E_m(1-V_f) + E_f V_f \tag{2.7}$$

In addition, if the composite is loaded transversely, the stress in the matrix is assumed to be the same as in the fibres. The transverse Young's modulus is expressed as (Reuss, 1929)

$$\frac{1}{E_c} = \frac{(1-V_f)}{E_m} + \frac{V_f}{E_f} \tag{2.8}$$

The well-known Voigt-Reuss rule is expected to be valid to a high degree of precision for continuous fibre reinforced composites. In fact, the iso-stress condition is not as accurate as the iso-strain condition since there are stress concentration regions above and below the fibres within composites under transverse load, as verified by the photoelastic experiments (Hull *et al.*, 1996). Nonetheless, these models provide upper and lower bounds for composite properties.

2.5.1.2. Shear lag model

The fibres in our materials are not in practice very long and for that reason the iso-strain assumption is not applicable. The most widely used model dealing with the effect of loading an aligned short-fibre composite disposed in continuous lines either end to end (Figure 2.11(a)) or with a slight overlap is the shear lag model (Cox, 1951). It describes the transfer of load from matrix to fibre near the fibre ends by means of interfacial shear stresses. A unit cell with length L and width D (Figure 2.11(b)) is assumed to contain a straight fibre with length l and diameter R embedded in a solid matrix. Let this aligned short fibre composite be subjected to an applied uniaxial strain ε along the x-direction. The axial displacements at distance x in the fibre and the matrix at the same point if the fibre were absent are denoted by u and v, respectively. The difference $(u-v)$, which represents the rate of transfer of load from matrix to fibre is assumed to be proportional to the shear stress at the interface τ_i or $d\sigma_f / dx$. By considering the force equilibrium in a free body diagram shown in Figure 2.11(c), one could obtain

$$\frac{d\sigma_f}{dx} = -\frac{4\tau_i}{R} = h(u-v) \tag{2.9}$$

where σ_f is the axial stress in the fibre and *h* is a constant. Since $\sigma_f = E_f du/dx$ from Hooke's law, and since $\varepsilon = dv/dx$, we have the ordinary differential equation

$$\frac{d^2\sigma_f}{dx^2} = h\left(\frac{\sigma_f}{E_f} - \varepsilon\right) \tag{2.10}$$

The general solution to equation (2.10) is given by

$$\sigma_f = E_f\varepsilon + C_1 \cosh \beta x + C_2 \sinh \beta x \tag{2.11}$$

where $\beta = \sqrt{h/E_f}$ and C_1 and C_2 are constants which could be obtained by applying the boundary conditions $\sigma_f = 0$ at $x = \pm l/2$. The stress field in the fibre is then given by

$$\sigma_f = E_f\varepsilon\left(1 - \frac{\cosh \beta x}{\cosh(\beta l/2)}\right) \tag{2.12}$$

Substituted into equation (2.9), the shear stress in the matrix is expressed as

$$\tau_i = E_f\varepsilon\sqrt{\frac{G_m/E_f}{2\ln(D/R)}}\frac{\sinh \beta x}{\cosh(\beta l/2)} \tag{2.13}$$

Since the model assumes no load is transferred across the end faces of a fibre (which is in fact not completely accurate), the tensile stress in a fibre builds up from the ends. The shear stress has a maximum at the fibre ends and a minimum at the fibre centre. Figure 2.12 shows schematic variations of stresses along the fibre which are verified via photoelasticity and Micro-Raman Spectroscopy (Mehan *et al.*, 2000). It is obvious that a longer fibre transfers the load more efficiently, and a stress transfer length exists which should be reached when

choosing the fibre aspect ratio λ ($\lambda = l/R$).

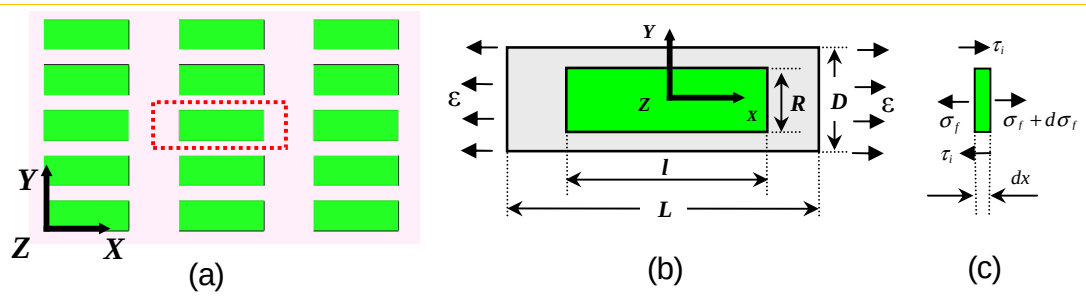

Figure 2.11 Schematic illustration of the shear lag model: (a) representative short fibre composite; (b) unit cell for analysis; (c) finite length *dx* and stresses around.

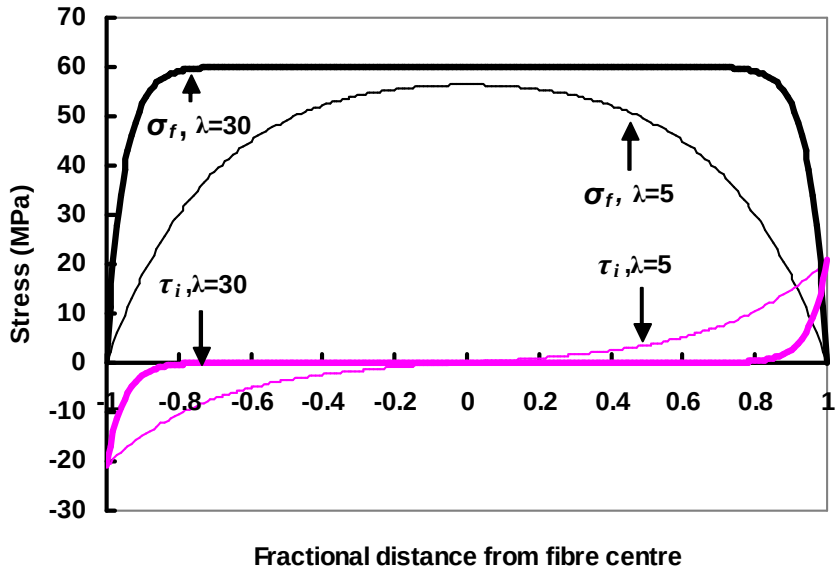

Figure 2.12 Predicted variations in fibre tensile stress (black lines) and interfacial shear stress (purple lines) along the length of a SiC whisker, *R*=0.5μm, V_f=10%, *e*=1x10^{-4}, E_f=600GPa, G_m=100GPa.

The mean stress in the fibre is computed as

$$\overline{\sigma}_f = \frac{2}{l}\int_0^{l/2}\sigma_f dx = E_f\varepsilon\left(1-\frac{\tanh(\beta l/2)}{\beta l/2}\right) \qquad (2.14)$$

Combining equation (2.14) and (2.7), the Young's modulus of the composite will be

$$E_c = E_f V_f \left(1 - \frac{\tanh(\beta l/2)}{\beta l/2}\right) + E_m(1 - V_f) \tag{2.15}$$

In order to solve for the constants h and β, consider next the displacement along the x-direction at an arbitrary point y in the matrix, w, where $w_{(y=R/2)} = u$, and $w_{(y=D/2)} = v$. The force equilibrium at $y=R/2$ and $y = y$ provides $2\pi y\tau = 2\pi(R/2)\tau_i$. The shear strain γ and stress τ at $y=y$ is then expressed as $\gamma = \frac{dw}{dy} = \frac{\tau}{G_m} = \frac{\tau_i}{2G_m}\frac{R}{y}$, where G_m is the shear modulus of the matrix. Integrating from $y=R/2$ to $y=D/2$, we obtain $v - u = \frac{\tau_i R}{2G_m}\ln\left(\frac{D}{R}\right)$. Combining with equation (2.9), we get

$$h = \frac{8G_m}{R^2 \ln(D/R)} \tag{2.16a}$$

$$\beta = \frac{2\sqrt{2}}{R}\sqrt{\frac{G_m/E_f}{\ln(D/R)}} \tag{2.16b}$$

2.5.1.3. Other models

Rule of mixtures and the shear lag models tend to give poor estimates for the thermo-mechanical properties of a composite where the aspect ratio is small and distribution is complicated. However, it is difficult for an analysis in terms of stress to combine reasonable simplicity with conceptual accuracy. More sophisticated methods are developed at the expense of the detailed stress information and are generally based on: (1) mean field method, which assumes a uniform stress distribution within fibres and matrix respectively, such as Eshelby's models (1957) and extended self-consistent model (Hill, 1965); or (2) variational principle in terms of energy dissipated, such as Hashin-Shtrikman's bounds (1962). Figure 2.13 shows schematic predictions of different models summarized by Mura (1987).

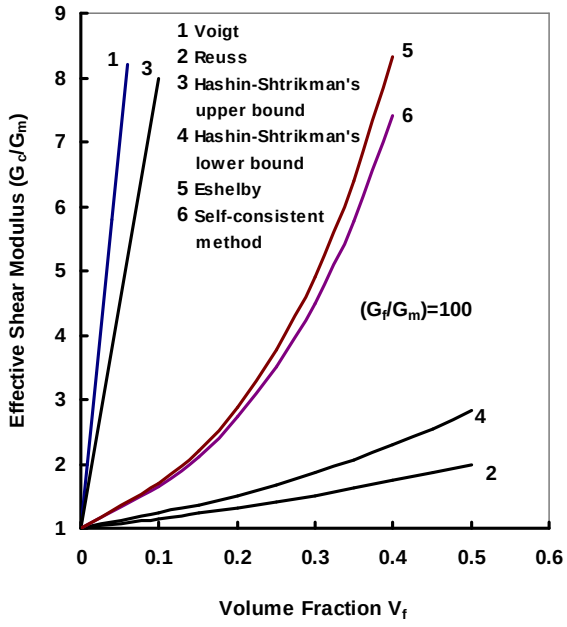

Figure 2.13 Effective shear modulus of particle composite vs volume fraction V_f, provided that the ratio of the fibre shear modulus to the matrix's was kept 100 (Mura, 1987).

2.5.2. Creep models for composite materials

2.5.2.1. Shear lag model

Several analytical models based on shear lag analysis are developed to predict the steady-state creep rate of an aligned short fibre composite (Mclean, 1972; Kelly *et al.*, 1972; Taya *et al.*, 1989). The frictional force between the creeping matrix and the more rigid fibres oppose the extension of the former producing an increased shear of the matrix and hence a shearing force. A common feature of these treatments is neglecting elastic strains, which are best applicable when the plastic strain is substantially greater than the elastic. For example, Mclean (1972) considered a simple case where rigid short fibres are embedded in a creeping matrix in shear obeying power-law constitutive law. Still, the load transfer to the fibre via direct stresses across their ends is generally neglected and a perfect bonding is assumed. A

geometrical argument shows that shear strain in the composite is amplified by $l/2(D-R)$ due to the presence of rigid fibre. Then the shear stress is amplified by $(l/2(D-R))^{1/n}$, where n is the stress exponent. If all the external work is dissipated through creep of the matrix, the stress of the composite is amplified as $\sigma_c = V_m(l/(D-R))^{1+1/n}\sigma_0$ in order to extend the composite at the same rate as that produced by σ_0 if fibres were absent. Considering force equilibrium as before, tensile stress along the fibre could be obtained as

$$\sigma_f = \frac{4n}{R(1+n)}\left(\frac{\dot{\varepsilon}}{\beta'}\right)\left[\left(\frac{l}{2}\right)^{1+1/n} - x^{1+1/n}\right] \qquad (2.17)$$

where β' is the appropriate proportionality factor. Figure 2.14 shows schematically the variation of fibre stress for several values of n. The plateau shaped distribution for elastic deformation is changed toward a continuously increasing one for creep deformation.

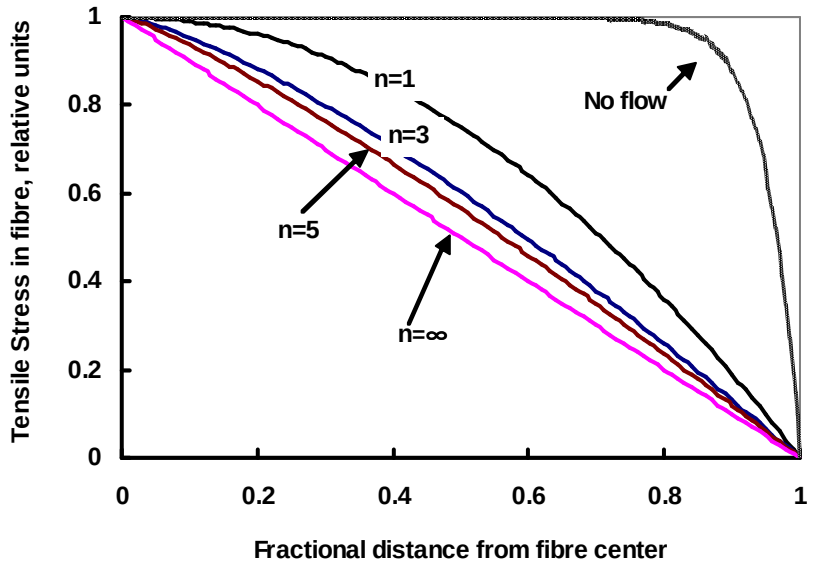

Figure 2.14 Predicted variations in fibre tensile stress (McLean, 1972).

2.5.2.2. Creep mechanisms in multiphase ceramics (Wilkinson, 1998)

The increase of creep resistance through the addition of hard, second-phase particles depends on the volume fraction, morphology and distribution of the reinforcing phase. In 1998, Wilkinson gave a critical review on the creep mechanisms in multiphase ceramics in terms of rheological theory ($\dot{\varepsilon} = \sigma / \eta$) which emphasizes the importance of network formation that is otherwise neglected by other theories. All systems considered have a reinforcing phase with a considerably higher creep resistance than the matrix and could be treated as if it were perfectly elastic, e.g., whisker-reinforced ceramics (e.g. Al_2O_3-SiC_w); infiltrated powder compacts (e.g. siliconized SiC) and glass-bonded ceramics (e.g. sintered Si_3N_4). There are several interactions that occur over the whole range of volume fraction. At low volume fractions, the inclusions behave independently of one another and the effect is due to the disturbance of the flow field around the inclusions. As the volume fraction of inclusions increases, interactions begin to take effect. A percolating network of point-to-point contacts is developed when the volume fraction is above a critical value, *point-contact percolation* threshold ϕ_{pcp}, which depends on inclusion morphology and orientation. For spherical particles of uniform size, this occurs at about 16vol% (Grannan *et al.*, 1981) and decreases for fibers with increasing aspect ratio. Theoretical calculations specific to a fiber geometry with a random distribution approximate the percolation threshold as (Nan, 1993):

$$\phi_{pcp} = \frac{0.7}{\lambda} \tag{2.18}$$

Thus, a very small volume fraction is needed for high-aspect ratio whiskers to develop an interconnected network (e.g., $\phi_{pcp} = 4vol\%$ for $\lambda = 20$). Since the whiskers are likely to orient normal to the hot pressing axis (HPA) during fabrication and more than one contact per particle is needed for a highly developed network, this value will in practice be larger, perhaps by a factor of two or so. Creep then requires the compatible deformation of this network (e.g., squeezing out of the matrix from near contact regions and bending of whiskers). As the volume fraction increases, a second threshold is reached which is referred to as the

facet-contact percolation threshold ϕ_{fcp}. It could be related to the random, close-packed structure, e.g. 63vol% for spherical particles, and considerably lower limit applies for elongated particles. However, a theoretical treatment for the onset of facet-contact percolation has yet to be developed. Within this structure, the rotation and long-range motion of individual inclusions becomes highly restricted, and creep is controlled by flow within the interfacet regions (e.g. flow of glass between Si_3N_4 grains). Figure 2.15 shows the schematic illustration of network development for point-contact percolation and facet-contact percolation (Wilkinson, 1998).

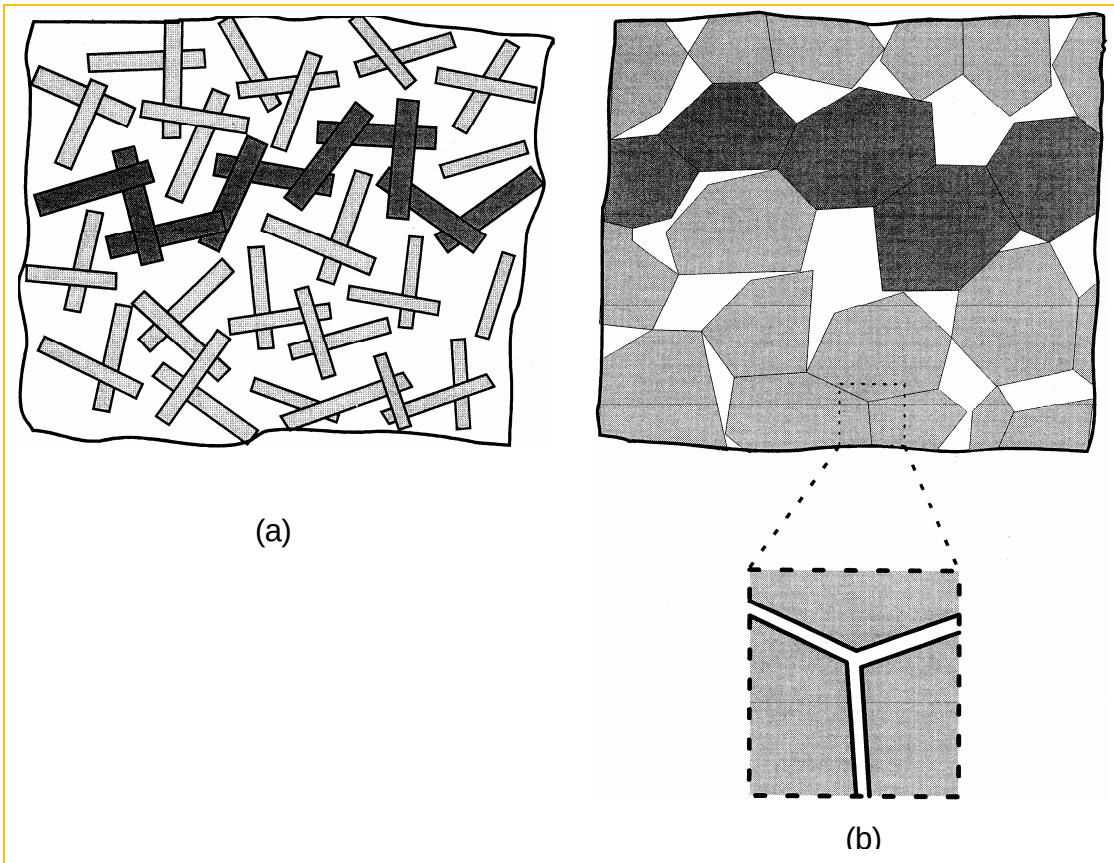

Figure 2.15 Schematic illustration of network development in multiphase ceramic materials: (a) point-contact percolation in a whisker- or platelet- reinforced ceramic; (b) facet-contact percolation with most of the particle interactions involve full facet contacts. Thin grain-boundary layers separate the facets (shown in the inset), and creep occurs by the squeezing of this material from between the facets under compression (Wilkinson, 1998).

In summary, composites consisting of discrete particles embedded in a creeping matrix can be divided into three distinct volume fraction regimes: (1) $V_f < \phi_{pcp}$; (2) $\phi_{pcp} < V_f < \phi_{fcp}$; (3) $V_f > \phi_{fcp}$. Models developed for different ranges of volume fractions have been reviewed and compared with the observed experimental data. For example, infiltrated powder compacts (siliconized SiC) and glass-bonded ceramics (sintered Si_3N_4) are well above the facet-contact percolation and the data from experiments agree well with the rheological model.

For particulate-reinforced ceramics, such as SiC whisker reinforced alumina, the range of volume fractions straddles the critical value for point-contact percolation. A series of models developed by Wilkinson and Pompe (1998) for the creep and anelastic recovery of whisker- and platelet-reinforced ceramics are also reviewed. These models provide critical explanations for the increase in creep resistance and the effect of network on the anelastic recovery observed in the whisker-reinforced ceramics. Three different creep mechanisms are envisaged (Wilkinson and Pompe, 1998):

(1) When $V_f < \phi_{pcp}$, the particles behave independently and their effects can be attributed mainly to the local increase in effective diffusion path. The increase of viscosity η (decrease of creep rate $\dot{\varepsilon}$) is modelled from the unconstrained rotation of particles in a viscous matrix (Figure 2.16 (a)). The matrix far from the particles inherits its intrinsic viscosity η_0 and the regions near the particles enclosed in dashed lines are constrained locally, which has a higher viscosity η_r. Then a composite homogenization procedure, described by the Hashin equation (Hashin, 1962) is employed to obtain the effective composite viscosity

$$\frac{\eta_{dl}}{\eta_0} = 1 + 2.5\frac{v_{con}}{1 - v_{con}} \tag{2.19}$$

with

$$v_{con} = \left(\frac{\lambda}{2} \langle \sin 2\theta \rangle + \langle \cos^2 \theta \rangle \right) \cdot V_f \qquad (2.19a)$$

where v_{con} is the constrained volume fraction and θ is the angle between loading direction and particle axis. This leads to viscosities up to a factor of two larger than for the unreinforced matrix.

(2) When $V_f > \phi_{pcp}$, a network is formed. Due to the hot pressing fabrication process, most whiskers align within the plane normal to the HPA (Hot pressing axis). Wilkinson and Pompe (1998) thus assumed an idealized regular whisker network with the whiskers forming a series of aligned layers, each one of which is oriented normal to the one below, as shown in Figure 2.16 (b). Under load, the whiskers first approach one another as the matrix is squeezed out from the near contact regions contributing a viscoplastic strain with a maximum value of $-(D-R)/D$ when the entire matrix is squeezed out of the contact. The viscosity due to this effect is given by

$$\frac{\eta_{vp}}{\eta_0} = \frac{2(1+f)}{k_p \lambda^2 f} \left[\left(\frac{f^2}{V_f} \right)^{1/3} - 1 \right]^{-3} \qquad (2.20)$$

where k_p is a stress concentration factor connecting the local stress σ and far field stress σ_{FF} through $\sigma = k_p \sigma_{FF}$ (e.g. $k_p = 1/(V_f f)^{2/3}$ for loading normal to the whisker plane, $k_p = 1/(2\sin 2\theta)$ for loading within the whisker plane), f is the packing efficiency of particles defining the anisotropy of packing through $l/L = f(R/D)$ with l, L, R and D defined in Figure 2.11. It has a minimum value when two layers of whiskers are contacting each other (R=D).

(3) In addition, the deformation of a whisker network will induce elastic bending of the whiskers. This leads to a viscoelastic strain with a maximum value of $-U/D$,

where U is the maximum elastic displacement of the whisker that would bend in the absence of matrix constraint. When the load is removed, the composite will be left in an internal stress state due to the elastic distortion of the whiskers which drives anelastic recovery (Section 2.6). The viscosity due to this effect is given by

$$\frac{\eta_{ve}}{\eta_0} = \frac{16}{\pi^4 k_p (fV_f)^{1/3}} \tag{2.21}$$

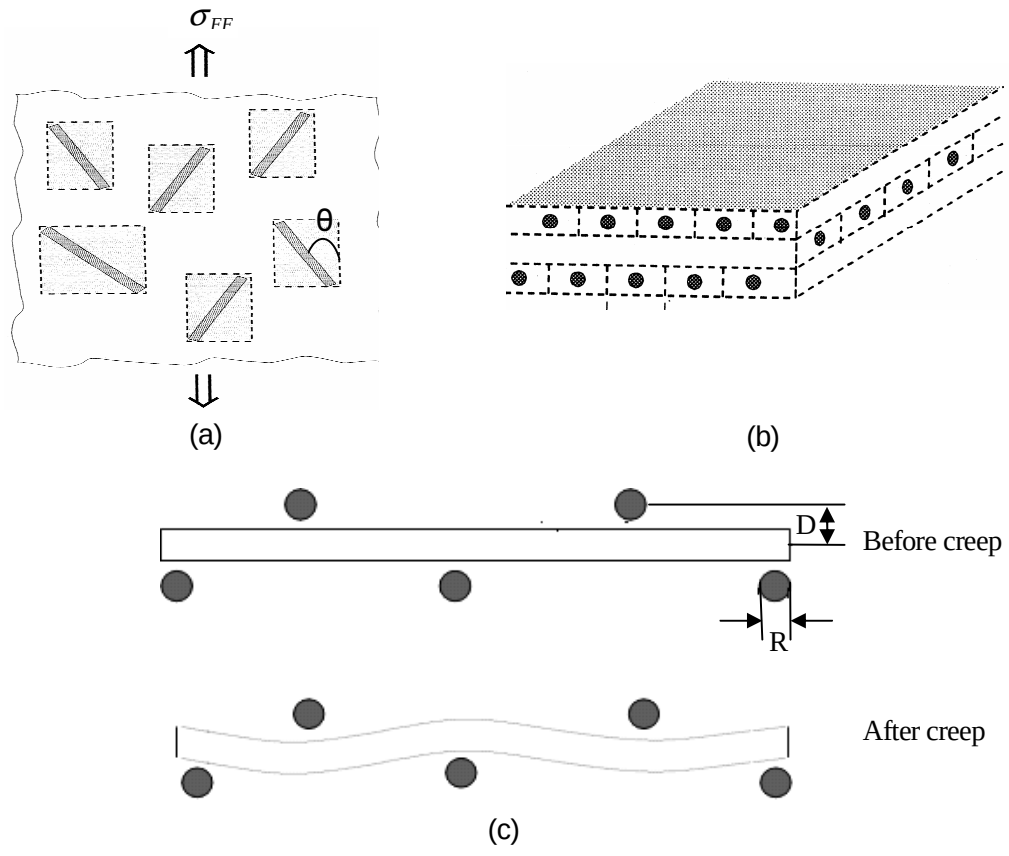

Figure 2.16 Schematic illustration of the assumed geometry (Wilkinson and Pompe, 1998): (a) dilute distribution of whiskers that rotate under the far-field stress; (b) an idealized regular whisker network; (c) bending of whisker network after creep.

All three mechanisms acting together govern the total viscosity. Figure 2.17 shows the normalized viscosity η / η_0 as a function of volume fraction and packing efficiency for three mechanisms. The viscosity due to viscoplastic strain η_{vp} increases significantly with increasing volume fraction as well as the viscosity due to dilute rotation η_{dl}. On the contrary, the viscoelastic viscosity decreases with increasing volume fraction. If the strain rates due to viscoelastic and viscoplastic flow are independent, the total viscosity of the composite is given by equation 2.22. Figure 2.18 shows the normalized total viscosity as a function of volume fraction. Smaller packing efficiency *f* produces a bigger viscosity for a fixed volume fraction. There is a change in the dominant mechanism from viscoplastic to viscoelastic flow as *f* decreases, shown in Figure 2.19.

$$\frac{1}{\eta_t} = \frac{1}{\eta_{vp} + \eta_{dl}} + \frac{1}{\eta_{ve}} \tag{2.22}$$

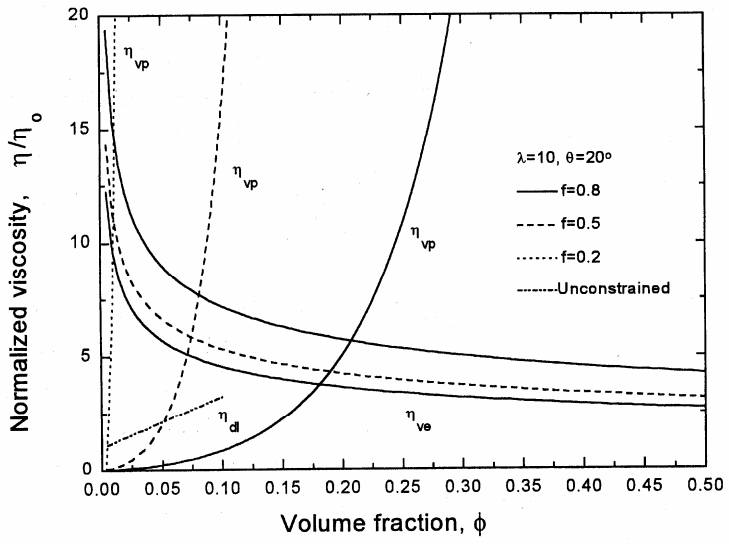

Figure 2.17 Normalized viscosity η / η_0 as a function of volume fraction (ϕ) and packing efficiency *f* for three mechanisms (Wilkinson and Pompe, 1998).

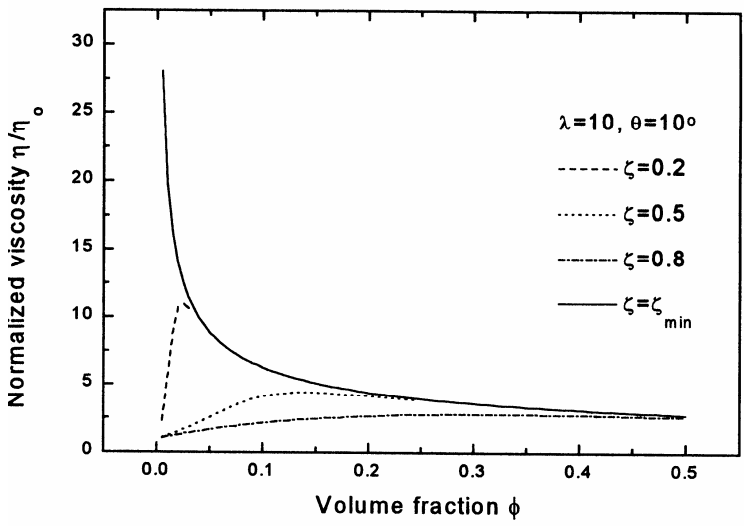

Figure 2.18 Normallized total viscosity (η / η_0) as a function of volume fraction (ϕ) and packing efficiency (*f*). The solid curve represents the viscosity due to viscoelastic creep when $f = f_{\min}$ (Wilkinson and Pompe, 1998).

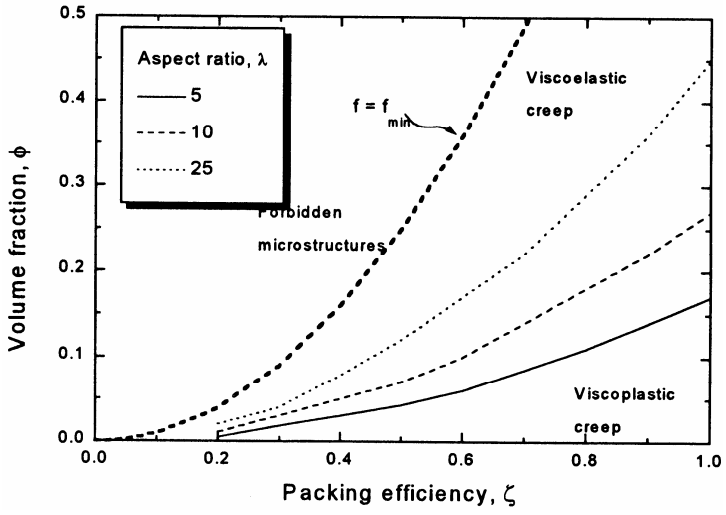

Figure 2.19 Predicted creep mechanism map of a constrained oriented whisker network, e.g. Al_2O_3-SiC_w with $\theta = 10^0$: The boundary separates regions dominated by viscoelastic and viscoplastic creep, which is sensitive to aspect ratio λ, especially at high values of packing efficiency (Wilkinson and Pompe, 1998).

These models do not provide very useful predictions as to the actual creep rates since the response is highly sensitive to the interconnectivity of the network, which changes during the creep process. However, they represent qualitatively the creep response of whisker- and platelet-reinforced ceramics, especially the viscoelastic creep which is demonstrated from the anelastic recovery observed in these composite systems, e.g. Al_2O_3-SiC_w.

2.6. Anelastic creep recovery

Elastic deformation is time independent, which means that an applied stress produces an instantaneous elastic strain that remains unchanged over the period of time the stress is maintained and upon the release of the load the elastic strain immediately returns to zero. Anelasticity implies a time dependent non-elastic behavior, also named as viscoelastic behavior of material. Specifically, in this work, it refers to the time-dependent-creep-strain recovery after the load is removed, due to the stored elastic energy inside. This section reviews the basic analogue model, experimental observations and hypothesized mechanisms for the anelastic behavior for Al_2O_3-SiC_w.

2.6.1. Kelvin-Voigt element

Viscous behavior is essentially dissipative, hence irreversible. The constitutive relationship is

$$\sigma = \eta\dot{\varepsilon} \tag{2.23}$$

where η is viscosity which is a material constant and in the case of linear viscous fluid, it is independent of the stress (Newtonian viscosity). In many instances, the viscosity is non-Newtonian and depends on the stress (usually increases as the stress increases) and the strain-rate-stress relationship is no longer linear (Poirier, 1985).

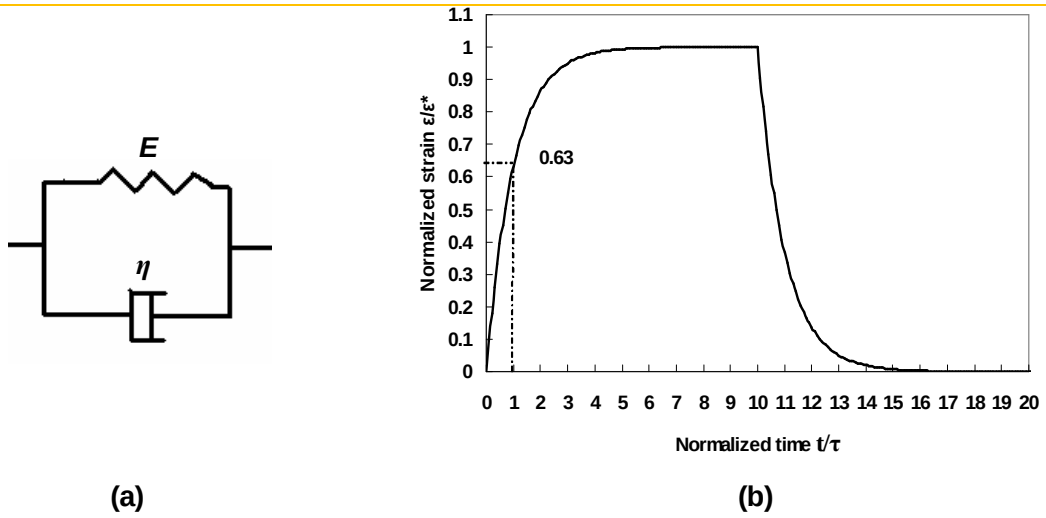

Figure 2.20 Kelvin-Voigt body: (a) spring and dashpot in parallel, (b) for an imposed stress, strain exponentially reaches its elastic value.

The simplest analogue model for anelastic behavior is the Kelvin-Voigt body, represented by a spring with spring constant E and a dashpot with viscosity η in parallel (Figure 2.20 (a)), which is widely used to fit creep relaxation data in the literature (Flügge, 1967). If a constant stress σ_0 is suddenly imposed on a Kelvin-Voigt body, the strain increases from zero to the maximum value $\varepsilon^* = \sigma_0 / E$ for infinite time; and if the load is removed, the strain decreases exponentially as the reverse process of the loading:

$$\varepsilon_{loading} = \varepsilon^* \left[1 - \exp\left(-\frac{t}{\tau} \right) \right] \tag{2.24}$$

$$\varepsilon_{unloading} = \varepsilon^* \exp\left(-\frac{t}{\tau} \right) \tag{2.25}$$

For both cases, $\tau = \eta / E$, named the characteristic relaxation time is used to characterize whether a given material behaves as a viscous fluid or rigid solid by the relative value of its characteristic relaxation time and the time scale considered.

2.6.2. Experimental observations

Anelastic recovery or the time-dependent back strain, is observed upon load removal in CMCs during creep deformation. From an engineering perspective, anelastic recovery limits the operating range of CMCs. From a scientific perspective, anelastic recovery can be studied in order to develop a better understanding of the complex interactions of the reinforcement network with the matrix. Anelastic recovery is not unique to ceramic matrix composites. It is observed in many material systems such as SiC whisker or particulate reinforced Al_2O_3 (Porter, 1989; Gu *et al.*, 1994, 1995; Deng *et al.*, 1999), SiC fiber reinforced Si_3N_4 (Holmes *et al.*, 1993), Al_2O_3 fiber reinforced Al alloys (Dragone *et al.*, 1992), Si_3N_4/MgO alloys (Lange *et al.*, 1980), Si_3N_4 (Arons *et al.*, 1980; Woodford *et al.*, 1998), Aluminum (Henderson *et al.*, 1965; Mills *et al.*, 1986), Titanium (Es-Souni, 2000), Steel (Beere *et al.*, 1987) and Copper alloys (Henderson, 1968).

The first report of anelastic recovery in SiC whisker reinforced alumina system was made by Porter (1989) who studied four point bending in a composite with 15vol% of SiC whiskers. More systematic studies on the anelastic recovery behaviour in SiC whisker reinforced Al_2O_3 composite were made by Gu *et al.* (1994, 1995), and Quan (2004), from which several general tendencies appear:

(1) No obvious anelastic recovery was observed in pure polycrystalline Al_2O_3 and Al_2O_3-SiC_w composite with whisker loading <10vol% (Figure 2.21).

(2) The recovered strain is reproducible and equal to about 1×10^{-3} upon load removal (Figure 2.22). It is independent of the total creep strain at which the load was removed as long as it is around 5×10^{-3} for the first cycle (Quan, 2004).

(3) Whiskers with low aspect ratio resulted in more anelastic recovery than whiskers with high aspect ratio (Figure 2.23).

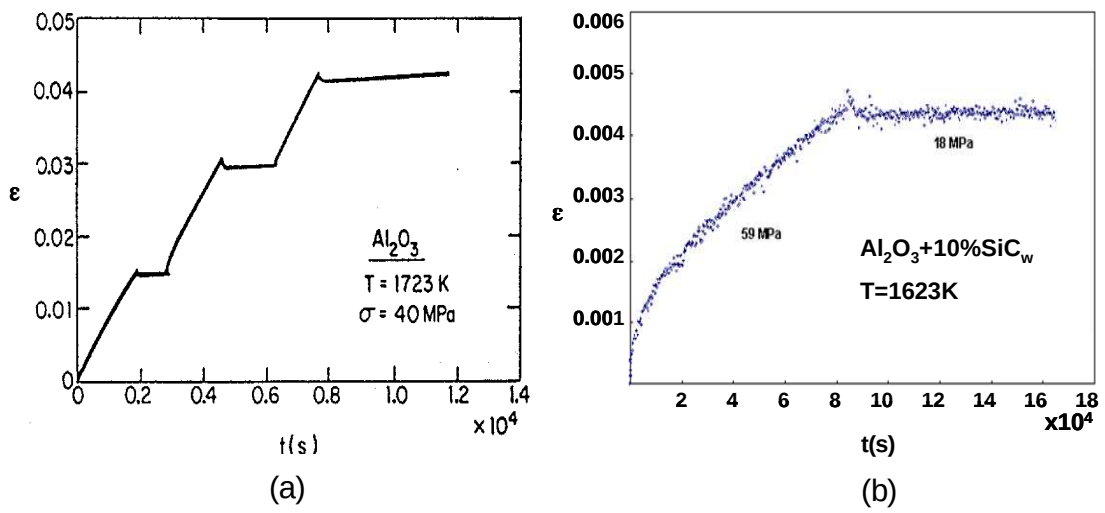

Figure 2.21 Strain vs. Time plot: (a) **Flexural creep test on pure Al_2O_3 (Gu *et al.*, 1994);** (b) **Tensile creep test on Al_2O_3 composite with 10vol% of SiC whisker (Quan, 2004).**

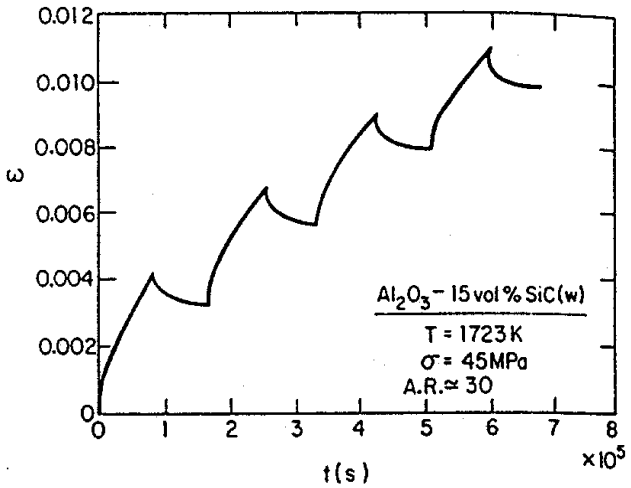

Figure 2.22 Strain vs. Time plot on composite with 15vol% SiC_w via flexural test (Gu *et al.*, 1995).

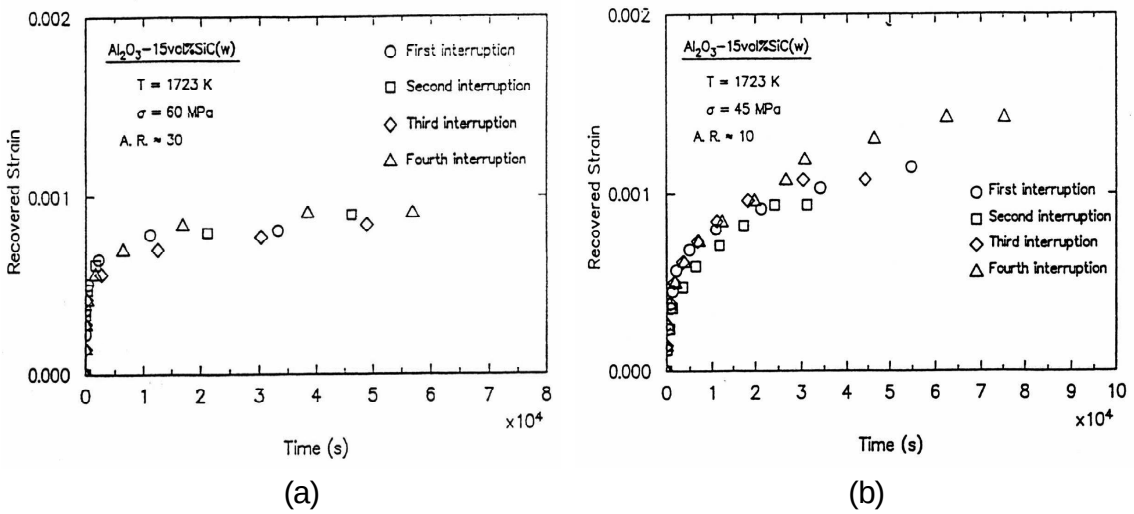

Figure 2.23 Recovered strain vs. Time plot (Gu *et al.*, 1995): (a) Al_2O_3-SiC_w composite with aspect ratio of 30; (b) Al_2O_3-SiC_w composite with aspect ratio of 10.

2.6.3. Anelastic recovery mechanism in Al_2O_3-SiC_w

Using TEM Lange *et al.* (1980) observed highly localized strain fields at grain boundaries in crept specimens of the Si_3N_4/MgO system, indicating a back stress building up during initial loading, which they believed is the source of the viscoelastic strain. Holmes *et al.* (1993) attributed the observed dramatic creep strain recovery in SiC fibre reinforced Si_3N_4 composites to the residual stress state developed in the composites upon unloading. In the study of Deng *et al.*(1999) on SiC particle reinforced Al_2O_3, the elongated grain morphology was thought to be the reason since the retarded strain recovery was observed in samples containing elongated Al_2O_3 grains instead of equiaxed ones. An interconnecting network composed of elongated Al_2O_3 grains shed the applied stress more than the equiaxed grains did. A residual stress state would exist between these two kinds of grains upon unloading and result in the anelastic strain. Gu *et al.* (1994, 1995) also used a modified Kelvin element to address the recovered strain behaviour in SiC whisker and particulate reinforced Al_2O_3 composites. However, the mechanisms responsible for this kind of phenomenon are not well explained. There are fundamental differences in their mechanisms due to the intrinsic

difference in the microstructure of the material, say, type of the matrix (metal or ceramic), shape of the inclusions (particle, continuous or discontinuous fibre/whisker) and the interconnection. This section summarizes two important sources hypothesized to be responsible for the recovery followed by some neutron diffraction results.

2.6.3.1. Dislocation evolution

The first is based on the evolution of dislocation structure that occurs during the loading and unloading processes. Examples of this include the unbowing of pinned network dislocations first proposed by Lloyd and McElroy (1974), subgrain migration and dissolution proposed by Pahutova *et al.* (1979) and backward motion of free dislocations within subgrains proposed by Gibeling and Nix (1981). In un-reinforced materials, particularly metals, these mechanisms are suspected to provide a recovery strain to approximately 1/3 of the elastic strain, and the slope of the anelastic recovered strain versus stress change is around 1.8/E, which is verified by the experimental results from Mills *et al.* (1986). Furthermore, transmission electron microscope (TEM) observations showing bowed dislocations between obstacles provide support for this mechanism (Beere *et al.*, 1987).

2.6.3.2. Creep strain misfit (Wilkinson and Pompe's bending model, Hertzian contact model)

The second mechanism of anelastic recovery is based on the misfit of creep strain between material components with different thermo-mechanical properties. The elastic energy, stored within the stiffer phase during the forward creep, is believed to be released upon the load removal to drive the anelastic recovery.

(A) Wilkinson and Pompe model

The analytical model of Wilkinson and Pompe (1998) for the creep and anelastic recovery of whisker-and platelet- reinforced ceramics characterizes this second origin of anelastic recovery. That work assumes the formation of a percolating network when the

whisker volume fraction reaches a certain threshold value determined by the whisker aspect ratio and distribution (as detailed in section 2.5.2). The percolating network undergoes pure elastic deformation while the matrix undergoes elastic-plastic deformation, and the unbending of the whisker network might be the dominant mechanism for creep recovery. The predicted viscoelastic strain is given by

$$\varepsilon = \frac{1}{32}\frac{k_p \sigma_{FF}}{E_w}\frac{1}{V_f f^{5/3}} \tag{2.26}$$

where E_w is the Young's modulus of whiskers, k_p, σ_{FF}, V_f and f are as in section 2.5.2. For 15vol% of SiC whiskers with an average misorentation of $<\theta>=10^0$, the predicted anelastic recovered strain ranges from a lower bound of $9.2\text{x}10^{-6}$ to an upper bound of 4, depending on the assumptions, primarily the density of whisker-to-whisker contacts. Although this covers the observed experimental data, the range is clearly too broad to give useful predictions.

The model of Wilkinson and Pompe is based on experimental observations of SiC_w reinforced Al_2O_3 composites, in which no significant dislocation activities were observed during creep. It was found that whisker addition significantly reduces the creep strain rate by impeding diffusion accommodated grain boundary sliding (GBS), the main creep mechanism in polycrystalline alumina (Cannon *et al.*, 1980; Heuer *et al.*, 1980). Meanwhile, the magnitude of the anelastic recovered strain is around 1×10^{-3} for the 15vol% SiC_w-Al_2O_3 composite, which is several times the elastic strain. Furthermore, pure alumina and composites containing less than 10vol% of whiskers show no significant time-dependent strain recovery when the load is removed during creep, suggesting the formation of whiskers network (Gu et al., 1994 ,1995; Quan, 2004).

(B) Neutron Diffraction data

From the systematic experimental work done by Quan (2004), due to the micron scale of whiskers and the small deformation, no observable bending of SiC whiskers were captured through TEM, which is consistent with the work of other researchers (Arellano-Lopez *et al.*, 1993, Nutt *et al.*, 1993). Moreover, the expected broadening of the diffraction

peak, due to non-uniform micro-strains introduced by whisker bending (theoretically predicted by the model, as will be illustrated in chapter 4), was not observed from neutron diffraction experimental data (Figure 2.24). On the contrary, a left shifting (0.072° to 0.1°) and narrowing (0.0056° to 0.0576°) of the diffraction peak was observed for Al_2O_3 containing 20-30vol% whiskers.

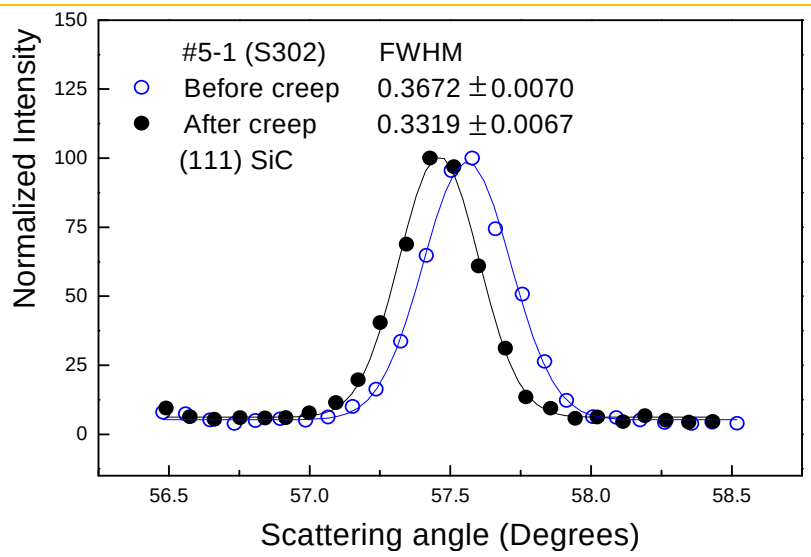

Figure 2.24 (111) SiC whisker peaks measured before and after creep (Quan, 2004).

This raises two possibilities as described by Quan in his Ph. D. thesis (2004). One is, as hypothesized in the Wilkinson and Pompe model (1998), whiskers do bend during the creep deformation. However, the peak broadening is insufficient to be measured experimentally. Indeed, based on theoretical calculations, Quan concluded that the maximum value of broadening due to pure bending is about FWHM=0.004^0 which is below the instrumental resolution for the technique he used. There can, however, be other factors contributing to the change in peak width, which makes the separation of the contribution from whisker bending alone very difficult. For example, hot pressing generates considerable compressive residual stresses in the whiskers (Table 2.3), which are also observed by other research groups via neutron and X-ray diffraction (Majumdar *et al.*, 1988, 1989; Predecki *et al.*, 1988; Abuhasan *et al.*, 1990). The compressive residual stresses might be alleviated during

the tensile creep test resulting in the left shifting of the peak position as shown in Fig 2.24 (Quan, 2004). The second possibility is that the effect of whisker bending is not the dominant mechanism, which requires some other mechanisms for relaxation.

Table 2.3 Lattice strains ($\times 10^{-3}$) measured at room temperature for SiC_w (Quan, 2004). Numbers in parenthesis are uncertainties. BC: before creep; AN: annealed; AC: after creep

Sapmle	30% BC	30% AN	30% AC	20% BC	10% BC
(111) plane	-3.65(0.08)	-3.42 (0.08)	-2.51 (0.09)	-3.95 (0.12)	-5.65 (0.15)

(C) Hertzian contact model

Based on the experimental results, especially the anelastic recovery phenomena observed in SiC particulate reinforced Al_2O_3 which cannot exhibit bending during creep deformation, Quan (2004) hypothesized that one possibility is the localized elastic point contacts between particles where large strain can be achieved under low stress owing to the Hertzian contact phenomenon. Figure 2.25 illustrates Hertzian contact between spherical particles and rods. It assumes the surrounding matrix induces rotation of the misaligned whiskers, then at the contact points normal forces F_p are generated to balance the moment formed by the shear stress τ acting along the matrix whisker interface. The normal force is calculated by (Quan, 2004):

$$F_p = 2r^2\sigma \sin 2\theta \tag{2.27}$$

where r is the radius of whiskers and θ is the misorientation angle. Then the displacement due to contact deformation is given as (Landau *et al.*, 1986):

$$h = F_p^{2/3}\left[\frac{9}{2}\left(\frac{1-\nu^2}{E}\right)^2\frac{1}{r}\right]^{1/3} \tag{2. 28}$$

where E and ν are the Young's modulus and Poisson ratio of the whisker, respectively. Then the strain at the loading direction is given by (Quan, 2004),

$$\varepsilon = \frac{2h}{L}\tan\theta = \frac{2r}{L}\left[\frac{3\sqrt{2}\sigma(1-\nu^2)}{E}\right]^{2/3}(\sin 2\theta)^{2/3}\tan\theta \qquad (2.29)$$

For Al_2O_3-SiC_w composite containing whiskers with an aspect ratio of 5 ($r/L = 0.1$) and an average misorentation of $<\theta>= 20^0$, the predicted anelastic recovered strain is around $3.3\text{x}10^{-4}$ if E=*427GPa* and ν=0.2.

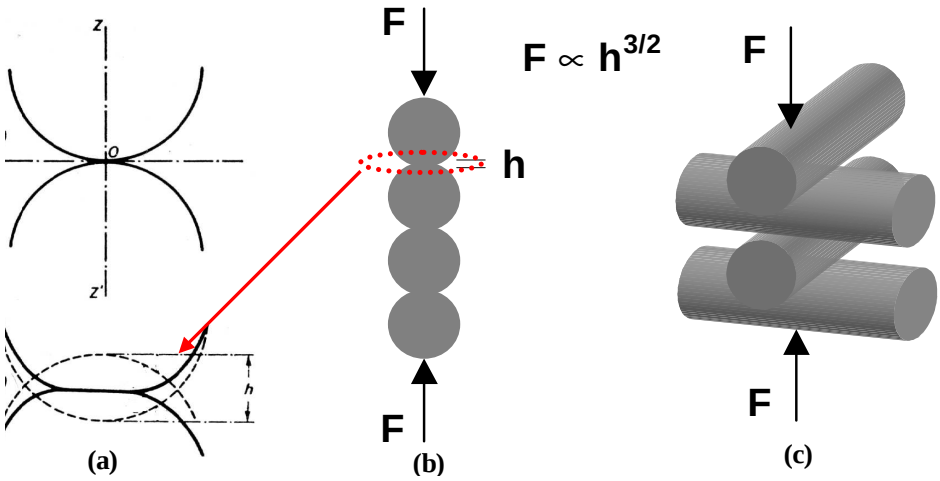

Figure 2.25 Schematic illustrations of Hertzian contact phenomena between (a) spheres and (b) rods in contact (Quan, 2004).

2.6.4. Summary

Both of the models reviewed in this section (related to bending and contact) assume the formation of an inclusion network and the pure elastic deformation of inclusions while the matrix creeps. The contact model seems to give a better consistency to the magnitude of observed recovered strain, say $\approx 3.3\text{x}10^{-4}$, which is the same order of those experimentally observed, e.g. $\approx 1\text{x}10^{-3}$. Furthermore, it predicts increasing strain with decreasing whisker aspect ratio, which is in accord with the experimental data by Gu *et al.* (1994, 1995). However, both of them lack support from direct observation in diffraction experiments due to instrument

resolution effects. Thus the mechanism for anelastic recovery in Al_2O_3-SiC_w composites is still not clear. One more important feature of the Wilkinson and Pompe model is the introduction of load transfer from matrix to inclusions through contact points in a constrained network in addition to the shear stress at the interface introduced in section 2.5.1.

2.7. Assessment of the literature

To date, the dominant mechanism, say whisker bending (Wilkinson and Pompe, 1998) or contact (Quan, 2004), which is responsible for the anelastic recovery of SiC_w reinforced Al_2O_3 is still unknown and the experimental diffraction data cannot be well explained. Furthermore, as mentioned before, traditional analytical approaches (Eshelby, 1957; Mura, 1987; Cox, 1951; Mclean, 1972; Kelly *et al.*, 1972; Taya *et al.*, 1989) idealize the stress/strain fields and neglect the interactions between inclusions when predicting the macroscale behaviours based on the properties of the microscale constituents. An arbitrary distribution of inclusions could be addressed in a relatively simple way without resorting to the intractable stress calculations using elasticity theory. However, the information neglected is critical for investigating the mechanisms of anelastic recovery. Furthermore, several research groups have attempted to study the diffraction peak from residual elastic strain distributions: in SiC particle reinforced Al_2O_3 composites using three idealized analytical models while lacking direct relation to the actual microstructure (Todd and Derby, 1993); in Tungsten Caribide-Nickel composites involving averaging elastic strain output from a representative FE model (Weisbrook *et. al.* 1994, 1995). However, no systematic numerical work combining these effects has been carried out to explain the deformation mechanisms of the whisker network, the effect of load transfer between whiskers and matrix through interfaces and contact points, and their relation to the subsequent diffraction patterns after deformation.

Consequently, the present study uses FEM combined with unit cell methodology to study the anelastic behavior of SiC_w-Al_2O_3 composites and local stress/strain fields based on

which the relative contributions of bending and contact will be addressed. A virtual numerical diffraction model has also been developed to connect the strain field determined by FEM to the expected diffraction pattern in terms of the peak width (***FWHM***) and peak position. The correlation between the deformation and diffraction pattern is studied and the effects of experimental conditions such as thermal stress are also investigated.

CHAPTER 3

FINITE ELEMENT SIMULATIONS

3.1. Assumptions and material properties

In the present study, several assumptions are made to simplify simulations:

(1) Steady state microstructures are considered, e.g., no grain growth, dislocation evolution and damage accumulations (such as voids and micro cracks) are permitted.

(2) Perfect bonding between matrix and whiskers is also assumed.

(3)As for the mechanical properties, isotropic elastic and elasto-creep deformation for SiC whiskers and Al_2O_3 matrix are studied respectively.

The assumption of steady microstructure is reasonable since neither of the first two mechanisms noted above are evident from the experimental observations (Arellano-Lopez *et al.*, 1993; Nutt *et al.*, 1993). Damage is also insignificant during the secondary creep stage even though it is critical during the tertiary creep stage which leads to the final rupture (section 2.4). The hypothesis of perfectly elastic whiskers is based on their high melting point (2730℃) as well as the observed whisker structural properties that are highly defective. It is observed that SiC whiskers are single crystals containing immobile partial dislocations, systematic stacking faults and core inclusions (Nutt, 1984). The low vacancy concentration in SiC whiskers and the long diffusion path yield a creep rate many orders of magnitude lower than that in the matrix. Material properties involved in the simulations are given in Table 3.1 (Munro, 1997) and Table 3.2 (Petrovic *et al.*, 1985; Wong *et al.*, 1997; Goldberg *et al.*, 2001). The steady state creep behaviour is expressed using an equivalent uniaxial power-law relation, *Norton form*, with a typical stress exponent of 1 for diffusional creep (Munro, 1997; Cannon et al., 1980; Heuer et al., 1980; Poirer, 1985).

$$\dot{\varepsilon}_{cr} = C\sigma \tag{3.1}$$

Table 3.1 Material properties of Al_2O_3 (Munro, 1997)

Temperature(℃)	20	500	1000	1200	1400	1500
E(GPa)	416	390	364	354	343	338
v	0.231	0.237	0.244	0.247	0.250	0.252
$C(S^{-1}\ MPa^{-1})$	0	0	2.67e-11	1.87e-09	4.4e-08	1.64e-07
CTE $(10^{-6}K^{-1})$	4.6	7.1	8.1	8.3	8.5	8.6

**CTE: Coefficient of thermal expansion

Table 3.2 Material properties of SiC_w (Petrovic *et al.*, 1985; Wong *et al.*, 1997; Goldberg *et al.*, 2001)

Temperature(℃)	230	330	630	1230	1700
E(*GPa*)	600	600	600	600	600
v	0.17	0.17	0.17	0.17	0.17
CTE $(10^{-6}K^{-1})$	3.8	4.3	4.8	5.5	5.5

**CTE: Coefficient of thermal expansion

3.2. Finite element Method

Generally, FEM is a numerical technique used to find approximate solutions for partial differential equations describing physical problems. From a mathematical point of view, FEM is a combination of the Galerkin approach (weak formulation) and piecewise polynomial interpolation with mathematical validity from the underlying Sobolev spaces (Marti, 1986). It originated from structural analysis with the pioneering work of Courant (1943) on a torsion problem and in this field is referred to as the virtual work or variational principal approach due to the physical background (Stolle, 2005). It has since been applied to other fields of continua such as thermal analysis and fluid flow while the term Galerkin method is more generally employed.

A critical advantage of FEM over analytical approaches is its versatility: arbitrary phase geometries and distributions, arbitrary loads and arbitrary boundary conditions can be handled in a straightforward manner and detailed local stress/strain fields in the matrix,

inclusions and along their interfaces can be computed while providing the overall behaviours as well. In this section, we will illustrate the basic theory of the finite element method, starting from the elastic analysis and then the creep problem.

3.2.1. Basic theory of finite element method

The general governing equation for 1D elastic analysis without body force is shown as

$$\sigma_{,x} = Eu_{,xx} = 0 \tag{3.2}$$

where $\sigma_{,x}$ is the derivative of stress with respect to x, $u_{,xx}$ is the second derivative of displacement with respect to x, and E is the Young's modulus. Suppose the case considered here is a bar with uniform cross-sectional area of A, subjected to a uniaxial end load f, as shown in Figure 3.1(a). The general procedure of FEM is to apply a test function u into the equation 3.2, then multiply it with some weight function w and integrate over the whole domain to minimize the residual

$$\int_L wEu_{,xx}dV = 0 \tag{3.3}$$

After integration by parts, we have

$$\int_L w_{,x}Eu_{,x}dV - \sigma Aw\Big|_0^L = 0 \tag{3.4}$$

Equation 3.4 is the weak form of the equation 3.2 which lowers the continuity requirement of function u from C^1 to C^0 at the expense of increase on the weight function w. This is also referred to as the weighted residual method. If the weight function w and test function u are in the same space, for example, the piecewise continuous polynomial, it is the Galerkin method. Furthermore, if the test function u represents the displacement field at equilibrium and the weight function w represents the small perturbation of displacement δu, this equation also

corresponds to the virtual work procedure since the work done by forces in equilibrium subjected to virtual displacement δu is zero.

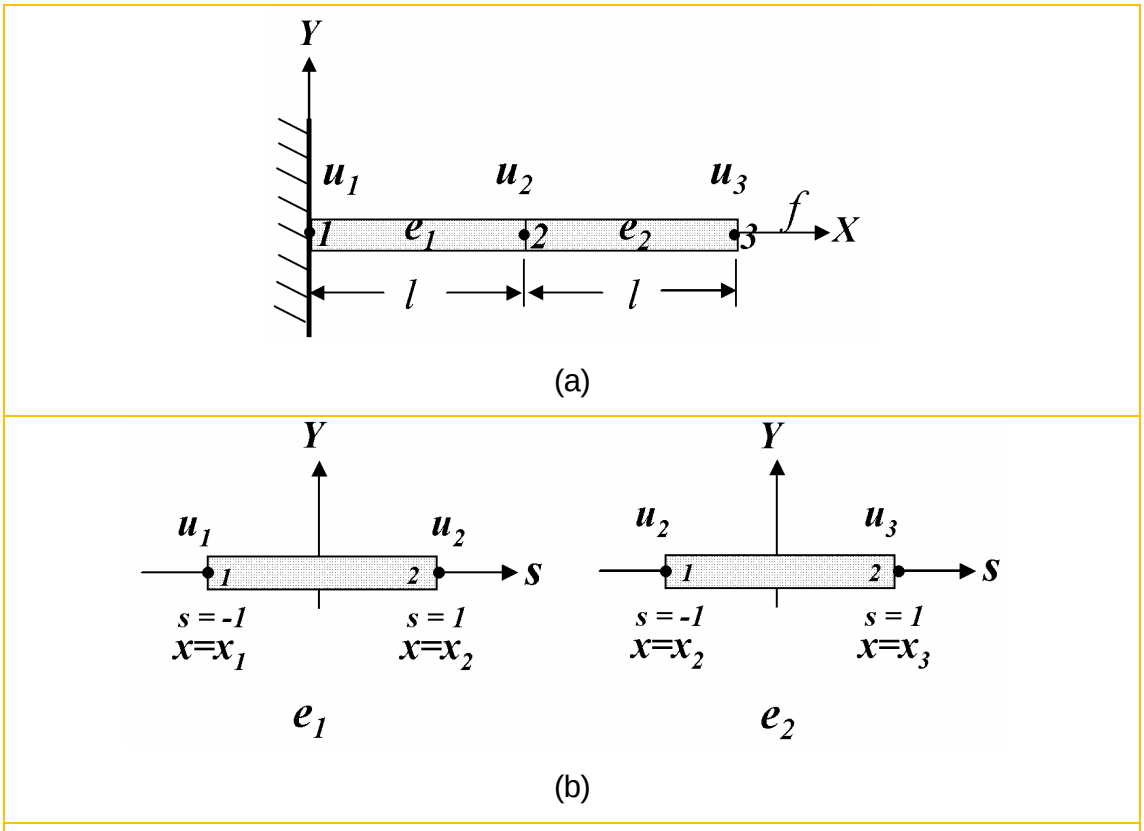

Figure 3.1 Schematic illustration of FEM (a) a bar under uniaxial end load *f* in global coordinate systems with element discretization; (b) line elements in local coordinate systems.

The whole domain is then discretized into finite subdomains called elements that are glued by the nodes at the element boundaries. For simplicity, only two elements with length of *l* are illustrated in the figure. There is a local coordinate system *s* associated with each element (Figure 3.1(b)). Its origin is located at the centroid of the element. The local and global (physical) coordinates can be mapped as

$$x = (1-s)x_1/2 + (1+s)x_2/2 \Rightarrow x = NX \qquad (3.5)$$

At the same time, the displacement field within the element might be interpolated as

$$u = (1-s)u_1/2 + (1+s)u_2/2 \Rightarrow u = Na_e \tag{3.6}$$

where the second part in each equation is the corresponding matrix form with $N = \frac{1}{2}[(1-s)\ \ (1+s)]$ containing the shape functions, $X = [x_1\ x_2]^T$ containing the global coordinates of the nodes, and $a_e = [u_1\ u_2]^T$ containing the unknown displacements at the nodes. The superscript *T* denotes transpose. The strain is conveniently defined as

$$\varepsilon = u_{,x} = \frac{\partial N}{\partial s}\frac{\partial s}{\partial x}a_e = B\frac{1}{|J|}a_e \tag{3.7}$$

where $B = \frac{1}{2}[-1\ \ 1]$ is the strain-displacement transformation matrix, and $|J| = \frac{\partial x}{\partial s} = \frac{l}{2}$ is the Jacobian resulted from the mapping between local and global system.

Substituting the matrix forms into equation 3.7 for each element we have

$$\delta a_e{}^T \int_{-1}^{1} B^T EAB\frac{1}{|J|}ds\ a_e - \delta a_e{}^T F_e = 0 \Rightarrow\Rightarrow ka_e = F_e \tag{3.8}$$

$$\text{with } k = \int_{-1}^{1} B^T EAB\frac{1}{|J|}ds = \frac{EA}{l}\begin{vmatrix} 1 & -1 \\ -1 & 1 \end{vmatrix} \tag{3.8a}$$

where *k* is the element stiffness matrix and F_e is the vector containing nodal loads already known. By adding the contribution from the two elements, we have the global form

$$Ka = F \Rightarrow\Rightarrow \frac{EA}{l}\begin{vmatrix} 1 & -1 & 0 \\ -1 & 1+1 & -1 \\ 0 & -1 & 1 \end{vmatrix} \begin{vmatrix} u_1 \\ u_2 \\ u_3 \end{vmatrix} = \begin{vmatrix} 0 \\ 0 \\ f \end{vmatrix} \tag{3.9}$$

where K is the global stiffness matrix which is a symmetric sparse matrix representing the coefficients of a set of simultaneous algebraic equations. Inverting the global stiffness matrix yields the displacement vector ($a = K^{-1}F$), which might be accomplished by Gauss elimination. This requires that K must be non-singular, satisfied by applying enough supports to eliminate the free body motion. In general, instead of obtaining a complete solution, the integration over domain while forming the stiffness matrix is obtained numerically through Gauss quadrature that yields the integration through some sampling points and weight functions. The procedure above is known as the isoparametric FEM since it uses the same functions for shape functions and for transformation from a "master element" to the actual nodal positions. With the increasing number of elements, the result converges to the accurate solution, which is referred to as h-refinement. There thus may be thousands of thousands of such equations for a complicated problem, which means that computer implementation is mandatory. Higher order of shape function might be employed yielding a faster convergence rate and it is referred to as p-refinement.

Furthermore, without getting into details, equation 3.8 could be obtained through minimizing the total potential energy. The total potential energy of the system is

$$\begin{aligned} \prod &= \text{strain energy - work done} \\ &= \frac{1}{2} a_e{}^T \int_{-1}^{1} B^T EAB \frac{1}{|J|} ds \; a_e - a_e{}^T F = \frac{1}{2} a_e{}^T k a_e - a_e{}^T F_e \end{aligned} \tag{3.10}$$

$$\text{with } \delta \prod = k a_e - F_e == 0 \tag{3.10a}$$

Thus, the solution obtained represents a minimum value of strain energy which means that the displacement field yielded is always an underestimate.

3.2.2. Finite element method in creep analysis

As described in equation 3.1, a creep problem is time dependent and thus can be treated as an initial value problem in the stress or strain. Generally, techniques required to solve nonlinear creep problems consist of two components: (1) a means of solving the elastic problem of the structure as discussed in section 3.2.1; (2) a means of solving the initial value problem (Boyle and Spence, 1983). Here we briefly describe the scheme without getting into details. Suppose the structure is subject to creep deformation along with elastic deformation, the total strain is decomposed into an elastic ε_{el} and a creep ε_{cr} component. Then we have

$$\sigma = D_E \varepsilon_{el} = D_E (\varepsilon - \varepsilon_{cr}) \tag{3.11}$$

where D_E is the matrix of elastic coefficients which is E in last section. Apply the Galerkin theorem to the equation 3.2 which holds also during creep, we obtain

$$\int_V B^T \sigma dV - F = 0 \tag{3.12}$$

where matrix B and F contain the same information as in the section 3.2.1. Then substituting the equation 3.11 into 3.12, there results

$$Ka - F_{cr} - F = 0 \tag{3.13}$$

$$\text{with } K = \int_V B^T D_E B dV \tag{3.13a}$$

$$\text{and } F_{cr} = \int_V B^T D_E \varepsilon_{cr} dV \tag{3.13b}$$

where the contribution from the creep deformation lies within the force F_{cr}. Combining the solution from equation 3.13 with the equation 3.11, we have

$$\sigma = D_E (Ba - \varepsilon_{cr}) = D_E B K^{-1} (F_{cr} + F) - D_E \varepsilon_{cr} \tag{3.14}$$

By rewriting the 3.14 in rate form, the equations of stress redistribution are then obtained for power law creep ($\dot{\varepsilon}_{cr} = C\sigma^n$)

$$\begin{aligned}\frac{d\sigma}{dt} &= D_E BK^{-1}(\dot{F}_{cr} + \dot{F}) - D_E\dot{\varepsilon}_{cr} \\ &= D_E BK^{-1}\int_V B^T D_E C\sigma^n dV + D_E BK^{-1}\dot{F} - D_E C\sigma^n\end{aligned} \tag{3.15}$$

Then the equation for the evolution of inelastic strain for power law creep is

$$\frac{d\varepsilon_{cr}}{dt} = CD_E{}^n\left(BK^{-1}\int_V B^T D_E\varepsilon_{cr}dV + BK^{-1}F - \varepsilon_{cr}\right)^n \tag{3.16}$$

The situation is now becoming a finite system of first-order initial value problems with an initial elastic deformation. The fundamental object of the algorithm next is to obtain the solution at a sequence of discrete instants of time, which are called time stepping. This is actually accomplished by integrating the inelastic strains (equation 3.16) over time (the "initial strain" method). The simplest algorithm applied in creep mechanics of the form $\frac{dy}{dt} = f(y,t)$, with $y(0) = y_0$ is

$$y_{i+1} = y_i + \Delta t_{i+1}\left[(1-\alpha)f_i + \alpha f_{i+1}\right] \tag{3.17}$$

where $0 \le \alpha \le 1$. When $\alpha = 0$ this is the explicit Euler algorithm, which needs data from previous step (forward integration) and is conditionally stable. When $\alpha \ge 1/2$ this is the implicit Euler scheme since it needs data unknown (backward integration) and iterations are needed to get the solution which needs to satisfy some error tolerance (cetol). The implicit algorithm is unconditionally stable when $\alpha \ge 1/2$ (Boyle and Spence, 1983).

In practice, it is convenient to employ an algorithm that can determine the step size automatically based on stability and accuracy. In ABAQUS/Standard, this automatic algorithm will first start from the explicit integration, the stable step size of which is calculated as that at any point in the model, the creep strain increment is not larger than the total elastic strain

$$\Delta t_s = 0.5 \frac{\bar{\varepsilon}_{el}\big|_t}{\dot{\bar{\varepsilon}}_{cr}\big|_t} \tag{3.18}$$

where $\bar{\varepsilon}_{el}\big|_t$ and $\dot{\bar{\varepsilon}}_{cr}\big|_t$ are the equivalent total elastic strain and the equivalent creep strain rate respectively, at time *t* the beginning of the increment. The critical time increment is calculated as

$$\Delta t_c = \frac{cetol}{\dot{\bar{\varepsilon}}_{cr}\big|_{t+\Delta t} - \dot{\bar{\varepsilon}}_{cr}\big|_t} \tag{3.19}$$

At every increment for which explicit integration is performed, the stable time increment is compared to the critical time increment. If $\Delta t_s < \Delta t_c$, Δt_s is used as the step size resulting in a limit imposed by the stability criterion rather than by accuracy considerations. If $\Delta t_s < \Delta t_c$ for nine consecutive increments, the program will then automatically switch to the implicit integration that is unconditionally stable.

3.3. Fundamentals of unit cell technique

There are many millions of whiskers inside a small volume, e.g. $1cm^3$, if the volume fraction is 15vol% and aspect ratio is 10. It is impractical to simulate the whole sample even based on the most powerful computers and best algorithms currently available. Generally accepted methodology in continuum micromechanics of composites is the Unit Cell Model. It assumes that the material has periodic microstructure and describes the macroscale and microscale behavior of inhomogeneous composites by studying a Reference Volume Element (RVE) with appropriate boundary conditions. By definition the RVE contains all the information necessary for the statistical description of a given microstructure. Generally, for a given periodic phase arrangement unit cells are nonunique (shown in Figure 3.2), depending

on the symmetries presented in the microgeometry, which, of course, refer to different kind of boundary conditions, e.g., symmetry boundary conditions, antisymmetry boundary conditions, periodicity boundary conditions and so on. BÖhm gives a detailed description in his unpublished report (1998).

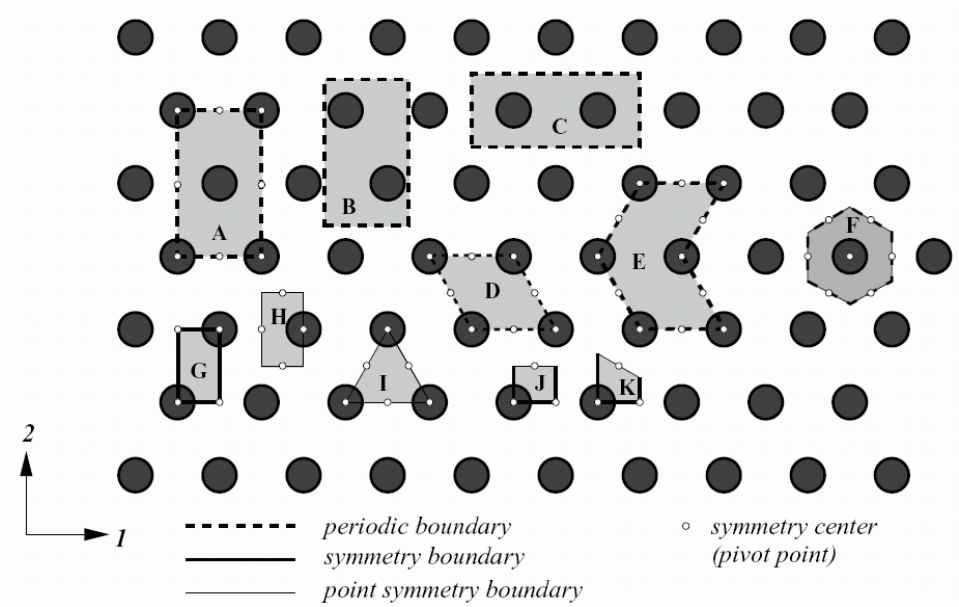

Figure 3.2 Schematic illustration of periodic hexagonal array of circular inclusions in a matrix and 11 unit cells that can be used based on symmetries present (BÖhm, 1998).

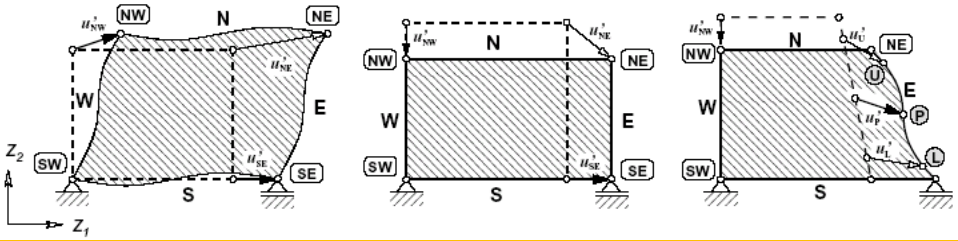

Figure 3.3 Sketch of periodicity (left), symmetry (center), and antisymmetry (right) boundary conditions as used with two-dimensional unit cells (BÖhm, 1998).

Periodic boundary conditions (PBCs)

Periodic boundary conditions are used on the unit cells which could tile the computational space by simple translation, e.g. A to F in Figure 3.2. They are the most general boundary conditions and could handle any possible deformation state of the unit cell as shown in Figure 3.3. They require the compatible phase distributions and finite element discretizations for each pair of faces (up and down, left and right, back and front):

$$u_{i(N)} = u_{i(S)} + u_{i(NW)};\ \ u_{i(E)} = u_{i(W)} + u_{i(SE)};\ \ u_{i(NE)} = u_{i(SE)} + u_{i(NW)};\ \ u_{i(SW)} = 0 \qquad (3.20)$$

where $i = 1, 2, 3$ are the indices of displacements along Z_1, Z_2, Z_3 **(*x*, *y*, *z*)** respectively; $u_{i(N)}$, $u_{i(S)}$, $u_{i(E)}$ and $u_{i(W)}$ are the displacements of the nodes on the planes *N*, *S*, *E* and *W* respectively; $u_{i(NW)}$, $u_{i(SE)}$ $u_{i(NE)}$ and $u_{i(SW)}$ are the displacements of the nodes *NW*, *SE*, *NE* and *SW* respectively.

Symmetry boundary conditions (SBCs)

In practice, due to the multi-point constraints incurred, finite element based unit cell studies using PBCs may be quite expensive in terms of computing time and memory required. For unit cells in which the faces of the cell coincide with symmetry planes of the phase arrangement and retained after deformation (e.g. unit cell G in Figure 3.2), PBCs can be simplified to symmetry boundary conditions (SBCs):

$$u_{2(N)} = u_{2(NW)};\qquad u_{1(E)} = u_{1(SE)};\qquad u_{2(S)} = u_{1(W)} = u_{i(SW)} = 0 \qquad (3.21)$$

where $u_{2(N)}$ and $u_{2(S)}$ are the displacements along Z_2 direction of the nodes on the planes *N* and *S* respectively; $u_{1(E)}$ and $u_{1(W)}$ are the displacements along Z_1 direction of the nodes on the planes *E* and *W* respectively; $u_{2(NW)}$ is the displacement along Z_2 direction of the node *NW*; $u_{1(SE)}$ is the displacement along Z_1 direction of the node *SE*; $u_{i(SW)}$ are the displacements of the node *SW*.

Antisymmetry boundary conditions (ASBCs)

Antisymmetry boundary conditions are even more limited in terms of the microgeometries since they require the presence of centers of point symmetry (pivot points). If *P* is the pivot point in Figure 3.3, the boundary conditions can be defined through

$$u_{2(N)} = u_{2(NW)}; \qquad u_{i(EU)} + u_{i(EL)} = u_{i(P)}; \qquad u_{2(S)} = u_{1(W)} = u_{i(SW)} = 0 \tag{3.22}$$

where $u_{i(EU)}$ and $u_{i(EL)}$ are the displacements of the nodes on the planes *EU* and *EL* respectively; $u_{i(P)}$ are the displacements of the node *P*.

It should be noted that although the detailed local stress and strain distributions near inclusions are accurate, they are only meaningful in the context of the modeled system and the interpretation of the local fields must be made with caution since the real material never exhibits the imposed periodicity as the model system.

3.4. Unit cells used in current study

Three kinds of geometries that are numerically constructed are employed in the current study to investigate the effects of whisker network on the anelastic behaviours, deformation mechanisms and diffraction patterns. Although an emerging technique preferred nowadays is to obtain an actual microstructure from X-ray tomography or serial sectioning with the aid of TEM or SEM in order to make a realistic comparison to actual experimental values (Chawla et al., 2006), a numerically reconstructed random geometry could also provide satisfactory information while studying the reinforcing effect of composites with considerably less procedures (Böhm *et al.*, 2002; Duschlbauer *et al.*, 2006, Kari *et al.*, 2007). Meanwhile, a fabrication process of hot pressing for Al_2O_3-SiC_w composites containing higher volume of whiskers yields a three-dimensional (3D) percolating plane random distribution (Quan, 2004). However, it is an unrealistic task since a minimum distance between any two cylinders is required for the practical application. This is due to grid resolution and the maximum

allowable model nodes imposed by the limited availability of computer memory, as well as a reasonable accuracy based on well shaped elements near the contact region. Thus, a 3D random unit cell is generated without percolation and two-dimensional (2D) percolating unit cells are generated by modifying the near contact regions. 3D single whisker unit cells are generated to provide the fundamental basis of how a whisker behaves alone and the corresponding diffraction pattern. All simulations were implemented through the commercial finite element package ABAQUS/Standard, version 6.8-3. Load control is employed while the stress is applied to the unit cells as concentrated load acting on a 'master node'. All 3D and 2D unit cells correspond to alumina composites containing whiskers with a diameter of 0.5 microns resulting in a unit of micron for reference.

3.4.1. 3D periodic random-oriented-short-fiber unit cell

Numerically generating the periodic 3D random-oriented-whisker micro-geometry is accomplished with the aid of Matlab based on a random sequential adsorption algorithm. The position of each whisker is described by its center point and two Euler angles, which are generated by Matlab's random number generator within a specific cube volume. Each new position can only be accepted if the new cylinder does not overlap any previous ones. Intersection testing of two cylinders is based on the projection method of Eberly (2008). At the same time, in order to retain the periodicity, any part of a fiber that extends beyond the face of the cubic domain is cut and shifted to the opposite face and intersection testing is carried out correspondingly. The minimum distance between neighboring cylinders is set at 5.6% of its diameter specified in the work of Böhm *et al.* (2002). A 3D multifiber unit cell containing 15 fibers of equal size, aspect ratio λ=5 at a total reinforcement volume fraction of 15% is shown in Figure 3.4. The unit cell was meshed with 10-node tetrahedra, C3D10M using ABAQUS CAE 6.7-1, which is recommended by ABAQUS documentation for a better accuracy in nonlinear calculations. The number of elements and nodes in the unit cell are 133224 and 191747, respectively. Displacement controlled creep analysis is performed following the PBCs (Böhm, 1998).

$$u_{i(x=a)} = u_{i(x=0)} + u_{i(x=a,y=0,z=0)} \quad (3.23)$$

$$u_{i(y=b)} = u_{i(y=0)} + u_{i(y=b,x=0,z=0)} \quad (3.24)$$

$$u_{i(z=c)} = u_{i(z=0)} + u_{i(z=c,x=0,y=0)} \quad (3.25)$$

$$u_{i(x=0,y=0,z=0)} = 0 \quad (3.26)$$

where $i = 1, 2, 3$ are the indices of displacements along ***x***, ***y***, ***z*** respectively; $u_{i(x=a)}$, $u_{i(x=0)}$, $u_{i(y=b)}$, $u_{i(y=0)}$, $u_{i(z=c)}$ and $u_{i(z=0)}$ are the displacements of the nodes on the planes at position $x = a$, $x = 0$, $y = b$, $y = 0$, $z = c$ and $z = 0$ respectively; $u_{i(x=a,y=0,z=0)}$, $u_{i(y=b,x=0,z=0)}$ and $u_{i(z=c,x=0,y=0)}$ are the displacements of the nodes at position $(a,0,0)$, $(0,b,0)$ and $(0,0,c)$ respectively.

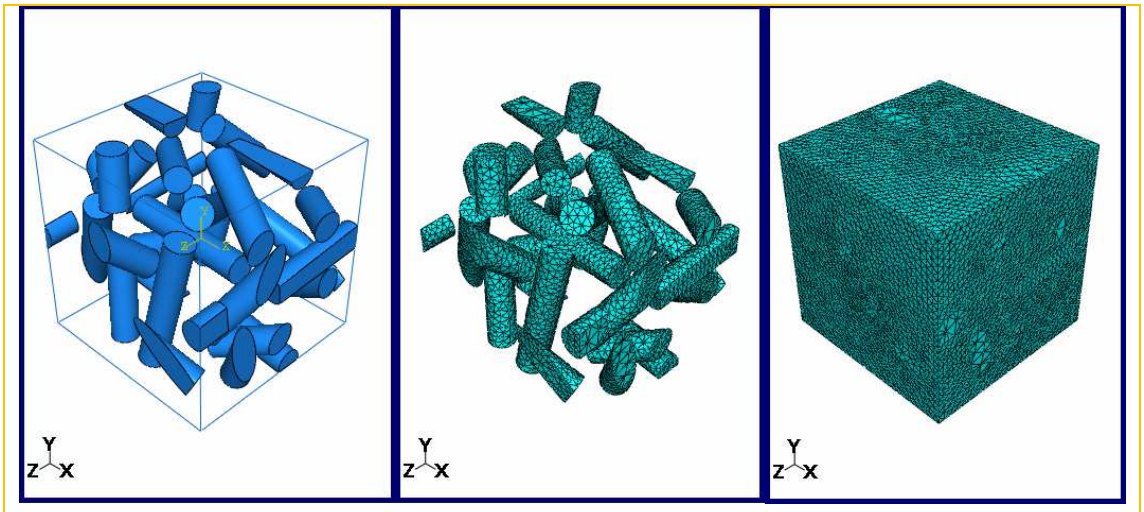

Figure 3.4 Periodic multi-whisker unit cell with randomly oriented whiskers: (a) fibres, (b) fibre meshing, (c) matrix meshing.

3.4.2. 2D oriented percolating unit cells

In order to study creep deformation in the context of a percolating network, the whiskers are assumed to form a series of parallel layers, each one of which is oriented perpendicular to the one below it. Typical whisker configuration for this case is shown in Figure 3.5, generated by ABAQUS CAE 6.8-3. The smallest RVE that can generate the entire idealized geometry by translation in the *x-y* plane is represented in the figure in dark dashed lines. Half of the RVE (rectangular *obcm*), containing a simple three point bending geometry is chosen with PBCs used for top and bottom boundaries *ob* and *cm*, and ASBCs used for left and right sides *bc* and *om* due to a "pivot point" placed in the middle of the boundary (BÖhm, 1998). Specifically,

$$u_{i(mc)} = u_{i(ob)} + u_{i(m)} \tag{3.27}$$

$$2u_{i(p)} = u_{i(cp)} + u_{i(bp)} \tag{3.28}$$

$$2u_{i(q)} = u_{i(mq)} + u_{i(oq)} \tag{3.29}$$

$$u_{i(o)} = 0 \tag{3.30}$$

where $i = 1, 2$ are the indices of displacements along ***x***, ***y*** respectively; $u_{i(mc)}$, $u_{i(ob)}$, $u_{i(cp)}$, $u_{i(bp)}$, $u_{i(mq)}$ and $u_{i(oq)}$ are the displacements of the nodes on the line mc, ob, cp, bp, mq and oq respectively; $u_{i(m)}$, $u_{i(p)}$, $u_{i(q)}$ and $u_{i(o)}$ are the displacements of the node *m*, *p*, *q* and *o* respectively.

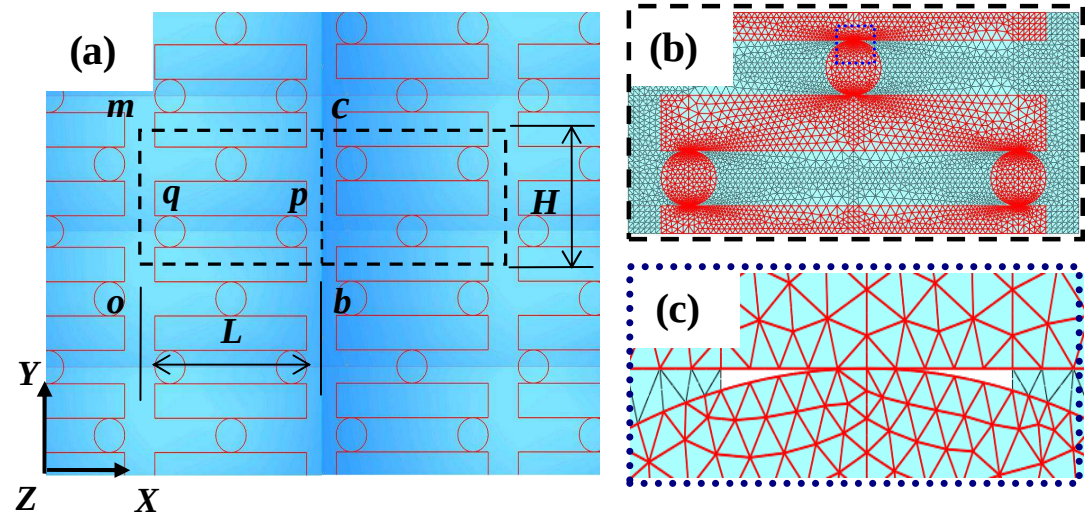

Figure 3.5 (a) Idealized micro-geometry of aligned percolating whisker network, λ=5; (b) 2D percolating unit cell with meshes, λ=7; (c) magnified view (~ 20 times) of contact region shown in square box in (b).

Table 3.3 Two-dimensional percolating unit cell parameters**

Aspect ratio λ	Length $L(\mu m)$	Height $H(\mu m)$	Volume fraction V_f (%)
3	2.1	2	50
5	3.1	2	50
7	4.1	2	50
10	5.6	2	50
15	8.1	2	50
20	10.6	2	50

**It should be noted that length L is dependent on the aspect ratio λ if volume fraction V_f, height H and system geometry are fixed.

The 2D mesh is generated with 6 node triangular elements, CPS6M from ABAQUS manual with average size of 0.05 (μm) except near the contact region where a smaller size of 0.006 (μm) is employed. Plane stress conditions are assumed. In order to assure element conformity in contact regions, a very small amount of the matrix is removed near each contact region, as depicted in Figure 3.5 (c). The length of the removed region is double the contact length, the latter of which is obtained from a separate simulation carried out based on the same whisker geometry but without matrix. It was found that there was no significant dependence

on simulation results on the size of this removed matrix region. Parameters of unit cells containing whiskers with varying aspect ratio are shown in Table 3.3, while Figures 3.6 showing the corresponding unit cells with meshes.

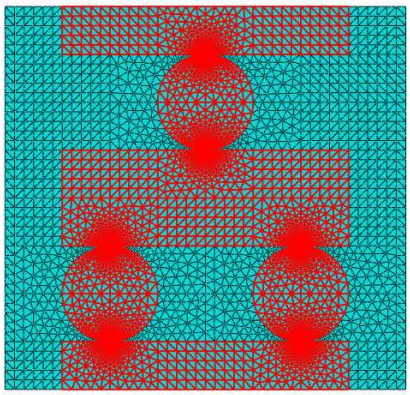

λ= 3

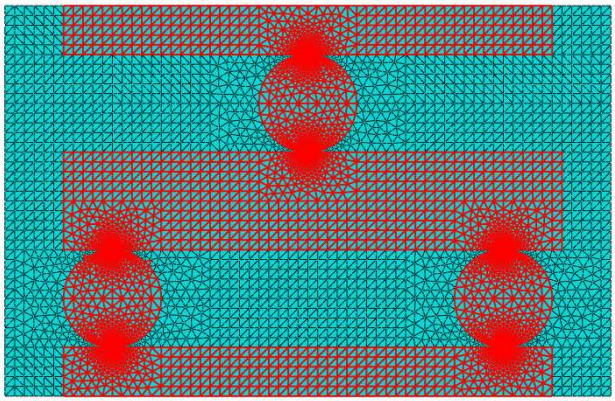

λ= 5

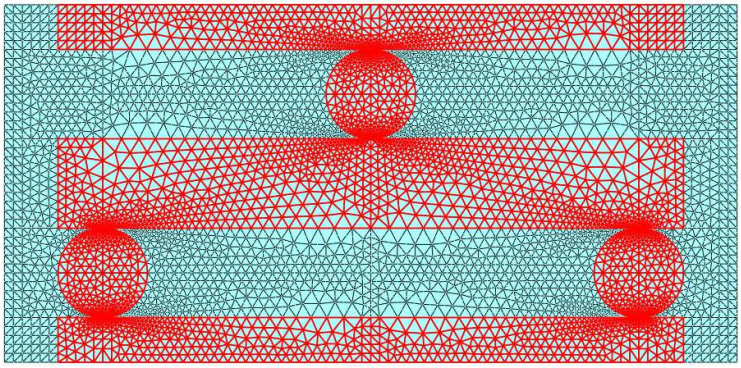

λ= 7

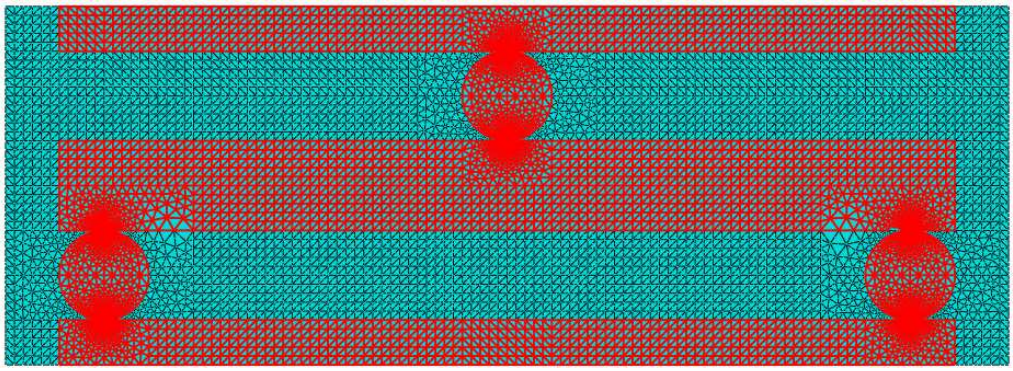

λ= 10

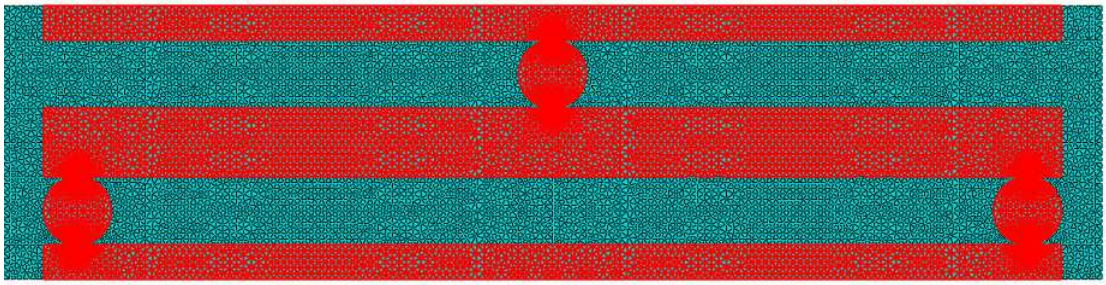

λ= 15

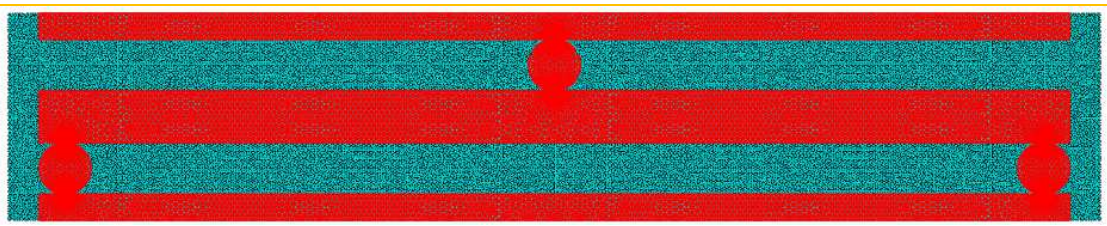

λ= 20

Figure 3.6 2D aligned percolating unit cells with meshes, from top to bottom with aspect ratios of 3, 5, 7, 10, 15 and 20. Red lines delineate the whiskers inside.

3.4.3. 3D single whisker unit cells

In order to study composites containing low volume fraction and/or unidirectionally aligned whiskers without interactions, single whisker unit cells with varying aspect ratio are also generated via ABAQUS CAE 6.8-3. Whiskers are assumed to be uniformly placed within the matrix while the ratios of whisker length (l) to cell length(L) and of whisker diameter(R) to cell width (D) are the same, that is $l/L = R/D$, as shown in Figure 3.7 (a) and (b). The smallest

repeating volume is enclosed in the dash lines, only one eighth of which is employed as the unit cell (Figure 3.7 (c) and (d)) with SBCs at boundaries. Table 3.4 shows the parameters of 3D single whisker unit cells with varying aspect ratio while keeping the volume fraction as 10%. The mesh is generated with 20 node hexagonal elements, referred to as C3D20R in the ABAQUS manual, with average size of 0.05 (μm), as shown in Figure 3.8.

$$u_{1(x=D/2)} = u_{1(x=D/2,y=0,z=0)} \tag{3.31}$$

$$u_{2(y=D/2)} = u_{2(x=0,y=D/2,z=0)} \tag{3.32}$$

$$u_{3(z=L/2)} = u_{3(x=0,y=0,z=L/2)} \tag{3.33}$$

$$u_{i(x=0,y=0,z=0)} = u_{1(x=0)} = u_{2(y=0)} = u_{3(z=0)} = 0 \tag{3.34}$$

where $i = 1, 2, 3$ are the indices of displacements along *x*, *y*, *z* respectively; $u_{1(x=D/2)}$ are the displacements along *x* direction of the nodes on the plane at position $x = D/2$; $u_{2(y=D/2)}$ are the displacements along *y* direction of the nodes on the plane at position $y = D/2$; $u_{3(z=L/2)}$ are the displacements along *z* direction of the nodes on the plane at position $z = L/2$; $u_{1(x=D/2,y=0,z=0)}$ are the displacements along *x* direction of the node at position $(D/2, 0, 0)$; $u_{2(x=0,y=D/2,z=0)}$ are the displacements along *y* direction of the node at position $(0, D/2, 0)$; $u_{3(x=0,y=0,z=L/2)}$ are the displacements along *z* direction of the node at position $(0, 0, L/2)$; $u_{i(x=0,y=0,z=0)}$ are the displacements of the node at position $(x = 0, y = 0, z = 0)$; $u_{1(x=0)}$, $u_{2(y=0)}$ and $u_{3(z=0)}$ are the displacements along *x*, *y* and *z* directions of the nodes on the plane at positions $x = 0$, $y = 0$ and $z = 0$ respectively.

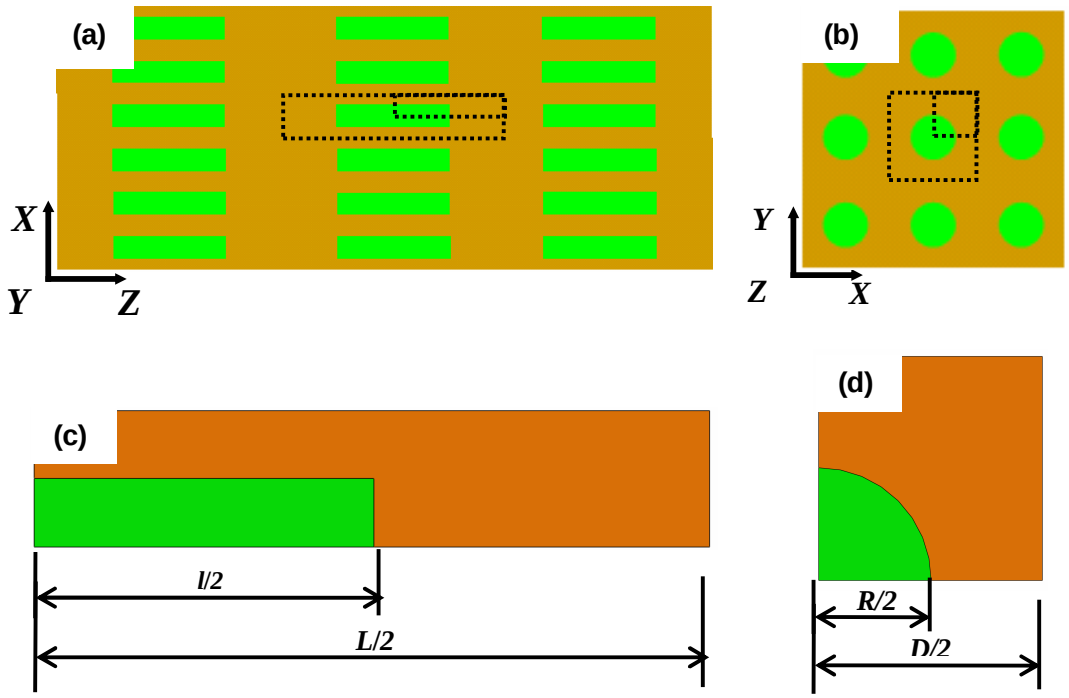

Figure 3.7 (a)&(b) Idealized micro-geometry of aligned whisker network, λ=5, V_f =10%, *l/L = R/D*; (c)&(d) unit cell used in the simulation.

Table 3.4 Three-dimensional aligned single whisker unit cell parameters**

Aspect ratio λ	Length *L/2*(*μm*)	Width *D*/2(*μm*)	Volume fraction V_f (%)
5	2.485	0.497	10
7	3.478	0.497	10
10	4.969	0.497	10
15	7.454	0.497	10
20	9.939	0.497	10

**It should be noted that the length *L* and W is dependent on the aspect ratio λ if the volume fraction V_f , and system geometry are fixed (*l/L = R/D*).

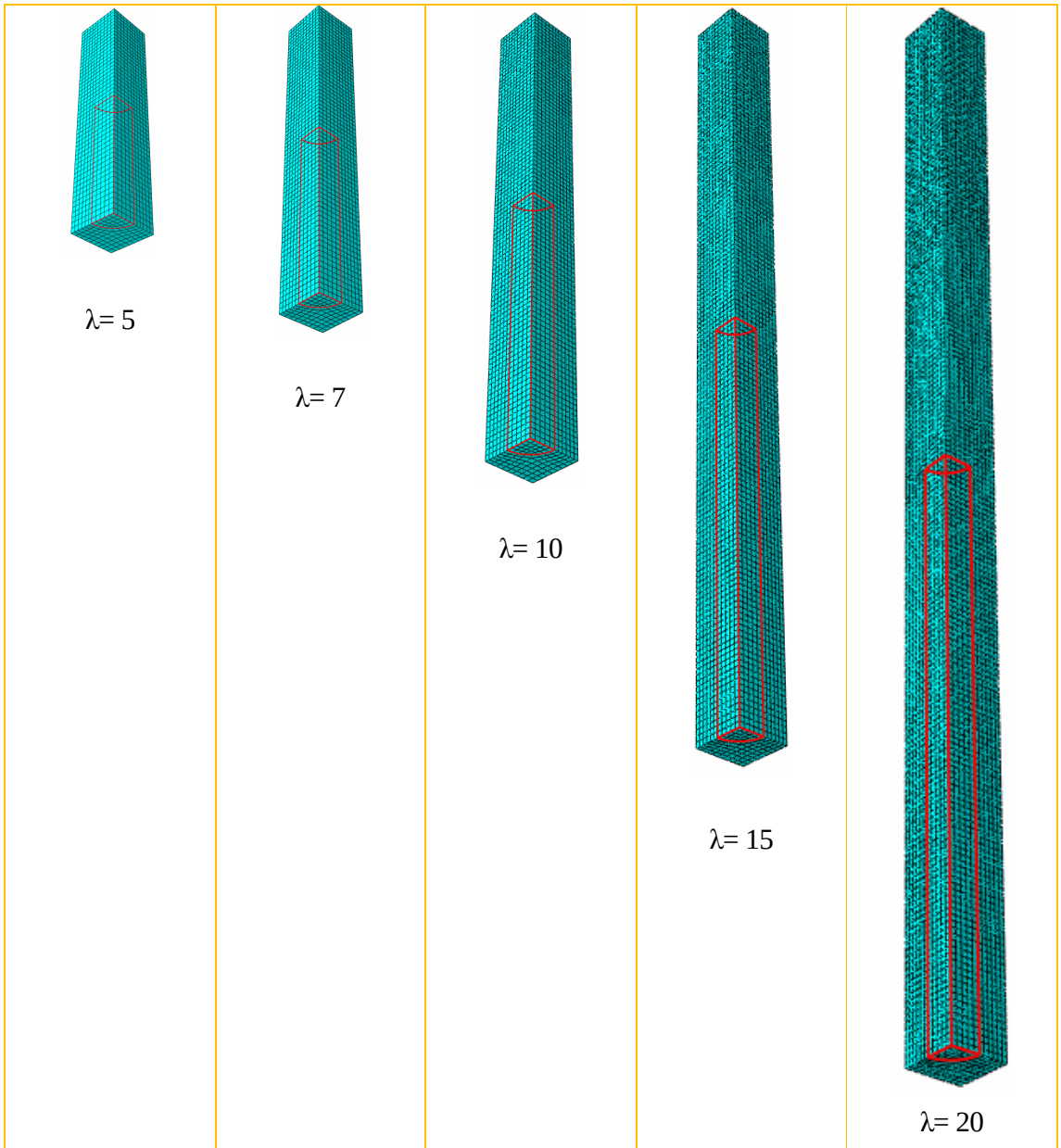

Figure 3.8 3D single whisker unit cells with meshes, from left to right with aspect ratios of 5, 7, 10, 15 and 20, red lines delineate the whiskers inside, element size is around 0.05.

3.5. Accuracy analysis and element selection

3.5.1. Source of Errors

Finite element modeling is a numerical approximation to the boundary value problem, which is only useful if it can be assured of reliability based on some analyses for accuracy. In general, there are three categories of errors associated with any simulation (Cook, 1995): (1) modeling error, due to the replacement of a physical problem by an approximate mathematical formalism; (2) discretization error, because the equation is solved in piecewise fashion by FEM in space and time; and (3) numerical error, since only a finite number of bits are used to represent each number by the computer. The first one will be discussed in the subsequent chapters. The third one can only be improved through choosing a *double precision* number format in any commercial FEM software in order to get a better accuracy, which is routinely used for current study. This section focuses on the error analysis from the second source.

The truncation error associated with the FEM treatment of the creep problem decomposes into two parts: one part is the discretization with respect to space and the other part is the discretization with respect to time. As introduced in section 3.2.1, FEM solution converges monotonically to the correct one with an increasing number of elements (*h*-refinement). This is guaranteed mathematically (Marti, 1986) and is verified by a patch test which is accomplished for each kind of element by commercial software already (e.g. ABAQUS Benchmark Manual). For the truncation error with respect to time, as introduced in section 3.2.2, the step size is controlled by the accuracy criterion (error tolerance) instead of the stability criterion. We are interested in what value of error tolerance would be enough for the creep analysis. Theoretically, the smaller the element size and error tolerance are, the more accurate the result is. However, we want to avoid the waste of time and computer resources associated with over-refinement.

This section studies both accuracy effects which can be controlled by users: element size and error tolerance (*cetol*). Since they are based on the results instead of the theoretical

predictions, they might be viewed as posterior error estimations. The study is based on the percolating unit cell in Figure 3.6 with aspect ratio λ=5. It is expected that this system could provide a representative study provided all unit cells used in the current study (Figure 3.4, 3.6 and 3.8) retain the same set of units: (1) it has the most complicated near contact regions although not the most complicated whisker distribution; (2) the stress redistribution greatly differs throughout the system since all the load will be transferred from the matrix to the whiskers (as detailed in Chapter 5), which is intrinsically related to the error tolerance (in equation 3.19). A compressive stress of -60MPa is applied in the *y* direction on the top surface with the boundary conditions illustrated in section 3.4.2.

3.5.2. Element selection

Generally, element selection is as important as the selection of element size during discretization with respect to space in order to get a reliable solution for a specific problem. In principle, hexahedrons (e.g. C3D20R in the 3D single whisker unit cells, Figure 3.8) are preferred since they are capable of providing a solution of equivalent accuracy at less cost. However, triangles (e.g. CPS6M in the 2D percolating unit cells, Figure 3.6) and tetrahedrons (e.g. C3D10M in the 3D random whiskers unit cell, Figure 3.4) are employed to obtain a high quality of elements for complex geometries. Quality of the elements can be assured with the aid of mesh verification function in ABAQUS CAE that highlights elements with extreme angles and aspect ratios. Normally, elements with second order interpolation function and reduced integration are chosen since the first one is capable of representing the curved boundaries (whiskers) more closely and of capturing the stress concentration more accurately, while the latter one is capable of mitigating the over stiffened matrix. In current study, modified triangular (CPS6M) and tetrahedral (C3D10M) elements are recommended by ABAQUS documentation for a better accuracy in nonlinear calculations especially contact problems via containing additional degrees of freedom.

3.5.3. Discretization with respect to space

Theoretically, the order of truncation error for FEM may be expressed as (Stolle, 2005)

$$O\left(h^{2(p+1-m)}\right) \tag{3.35}$$

where h is the size of the element, p is the order of polynomial and m is the highest order derivative of displacement for calculating strain. Generally, by study of how the sequence converges (linear extrapolation) we might be able to conclude the error of results from the finest mesh. However, the geometry used in the current study is very complicated and biased element size is used in order to capture the stress gradient around the contact area (Figure 3.5 and 3.6). The relationship of Equation 3.35 might not be evident. So a series of simulations with different element sizes are carried out to study the effect of h-refinement in the sense that the discretization error with respect to time plays no role for elastic deformation. Results (Figure 3.9) for average element sizes of $0.05\,\mu m$, $0.08\,\mu m$ and $0.125\,\mu m$ (except the near contact regions) are in substantial agreement, indicating that convergence is almost complete.

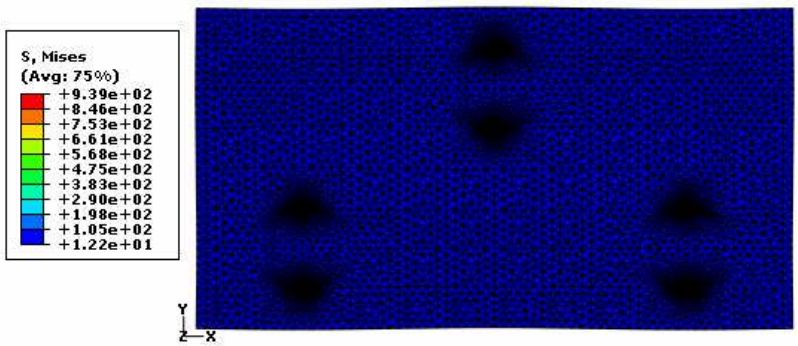

h=0.05 μm

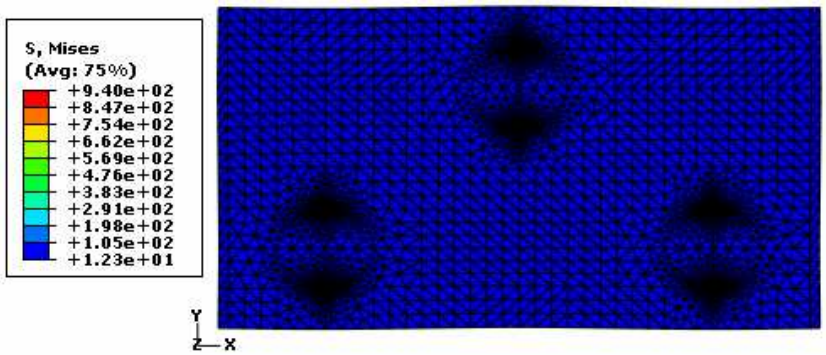

h=0.08 μm

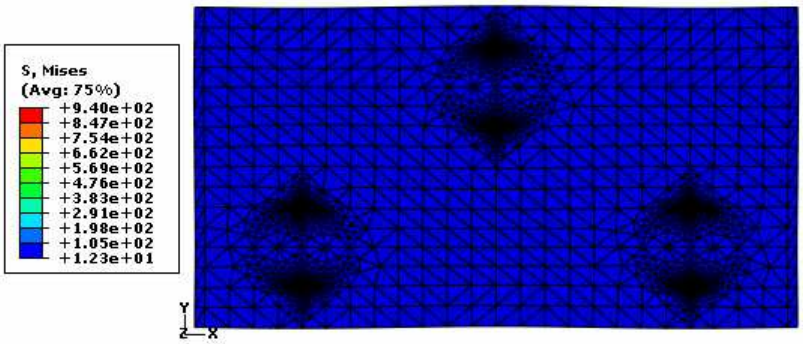

h=0.125 μm

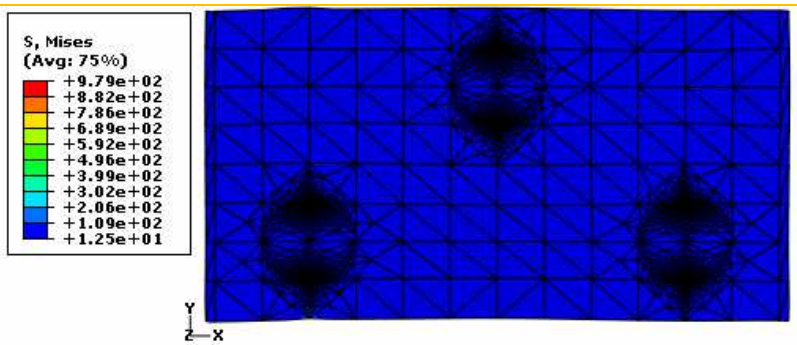

h=0.25 μm

Figure 3.9 Von Mises Stress for different element sizes with deformation scale factor of 1145, based on unit cell in Figure 3.6 with λ=5, $\sigma_{applied}$ = -60MPa.

3.5.4. Discretization with respect to time

A series of simulations with *cetol* (error tolerance) ranging from 1×10^{-1} to 1×10^{-7} are carried out to study the effect of error tolerance in the sense that the discretization error with respect to space plays no role by choosing the element size as 0.05 (μm). Creep time is 264,960 seconds at temperature of 1200℃ in order to obtain a total strain of 0.5% (that is the displacement along *y* direction U2 is around 0.01 μm) which is a value involved frequently in subsequent chapters. It is found that the result converges with difference less than 1% after $cetol=1\times10^{-3}$, as shown in Figure 3.10 which plots the U2 on the top surface versus the loading time. However, the CPU time increases by more than 3 times from $cetol=1\times10^{-5}$ to $cetol=1\times10^{-6}$ and 5 times to $cetol=1\times10^{-7}$ while making no significant difference in the accuracy (with a difference less than 0.15%), as shown in Figure 3.11. Therefore, the error tolerance is generally between the values of 1×10^{-3} and 1×10^{-5} for all simulations in order to obtain a good balance between the accuracy and computer time.

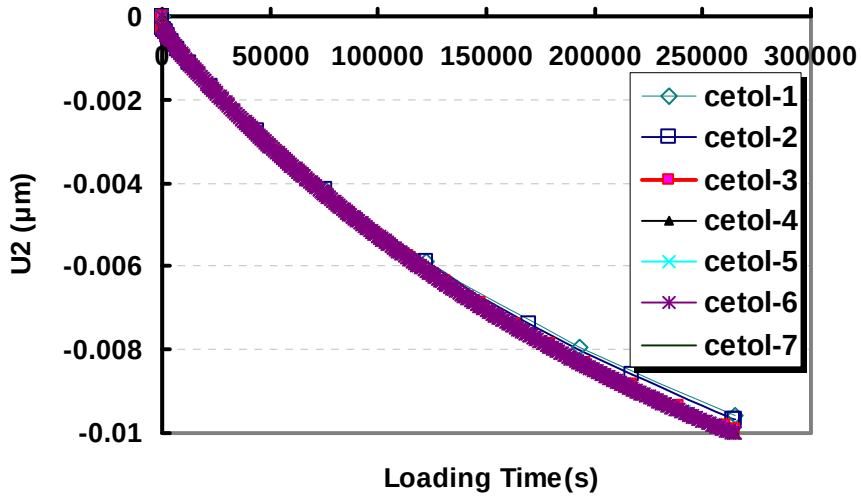

Figure 3.10 Displacement along y direction (U2) versus loading time for different value of error tolerance (cetol) from 1×10^{-1} (cetol-1) to 1×10^{-7} (cetol-7) based on unit cell in Figure 3.6 with λ=5, $\sigma_{applied}$ = -60MPa, element size = 0.05 (μm).

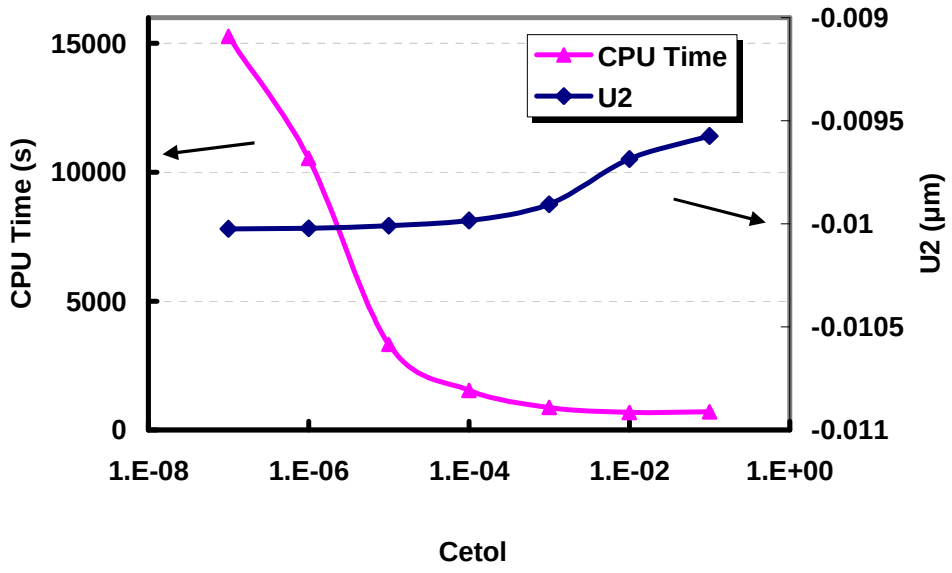

Figure 3.11 Error tolerance (cetol) versus CPU time and error tolerance versus U2 at time 264960 seconds, based on unit cell in Figure 3.6 with λ=5, $\sigma_{applied}$ = -60MPa, element size = 0.05 (μm).

CHAPTER 4

VIRTUAL MODEL OF DIFFRACTION

4.1. Introduction

Diffraction experiments are widely employed to determine the crystal structures as well as to provide information on stresses within samples. For most cases, data is extracted from the diffraction experiments to provide such information. However, in the current study, a reverse process is needed. This chapter proposes a virtual diffraction model that can be used as the framework to analyze the relationship between the deformation mechanisms predicted by our FEM simulations and the diffraction pattern we would expect to see experimentally: section 4.2 outlines the fundamentals of the classical diffraction theory (Klug *et al.*, 1974; Warren, 1990; Pecharsky *et al.*, 2003); section 4.3 details the derivation of the virtual diffraction model connecting the strain fields obtained from FEM simulations to the expected diffraction patterns in terms of peak position and peak width (FWHM); lastly, verification of the virtual diffraction model will be carried out in section 4.4. This model will be specifically applied to the deformation of Al_2O_3-SiC_w composites in chapter 6.

Although X-ray diffraction is used as an example in section 4.2, it is the same frame for all types of diffraction sources including neutron diffraction and electron diffraction. They all have a wavelength λ_D (at the level of Angstrom, $10^{-10}m$) comparable with the interatomic spacing, which is essential for diffraction. The difference is that X-rays and electrons interact with the electron clouds surrounding the atoms and are angle-dependent, while neutrons interact with the nuclei of the atoms and are not angle-dependent, in addition to a higher penetration depth.

4.2. Fundamentals of the diffraction theory

When an X-ray beam falls on an atom, it may be absorbed with the ejection of an electron from the atom or it may be scattered. For the latter case, the X-ray may be scattered elastically (no energy lost which means no modification of the wavelength) or inelastically (Compton modified scattering, yielding a longer wavelength). Both of them are useful in determining the materials structures. For stress and strain analysis, we emphasize the elastic scattering.

Since atoms within crystals are periodically arranged in three dimensional lattices, the diffracted *X*-rays from each atom interfere with each other, giving constructive or destructive interference due to their phase difference, which in turn results in strong intensity (proportional to the square of the amplitude of the resulting wave) in some particular directions. Bragg's law, shown in equation (4.1), is the most straightforward way of predicting the relationship between those directions and the crystallographic inter-planar spacing. It considers the scattering from a periodic lattice as the interference of reflections from each crystallographic plane, where the difference in travelling distance should be the integral multiple of the wavelength, as shown in Figure 4.1.

$$2d_{hkl}\sin\theta = \lambda_D \tag{4.1}$$

where d_{hkl} is the inter-planar spacing, θ is the angle between the incident beam and plane, λ_D is the wavelength of the incident beam.

It is convenient to express Bragg's law in a vector form. If S_0 and S are unit vectors in the directions of the incident and diffracted beams, $S - S_0$ is perpendicular to the *hkl* planes with magnitude of $|S - S_0| = 2\sin\theta$. Substituting these definitions into Bragg's law gives

$$\frac{|S - S_0|}{\lambda_D} = \frac{2\sin\theta}{\lambda_D} = \frac{1}{d_{hkl}} \equiv H_{hkl} \tag{4.2}$$

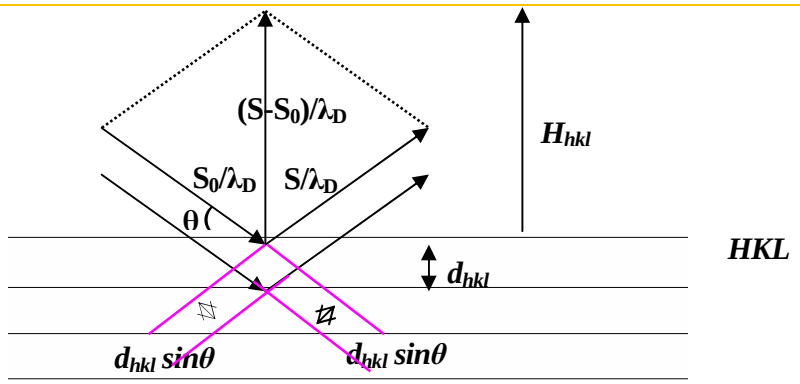

Figure 4.1 Relations involved in the vector representation of the Bragg law.

We can construct vectors S_0/λ_D, S/λ_D and H_{hkl} as shown in Figure 4.1. In terms of the reciprocal lattice H_{hkl} is written as

$$H_{hkl} = hb_1 + kb_2 + lb_3 \tag{4.3}$$

where h, k and l are the Miller indices of the planes and b_1, b_2 and b_3 are the reciprocal vectors of the crystal, which are defined as (Warren 1990):

$$b_1 = \frac{a_2 \times a_3}{a_1 \cdot a_2 \times a_3} \quad b_2 = \frac{a_3 \times a_1}{a_2 \cdot a_3 \times a_1} \quad b_3 = \frac{a_1 \times a_2}{a_3 \cdot a_1 \times a_2} \tag{4.4}$$

in which, a_i is the vectors in the normal lattice. There are two important relations between the two vector spaces (Warren, 1990):

(1) The (hkl) plane in the normal lattice corresponds to a point in the reciprocal lattice with position vector of $hb_1 + kb_2 + lb_3$ normal to the plane with the length of $1/d_{hkl}$;

(2) $$a_i \cdot b_j = \begin{cases} 1, & i = j, \\ 0, & i \neq j. \end{cases} \tag{4.5}$$

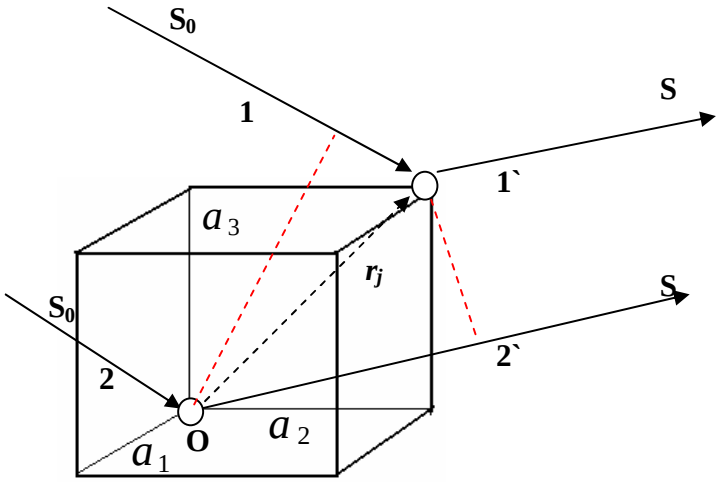

Figure 4.2 Schematic illustration of the interference of two atoms in a unit cell.

A crystal can be viewed as an infinite three dimensional packing of identical unit cells. In *X*-ray diffraction, the structure factor F_{hkl} is derived by considering the interference of scattered *X*-rays from all the atoms in the unit cell. It contains information to determine the scattering power of a crystal. Figure 4.2 shows the interference of scattered waves of two atoms. S_0, S and a_i have their usual meanings, r_j is the position vector of the j^{th} atom.

$$r_j = x_j a_1 + y_j a_2 + z_j a_3 \tag{4.6}$$

The difference of the wave travelling distance δ_j is given by

$$\delta_j = r_j \cdot s - r_j \cdot s_0 = r_j \cdot (s - s_0) \tag{4.7}$$

The phase difference of the two waves is given by

$$\varphi_j = \frac{2\pi}{\lambda}\delta_j = 2\pi (h x_j + k y_j + l z_j) \tag{4.8}$$

It is convenient to express the propagation of a wave in terms of the quantum mechanical free-space traveling wave function. For the scattered wave of the j^{th} atom, the phase shift in the complex wave functions of the X-rays scattered from the two atoms is given by:

$$\psi_j = |\psi_j| e^{i\varphi_j} = f_j e^{2\pi i(hx_j + ky_j + lz_j)} \tag{4.9}$$

where f_j is the amplitude of unmodified scattering per atom expressed in electron units (amplitude in units of the amplitude from a single electron) of the j^{th} atom.

$$f = \frac{\text{amplitude-of-unmodified-scattering-per-atom}}{\text{amplitude-of-unmodified-scattering-per-electron}} \tag{4.10}$$

Suppose there are ***N*** atoms in the unit cell, the resulting scattered wave amplitude is the summation of scattered amplitudes by all atoms. The structure factor F_{hkl} thus becomes (Pecharsky, 2003):

$$F_{hkl} = \sum_{j=1}^{N} f_j e^{2\pi i(hx_j + ky_j + lz_j)} \tag{4.11}$$

From the structure factor F_{hkl}, it is straightforward to see that due to the symmetry within the crystalline structure, only certain (hkl) planes satisfying certain conditions have the potential to give out the diffraction peak in a diffraction experiment. Adding up all the scattered waves from each unit cell within a strain free crystal, Warren (1990) proved that if the size of the crystal is large enough, for example, hundreds of times the size of the unit cell, the resulting scattered beam should have an extremely sharp intensity profile. However, the observed diffraction peak is broadened, displaced from its theoretical angle 2θ on the goniometer scale, and even more or less asymmetrical, as shown in Figure 4.3. This is attributed to two general sources (Klug *et al.*, 1974):

(1) Physical broadening from the crystallite-size distribution, magnitude and distribution of lattice strain, which defines the pure diffraction profile $f(\varepsilon)$;

(2) Instrumental broadening from the wavelength distribution of the incident beam (lack of monochromatism), flat specimen surface, specimen transparency and aberrations introduced from the geometrical properties of the diffractometer, which defines the weight function $g(\varepsilon)$.

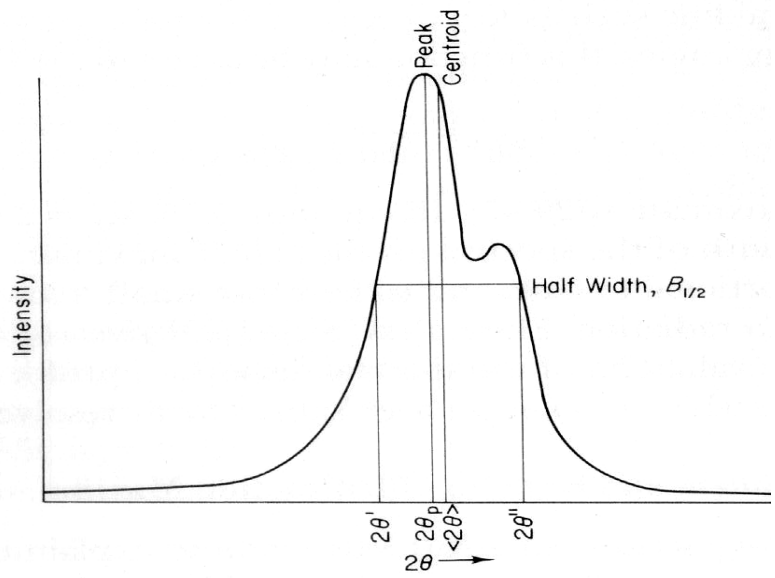

Figure 4.3 A typical observed line profile (Klug *et al.*, 1974).

The observed profile $h(\varepsilon)$ is the convolution of the pure diffraction profile $f(\varepsilon)$ and the weight function $g(\varepsilon)$ (Klug *et al.*, 1974). The pure diffraction line profile $f(\varepsilon)$ could be obtained via deconvoluting the observed line profile $h(\varepsilon)$ to yield the information needed. However, it involves extensive and tedious computations, e.g. Fourier transformation (Stokes, 1948). For many practical applications where only relative numerical results are needed, direct measurements of the profile width would be employed instead. Generally, peak position and peak breadth are critical characters used to determine the inter-planar spacing, and the crystallite size and lattice strain, respectively.

4.3. Relation between diffraction and deformation in Al_2O_3-SiC_w

For the present study, since the long axes of the SiC whiskers are coincident with the **[**111**]** crystallographic direction, while the long range order of three other off-axis **{**111**}** planes are destroyed during crystal growth (Nutt, 1984), the **(**111**)** plane diffraction peak is related primarily with the normal strain along the whisker axis, e.g., ε_{xx} if the whisker axis is parallel to the ***x*** direction in space coordinate. According to Bragg's law, $2d_{hkl}\sin\theta = \lambda_D$, it is simple to verify that non-uniform microstrains (Figure 4.4 (c)) would result in a broadening and perhaps also a shift of diffraction angle, while uniform microstrains (Figure 4.4 (b)) would only result in a shift of the diffraction angle. The vertical lines in Figure 4.4 represent the (111) planes normal to the whisker axis. If the (111) peak of the crept sample becomes broadened when comparing with the one before creep, this provides support for the bending mechanism of anelastic recovery (Wilkinson *et al.*, 1998).

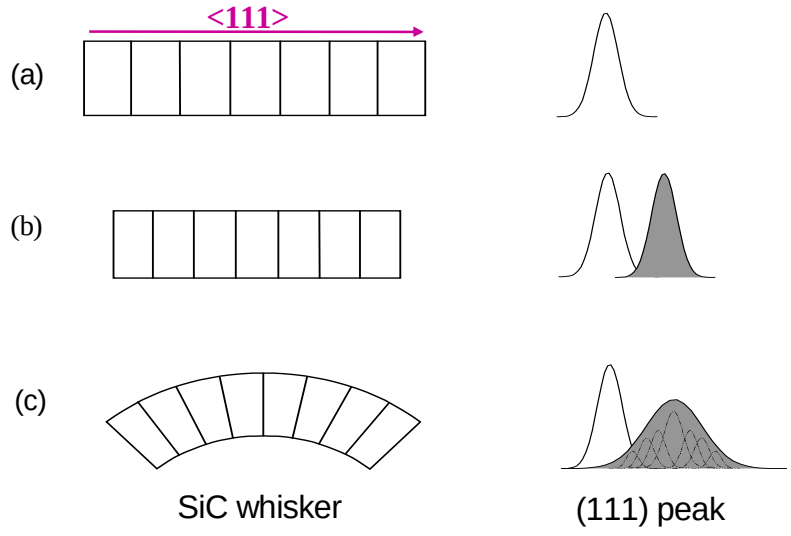

Figure 4.4 Schematic illustration of change in the shape and position of (111) peak due to lattice deformation: (a) without deformation (b) uniaxial compression and (c) bending.

4.4. Development of the diffraction model

4.4.1. Model construction

Mathematically the most significant measures of peak position and peak width are the centroid (equation (4.12)) and variance (equation (4.13)) due to the additivity of these two parameters through convoluting the pure diffraction profile $f(\varepsilon)$ and the weight function $g(\varepsilon)$ (Klug *et al.*, 1974):

$$< 2\theta >= \frac{\int 2\theta I(2\theta) d(2\theta)}{\int I(2\theta) d(2\theta)} \tag{4.12}$$

$$W_{2\theta} = < (2\theta - < 2\theta >)^2 >= \frac{\int (2\theta - < 2\theta >)^2 I(2\theta) d(2\theta)}{\int I(2\theta) d(2\theta)} \tag{4.13}$$

where $I(2\theta)$ is the intensity at the diffraction angle in terms of 2θ on the goniometer scale which acts as the probability density function. The theoretical advantage gained as a result of the additivity of variances is more than offset in practical use due to the sensitivity of the variance on background (Klug *et al.*, 1974). Use of variance on the peak width is referred to also as the Wilson method (1963). Meanwhile, other parameters such as integral breadth and full width at half maximum (*FWHM*) are also frequently used to characterize the peak profile while line profiles $f(\varepsilon)$, $g(\varepsilon)$ and $h(\varepsilon)$ are assumed.

In order to deal with the centroid and variance that originates from the strain field separately and independently from other factors, crystallite size and instrument effects are assumed constant during the calculation, which is physically sound since microstructures of SiC_w reinforced Al_2O_3 composites undergo no significant changes during the creep deformation and the same diffraction experimental set up were applied each time. Furthermore, only elastic inter-planar spacing changes are taken into account which is conformable to the isotropic elastic deformation of SiC whiskers (refer to Section 3.1). Each element of our FEM simulations is treated as a quasi-diffraction-domain that yields a diffraction peak behaving as a

delta function with position and intensity determined by the strain and volume of the corresponding element respectively. Moreover, the volume of the element is big enough compared with the crystallographic unit cell in Warren's work (1990) to justify that the size and shape effect of each element can be ignored. A profile from such a deformed FEM sample is comprised of a superposition of diffraction maxima from all such elements with different weights *v*.

The mathematical development of our diffraction model begins by differentiating the Bragg's law $2d_{hkl}\sin\theta = \lambda_D$

$$2d_{hkl}\cos\theta\Delta\theta + 2\sin\theta\Delta d_{hkl} = \Delta\lambda_D \tag{4.14}$$

where d_{hkl}, θ, λ_D, and Δd_{hkl}, $\Delta\theta$, $\Delta\lambda_D$ are the inter-planar spacing of *hkl* planes, the diffraction angle and the wavelength of the diffraction source respectively, along with their corresponding changes. Since $\Delta\lambda_D = 0$ due to constant instrumental broadening, a small local strain shifts the reflection by

$$\Delta\theta = -\tan\theta_0\varepsilon \tag{4.15}$$

where θ_o is the diffraction angle for zero strain, $\Delta\theta$ is the shift of the diffraction angle due to strain ε which is the ratio of the change of the inter-planar spacing to the strain free spacing. By replacing the intensity, in other words the probability density function, with the volume of the element, the centroid and the variance of the diffraction line profile are expressed as

$$<2\theta>=\frac{\sum_{i=1}^{n}2\theta_i V_i}{\sum_{i=1}^{n}V_i} \tag{4.16}$$

$$W_{2\theta}=\frac{\sum_{i=1}^{n}(2\theta_i-<2\theta>)^2 V_i}{\sum_{i=1}^{n}V_i} \tag{4.17}$$

where the summation goes over all elements. Substituting the equation (4.15) into (4.16) and (4.17), the centroid and the variance of the diffraction line profile due to the finite strain distribution are expressed by

$$< 2\theta >= -2\tan\theta_0 \frac{\sum_{i=1}^{n} \varepsilon_i V_i}{\sum_{i=1}^{n} V_i} + 2\theta_0 \tag{4.18}$$

$$W_{2\theta} = 4\tan^2\theta_0 \frac{\sum_{i=1}^{n} \left(\frac{\sum_{i=1}^{n} \varepsilon_i V_i}{\sum_{i=1}^{n} V_i} - \varepsilon_i \right)^2 V_i}{\sum_{i=1}^{n} V_i} \tag{4.19}$$

where V_i and ε_i are the volume and strain of the i^{th} element, while $\boldsymbol{n}$ is the total number of elements obtained from the FEM simulations. Furthermore, since the variance, which has units of θ^2, is not a straightforward parameter to compare with the peak width, the full width at half maximum ($FWHM$), with units of θ, is obtained in order to compare with the neutron diffraction experimental data that is normally fitted with the Gaussian function. Finally the expressions for $FWHM$ is given by

$$FWHM = 2\sqrt{2\ln 2}\sqrt{W_{2\theta}} = 4\sqrt{2\ln 2}\tan\theta_0 \sqrt{\frac{\sum_{i=1}^{n} \left(\frac{\sum_{i=1}^{n} \varepsilon_i V_i}{\sum_{i=1}^{n} V_i} - \varepsilon_i \right)^2 V_i}{\sum_{i=1}^{n} V_i}} \tag{4.20}$$

One thing to mention is that equations 4.18 and 4.20 yield units of arc (radians) which should be converted into degrees by multiplying $180/\pi$ before comparing with the experimental data.

4.4.2. Model implementation through ABAQUS

The diffraction model is implemented through an ABAQUS post-processing algorithm with the aid of the Python language. For the present study, the **(**111**)** plane diffraction peak is associated with the normal strain along the whisker axis, e.g., E_{11} ($\mathcal{E}_{xx}$) for the 2D percolating unit cells (Figure 3.6) and E_{33} ($\mathcal{E}_{zz}$) for the 3D single whisker unit cells (Figure 3.8) in space coordinates. For the case of the 3D randomly-oriented-short-fibre unit cell (Figure 3.4), the strain field within each whisker is transformed with respect to its local coordinate system before calculating the $FWHM$ and 2θ to maintain a one to one assignment. The strain at the element centroid is employed during simulation. All the predictions possess a volume average character and are based on the diffraction angle $2\theta = 56°$ here for the (111) peak, while $56.36°$ is used in chapter 6 according to the neutron diffraction experiments of Quan (2004).

4.5. Verification of the diffraction model

In this section, verification of the diffraction model including the accuracy as well as the dependence on the element size is conducted to assure the overall quality of the present study. Model accuracy is accomplished by comparing the diffraction pattern predictions obtained from the numerical diffraction model and the analytical solution for the case of a simple supported beam under load as shown in Figure 4.5 (a). The beam possesses the properties of SiC whisker with a height of 0.5 μm and an aspect ratio of 20, and is subject to bending induced by the center load $F = 5MN$ and to tension induced by the end traction $P = 100MPa$ simultaneously. Element size dependence is examined by comparing the predictions based on different element size.

4.5.1. Diffraction model predictions

Numerically, FEM simulations of the beam under load are carried out first through ABAQUS standard to provide the strain fields which will be used as inputs for the subsequent

diffraction pattern simulations through the ABAQUS post-processor to predict *FWHM* (equation 4.20) and peak position (equation 4.18). Due to the symmetric distributions of the loads, supports and resulting strain fields, only half of the beam is simulated with SBCs used at the center. The geometry is meshed through ABAQUS CAE 6.8-3 with 8-node rectangular elements which is referred to as CPS8R in the ABAQUS manual. Two kinds of meshes with element size of 0.05 μm and 0.1 μm are employed in order to check the dependence on element size due to the intrinsic volume average character of the diffraction model. Figure 4.5 (b) and (c) show the strain field distributions based on the two meshes. Meanwhile, Table 4.1 summarizes the predictions of *FWHM* and peak position from the numerical diffraction simulations together with the values obtained analytically in the next section.

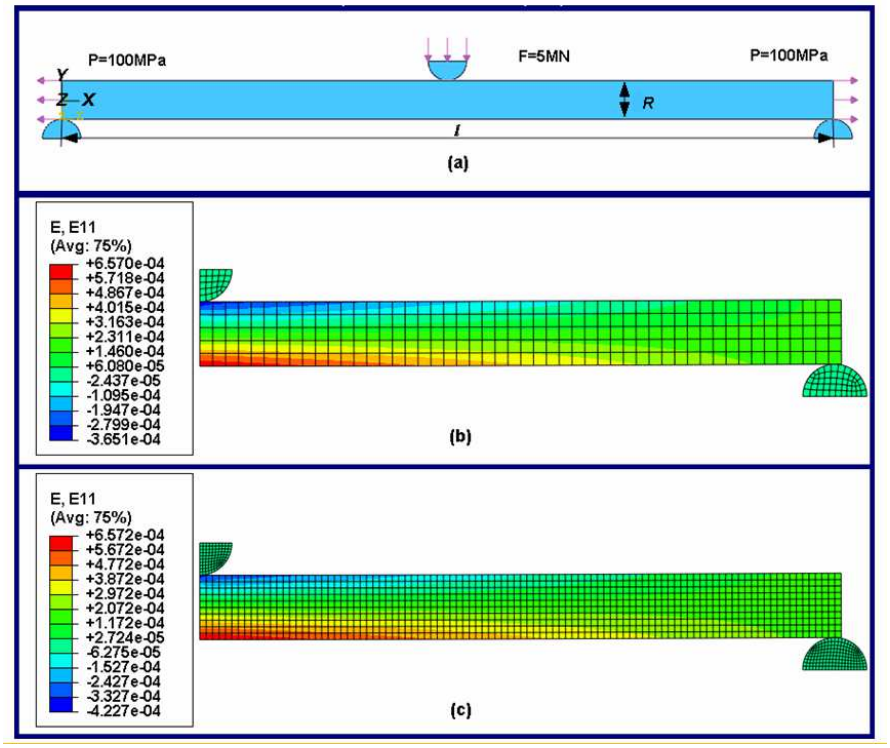

Figure 4.5 Diffraction model verification: (a) schematic illustration of a simple supported beam with height of 0.5μ*m* and span of 9.9μ*m* under bending and tension; (b) normal strain (E_{11} or ε_{xx}) distribution obtained from FEM simulations with element size around 0.1μ*m*; (c) with element size around 0.05μ*m*.

4.5.2. Analytical model predictions

Analytically, the resulting elastic response of the system is the sum of the responses from bending and tension independently according to the principle of superposition in physics. Without getting into a detailed derivation, the normal stress along the axis of a bent beam is given by (Wang *et al.*, 2000)

$$\sigma_{xx} = \frac{My}{I} \tag{4.21}$$

Here σ_{xx} is the normal stress along *x* direction. I is the second moment of area of the whisker cross section ($I = \frac{R^3}{12}$ for unit thickness into the *z* direction with *R* the height of the beam). y is position through the thickness of the beam running from *–R/2* to *R/2*. M is the bending moment with $M = \frac{1}{2}Fx$ for $(0 \le x \le \frac{1}{2}l)$ and $M = \frac{1}{2}F(l-x)$ for $(\frac{1}{2}l \le x \le l)$ (where l is the span of the beam) which is characterized by a symmetric distribution with respect to the axis of $x = \frac{1}{2}l$ for a center loaded beam. Therefore, it is obvious that the normal stress possessing a symmetric distribution with respect to the axis of $x = \frac{1}{2}l$ and an antisymmetric distribution with respect to the *x* axis yields a mean value of zero if the end effects are neglected based on the Saint-Venant principle (Timoshenko *et al.*, 1970). The normal strain behaves the same since $\varepsilon_{xx} = \frac{\sigma_{xx}}{E}$, and can be expressed as

$$\varepsilon_{xx} = \frac{1}{2}\frac{F}{EI}xy \qquad \text{for } (0 \le x \le \frac{1}{2}l) \tag{4.22}$$

The variance for a continuous variable 2θ is given by

$$W_{2\theta} = \frac{\int (2\theta - <2\theta>)^2 d(2\theta)}{\int d(2\theta)} \tag{4.23}$$

By substituting equation (4.15) into (4.23) and taking advantage of the zero value of the centroid ($<2\theta>=0$) resulting from the zero mean value of the normal strain ε_{xx}, the variance of the diffraction peak can be rewritten as a function of strain:

$$W_{2\theta} = \frac{\int (2\tan\theta_0 \varepsilon_{xx})^2 d(\varepsilon_{xx})}{\int d(\varepsilon_{xx})} \tag{4.24}$$

By substituting equation (4.22) into equation (4.24) and integrating over the left half of the beam ($0 \le x \le l/2$, $-R/2 \le y \le R/2$) due to the symmetry with respect to the axis of $x = \frac{1}{2}l$, the variance of the diffraction peak for a bent beam is given by

$$W_{2\theta} = \left(\frac{1}{12} \frac{F \tan\theta_0 Rl}{EI} \right)^2 \tag{4.25}$$

The analytical solution of the $FWHM$ for a beam under symmetric bending is expressed as

$$FWHM = \frac{\sqrt{2\ln 2}}{6} \frac{F \tan\theta_0 Rl}{EI} \tag{4.26}$$

Meanwhile, the symmetric bending does not contribute to the peak position since the mean value of the normal strain ε_{xx} is zero as argued before. In contrast, for the case of uniaxial tension, it has no contribution to the peak width, while contributing only to the peak position which could be calculated through equation (4.15) together with $\varepsilon_{xx} = \frac{\sigma_{xx}}{E}$:

$$\Delta 2\theta = -\frac{2\tan\theta_0 P}{E} \tag{4.27}$$

Comparison of the analytical predictions to those of the diffraction model is shown in Table 4.1. Same as before, equations 4.26 and 4.27 yield units of arc, which should be converted into degree by multiplying $180/\pi$.

4.5.3. **Summary**

Analytical predictions of the *FWHM* and peak position obtained through equations (4.26) and (4.27) are summarized in Table 4.1 together with the predictions from the two numerical diffraction simulations with varied element size. The diffraction model correctly calculates the changes of peak width and peak position, e.g. with differences of 0.97% (*FWHM*) and 0.098% ($\Delta 2\theta$) between the analytical predictions and the numerical diffraction simulations based on the element size of 0.05 *um*, a common value of FEM discretization used in the current study. Moreover, no dependence on the element size is observed since doubling the element size results only in a difference of 1.5% for *FWHM* and no difference for $\Delta 2\theta$. Meanwhile, the subtle difference between the two simulations is due mainly to the FEM calculations which depend on element size inherently, as shown in Figure 4.5 (b) and (c).

Table 4.1 Comparisons of $FWHM$ and $\Delta 2\theta$ for (111) peak between the diffraction model and analytical solution (in degree). (b): with element size around 0.1 μm (Figure 4.5 (b)), (c): with element size around 0.05 μm (Figure 4.5 (c)).

	Analytical solution	Diffraction model (c)	Diffraction Model (b)
$FWHM$ (***111***)	0.02366	0.02343	0.02307
$\Delta 2\theta$ (***111***)	-0.01015	-0.01016	-0.01016

CHAPTER 5

ANELASTIC BEHAVIOR MODELING OF Al_2O_3-SiC_w

5.1. Introduction

As discussed in the introduction of this Thesis, to date, the mechanisms responsible for the anelastic creep of SiC_w reinforced Al_2O_3 are still not well explained and no systematic numerical work has been carried out based on a unit cell methodology to explain how the elastic energy is stored within the network and how whiskers interact with each other. In order to address the aforementioned questions, this chapter examines creep deformation and anelastic recovery numerically in an Al_2O_3 matrix reinforced by whisker networks aligned in a 2D and 3D-random geometry (as illustrated in chapter 3). The Finite Element Method (FEM) will be used to calculate the local strain and stress fields. The deformation mechanisms of the whisker network and the relative contributions of bending and contact will be addressed. The investigation is carried out without considering the thermal effects. The material properties employed are illustrated in Table 5.1, which correspond to the data around 1200℃ in section 3.1.

Table 5.1 Material properties of Al_2O_3 and SiC_w

Property Material	$E(GPa)$	Poisson ratio	n	$C(S^{-1}\ MPa^{-1})$
SiC	600	0.17		
Al_2O_3	354	0.247	1	1.87×10^{-9}

5.2. Percolation of the whisker network

A percolation threshold is a mathematical concept used to describe the formation of long-range connectivity in systems. It has a broad range of application in various physical phenomena, such as electronic transport, the glass transition and the Anderson transition (Zallen, 1983). For spherical particles, it occurs at about 16vol% (Grannan *et al.*, 1981) and

decreases for fibres with increasing aspect ratio. Theoretical calculations specific to the fibre geometry approximate the percolation threshold for a random orientation as (Nan, 1993):

$$\phi_{th} = 0.7 / \lambda \qquad (5.1)$$

where λ is the whisker aspect ratio. In the cases studied here, for an aspect ratio of 20, a percolating path consisting of random contacts is formed when whisker volume fraction is above 4vol%. The percolating network is characterized by the ability to (statistically) enable load transfer across the unit cell. If the whisker distribution is not completely random due to hot pressing for example (the process by which SiC whisker reinforced Al_2O_3 is fabricated), the percolation threshold will be larger by about a factor of two for the same effective load transfer (Wilkinson *et al.*, 1998). The load transfer characteristics of a percolation threshold offer a plausible explanation of why pure alumina and composites containing less than 10vol% of whiskers show no significant time-dependent strain recovery when the load is removed during creep. This is consistent with the work of Favier *et al.* (1997) on a latex composite reinforced with cellulose fibers, which shows an unusual high value of elastic modulus when the volume fraction of cellulose fibers is above a particular value, a result that cannot be explained by the traditional mean field theory wherein fibers interactions are ignored. Their results can be explained analytically by incorporating the effect of fiber volume fraction via percolation theory.

In this section, we study the role of a percolating network on the anelastic behavior of Al_2O_3-SiC_w composites based on a 3D multi-whisker unit cell containing 15 fibres of equal size and aspect ratio (λ=5) at a reinforcement volume fraction of 15%. From percolation theory, composites with these parameters should form a percolating network, which is assumed to be a prerequisite of anelastic recovery observed in the Wilkinson and Pompe work (1998). As mentioned before, the 3D unit cell was constructed without perfect contacts deliberately. If the predicted magnitude of anelastic recovery based on this non-percolating geometry does not match experiments, a percolating network is demonstrated to be necessary. In Al_2O_3 composites, the typical experimental magnitude of the recovered anelastic strain is

around 1×10^{-3} when the SiC volume fraction is equal to or greater than 15% for whiskers, as well as particles (Gu *et al.*, 1994&1995; Deng *et al.*, 1999; Quan, 2004). Although this magnitude can be reproducible, it first appears when the total creep strain is around 5×10^{-3}. Figure 5.1 shows the simulated stress versus time for the case of creep deformation of a unit cell with randomly packed whiskers at 15vol%. In the simulation, an initial stress of 60MPa is subsequently reduced to 20MPa, analogously to recent experiments of Quan (2004). When the stress is reduced after 25 hours of creep deformation with the total accumulated strain of 5×10^{-3}, an instantaneous elastic contraction is observed, followed by a plateau of almost no time-dependent back strain for about 2 hours, after which forward creep strain is once again observed. As suspected, the lack of back strain in our simulations indicates that without an effective percolating network, elastic energy stored within the whiskers is dissipated locally without a detectable global back strain upon unloading. This result thus suggests the necessity of a percolating network for significant anelastic behavior to be observed.

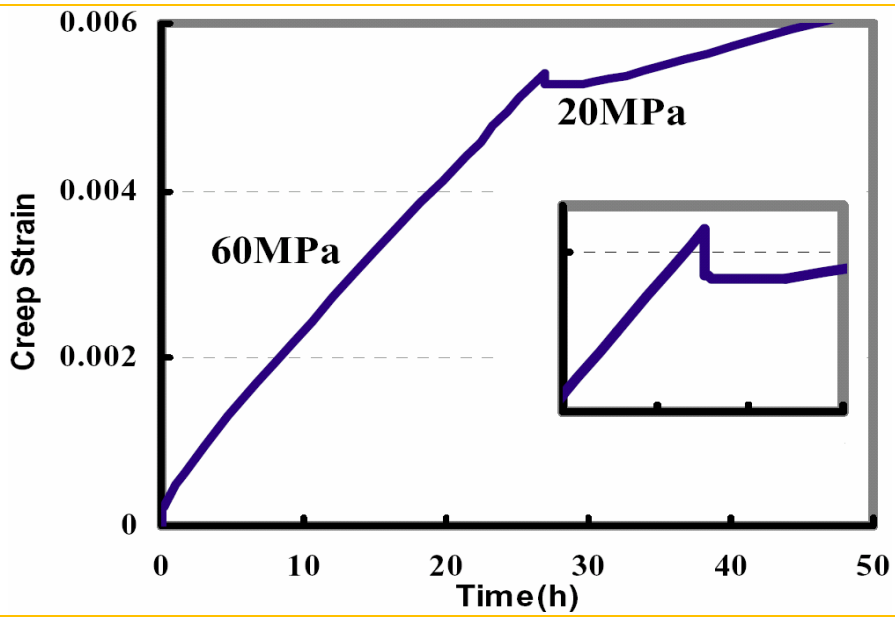

Figure 5.1 Stress reduction-Strain transient curve for the random, three-dimensional multi-whisker unit cell without contact, $\sigma_{applied}$ =-60MPa, σ_{final} =-20MPa.

It is also noted that in experiments, the 20MPa final stress may indicate a threshold stress for the creep deformation of Al_2O_3 ceramics below which no creep will occur because the grain boundaries will no longer act as the sources and sinks of defects needed for diffusional creep (Chiang *et al.*, 1997). Besides the absence of a percolating network, this could be a possible reason for not observing any back strain for pure alumina and alumina composites with low volume fraction of SiC_w. Further experiments investigating the threshold stress of the creep deformation of alumina are required to better incorporate the role of threshold stresses into the constitutive equations of FEM models.

5.3. Deformation mechanism of the 2D percolating whiskers network

The results of the previous section demonstrated the necessity of a 3D percolating network, which is achieved by an inclusion volume fraction above a threshold value. This section examines the role of whisker interactions in 2D networks that model the cross section of a 3D percolating network of regularly arranged whiskers, as described before. While these networks are not the same as a random 3D network, it is expected that they can still provide valuable insight into the role of whisker bending versus contact during creep deformation. Plane stress is assumed.

5.3.1. Typical stress reduction-strain transient and relaxation curves

Figure 5.2 shows a typical creep strain curve (solid line) from a simulation based on the percolating unit cell with aspect ratio of 5 and compressive stress of 75MPa along the ***y*** direction. Within the first 200 hours the strain increases rapidly then almost saturates at the value of 9.64×10^{-3} which is named the maximum recoverable strain ε^* and used to describe the capability of the network to provide anelasic recovered strain. Owing to the percolating geometry of these 2D simulations, all the accumulated strain is recovered within 500 hours after complete unloading. This process is driven by the elastic energy stored within the network at the unloading stage, exactly the reverse of what happens in the loading process.

When the total forward strain is 5×10^{-3} as shown in Figure 5.2 (dashed line), a significant amount of anelastic strain is observed even when the stress is only partially reduced. This indicates that unloading proceeds until a balanced state between the simulated residual stress and internal stress is achieved.

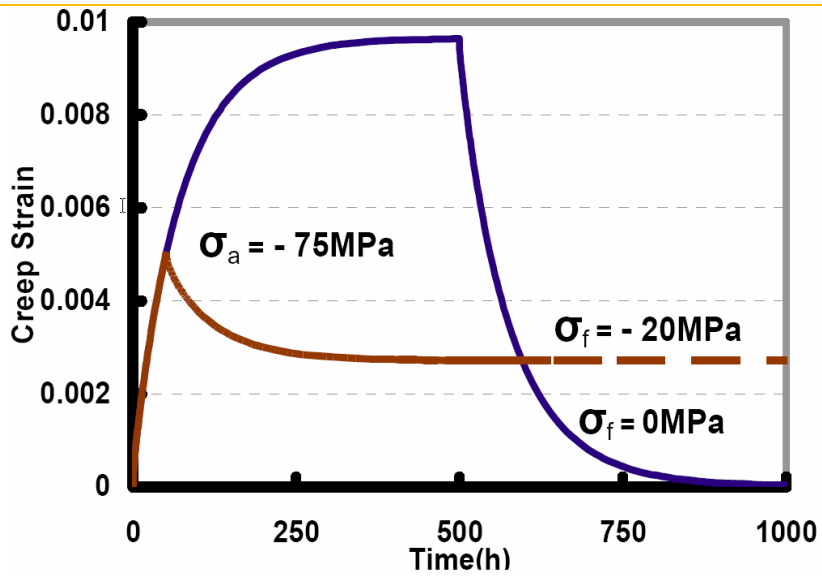

Figure 5.2 Stress reduction-Strain transient curve for 2-D percolating network, λ=5, $\sigma_{applied}$ = -75MPa, the solid line shows the asymptotic curve, the dotted line shows the behaviour while unloading at the strain of 5×10^{-3} with a final stress of -20MPa.

The asymptotic curve of the unloading part in Figure 5.2 can be expressed by

$$\ln\left(\frac{\varepsilon}{\varepsilon^*}\right)=-\frac{1}{\tau}t \qquad (5.2)$$

where ε and ε^* are the instant strain and asymptotic strain, respectively, while τ is the characteristic relaxation time and t is time. A straight line with the slope of $-1/\tau$ is generated as shown in Figure 5.3 when plotting $\ln\left(\varepsilon/\varepsilon^*\right)$ versus t. Reversing the slope yields the characteristic relaxation time τ used to characterize whether a given material behaves as a viscous fluid or rigid solid by the relative value of its characteristic relaxation

time τ (Poirier, 1985). This analysis shows that the unit cell model examined here behaves as an effective Kelvin-Voigt model consisting of spring and dashpot in parallel, the simplest analogue model of viscoelastic response. The characteristic relaxation time is 82h for the case examined here.

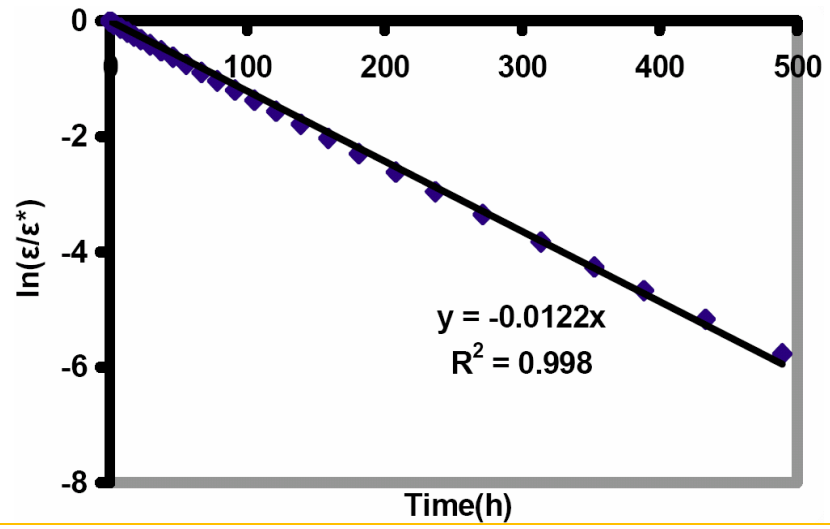

Figure 5.3 Plot of natural log of the fraction of recovered strain vs time, λ=5, σ_a = -75MPa.

5.3.2. Relative contribution of bending and contact effects

Our simulations suggest that creep strain accumulates in the matrix while the applied load is transferred from the matrix to the whisker network, saturating eventually to a maximum accumulated strain ε^* when the entire load is carried by the whisker network. Figure 5.4 and Figure 5.5 show the stress distribution of S_{11} and S_{22}, the normal stress along the ***x*** and ***y*** directions respectively, at full loading of a typical whisker network. It is seen that the whiskers behave similarly to three-point loaded bending beams during deformation. The matrix around the whiskers is made invisible for clarity. Half of the whisker "beam" is under axial tension and the other half is under axial compression. Maximum normal stress S_{11} occurs at the mid-span of the beam with positive and negative values corresponding to the tensile and

compressive part respectively. Normal stress S_{22} is distributed near the contact region, reflecting a contribution of the contact effect. The deflection of the top surface of the center whisker clearly illustrates a bending shape and a non-smooth concave region near the contact region, as shown in Figure 5.6.

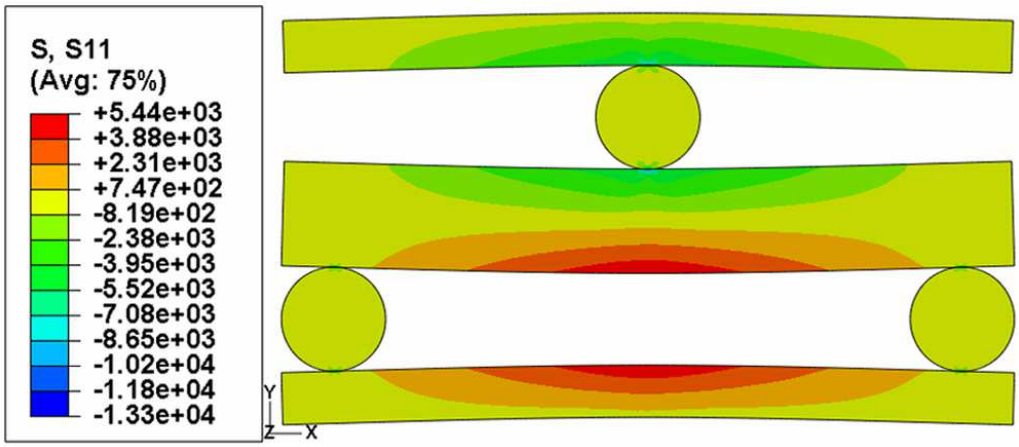

Figure 5.4 S_{11} distribution within whisker network with invisible (white regions) matrix, λ=7, $\sigma_{applied}$ = -75MPa.

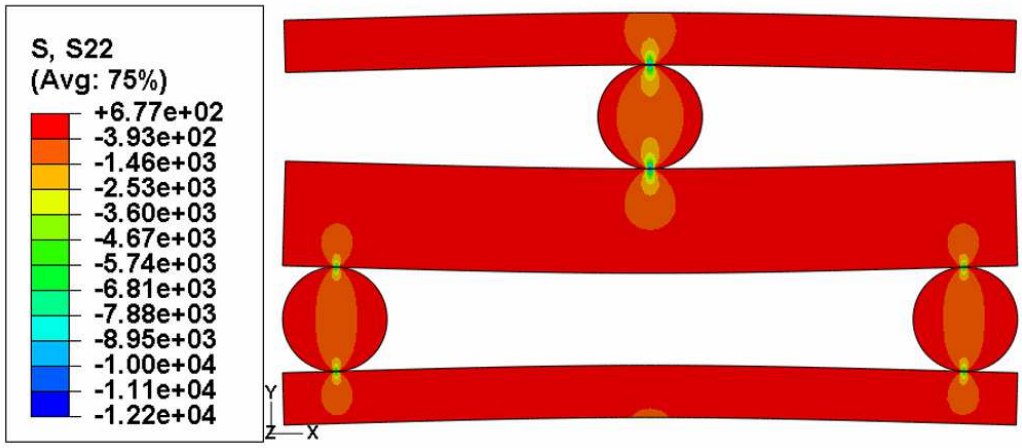

Figure 5.5 S_{22} distribution within whisker network with invisible matrix, λ=7, $\sigma_{applied}$ = -75MPa.

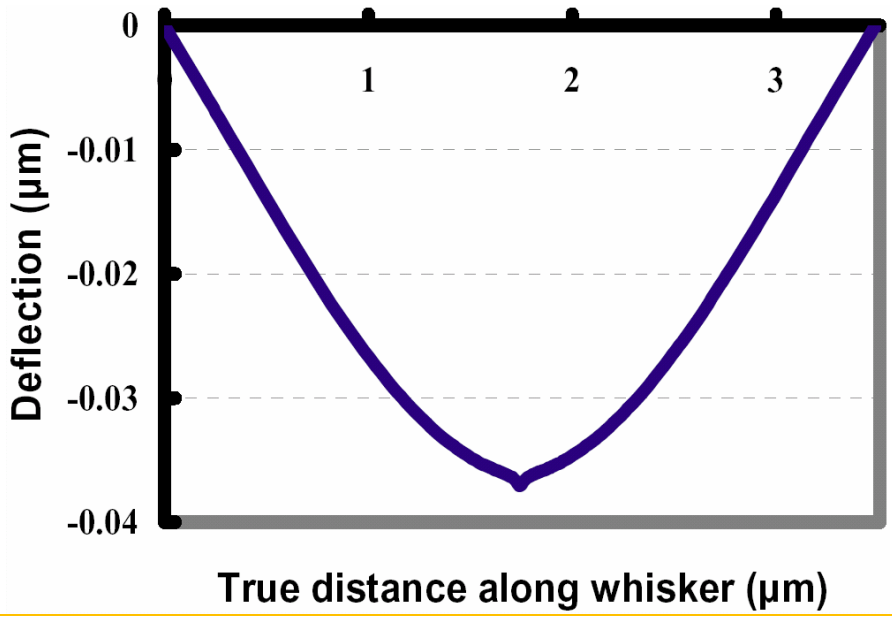

Figure 5.6 Deflection along the middle whisker, λ=7, $\sigma_{applied}$ = -75MPa.

As expected, simulations show that bending and contact occur at the same time. The relative percentage of the two deformation mechanisms are calculated from an energy point of view. The calculation is done on ABAQUS 6.7.1 through post-processing using the Python language. Specifically, the energy contribution from bending is given by

$$p_{(Bending)} = \frac{\sum_{i=1}^{n} \sigma_{11}^{i} \times \varepsilon_{11}^{i} \times V_i}{\sum_{i=1}^{n} (\sigma_{11}^{i} \times \varepsilon_{11}^{i} + \sigma_{22}^{i} \times \varepsilon_{22}^{i} + 2\sigma_{12}^{i} \times \varepsilon_{12}^{i}) \times V_i} \tag{5.3}$$

while the energy contribution from contact is given by

$$p_{(contact)} = \frac{\sum_{i=1}^{n} \sigma_{22}^{i} \times \varepsilon_{22}^{i} \times V_i}{\sum_{i=1}^{n} (\sigma_{11}^{i} \times \varepsilon_{11}^{i} + \sigma_{22}^{i} \times \varepsilon_{22}^{i} + 2\sigma_{12}^{i} \times \varepsilon_{12}^{i}) \times V_i} \tag{5.4}$$

where n is the number of elements in the whisker network, V_i is the volume of i^{th} element, σ_{11}^i and ε_{11}^i are the normal stress and strain along x direction for i^{th} element respectively, σ_{22}^i and ε_{22}^i are the normal stress and strain along y direction for i^{th} element respectively, σ_{12}^i and ε_{12}^i are the shear stress and strain for i^{th} element respectively. The remaining energy is contributed to shear deformation which is illustrated also in Figure 5.7 for comparison.

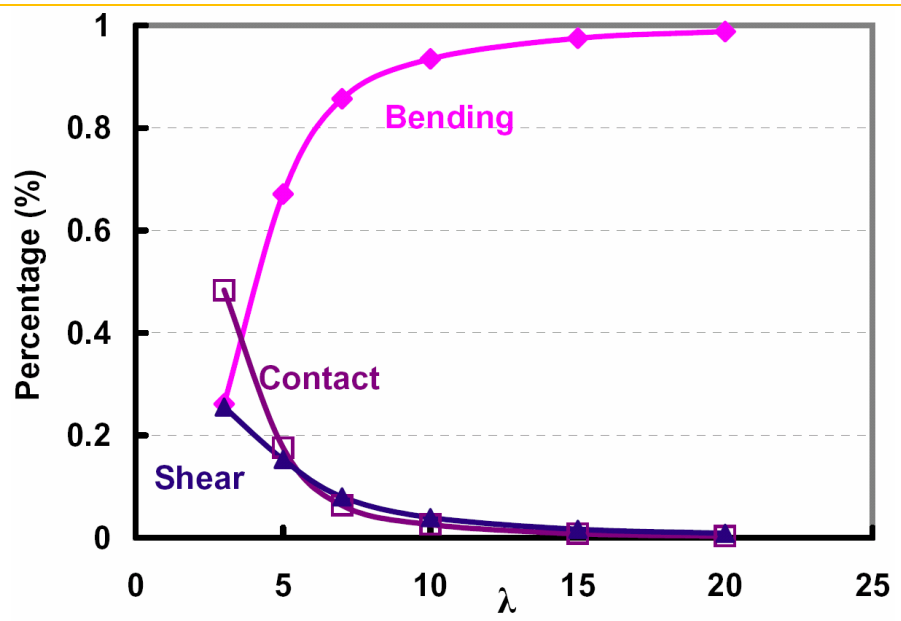

Figure 5.7 Contribution of two deformation forms in terms of percentage versus aspect ratio.

Figure 5.7 shows the contribution of the bending and contact effects for the total energy storage versus the whisker aspect ratio. It is clear that the bending contribution increases rapidly as the aspect ratio increases, then almost saturates at 100%. Even when the aspect ratio is 7, bending effect contributes to 87% of the total elastic energy. Furthermore, for the specific aspect ratio, the contribution of each deformation form, bending or contact, remains relatively the same as the creep deformation continues. Although the well aligned whisker distributions used here idealize the situation, it is expected that the generic features of

Figure 5.7 will also hold for a random network of whiskers, i.e., the contribution of bending will tend to unity as whisker aspect ratio increases. Meanwhile, the role of contact is not expected to be very significant, even at small aspect ratios. Therefore, the shape of whiskers could be simplified for the study of 3D random percolating network, although the same is not true for networks of cylindrical-shaped whiskers. It should be stressed, however, that the shear force at the interface between matrix and whiskers may induce a tensile or compression deformation, the relative importance of which will depend on the angle between the loading direction and whisker alignment, and whisker distribution. The relative contribution of bending and such tensile deformation is suggested as a future study.

5.3.3. Comparison of FEM results with the analytical model

In this section, our FEM simulations are compared with an analytical model of Wilkinson and Pompe (1998) for the creep and anelastic recovery of whisker-and platelet-reinforced ceramics, which is based on creep and Euler's beam theory. The procedure for obtaining the analytical solution (ε_M^* and τ_M) is described below in section 5.3.3.1. The numerical results (ε^* and τ) are extracted from the FEM simulations through the same procedure as illustrated in section 5.2.1. The dependences of the maximum recoverable strain and the characteristic relaxation time on the whisker aspect ratio and the material properties are then examined.

5.3.3.1. Analytical model construction

Modification to the governing equation presented (Wilkinson *et al.*, 1998) was made in order for the analytical model to conform to the 2D percolating unit cell model used in this study (as shown in Figure 5.8). The reader is referred to Appendix A for the complete derivation of the modified analytical model.

For a unit cell with length ***L*** (***ob,*** along ***x*** direction in Figure 3.4), Height ***H*** (***bc,*** along ***y*** direction in Figure 3.4) and depth ***W*** (***z*** direction into the paper in Figure 3.4), the governing equation for a whisker embedded in a creeping matrix is

$$-E_w I \frac{\partial^4 u}{\partial x^4} = 2\frac{1}{C}\frac{W}{(H/2)}\dot{u}(x,t) + F\delta(x) \qquad (5.5)$$

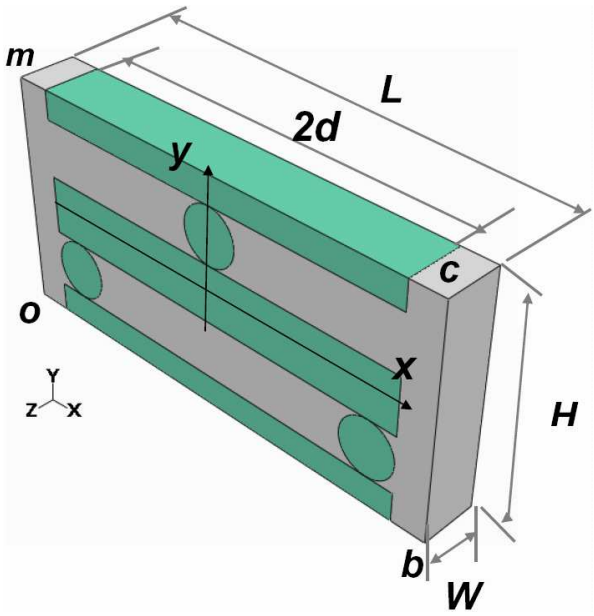

Figure 5.8 Simplified 2D bending unit cell: *W*, *H* and *L* are the width, height and length of the unit cell, 2*d*=λ*2*r* is the length of whisker with radius of *r* and aspect ratio of λ.

from which the predicted maximum strain recovery is

$$\varepsilon_M^* = \frac{L\sigma}{16r}\frac{\lambda^3}{E_w} \qquad (5.6)$$

and the characteristic relaxation time is

$$\tau_M = \frac{12}{\pi^4}\frac{\lambda^4}{CE_w} \qquad (5.7)$$

where $\boldsymbol{E_w}$ is the Young's modulus of the whisker, $\boldsymbol{I}$ is the second moment of area of the whisker cross section ($I = \frac{W(2r)^3}{12}$), $\dot{u}(x,t)$ and u are the displacement rate and displacement normal to the whisker planes along $\boldsymbol{y}$ direction respectively, $\delta(x)$ is the Dirac delta function describing localized nature of the contact force $\boldsymbol{F}$ at $\boldsymbol{x}$=0, and $\boldsymbol{C}$ is the creep constant of the matrix.

5.3.3.2. Aspect ratio dependence

(A) Maximum recoverable strain

Our FEM results are in qualitative agreement with the analytical model. However, they deviate from it quantitatively. For example, for an aspect ratio of 7 and stress of 75MPa, the maximum recoverable strain predicted by the FEM model is about $\varepsilon^* = 32.27\times10^{-3}$, while the analytical model predicts a strain that is higher by 26%, with $\varepsilon_M^* = 43.95\times10^{-3}$. This discrepancy is mainly due to the geometric factor that enters the analytical model. First, the support-points of the whisker are not exactly located at the two ends, and ε_M^* is calculated assuming that the span between the support-points is proportional to the aspect ratio λ. It also neglects the end effect. These approximations lead to an overestimation of the maximum recoverable strain ε_M^*. To test this hypothesis the maximum recoverable strain was re-calculated using a whisker span of $\lambda-1$. For this span, the analytical model gives $\varepsilon_{M(\lambda-1)}^* \sim 27.675\times10^{-3}$, 14% less than the FEM result. The effective span should thus lie between these two values. For example, only an 8% difference is obtained when the coefficient of the effective span is taken as λ-0.5 resulting in a $\varepsilon_{M(\lambda-0.5)}^*$ around 35.19×10^{-3}. Despite the discrepancies due to the aforementioned contact effects and inherent underestimating from Euler's beam theory for small aspect ratio (Wang *et al.*, 2000) which neglects the shear deformation (as shown in Figure 5.7), this difference between the FEM simulation and the analytical model will decrease as the aspect ratio increases, resulting in an averaged difference of 4% after adjusting for the end effect.

To characterize the aspect ratio dependence of strain recovery exclusively, the maximum recoverable strain is scaled by the length $\boldsymbol{L}$ and applied stress σ for both the FEM results and the analytical solutions during comparison ($\varepsilon^{*'} = \varepsilon^{*} / L\sigma$). Generally, for the same applied stress, the maximum recoverable strain ε^{*} increases significantly with increasing aspect ratio, due to the inherently much more compliant whisker network, as well as the increasing load that is proportional to the increasing unit cell length $\boldsymbol{L}$. Because of this, during FEM simulations, smaller stresses are applied to the unit cell with high aspect ratios in order to avoid an over-deformed network by keeping the maximum recoverable strain ε^{*} less than 5×10^{-2}. Typical values of $\boldsymbol{r}$ =0.25 and $\boldsymbol{E_w}$ =600GPa are substituted into Equation (5.6). We obtain the maximum recoverable strain as a function of the aspect ratio for the analytical model (red solid line in Figure 5.9) given by

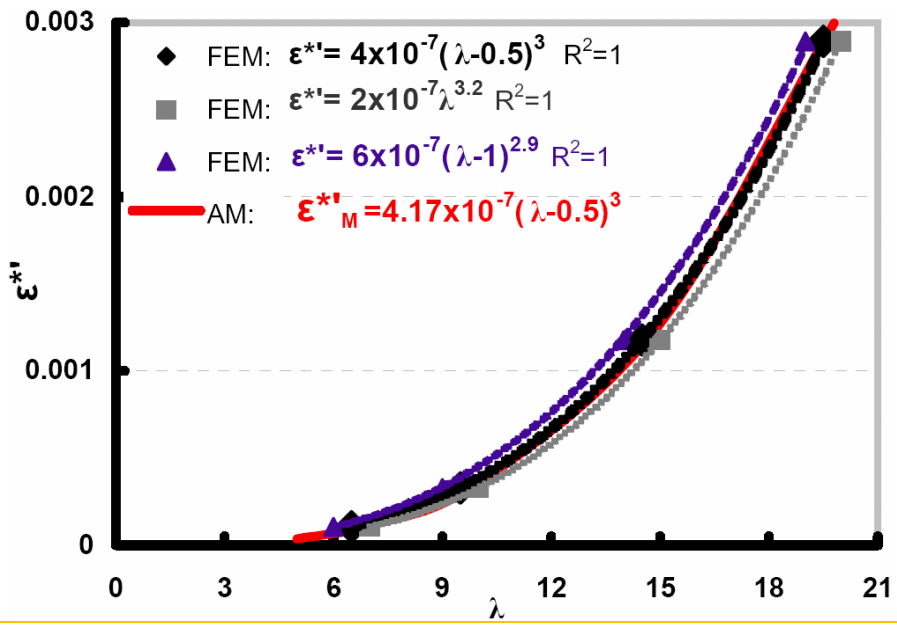

Figure 5.9 Scaled maximum recoverable strain versus aspect ratio, finite element model (FEM): dotted trend lines with the fitting equations; analytical model (AM): solid line and the equation in red for comparison.

$$\varepsilon_M^{*\,'} = 4.17\times10^{-7}(\lambda-0.5)^3 \quad (5.8)$$

At the same time, fitting the corresponding scaled FEM results gives (black dotted lines in Figure 5.9)

$$\varepsilon^{*\,'} = 4\times10^{-7}(\lambda-0.5)^3 \quad (5.9)$$

Equation (5.8) and equation (5.9) are within 4% of each other. Furthermore, when the FEM data is fitted with λ and λ-1, we obtain $\varepsilon^{*\,'} = 2\times10^{-7}\lambda^{3.2}$ and, $\varepsilon^{*\,'} = 6\times10^{-7}(\lambda-1)^{2.9}$ (dashed lines in Figure 5.9). These results confirm the hypothesis of overestimation and underestimation due to end effects.

(b) Characteristic relaxation time

The analytical model consistently estimates a lower relaxation time than does the FEM simulations. For example, when the aspect ratio is 7 and applied stress is 75MPa, the characteristic relaxation times from the two models are 250h and 73.2h, respectively. The ratio of these results is maintained for all aspect ratios since

$$Log(\tau_M) = 4Log(\lambda) - 1.51 \quad (5.10)$$

$$Log(\tau) = 4Log(\lambda) - 1.01 \quad (5.11)$$

which were obtained from the analytical model and the FEM results, as shown in Figure 5.10. It is found that the end effects are not significant since the data fitted with $\lambda - 0.5$ yields a poorer result, as shown in Figure 5.10 with grey line.

One possibility for the underestimation of the analytical model is that the governing equation (5.5) attributes the varying reaction force to the matrix only and neglects the fact that contacts point loads also change with time during the unloading process. A smaller characteristic relaxation time, or faster strain rate of decay, was obtained for a high stress in the matrix from the analytical model as compared with the FEM simulations. This is because

most of the stress is actually carried by whiskers instead of the matrix in the FEM simulations. However, the analytical model does capture the general trend of the unit cell FEM simulations, with respect to the power law dependence on the aspect ratio.

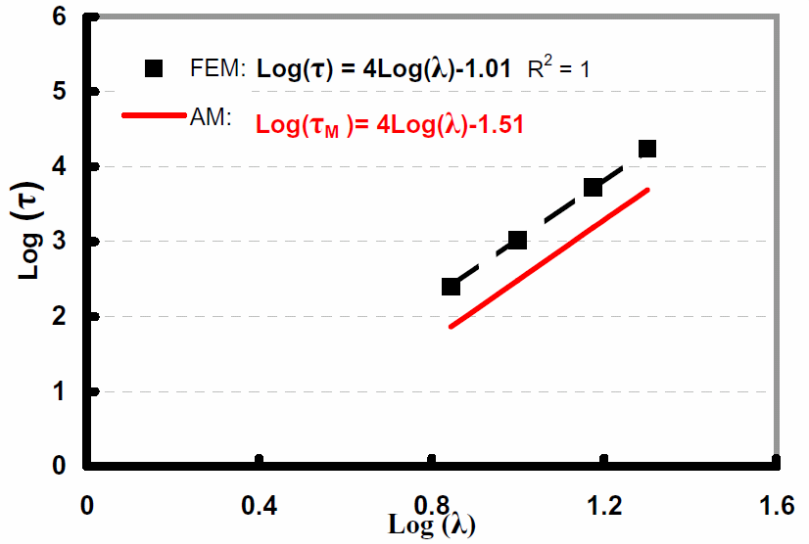

Figure 5.10 Characteristic relaxation time versus aspect ratio, finite element model (FEM): dotted trend lines with the fitting equations; analytical model (AM): solid line and the equation in red for comparison.

5.3.3.3. Material mechanical property dependencies

For the case of the material constant dependencies, we performed simulations on the 2D unit cell model with aspect ratio of 5. One parameter at a time was varied, while keeping all others fixed, as described in Table 5.1.

(A) Maximum recoverable strain

As predicted by the analytical model, one important parameter was found to play an important role on the maximum recoverable strain: the Young's modulus of the whisker. Figure 5.11 shows the whisker elastic modulus dependence of the maximum recoverable strain. The analytical model predicts the behaviours according to

$$\varepsilon_M^* = 7.06\times10^3 E_w^{-1} \quad (5.12)$$

Fitting the data from the FEM results yields:

$$\varepsilon^* = 5.96\times10^3 E_w^{-1} \quad (5.13)$$

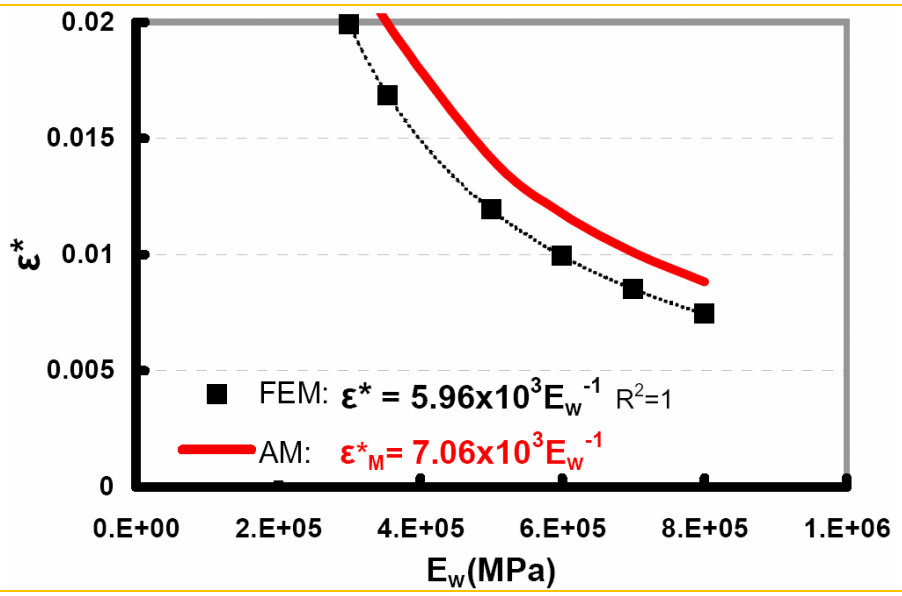

Figure 5.11 Maximum recoverable strain versus Young's modulus of the whisker, λ=5, $\sigma_{applied}$ = -100MPa.

(B) Characteristic relaxation time

As predicted by the analytical model, two parameters were found to play an important role on the characteristic relaxation time: the Young's modulus of the whisker and the creep constant of the matrix.

Figure 5.12 shows the whisker elastic modulus dependence of the characteristic relaxation time. The analytical model predicts the behaviours as according to

$$Log(\tau_M) = -Log(E_w) + 7.06 \quad (5.14)$$

Fitting the data from the FEM results yields:

$$Log(\tau) = -Log(E_w) + 7.51 \quad (5.15)$$

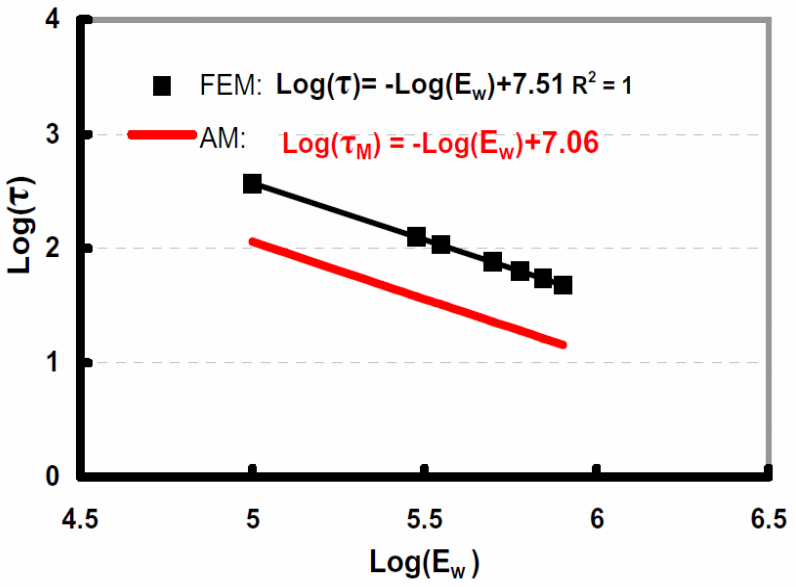

Figure 5.12 Characteristic relaxation time versus Young's modulus of the whisker, λ=5, $\sigma_{applied}$ = -100MPa.

Figure 5.13 shows the matrix creep constant dependence of the characteristic relaxation time. From the analytical model, the relation is expressed by

$$\log(\tau_M) = -\log(C) - 7.45 \quad (5.16)$$

Meanwhile, the FEM results are approximated by

$$\log(\tau) = -\log(C) - 7.02 \quad (5.17)$$

Once again, the analytical model captures the critical inverse dependence on E_w and C, despite overestimating and underestimating quantitatively the values from the FEM simulations for the maximum recoverable strain and characteristic relaxation time respectively. Although Figures 5.11 to Figure 5.13 present the material properties dependence based on aspect ratio of 5, a bigger value of aspect ratio would actually show an even better agreement between FEM simulations and the analytical model which this work extends since the

contribution from contact effect is smaller and the analytical model is based on beam theory which favors a large aspect ratio.

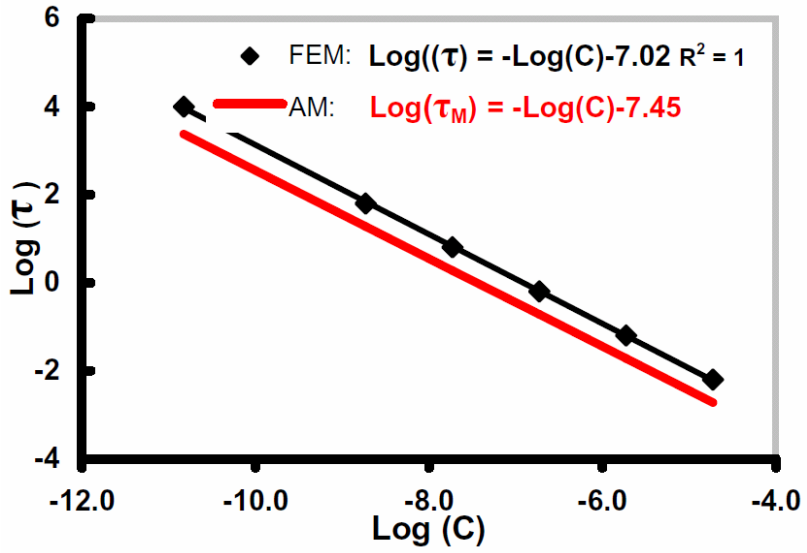

Figure 5.13 Plot of logarithm of characteristic relaxation time versus logarithm of creep constant, λ=5, $\sigma_{applied}$ = -100MPa.

Furthermore, the effects from the rest of the material properties (in Table 5.1), such as the creep constant and Young's modulus of the matrix on the maximum recoverable strain, and the Young's modulus of the matrix on the characteristic relaxation time, are also studied, which show no dependence confirming the analytical model prediction.

5.4. Extrapolation to the 3D percolating whiskers network

The useful study above is based on the plane stress assumption. However, both plane stress and plane strain assumptions involve an idealization of reality to some extent. The real physical problem is three dimensional. The effect of this might be extrapolated however from the combined study of plane stress and plane strain conditions. This section provides some

understanding of the behaviour for the percolating unit cells with the plane strain condition while keeping other properties the same.

5.4.1. Typical creep strain curves for plane strain condition

Figure 5.14 shows typical creep strain curves from simulations based on the 2D percolating unit cells, under the plane strain condition, at a compressive stress of 10MPa along the ***y*** direction. As for the plane stress condition in section 5.3, the strain increases rapidly at first and then almost saturates at maximum recoverable strain ε^*. Owing to the percolating geometry of the 2D simulations, all the accumulated strains are recovered upon load removal provided there is enough time allowed. In order to plot all the data in one figure for a clear comparison, simulations with different aspect ratios are carried out with different values of creep constant C which controls the rate of creep, in other words, the time needed for saturation.

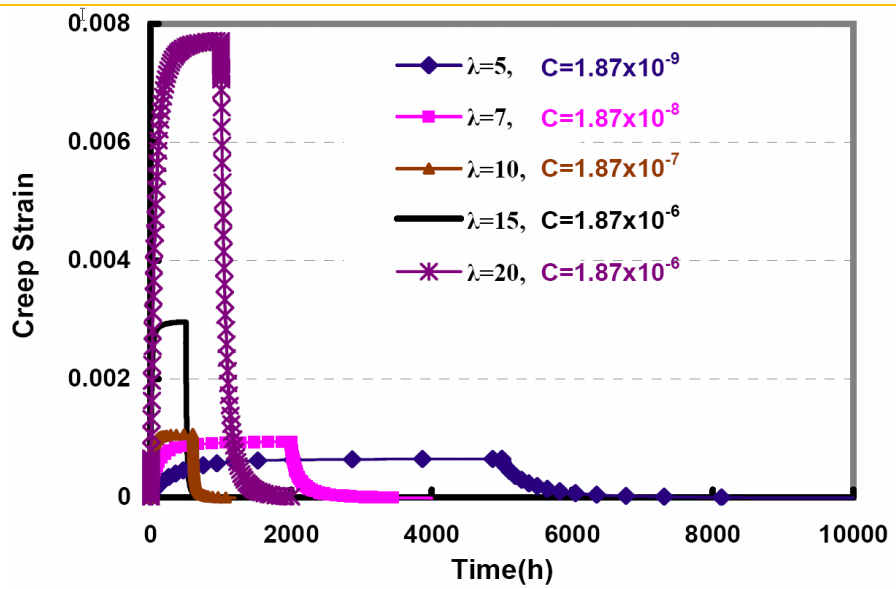

Figure 5.14 Stress reduction-Strain transient curves for 2D percolating network with varied aspect ratio and plane strain condition, $\sigma_{applied}$ = -10MPa.

However, a single value of characteristic relaxation time could not be obtained for each aspect ratio since all the plots of $\ln\left(\varepsilon / \varepsilon^{*}\right)$ versus t could not all be fitted by straight lines, as shown in Figure 5.15(a). For comparison, results based on the plane stress conditions (section 5.3) are shown in Figure 5.15(b). This suggests that 2D percolating unit cells with plane strain condition still behave as effective Kelvin-Voigt models but with a spectrum of the characteristic relaxation times τ for each aspect ratio. Thus, only the maximum recoverable strain ε^{*} is extracted for future analysis and the characteristic relaxation time τ is studied qualitatively. Furthermore, plane stress condition normally yields larger recoverable strain and smaller characteristic relaxation time than plane strain condition does indicating that the plane stress condition is more compliant due to the generic compensation mechanism during deformation which will be illustrated in section 5.4.2. However no quantitative comparisons can be made between them while some trends are similar.

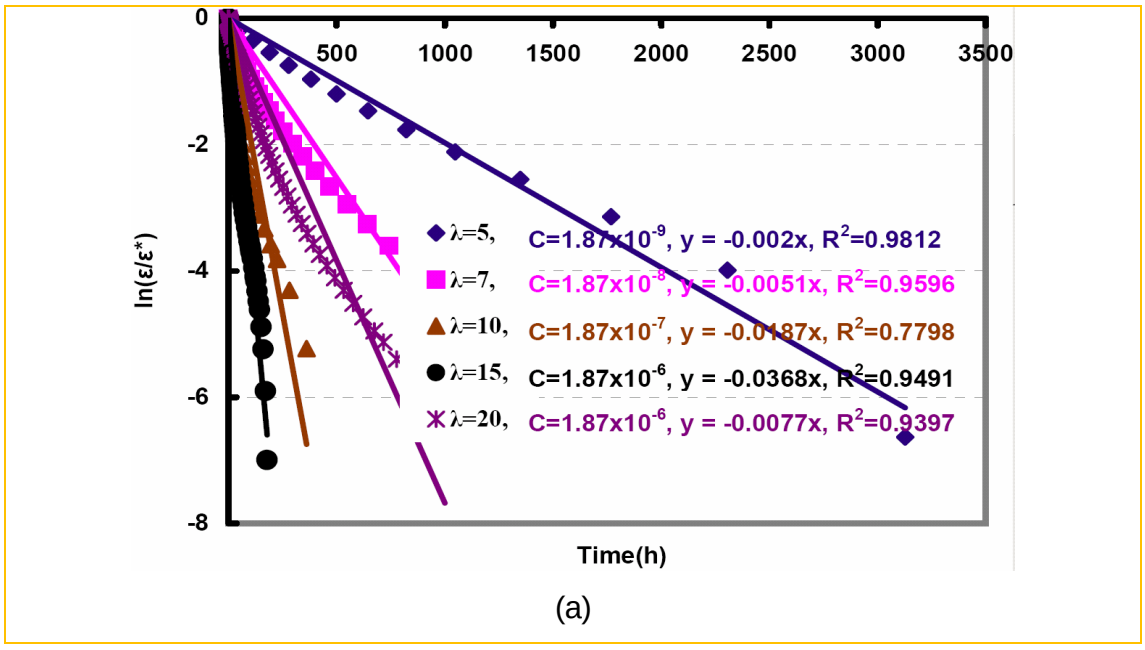

(a)

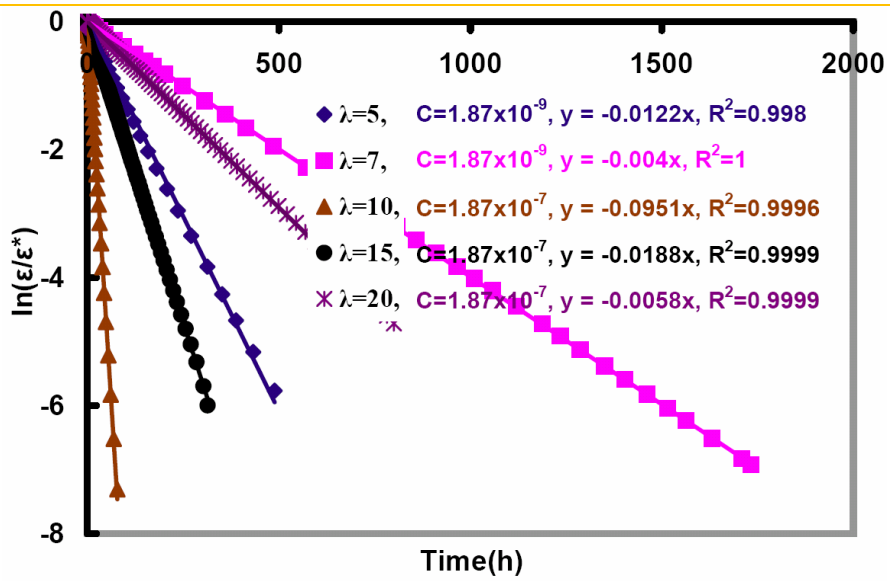

(b)

Figure 5.15 Plot of natural log of the fraction of recovered strain vs time for different aspect ratios: (a) with plane strain condition, $\sigma_{applied}$ = -10MPa; (b) with plane stress condition, $\sigma_{applied}$ = -75MPa, -75MPa, -10MPa, -5MPa and -1MPa for aspect ratios of 5, 7, 10, 15 and 20 respectively.

5.4.2. Deformation mechanisms for plane strain condition

Our simulations suggest that for both plane stress and plane strain conditions creep strain accumulates in the matrix while the applied load is transferred from the matrix to the whisker network, saturating eventually to a maximum accumulated strain ε^* when the entire load is carried out by the whisker network. For plane stress, the whiskers behave like a simply supported three-point bending beam, as studied in section 5.3. For plane strain condition, if there is no matrix, the whiskers behave like a simply supported three-point bending plates with typical stress distributions shown in Figures B-1 to B-3 in Appendix B, which resemble those cases for the plane stress condition: (1) Half of the plate is under tension and the other half is under compression. (2)Maximum bending stress $\boldsymbol{S_{11}}$ occurs at the mid-span of the plate with positive and negative values corresponding to the tensile and compressive part respectively. However, for the plane strain condition of 2D percolating unit cells with matrix, the stress distributions within whiskers are complicated.

Figure 5.16 and Figure 5.17 show the stress distribution of S_{11} and S_{22}, normal stress along the x and y direction respectively, at full loading of whisker networks with different aspect ratios. As before, the matrix around the whiskers is made invisible for clarity. Although S_{22} is still non-zero primarily within the contact region, the bending stress S_{11} does not resemble the profile of a simple bending plate any more. This becomes clear from the deformed profile of the whiskers, as shown in Figure 5.18, which shows the deflection of the center lines of the center whiskers. The profile for large aspect ratios is quite complex.

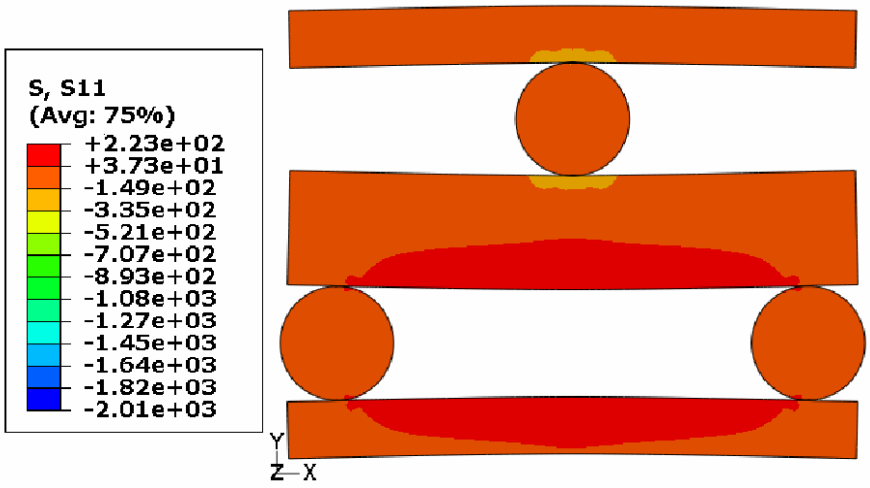

(a) λ= 5, Deformation scale factor 30

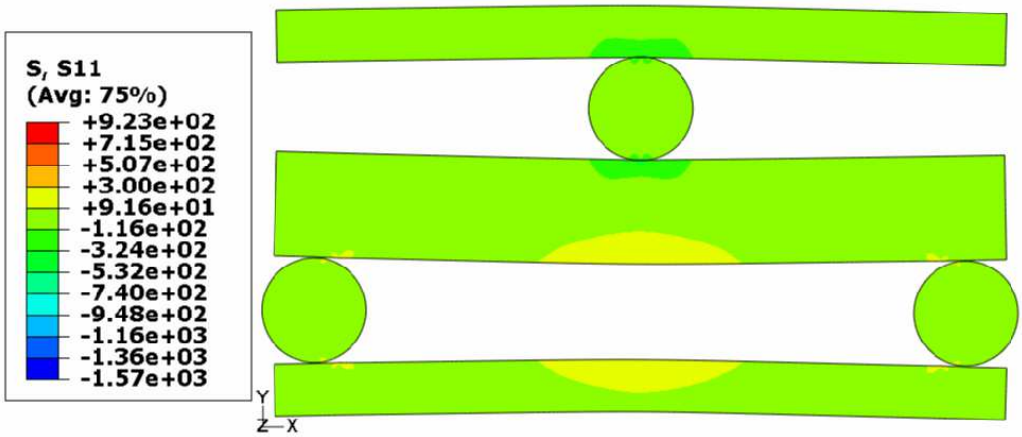

(b) λ= 7, Deformation scale factor 30

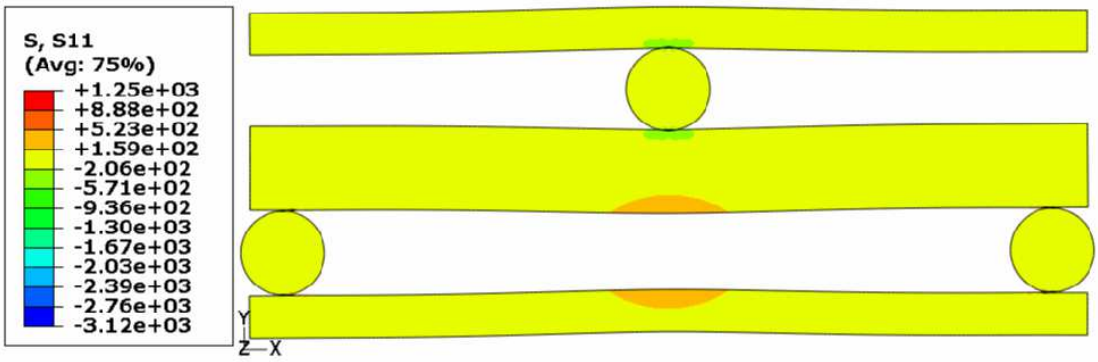

(c) λ= 10, Deformation scale factor 30

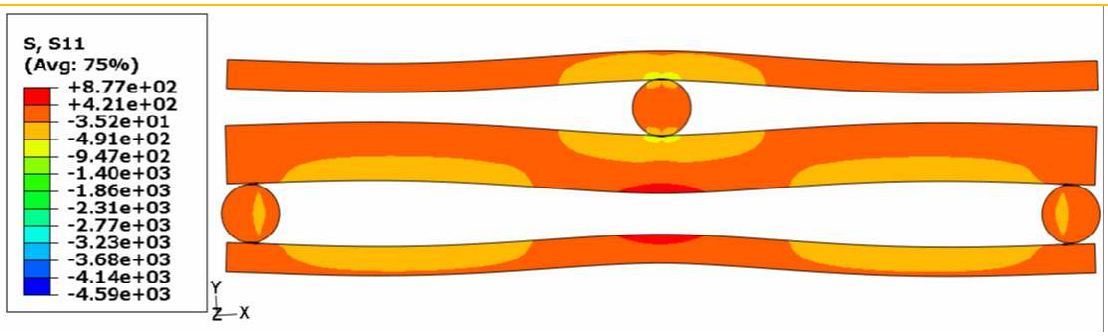

(d) λ= 15, Deformation scale factor 30

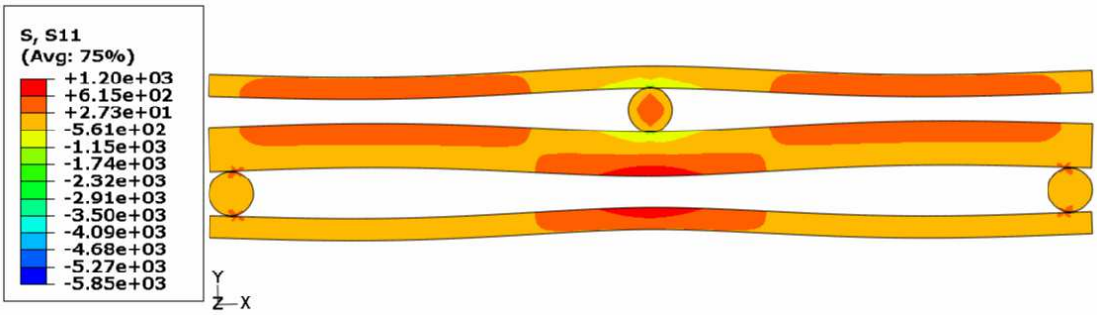

(e) λ= 20, Deformation scale factor 10

Figure 5.16 S_{11} **distribution within whisker network with invisible (white regions) matrix for aspect ratio from 5 to 20 with plane strain condition,** $\sigma_{applied}$ **= -10MPa.**

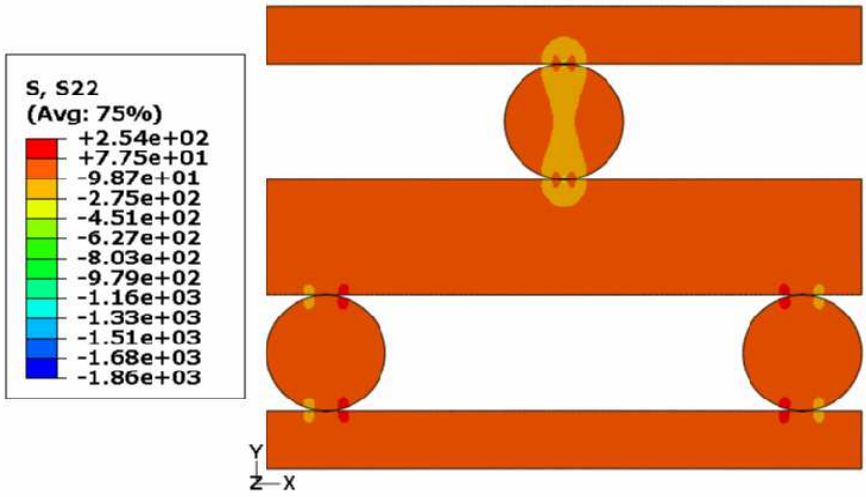

(a) λ= 5, Deformation scale factor 1

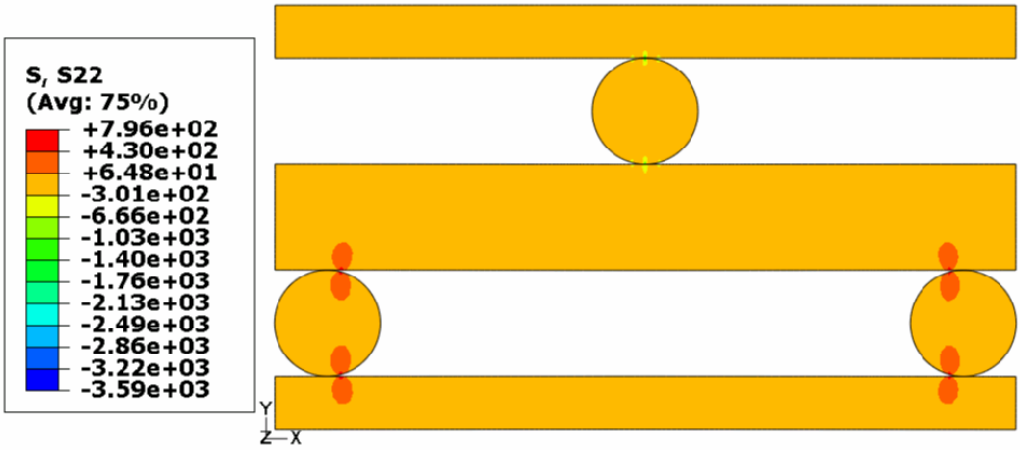

(b) λ= 7, Deformation scale factor 1

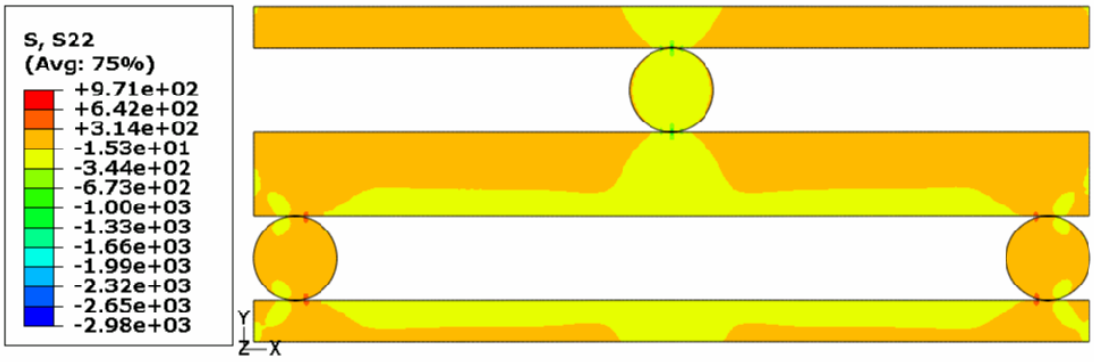

(c) λ= 10, Deformation scale factor 1

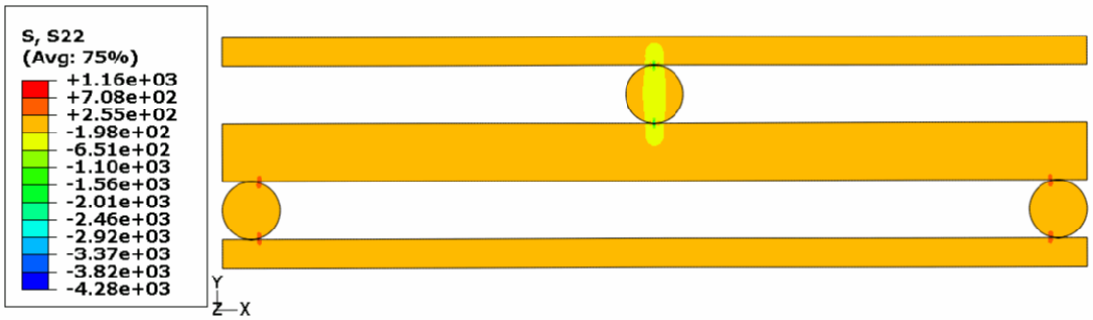

(d) λ= 15, Deformation scale factor 1

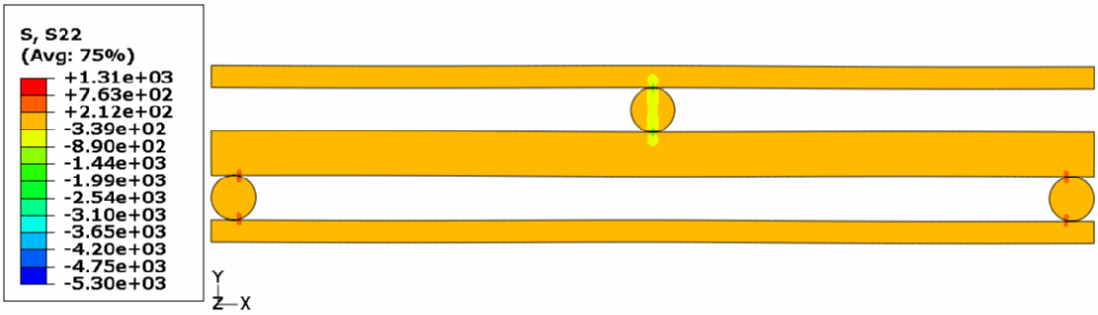

(e) λ= 20, Deformation scale factor 1

Figure 5.17 S_{22} **distribution within whisker network with invisible (white regions) matrix for aspect ratio from 5 to 20 with plane strain condition,** $\sigma_{applied}$ **= -10MPa.**

It is speculated that the matrix which surrounds the whiskers plays a critical role on the deformed state of the whiskers. Generally, the beam (plane stress) and plate (plane strain) sustain the vertical load through bending and deflect normal to the surface. If the deflection is not big, normally less than one-half of the thickness, the middle surface (halfway between top and bottom surfaces) remains unstressed (Young, 1989). The part of the beam/plate under compression wants to expand sideways with strain $\varepsilon_z = -v\varepsilon_x$ due to the Poisson ratio effect. For plane stress condition, the expansion is permitted and σ_z remains essentially zero. But for plane strain condition, the strain is zero resulting in a stress of $\sigma_z = v\sigma_x$. The situation for the matrix is almost the same. For plane stress conditions, the matrix could flow out from the stressed region and extend into the ***z*** direction resulting in insignificant effect on the whiskers deformation. However, for plane strain condition, the matrix, especially the part within the lower half of the unit cells, is confined within the region. It could only extend horizontally

and/or vertically to maintain the volume that is unchanged during creep deformation. This results in the complicated wavy shapes after deformation as shown in Figure 5.18. Furthermore, the mean value of bending stress S_{11} within whiskers is no longer zero as shown in Figure 5.19 suggesting stretching to some extent and the neutral plane is no longer stress zero. This is called the diaphragm stress (Young, 1989). It increases with the aspect ratio and remains almost constant indicating the same trend of the effect of the matrix. Due to this diaphragm stress, stresses for a given load are generally less or stresses for a given deflection are greater than the case of unit cells without matrix (Appendix B), e.g., for aspect ratio 10 with -10MPa applied stress, $\boldsymbol{S_{11}}$ within whiskers are within the range of 1.5×10^{3} to -5.79×10^{3} MPa and 1.25×10^{3} to -3.12×10^{3} MPa for unit cells without and with matrix respectively. As for plane stress, the mean value of S_{11} is essentially zero indicating insignificant stretching of the whiskers. It appears that plane strain leads to results that are non-physical, such as the wavy shape. This is the direct result of how the material compensates for the requirement to eliminate strain in one direction. This suggests that the plane stress approach is more reliable in that it leads to more physically sensible results.

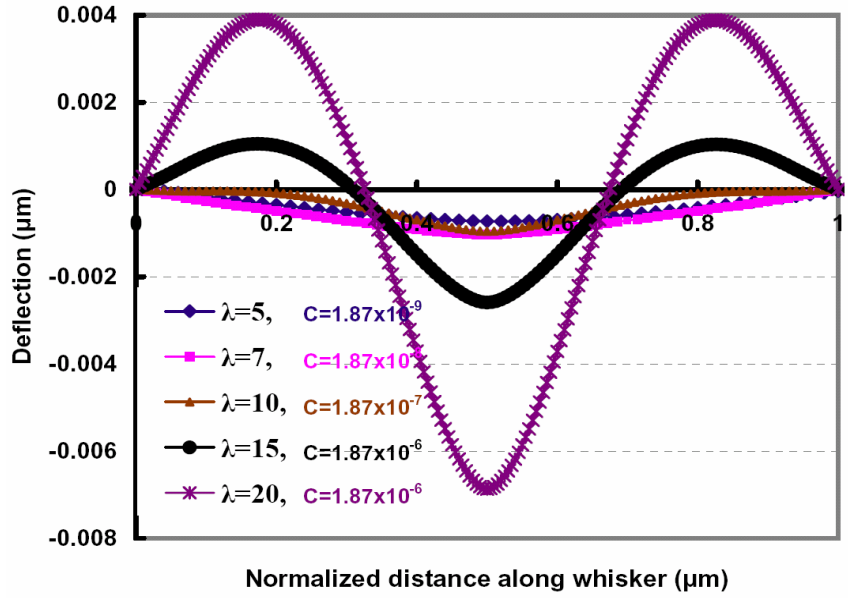

Figure 5.18 Deflection of the neutral line along the middle whisker, plane strain condition, $\sigma_{applied}$ = -10MPa.

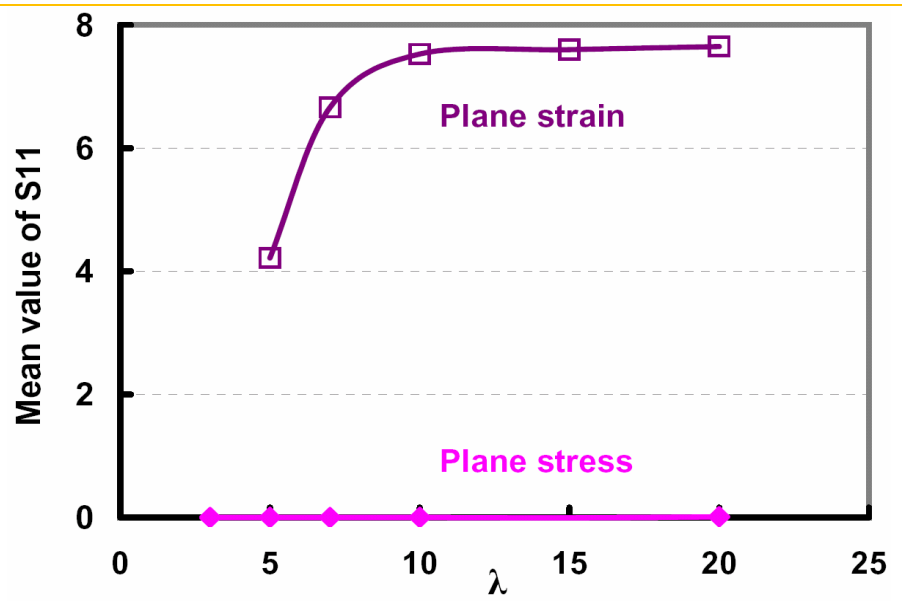

Figure 5.19 Mean value of S_{11} within whiskers for plane stress and plane strain conditions respectively, $\sigma_{applied}$ = -10MPa.

The contribution of the bending and contact effects is also calculated based on equations 5.3 and 5.4. The remaining energy storage is attributed to the shear deformation as before. Figure 5.20 shows the contribution of each deformation to the total energy storage versus the whisker aspect ratio. As before, three kinds of deformations coexist. However, no general trend could be captured. It seems on the surface that the bending contribution decreases first and then increases finally for high aspect ratio with the other two mechanisms increasing first and then decreasing. However, the data should be interpreted with caution, e.g., S_{11} is no longer attributed only to the bending but also elongation of the whiskers resulted from the matrix deformation instead of from the large deflection that happens for a plate when there is no matrix.

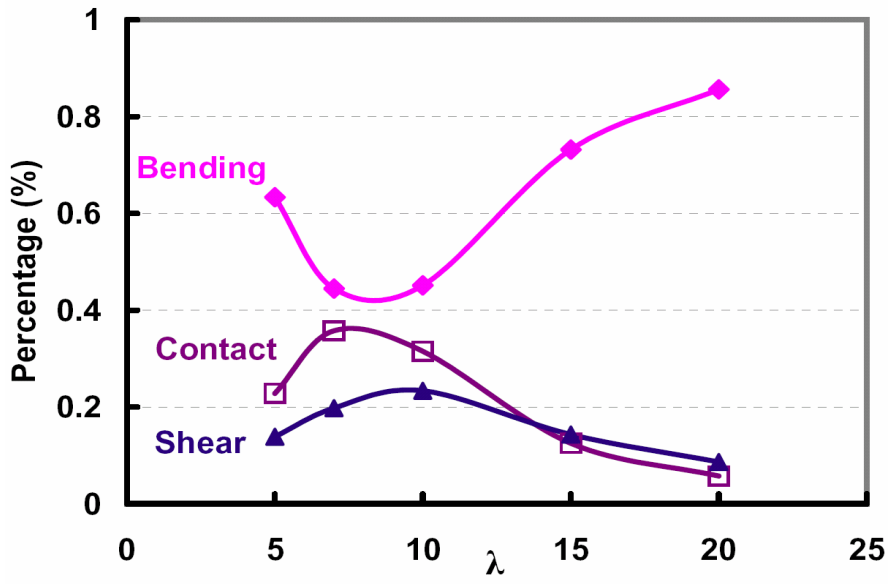

Figure 5.20 Contribution of deformation forms in terms of percentage versus aspect ratio, plane strain condition, $\sigma_{applied}$ = -10MPa.

5.4.3. Comparison of FEM results with the analytical model

In this section, our FEM simulations with the plane strain condition are compared with an analytical model which inherits the theory of Wilkinson and Pompe (1998) for the creep and anelastic recovery of whisker-and platelet- reinforced ceramics. The procedure for obtaining the analytical solution (ε_M^* and τ_M) is described below in section 5.4.3.1. The numerical results (ε^* and τ) are extracted from the FEM simulations through the same procedure as illustrated in section 5.4.1. The dependencies of the maximum recoverable strain and the characteristic relaxation time on the whisker aspect ratio and the material properties are then examined.

5.4.3.1. Analytical model construction for plane strain condition

The analytical model is constructed based on the model in section 5.3.3.1. The only modification is to use the simple bending plate theory ($-D\frac{\partial^4 u}{\partial x^4} = q$) to replace the Euler's

simple bending beam theory ($-E_w I \frac{\partial^4 u}{\partial x^4} = q$) (Cook and Young, 1985). For a unit cell with length ***L*** (***ob,*** along the ***x*** direction in Figure 3.4), height ***H*** (***bc,*** along the ***y*** direction in Figure 3.4) and depth ***W*** (***z*** direction into the paper in Figure 3.4), the governing equation for a whisker embedded in a creeping matrix with plane strain condition is

$$-D\frac{\partial^4 u}{\partial x^4} = 2\frac{1}{C}\frac{W}{(H/2)}\dot{u}(x,t) + F\delta(x) \tag{5.18}$$

where D is the flexural rigidity ($D = \frac{E_w W(2r)^3}{12(1-\nu^2)} = \frac{E_w}{(1-\nu^2)} I$), $\boldsymbol{E_w}$ is Young's modulus of the whisker, ***I*** is the second moment of area of the whisker cross section ($I = \frac{W(2r)^3}{12}$), $\dot{u}(x,t)$ and u are the displacement rate and displacement normal to the whisker planes along ***y*** direction respectively, $\delta(x)$ is the Dirac delta function describing the localized nature of the contact force ***F*** at ***x***=0, and ***C*** is the creep constant of the matrix.

By comparing equation 5.5 and 5.18, it is easy to note that a simply supported three-point bending plate ($\varepsilon_z = 0$ or $W \gg 2r$) might be analyzed as a simply supported three-point bending beam ($\sigma_z = 0$ or $W \sim 2r$) provided that E_w is increased by dividing it by $1-\nu^2$. Then following the same procedure as in Appendix A, for the plane strain condition, the predicted maximum strain recovery is

$$\varepsilon_M^* = \frac{L\sigma}{16r}\frac{\lambda^3}{E_w}(1-\nu^2) \tag{5.19}$$

and the characteristic relaxation time is

$$\tau_M = \frac{12}{\pi^4}\frac{\lambda^4}{CE_w}(1-\nu^2) \tag{5.20}$$

It seems on the surface that the FEM simulations with plane strain condition should behave similar as the plane stress condition did (section 5.3) if comparing equations 5.6, 5.7, 5.19 and 5.20. However, the situation is far beyond the predictions indicated by the theory above.

5.4.3.2. Aspect ratio dependence

(A) Maximum recoverable strain

As before (section 5.3.3.2), the maximum recoverable strain is scaled by the unit cell length $\boldsymbol{L}$ and the applied stress σ ($\varepsilon^{*'} = \varepsilon^{*} / L\sigma$). From Figure 5.21, the scaled maximum strain does not give a good match. For the plane strain condition, there is a big deviation between the FEM simulations and the analytical model (equation 5.19) which seems much closer to the FEM results with plane stress condition instead.

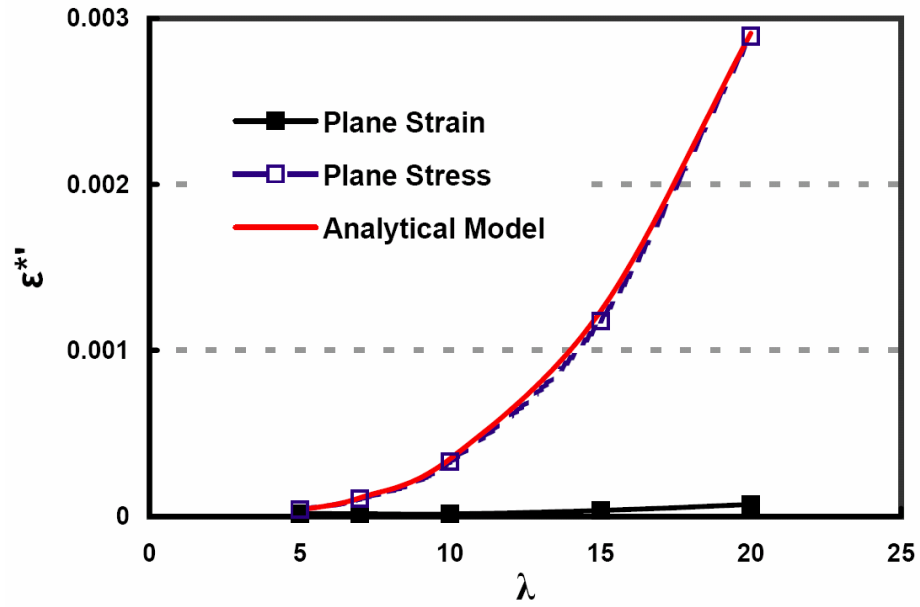

Figure 5.21 Scaled maximum recoverable strain versus aspect ratio for FEM with plane stress and plane strain ($\sigma_{applied}$ =-100MPa) conditions and for analytical model with plane strain condition.

This is because the governing equation 5.5 and 5.18 account for the deflection from the bending stress only. It assumes that whiskers carry the load only by bending which is reasonably true for plane stress condition as indicated in Figure 5.7, but inaccurate for the plane strain condition as indicated in Figure 5.19 and 5.20 that show the effect of diaphragm stress as well as the contact and shear effects. Due to these factors, especially the diaphragm stress, the unit cells with plane strain condition are stiffer than indicated by the ordinary theory and the load-deflection and load-stress relations are nonlinear as shown in Figure 5.22, Figure 5.23 and Table 5.2. Concentrated loads used for each unit cell should be divided by their length ***L*** to get the values of stresses applied, e.g. 1N corresponds to 0.32MPa, 0.24MPa, 0.18MPa, 0.12MPa, 0.09MPa for aspect ratios of 5, 7, 10, 15 and 20 respectively.

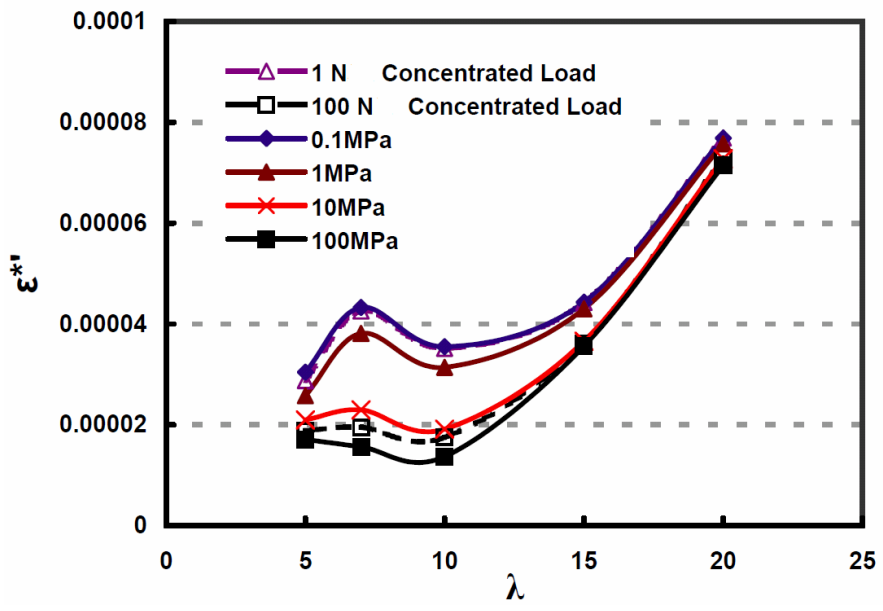

Figure 5.22 Scaled maximum recoverable strain versus aspect ratio for plane strain condition with varied loading conditions for comparison.

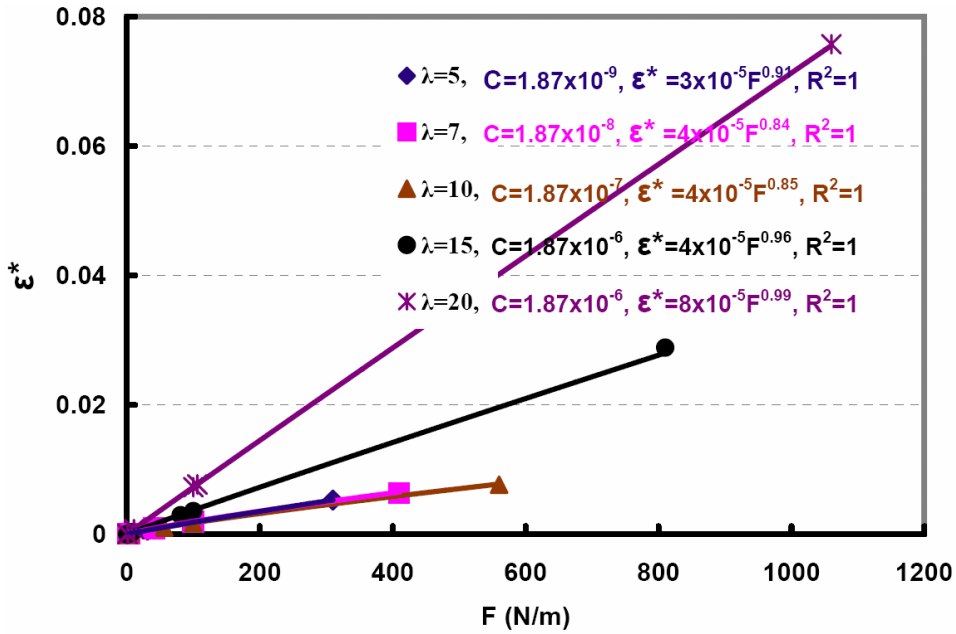

Figure 5. 23 Maximum recoverable strain versus load with the fitting equations.

Table 5.2 Maximum recoverable strain from FEM predictions (From Figure 5.24) and analytical model (AM) for 2D percolating whisker unit cells based on plane strain condition

Aspect ratio λ	FEM	AM
5	$\varepsilon^* = 3\times10^{-5}F^{0.91}$	$\varepsilon_M^* = 5.06\times10^{-5}F$
7	$\varepsilon^* = 4\times10^{-5}F^{0.84}$	$\varepsilon_M^* = 1.39\times10^{-4}F$
10	$\varepsilon^* = 4\times10^{-5}F^{0.85}$	$\varepsilon_M^* = 4.05\times10^{-4}F$
15	$\varepsilon^* = 4\times10^{-5}F^{0.96}$	$\varepsilon_M^* = 1.37\times10^{-3}F$
20	$\varepsilon^* = 8\times10^{-5}F^{0.99}$	$\varepsilon_M^* = 3.24\times10^{-3}F$

No quantitative relationship could be found between the maximum recoverable strain and the aspect ratio (Figure 5.22). Two opposing mechanisms are speculated to control the deflection/strain: the aspect ratio and the matrix within the confined region. A bigger aspect ratio suggests a larger strain obtained for the same unit load as analyzed before. On the contrary, a bigger aspect ratio also means a larger volume of the matrix with bigger effect on

the diaphragm stress decreasing the deflection. The maximum strain from FEM deviates from the analytical model more severely for bigger aspect ratio (Table 5.2) suggesting the latter effect, e.g. from the factor of up to 2 for aspect ratio of 5 to the factor of up to a 100 for the aspect ratio of 20. With the combination of these two factors, the scaled maximum strain seems to increase first, then decrease and finally increase again with the aspect ratio for most values of the applied stresses (Figure 5.22). For 100MPa applied stress in Figure 5.22, the scaled maximum strain decreases first, then increases with the aspect ratio suggesting the bigger effect of the confined matrix under higher applied stress due to severe deformation. Furthermore, the observation that the scaled maximum strain increases with decreasing applied stress for each aspect ratio also confirms this effect.

Furthermore, Appendix B illustrates the FEM results on unit cells without a matrix under plane strain conditions. They all agree well with equation 5.19 providing support for the above argument that the behaviour of the 2D percolating unit cells with plane strain condition originates from the matrix.

(b) Characteristic relaxation time

As analyzed in section 5.4.1, no single value of the characteristic relaxation time could be obtained. Thus the effect of the aspect ratio is studied qualitatively. In general, the characteristic relaxation time increases with increasing aspect ratio as shown in Figure 5.15. Furthermore, compared with the plane stress condition, extended loading time needed for creep strain saturation is observed by a factor of up to 10 for the plane strain condition suggesting the same trend of characteristic relaxation time. One more thing to mention is that the relaxation curve also depends on the applied stress (shown in Figure 5.24) as the case of the maximum recoverable strain. Bigger applied stress seems to produce a quicker relaxation speed and this dependence decreases with the aspect ratio such that for aspect ratios of 15 and 20 all the curves converge into one.

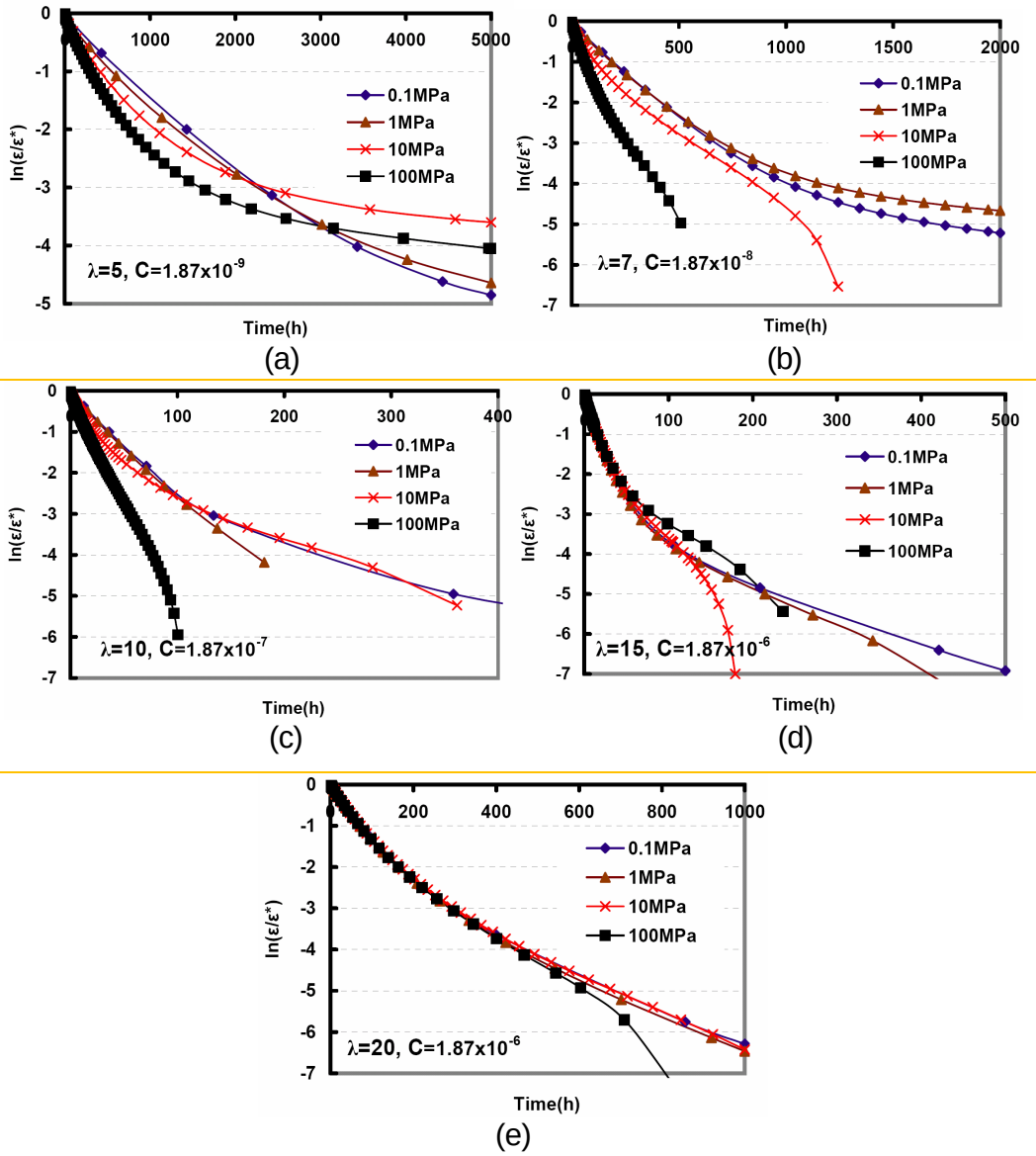

Figure 5.24 Plot of natural log of the fraction of recovered strain vs time with varied applied stress for different aspect ratio.

5.4.3.3. Material mechanical property dependences

For the case of the material constant dependencies, we performed simulations on the 2D unit cell model with aspect ratio of 10. One parameter at a time was varied, while keeping

all others fixed, as described in Table 5.1 except that the creep constant is taken as 1.87×10^{-7} instead of 1.87×10^{-9}.

(A) Maximum recoverable strain

Unlike the situation of plane stress condition, several parameters were found to play important roles on the maximum recoverable strain: the Young's modulus of two constituents and the Poisson ratio of two constituents. Figure 5.25 shows the elastic modulus dependence of the maximum recoverable strain. The analytical model predicts the behaviours as according to

$$\varepsilon_M^* = 25E_w^{-1} \tag{5.21}$$

Fitting the data from the FEM results yields:

$$\varepsilon^* = 0.25E_w^{-0.77} \tag{5.22}$$

However, fitting the FEM results still yields a dependence on the Young's modulus of the matrix which is not predicted from the analytical model:

$$\varepsilon^* = 5.2\times10^{-3}E_m^{-0.18} \tag{5.23}$$

where E_w and E_m are in units of GPa. According to the analytical model, there should be no dependence of the matrix elastic modulus. The Young's modulus of the two constituents affects the deflection as well as the deformed shape of the whiskers. Bigger whisker elastic modulus results in smaller deflection and a straighter shape as shown in Figure 5.26. On the contrary, bigger matrix elastic modulus results in smaller deflection and more wavy shape as shown in Figure 5.27. Poisson ratio of the two constituents was found to affect the maximum recoverable strain as shown in Figure 5.28 which is also not supported by the analytical model.

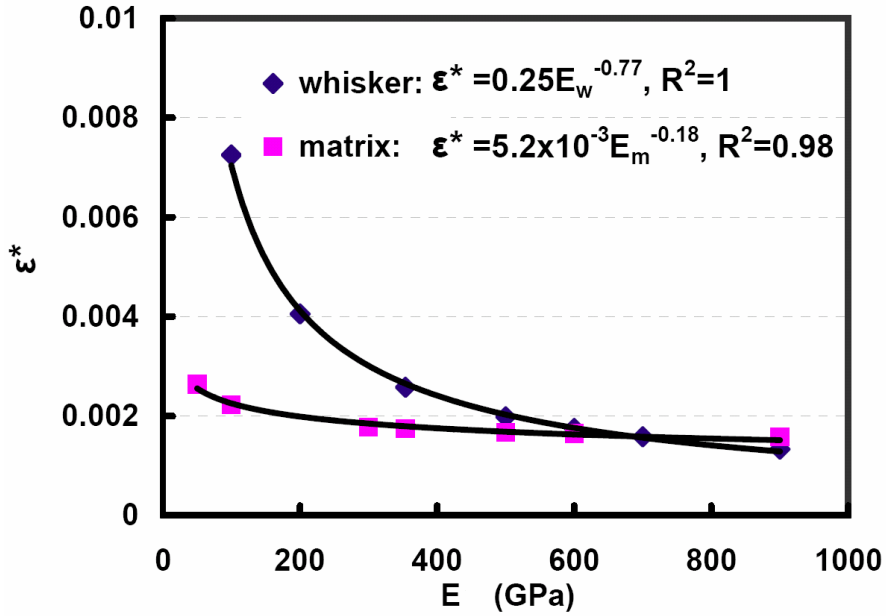

Figure 5.25 Maximum recoverable strain versus Young's modulus, plane strain condition, λ=10, $F_{applied}$ = -100N.

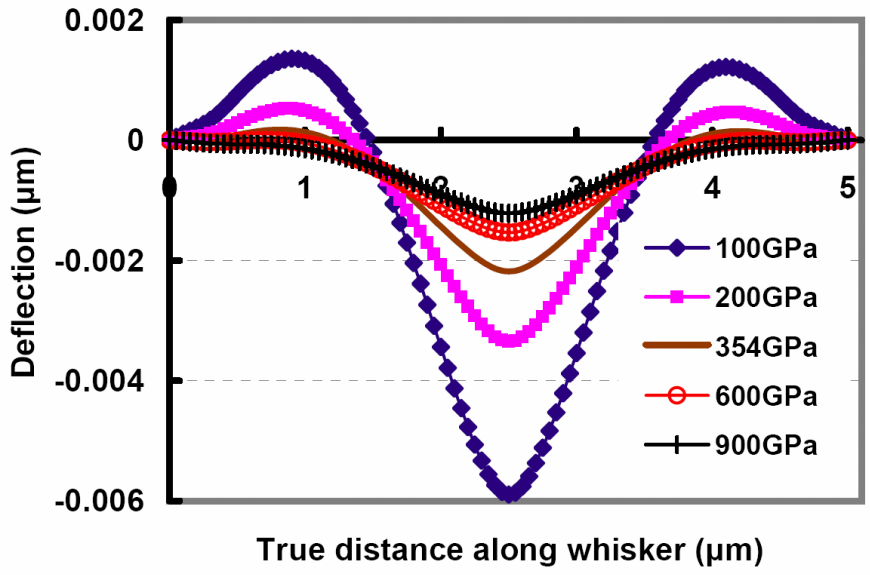

Figure 5.26 Deflection of the neutral line along the middle whisker for varied Young's modulus of the whisker, plane strain condition, λ=10, $F_{applied}$ = -100N.

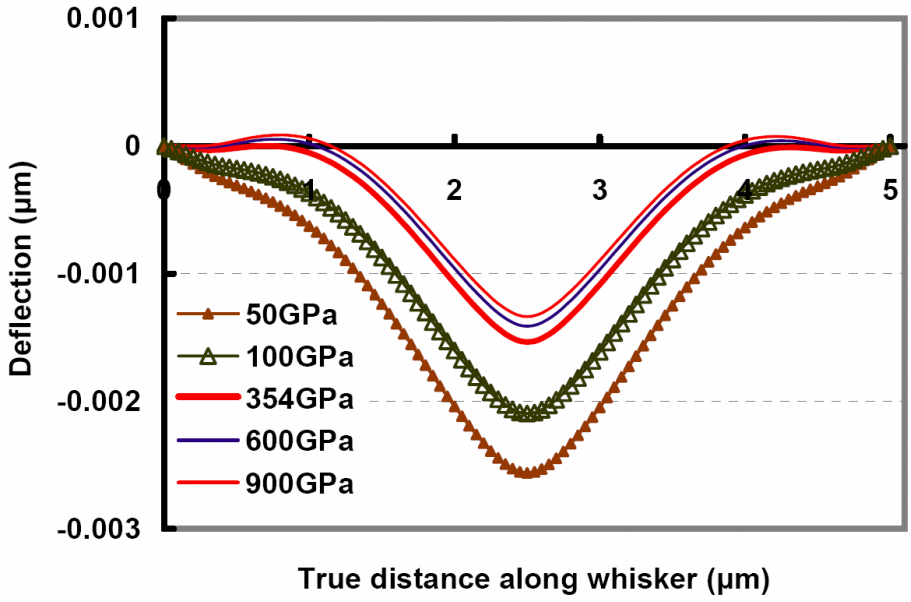

Figure 5.27 Deflection of the neutral line along the middle whisker for varied Young's modulus of the matrix, plane strain condition, λ=10, $F_{applied}$ = -100N.

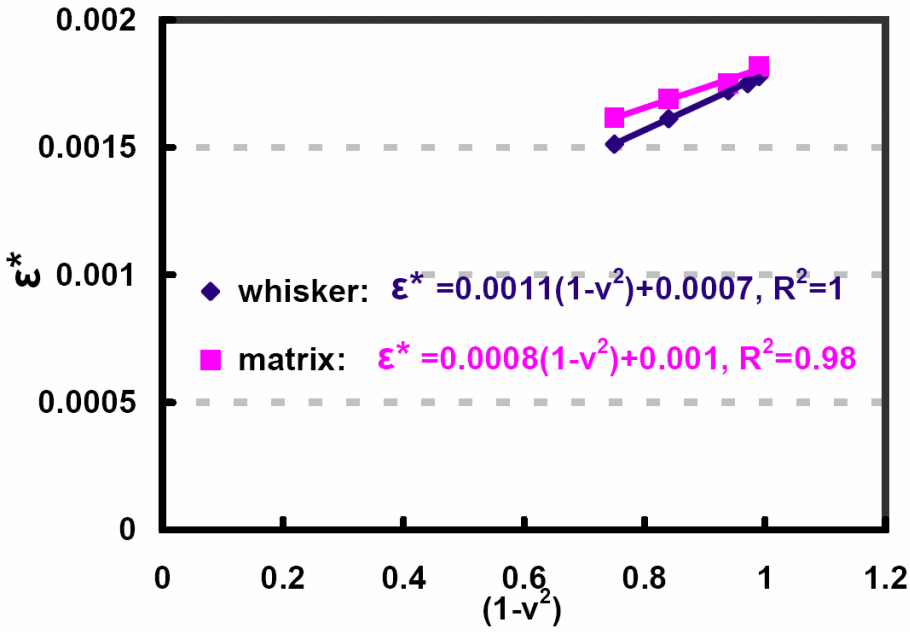

Figure 5.28 Maximum recoverable strain versus Poisson ratio, plane strain condition, λ=10, $F_{applied}$ = -100N.

(B) Characteristic relaxation time

From the analytical model (equation 5.20), two important parameters were expected to play an important role in determining the characteristic relaxation time: the Young's modulus of the whisker and the creep constant of the matrix. However, the Young's moduli of both constituents were found to affect the relaxation curve (Figure 5.29 and Figure 5.30), as well as the creep constant of the matrix (Figure 5.33) which shows an inverse relationship with the characteristic relaxation time as predicted by the analytical model. Poisson ratios were found to have essentially no effect.

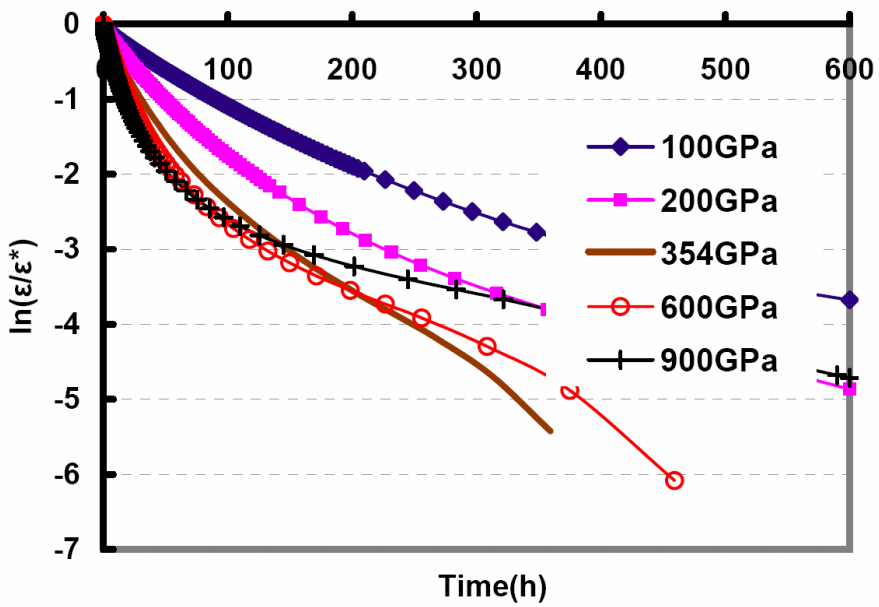

Figure 5.29 Plot of natural log of the fraction of recovered strain vs time for varied Young's modulus of the whisker, plane strain condition, λ=10, $F_{applied}$ = -100N.

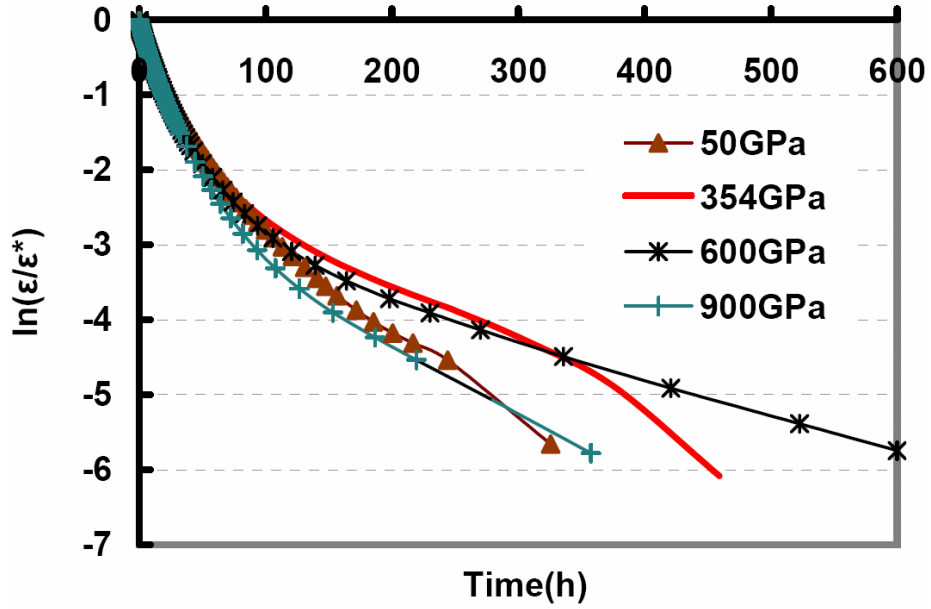

Figure 5.30 Plot of natural log of the fraction of recovered strain vs time for varied Young's modulus of the matrix, plane strain condition, λ=10, $F_{applied}$ = -100N.

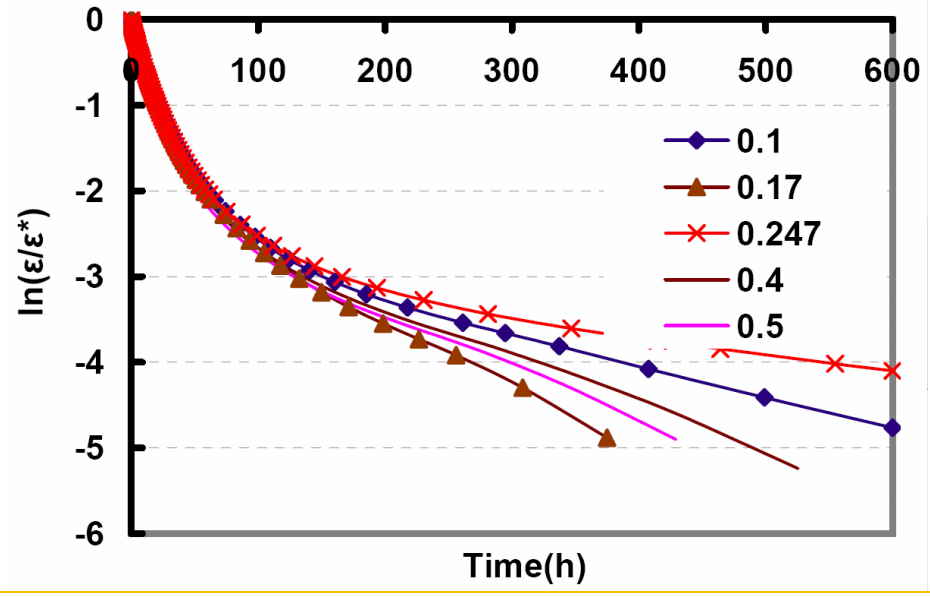

Figure 5.31 Plot of natural log of the fraction of recovered strain vs time for varied Poisson ratio of the whisker, plane strain condition, λ=10, $F_{applied}$ = -100N.

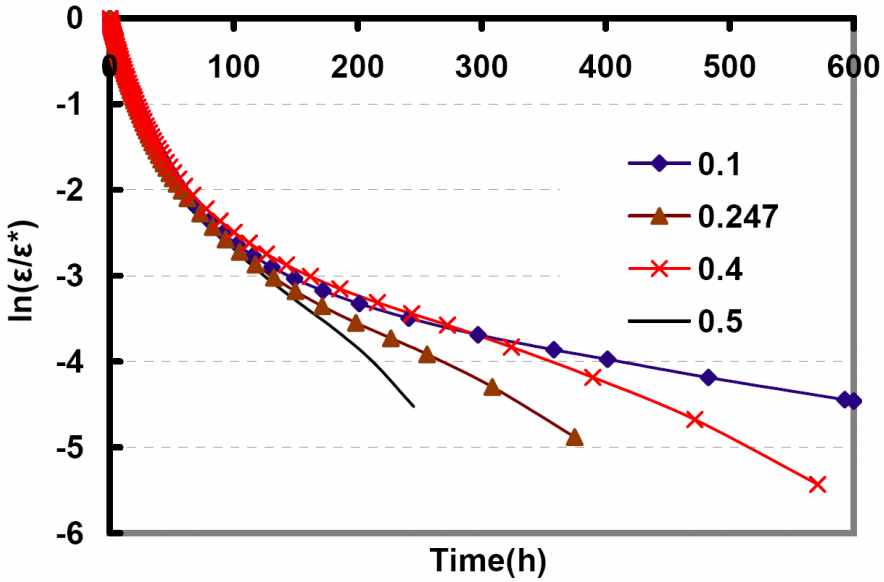

Figure 5.32 Plot of natural log of the fraction of recovered strain vs time for varied Poisson ratio of the matrix, plane strain condition, λ=10, $F_{applied}$ = -100N.

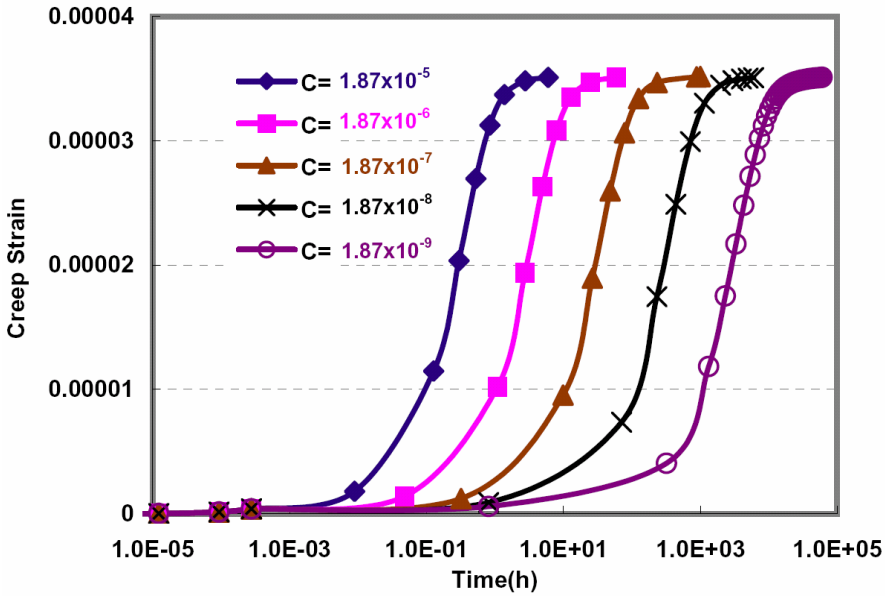

Figure 5.33 Creep strain versus time for different creep constants *C*, plane strain condition, λ=10, $F_{applied}$ = -1N.

For 2D percolating unit cells with plane strain condition, FEM results yield dependences on the parameters which were not predicted by the analytical model originated from the Wilkinson and Pompe model (1998). This is due to the confined matrix during deformation. However, the real situation is close to a plane stress condition instead of plane strain condition since the matrix could flow anywhere and each phase is percolating through the whole geometry. Furthermore, the whisker is suitably represented by a beam instead of by a plate. We therefore conclude that the analytical model captures the critical parameter controlling the deformation.

5.5. Conclusions

We have verified the critical importance of a percolating whisker network for the anelastic recovery based on the 3D multi-whisker random unit cell. We then demonstrated that bending is the dominant mechanism during the creep deformation of a composite containing a well aligned percolating whisker network based on the 2D unit cell model. Good qualitative agreement was found between our FEM simulations and the analytical model of Wilkinson and Pompe with regards to the maximum recoverable strain and the characteristic relaxation time. Despite the deviations in absolute magnitude, the analytical model captures all the critical properties characterizing the deformation mechanisms or strain recovery. These include: the maximum recoverable strain is inversely proportional to the whisker's Young's modulus and proportional to the third power of the aspect ratio; the characteristic relaxation time is inversely proportional to the whisker's Young's modulus and creep pre-exponent constant, and proportional to the fourth power of the aspect ratio. We demonstrated that plane stress condition better represents the real situation over plane strain condition since the matrix could flow out from the deformed region and a beam is more suitable to describe a whisker. Therefore, even though the FEM results on 2D percolating unit cells with plane strain conditions show some behaviours which are not predicted by the analytical model due to the confined matrix, we conclude that the Wilkinson and Pompe model is able to describe the deformation of a percolating geometry.

CHAPTER 6

CORRELATION BETWEEN DIFFRACTION AND DEFORMATION

6.1. Introduction

As noted earlier, there is a lack of experimental diffraction data to support the theory developed in the last two chapters. The models suggest an increase of peak width representing the non-uniform stress field distribution due to bending. This is not generally observed. This is the motivation for the current study. From experiments, a narrowing (0.0056° to 0.0576°) and left shifting (0.072° to 0.1°) of the diffraction peak was observed experimentally for Al_2O_3 containing 20-30vol% of whiskers when comparing the samples after creep with the ones before creep from the hot pressing fabrication process (Quan, 2004). As mentioned in the literature review, one possible reason for the lack of experimental support for whisker bending is that it is too small to be detected. Other factors such as thermal stresses due to different CTEs of the two components, and the whisker network deformation and load transfer during creep also need to be considered. This chapter attempts to provide relatively comprehensive correlations between the diffraction patterns and those factors via the framework (illustrated in Chapter 4) which transfers the information between the FEM simulations (strain fields for specific loading cases) and the virtual diffraction modeling (peak width and position). Virtual testing results are also compared with the analytical results and the experimental data.

Section 6.2 addresses the peak width and position associated with various deformation modes based on simulations from a stress free state excluding thermal effects. Section 6.3 outlines the effects of thermal stresses resulting from the cooling stage after creep and hot pressing process interactively with the deformation modes to uncover these contradicting trends. For samples after creep, unit cells are deformed at 1400℃ to a creep strain of 0.005 followed by cooling to 20℃ under load within 1 hour to mimic the

experimental cooling stage in air. The reason for choosing 1400℃ is that it is the thermal stress free temperature after the hot pressing process (Majumdar *et al*., 1989). Meanwhile, the strain of 0.005 is the maximum creep strain involved in Quan's experiments and as demonstrated later the strain incorporates the load transfer processes. For samples before creep (FEM simulations in section 6.3), the unit cells are cooled under load (e.g. -50MPa) from 1700℃ to 20℃ within 1 hour to mimic the experimental cooling stage after the hot pressing fabrication process.

Three whisker networks are employed: 3D random (section 3.4.1), 2D percolating (section 3.4.2) and 3D aligned (section 3.4.3) unit cells. It has been shown that bending is dominant for the 2D percolating geometry with even a small aspect ratio (chapter 5) and elongation or contraction is dominant for the 3D aligned geometry with the stress field distributing as described by the shear lag model (Cox, 1951) and verified by experiment (Mehan *et al.*, 2000). Meanwhile, the 3D random unit cell might provide information for a random geometry which is closer to the real case even without percolation.

Materials properties incorporated in the FEM simulations are illustrated in Section 3.1 (Table 3.1 & 3.2). Generally, for creep deformation simulations, external loads for 3D random and 3D aligned unit cells are tensile along the *z* direction, while the ones for those 2D percolating unit cells are compressive along the *y* direction for both section 6.2 and 6.3. The external loading directions are along the *y* direction for FEM simulations of hot pressing.

6.2. Peak width and position due to deformation

6.2.1. Effect of whisker network

Figure 6.1 shows typical creep strain curves from simulations based on 3D random, 2D percolating and 3D aligned unit cells with aspect ratio of 5 and a stress of 60MPa at 1200 ℃. For the 2D percolating geometry, creep strain saturates at the maximum recoverable strain ε^* representing an entire load transfer process from matrix to whisker network. However, a

shift of the strain rate occurs for the other two non-percolating geometries (3D random and 3D aligned unit cells), which seems to suggest a partial load transfer process within the system. The creep strain then continues at a relatively constant reduced rate.

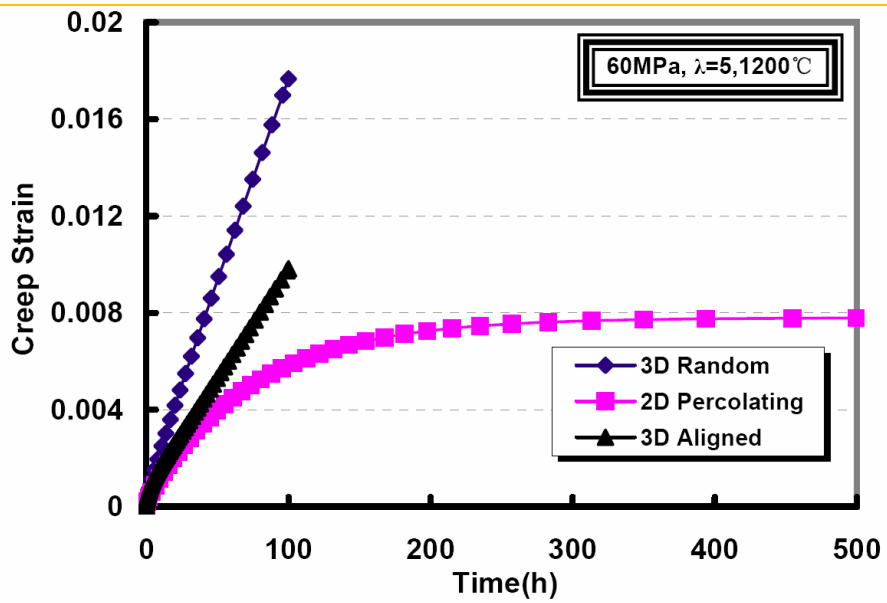

Figure 6.1 Creep strain versus time for three kinds of whisker networks: 3D random, 2D percolating and 3D aligned unit cells, λ=5, $\sigma_{applied}$ = 60MPa, T=1200℃.

Generally, the peak width increases with creep strain as shown in Figure 6.2 suggesting that deformation introduces a non-uniform stress field even for a single aligned whisker embedded in the matrix while a uniform stress field occurs for the case without a matrix (demonstrated in section 4.5). For the 2D percolating geometry, *FWHM* increases with creep strain and saturates in accordance with the completion of the load transfer process (purple lines in Figure 6.2). This mechanism is clearer if *FWHM* is plotted versus time in Figure 6.3. However, *FWHM* for the 3D aligned unit cell also saturates according to the shift of the strain rate, suggesting a complete load transfer process. Due to the non-percolating geometry, the continuing creep strain comes from the un-reinforced matrix for the 3D aligned unit cell. As for the case of the 3D random geometry, a shift occurs for the *FWHM* increase rate, which is associated with the partial load transfer process within the system and the

FWHM continues increasing after that, suggesting the continuing process of load transfer. In general, bending and random geometry are the main sources of peak broadening compared with the simple stretch deformation mechanism. However, it depends on the extent of creep strain, e.g. bending and elongation result in a same level of *FWHM* and the random geometry contributes more when the creep strain is less than 2×10^{-3}. Bending (2D percolating) takes the dominant position over random geometry when the creep strain is bigger than 4.4×10^{-3}.

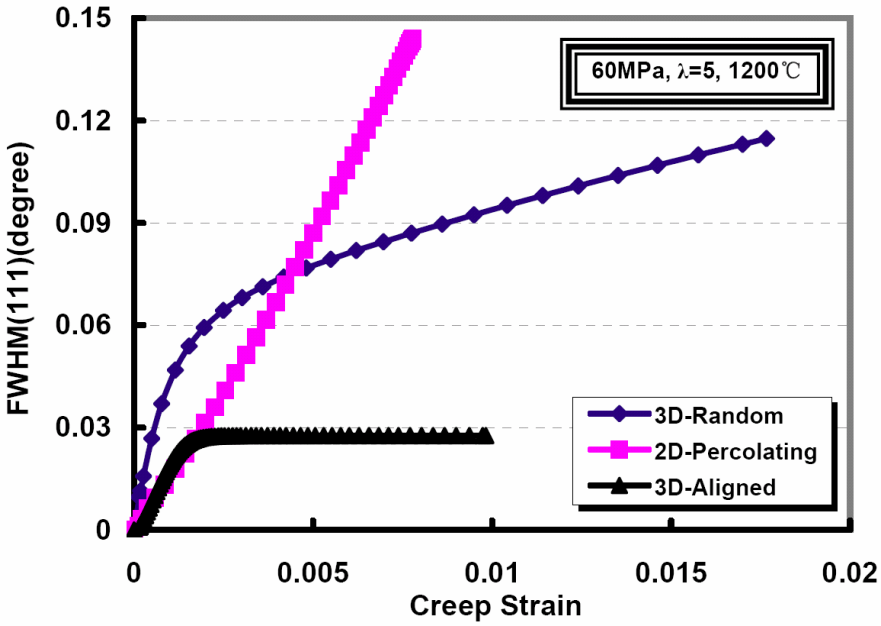

Figure 6.2 FWHM versus creep strain for three kinds of whisker networks: 3D random, 2D percolating and 3D aligned unit cells, λ=5, $\sigma_{applied}$ = 60MPa, T=1200℃.

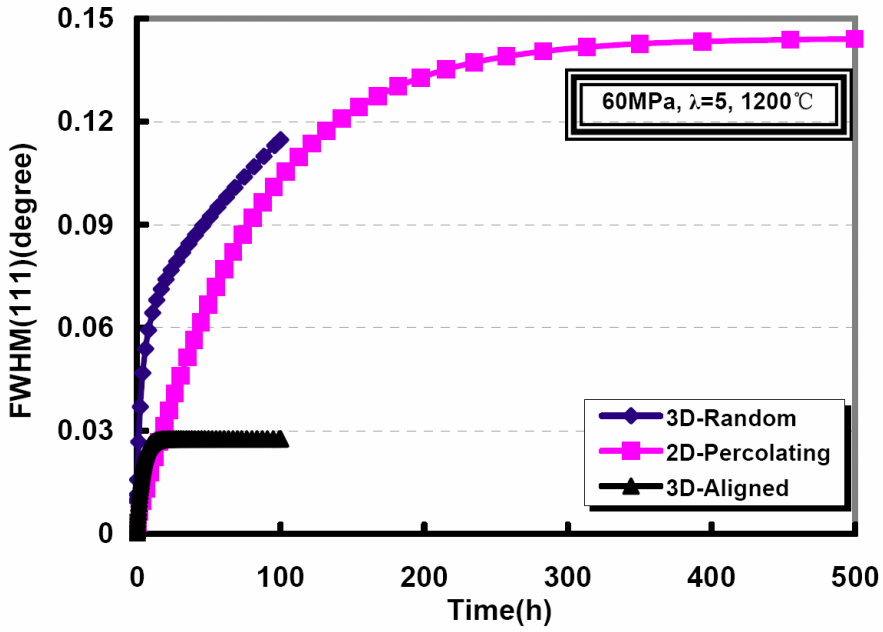

Figure 6.3 FWHM versus time for three kinds of whisker networks: 3D random, 2D percolating and 3D aligned unit cells, λ=5, $\sigma_{applied}$ = 60MPa, T=1200℃.

The peak position (shown in Figure 6.4) shifts to a lower value and saturates for all three geometries after a small amount of creep strain. However, the 2D percolating geometry (bending, purple line in Figure 6.4) saturates earlier, i.e. at a smaller creep strain compared with the peak width, while the 3D aligned (elongation, black line in Figure 6.4) and 3D random geometries (blue line in Figure 6.4) saturate at almost the same creep strain as for the case of peak width representing the load transfer process. This suggests that elongation results in a significant shift of the peak position compared with the bending (2D percolating) and random geometry. Meanwhile, it is straightforward to specify that when the stress status is changed (e.g. from tensile to compressive), the peak position would shift to the opposite direction while the peak width would be consistent as before.

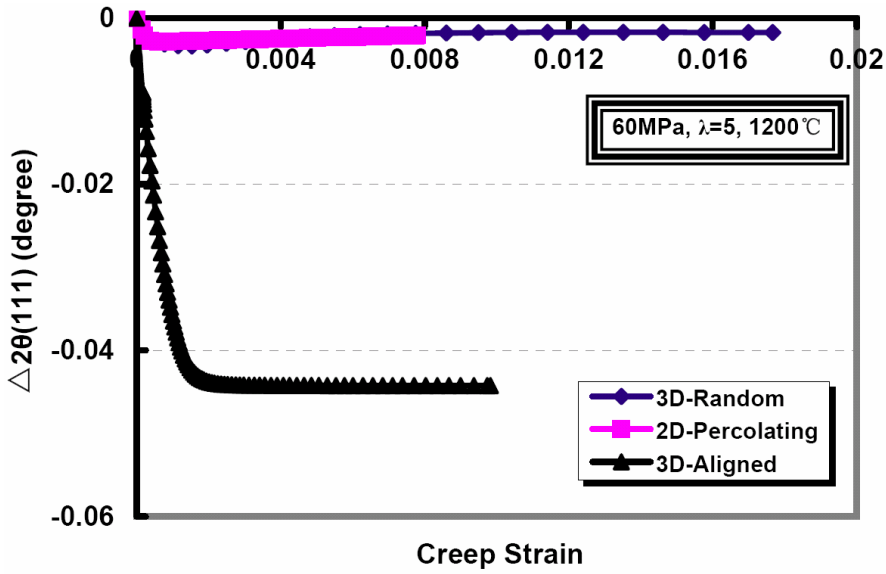

Figure 6.4 Peak shift versus creep strain for three kinds of whisker networks: 3D random, 2D percolating and 3D aligned unit cells, λ=5, $\sigma_{applied}$ = 60MPa, T=1200℃.

6.2.2. Effect of applied stress

It has been shown above that the creep strain determines the peak position and width. This section examines the effect of the external stress if the value of the creep strain is fixed. Three values of stress 60MPa, 75MPa and 100MPa, are applied to the three whisker networks with aspect ratio of 5. Figure 6.5, Figure 6.6 and Figure 6.7 show the creep strain versus time for 3D aligned, 2D percolating and 3D random unit cells at 1400℃. Larger value of the applied stress yields the same value of creep strain in a quicker time regardless of the different network.

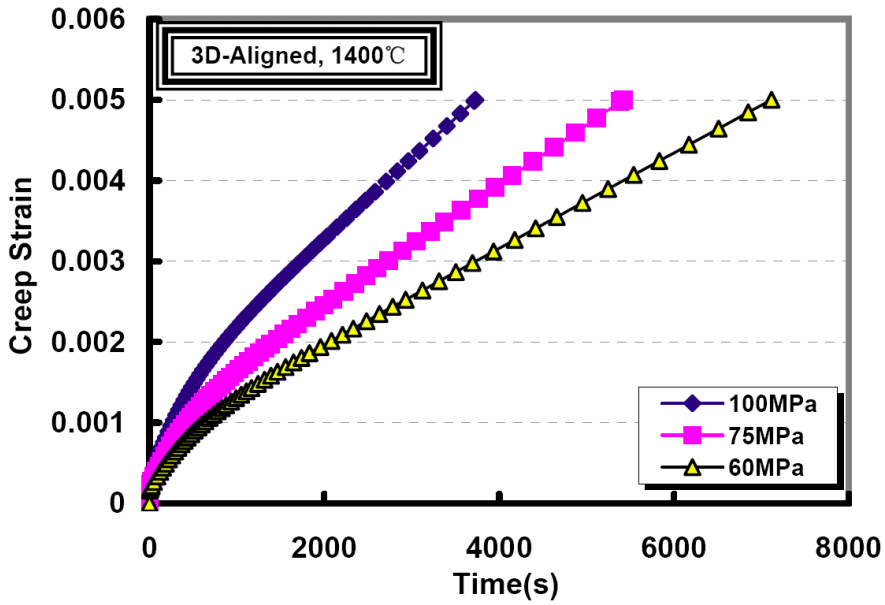

Figure 6.5 Creep strain versus time with different applied stresses for 3D aligned unit cell, λ=5, T=1400℃.

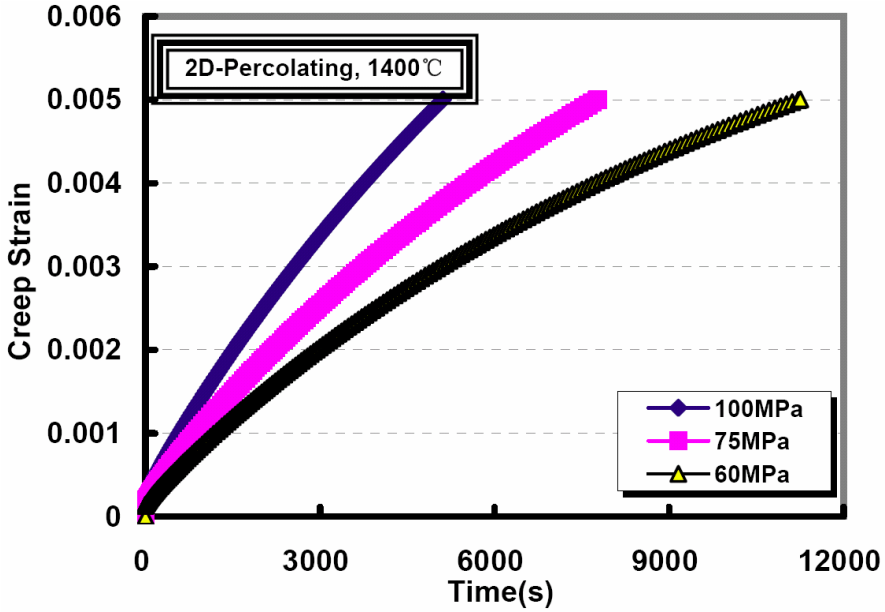

Figure 6.6 Creep strain versus time with different applied stresses for 2D percolating unit cell, λ=5, T=1400℃.

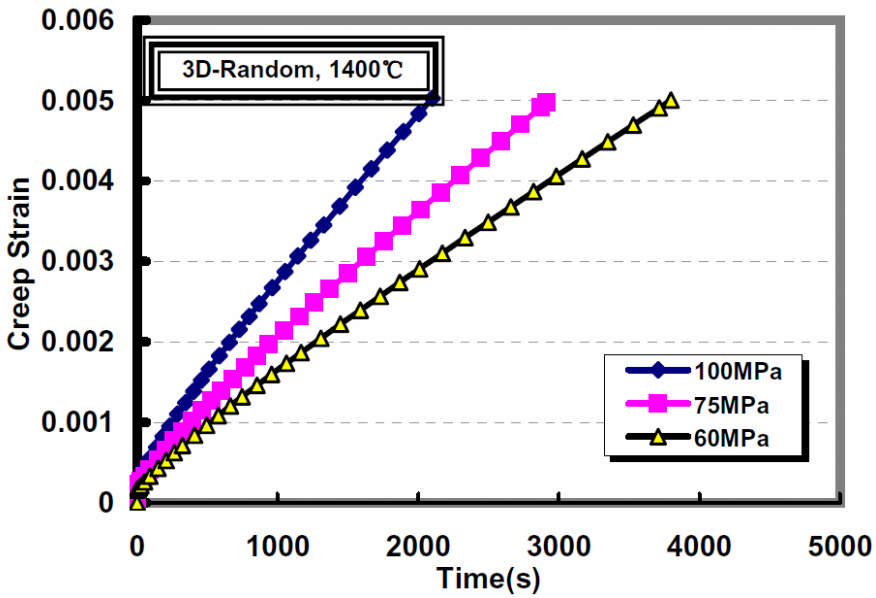

Figure 6.7 Creep strain versus time with different applied stresses for 3D random unit cell, λ=5, T=1400℃.

Figure 6.8 and Figure 6.10 show the peak width and peak position under different applied stress for three geometries. The non-percolating geometries (3D random and 3D aligned unit cells) show that the peak width (*FWHM*) depends on the applied stress representing the characteristics of the internal stress distribution range on the external applied stress for a certain creep strain. However, such dependence is not observed for the 2D percolating geometry although this still exists for the elastic deformation (stage 1 as shown in Figure 6.9). The reason for this is that the total creep strain is attributed to the bending of the internal whisker network and a fixed creep strain results in almost the same level of bending for different applied stress. However, small deviations are still observed (Figure 6.9), e.g. larger stress yields a smaller *FWHM* at first (stage 2); then as creep proceeds, larger stress yields higher *FWHM* (stage 3); finally when the total creep strain is accumulated to some extent, larger stress yields smaller *FWHM* and the difference increases (stage 4) to the limit at which the maximum strain is approached. Actually, the total creep strain consists of the elastic and creep components. Larger stress yields smaller net creep strain due to whisker bending for a fixed creep strain since a bigger elastic strain results, which means a narrow stress

distribution and thus smaller *FWHM*. At the same time, larger stress introduces a higher stress concentration around the contact points as the load is being transferred from the matrix to the whisker network resulting a broader stress distribution and thus greater *FWHM*. These two mechanisms compete with each other yielding the behaviours in 3 stages as shown in Figure 6.9.

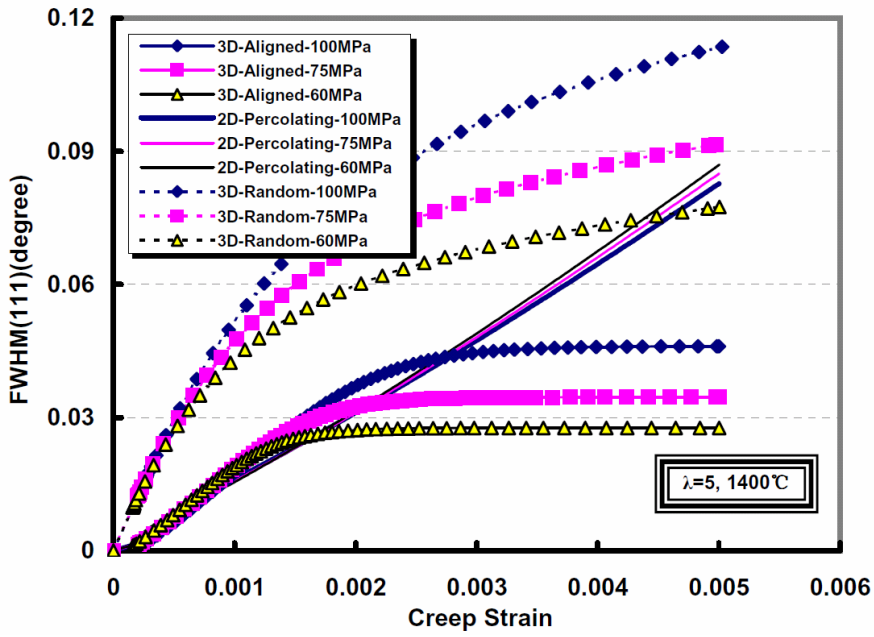

Figure 6.8 *FWHM* versus creep strain under different applied stresses for 2D percolating, 3D aligned and 3D random unit cells, λ=5, T=1400℃.

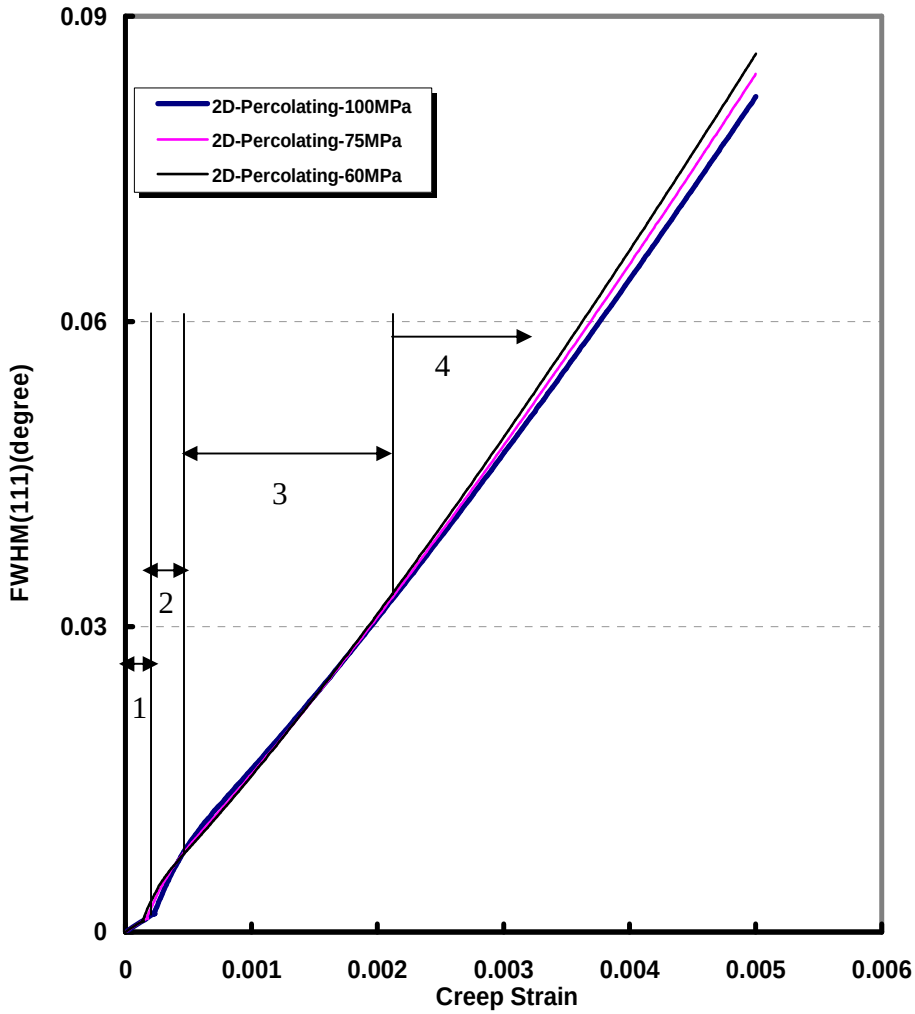

Figure 6.9 Enlarged view of *FWHM* versus creep strain for 2D percolating unit cell , λ=5, T=1400℃.

All three geometries exhibit a relative dependence on the applied stress in terms of peak-shift (Figure 6.10 and 6.11), representing the consistency between the mean stress inside the whisker network and the external applied stress regardless of its distribution. In general, larger stress shows the behaviour of rate changing representing the load transfer process around a larger total creep strain no matter if it is a completed process or not.

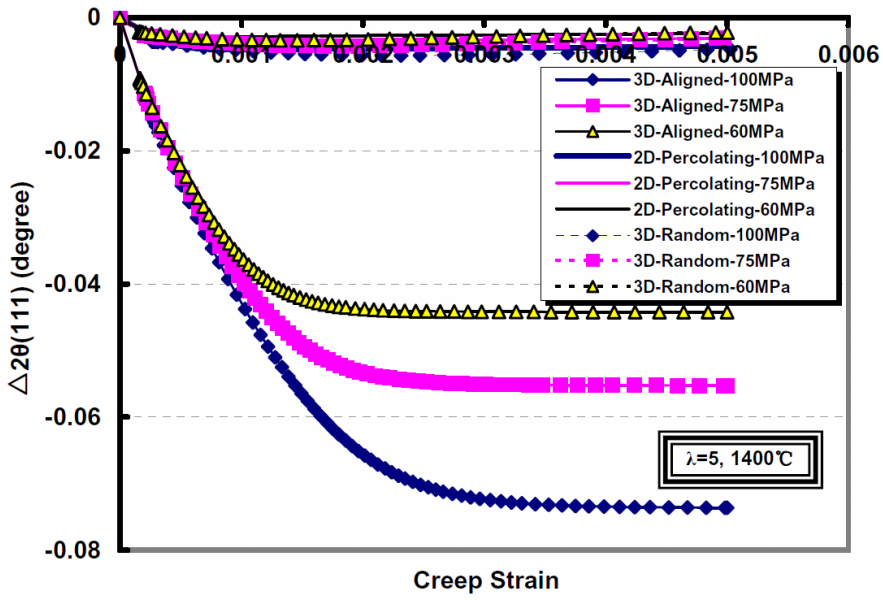

Figure 6.10 Peak shift versus creep strain under different applied stresses for 2D percolating, 3D aligned and 3D random unit cells, λ=5, T=1400℃.

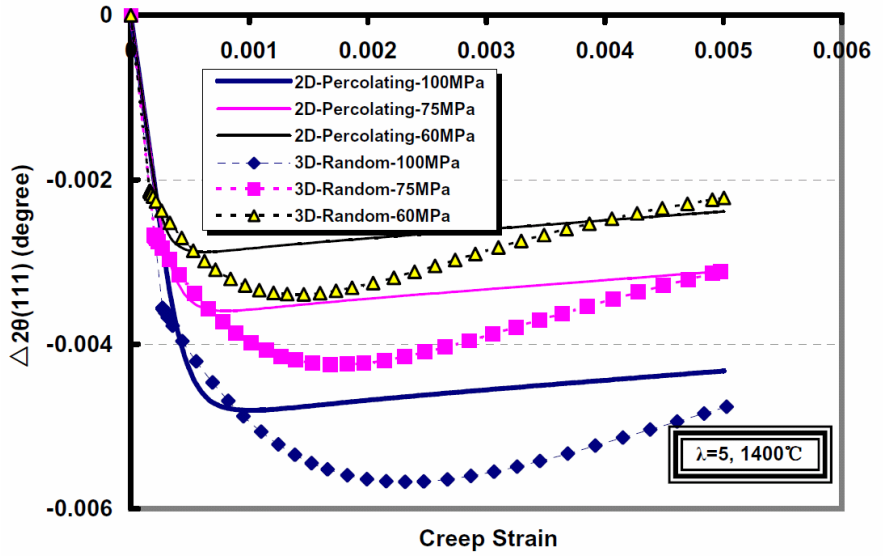

Figure 6.11 Peak shift versus creep strain under different applied stresses for 2D percolating and 3D random unit cells, λ=5, T=1400℃.

6.2.3. Effect of aspect ratio

Simulations above are based on the unit cells with aspect ratio of 5. This section studies the effect of aspect ratio for three kinds of whisker networks and relates the simulation results to the analytical models. Unit cells with aspect ratios of 5, 7, 10, 15 and 20 are deformed under stresses 60MPa, 75MPa and 100MPa. Please refer to Appendix C for Figures of the creep strain versus time, *FWHM* versus creep strain, and peak-shift versus strain for the simulations with varied aspect ratios under varied stresses.

6.2.3.1. 2D percolating geometry

As before, larger stress always yields the same value of creep strain in a quicker time for all aspect ratios (as shown in Figures C-1 to C-2). Although the unit cell with a bigger aspect ratio has a longer characteristic relaxation time τ (as demonstrated in chapter 5), it approaches the creep strain of 0.005 in a shorter time since it is more flexible (bigger maximum recoverable strain ε^*) if other conditions are fixed. Peak width and peak position behave similarly for all aspect ratios (as shown in Figures C-4 to C-9): (1) *FWHM* increases with the creep strain; (2) peak position shifts to a lower value and almost saturates.

Generally, for a fixed strain, e.g. 0.005, peak width decreases with the aspect ratio for the 2D percolating geometry and reaches a limit as shown in Figure 6.12. Meanwhile, peak position shifts to a lower value for a bigger aspect ratio as shown in Figure 6.13. Bending contributes mainly to the peak width instead of peak position with a difference of one order of magnitude. Furthermore, no dependence of the *FWHM* to the external stress has been observed since the three lines representing varied stresses almost merge into one line. However, the peak shifting is found to be dependent on the external stress, which is consistent with the previous results.

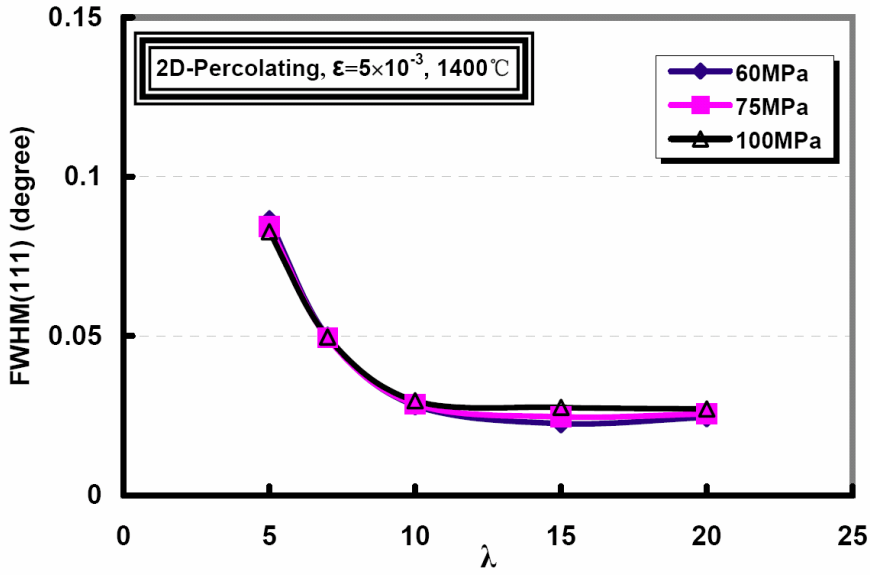

Figure 6.12 ***FWHM*** **versus aspect ratio for 2D percolating unit cells with λ=5, 7, 10, 15 and 20, T=1400℃,** $\sigma_{applied}$ **= -60MPa, -75MPa and -100MPa.**

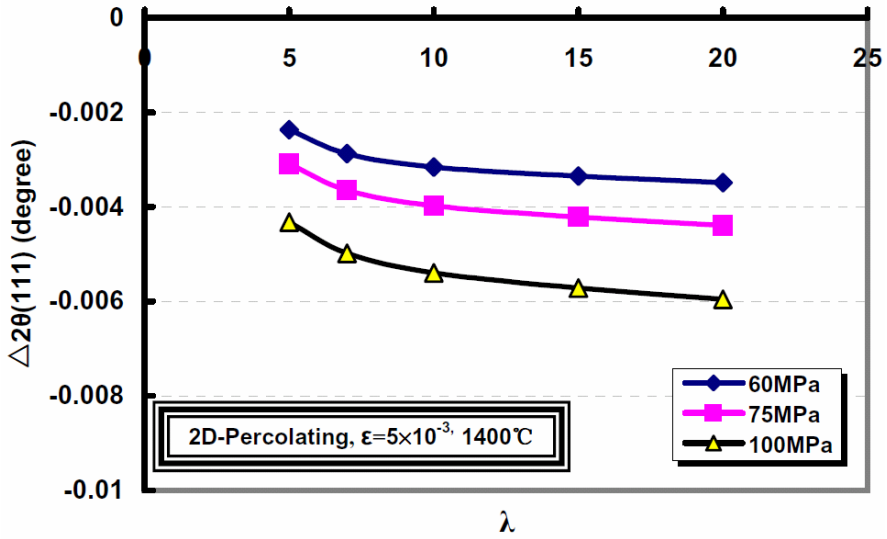

Figure 6.13 Peak shift versus aspect ratio for 2D percolating unit cells with λ=5, 7, 10, 15 and 20, T=1400℃, $\sigma_{applied}$ **= -60MPa, -75MPa and -100MPa.**

A simple analytical model could be constructed based on the analysis presented above. We have demonstrated the peak width for a simple bent beam in chapter 4 and the strain due to a center load in appendix A. It is straightforward to substitute the load *F* in equation 4.26 and span $2d = \lambda \times R$ with equation A.14A to yield the *FWHM* in terms of strain:

$$FWHM = 8\sqrt{2\ln 2}\tan\theta_0 \frac{\varepsilon}{\lambda^2 R} \qquad (6.1)$$

where θ_0 is the stress free diffraction angle, λ is the aspect ratio, *R* is the diameter of the whisker and ε is the strain of the unit cell which is actually the deflection of the beam (which is u_∞^* in appendix A). This equation suggests that the peak-width representing the stress field distribution within the whisker network for a fixed strain (deflection) of the unit cell is a problem of geometry since it contains no material properties and experimental conditions at all. It is straightforward from it to understand the non-dependence of peak width on the external stress, and the decreasing tendency of peak width with the aspect ratio although no limit is predicted. However, this equation can only provide some general trend since it is based on a beam without a matrix which is critical for the deformation of the beam inside. For example, the maximum peak width is 0.144^o (Figure 6.3) which is smaller than the value of 0.18^o if calculated using equation 6.1 with the inputs of $\varepsilon = 0.007784$ and $\lambda = 5$. Discrepancy comes from several sources. One important source is that the strain obtained directly from the unit cell deviates from the deflection of the beam due to the end effect specified in Section 5.3.3.2. Furthermore, based on the simple bent beam, no peak-shift could be predicted since it assumes no deformation on the central plane while it is the source of peak-shift of our simulations.

6.2.3.2. 3D aligned whisker geometry

As before, larger stress always yields the same value of creep strain in a quicker time for all aspect ratios (as shown in Figures C-10 to C-12). The unit cell with a larger aspect ratio has a more significant strain rate shifting and approaches the creep strain of 0.005 in a longer time if other conditions are fixed. This represents an increasing reinforcing effect of the larger aspect ratio and is consistent with the prediction based on the shear lag model (Cox, 1951 and Mclean, 1972). Peak width and peak-shift behave similarly for all aspect ratios under different

external stresses (as shown in Figures C-13 to C-18): (1) *FWHM* increases with the creep strain and then saturates when all the load is transferred to the whisker; (2) peak position shifts to a lower value and saturates when all the load is transferred to the whisker.

Generally, for the 3D aligned geometry with a fixed strain, i.e., 0.005, both peak width (Figure 6.14) and peak-shift (Figure 6.15) increases with the aspect ratio. These behaviours imply a broader distribution and higher value of mean stress inside the whisker network resulting from the increasing reinforcing effect of a larger aspect ratio. Elongation is the main deformation mechanism for the 3D aligned geometry, which contributes to the peak width and peak position at the same order of magnitude. Normally, a plateau shaped stress distribution from elastic deformation is changed toward a continuously increasing one for creeping deformation based on shear lag model (Mclean, 1972, Figure 2.14). Furthermore, the peak width and peak-shift also depends on the external stress for different aspect ratios.

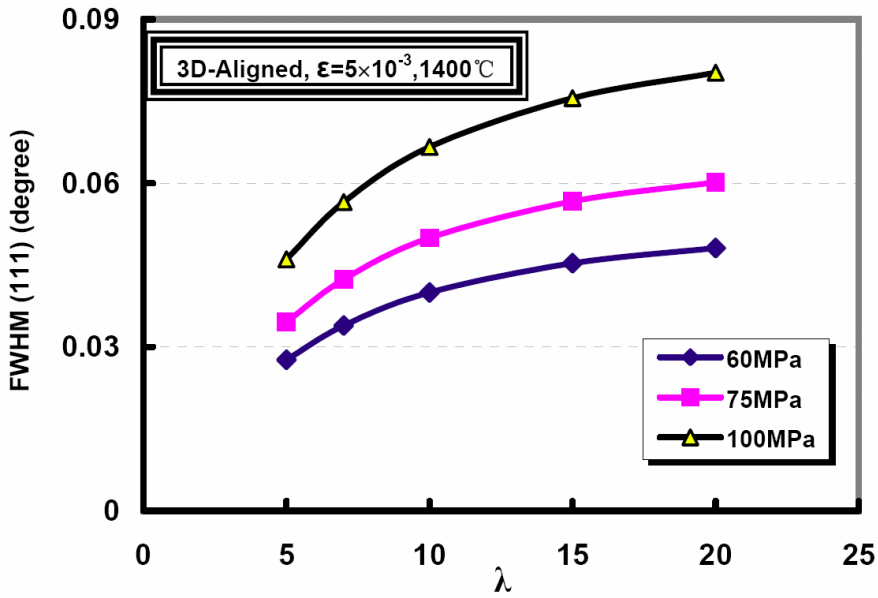

Figure 6.14 ***FWHM*** **versus aspect ratio for 3D aligned unit cells with λ=5, 7, 10, 15 and 20, T=1400℃,** $\sigma_{applied}$ **= 60MPa, 75MPa and 100MPa.**

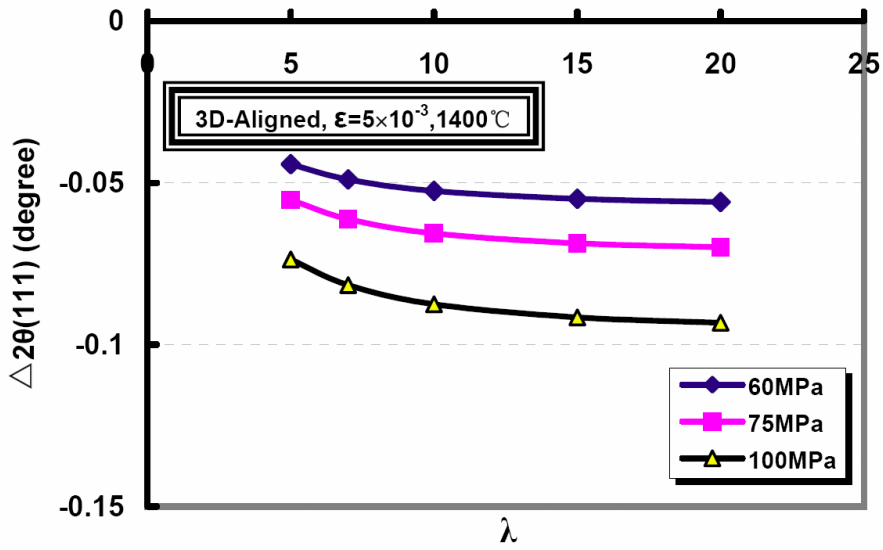

Figure 6.15 Peak shift versus aspect ratio for 3D aligned unit cells with λ=5, 7, 10, 15 and 20, T=1400℃, $\sigma_{applied}$ = 60MPa, 75MPa and 100MPa.

6.2.4. Summary

The relationships between the peak width and position with the deformation modes have been extensively studied. Generally, peak width increases with the creep strain and peak-shift represents the inside mean stress state whose sign is related to the external stress state. However, different geometries behave differently due to the internal load transfer process. Both 2D percolated and 3D aligned geometries exhibit saturation of the peak width and peak-shift with increasing creep strain (Figure 6.3 and 6.4) suggesting a complete load transfer process, although they have different deformation mechanisms: bending for the 2D percolating geometry and elongation for the 3D aligned geometry. However, the 3D random geometry exhibits a partial peak broadening while the peak-shift almost saturates. 2D percolating and 3D random geometries contribute mainly to the peak width instead of the peak-shift during the deformation with an order of magnitude difference, while the 3D aligned geometry contributes almost equally. For a fixed strain, e.g. 0.005, the 2D percolating geometry demonstrates non-dependence of peak width on the external stress due to

percolating and the dominant bending mechanism, while other two geometries show the dependence. However, all three geometries show the dependence of peak-shift on the external stress. Furthermore, for a specific strain, e.g. 0.005, the 2D percolating geometry shows that the peak width decreases with the aspect ratio down to a limit (Figure 6.12), while peak position shifts to a smaller angle for a bigger aspect ratio (Figure 6.13). However, the 3D aligned geometry shows that peak width increases with the aspect ratio (Figure 6.14), while peak-shift is more significant for a bigger aspect ratio (Figure 6.15). Therefore, for an initially stress free state, deformation inevitably yields non-uniform distributions of stress fields inside the whisker network embedded in the matrix, which results mainly in peak broadening.

6.3. Peak width and position with thermal stress

6.3.1. Effect of whisker network during cooling after creep

Figure 6.16 shows the simulated total strain, which is essentially the sum of the creep strain and thermal strain, versus time, based on unit cells with an aspect ratio of 5, subjected to an applied stress of 60MPa, at 1400℃. Due to the different stress states, the 2D percolating unit cell (compressive along the *y* direction) shows an increase of total strain during the cooling stage following the creep strain of 0.005 since the creep and thermal strains have the same sign. However, the 3D random and aligned unit cells (tensile axis along the *z* direction) show a decrease since the thermal contraction opposes the creep strain.

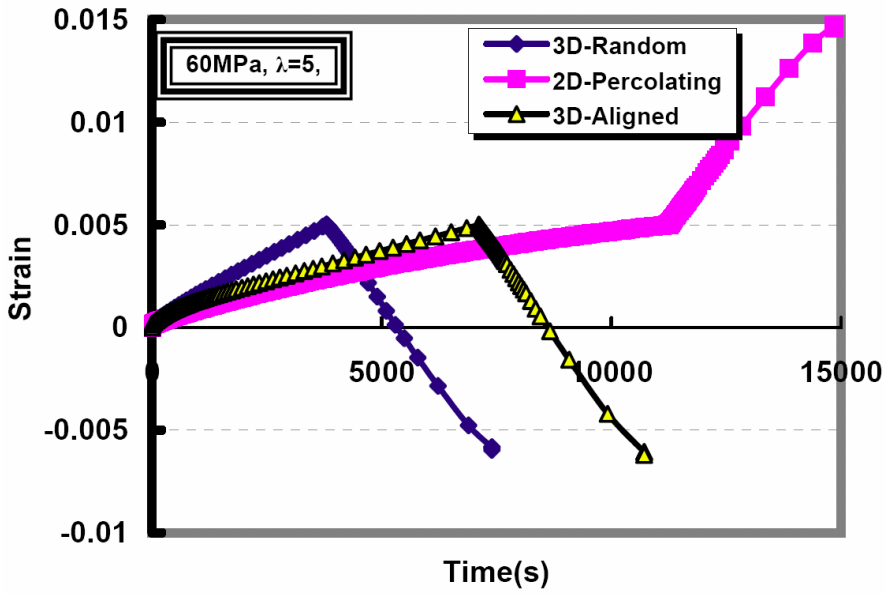

Figure 6.16 Strain versus time for three whisker networks (3D random, 2D percolating and 3D aligned unit cells), with λ=5, $\sigma_{applied}$ = 60MPa, as they are deformed to a strain of 0.005 at 1400℃, then cooled to 20℃.

For the 3D random and 2D percolating unit cells, *FWHM* (Figure 6.17) continues increasing during the cooling stage indicating a more inhomogeneous stress distribution. On the contrary, for the 3D aligned unit cell peak width decreases first to a minimum value of 0.01421° around 926℃ which is slightly before the minimum total strain occurs at around 810℃ and then increases with the further drop of temperature to a final value of 0.04306°. Still, the random and percolating geometries contribute mainly to the peak width (final values of 0.1194° and 0.1298° respectively).

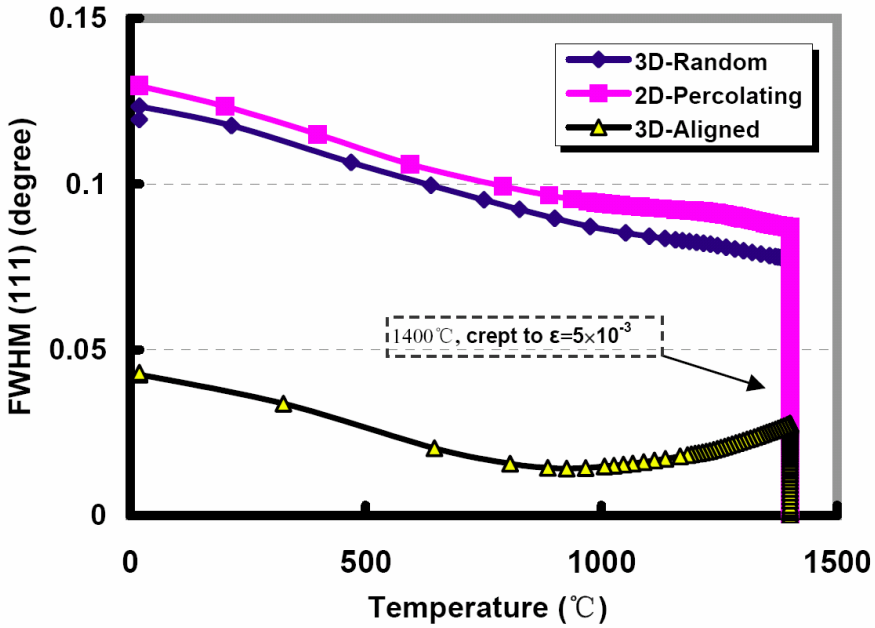

Figure 6.17 ***FWHM*** **versus temperature for three whisker networks (3D random, 2D percolating and 3D aligned unit cells), with λ=5,** $\sigma_{applied}$ **= 60MPa, as they are deformed to a strain of 0.005 at 1400℃, then cooled to 20℃.**

For all three unit cells, peak positions (Figure 6.18) shift to higher values indicating a compressive mean stress state due to the thermal contraction during the cooling stage. The random geometry still has the biggest value of peak shifting (0.1719°) while the percolating has the smallest value (0.04764°). Due to the negative contribution from the tensile deformation, the peak-shift for the 3D aligned geometry has a zero value around 926℃ and a final value of 0.1162° is obtained. Furthermore, a higher value of peak-shift (closer to that from the 3D random geometry) could be extrapolated for a compressive external stress along the *z* direction (whisker axis) as we might move up the line horizontally.

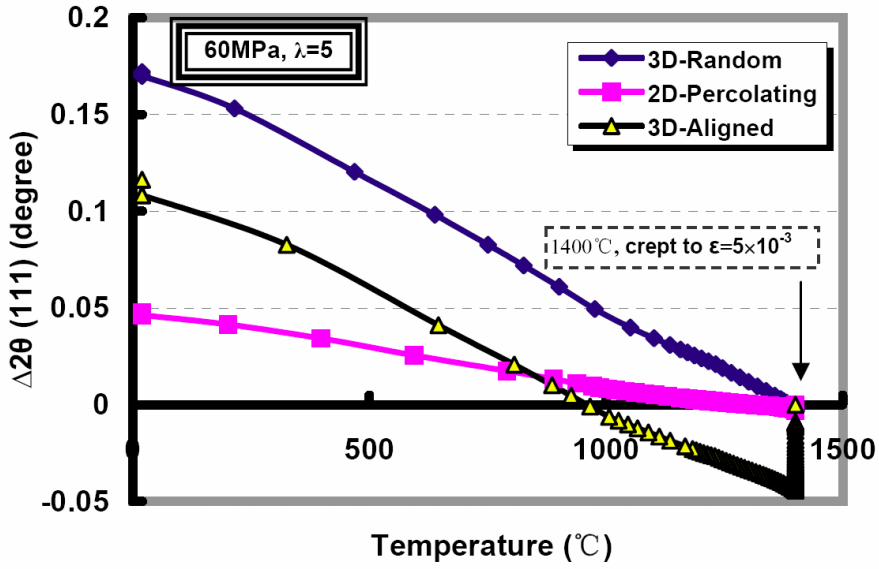

Figure 6.18 Peak-shift versus temperature for three whisker networks (3D random, 2D percolating and 3D aligned unit cells), with λ=5, $\sigma_{applied}$ = 60MPa, as they are deformed to a strain of 0.005 at 1400℃, then cooled to 20℃.

6.3.2. Effect of whisker network during cooling after hot pressing

Figures 6.19 and 6.20 show the simulated peak-width and -shift versus temperature from 1700℃ to 20℃ based on the unit cells with aspect ratio of 5 and compressive stress of 50MPa during cooling after hot pressing. They behave similarly to the Figures 6.17 and 6.18 respectively, representing a similar competing process between the creep strain and the thermal strain.

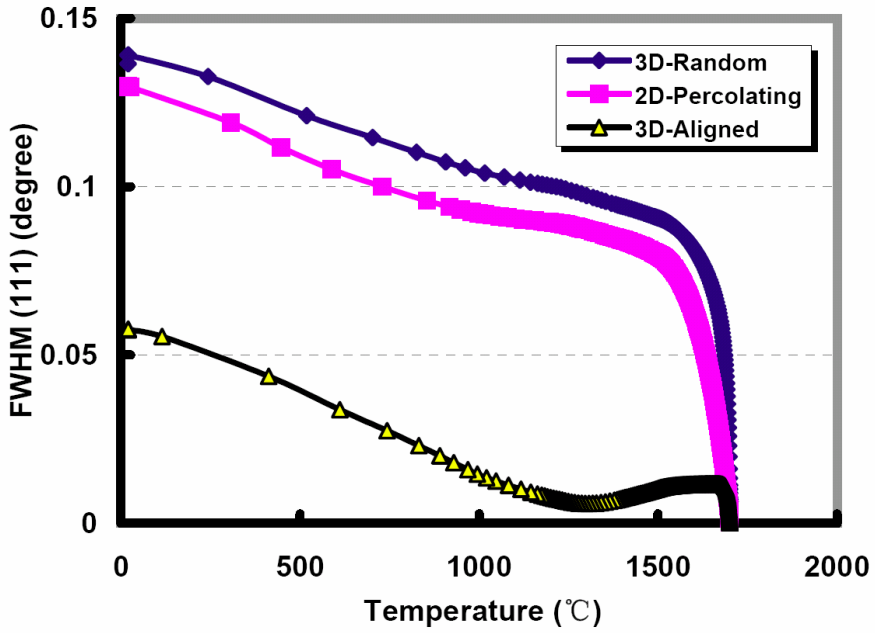

Figure 6.19 *FWHM* **versus temperature after hot pressing for three kinds of whisker networks: 3D random, 2D percolating and 3D aligned unit cells, with λ=5,** $\sigma_{applied}$ **= - 50MPa.**

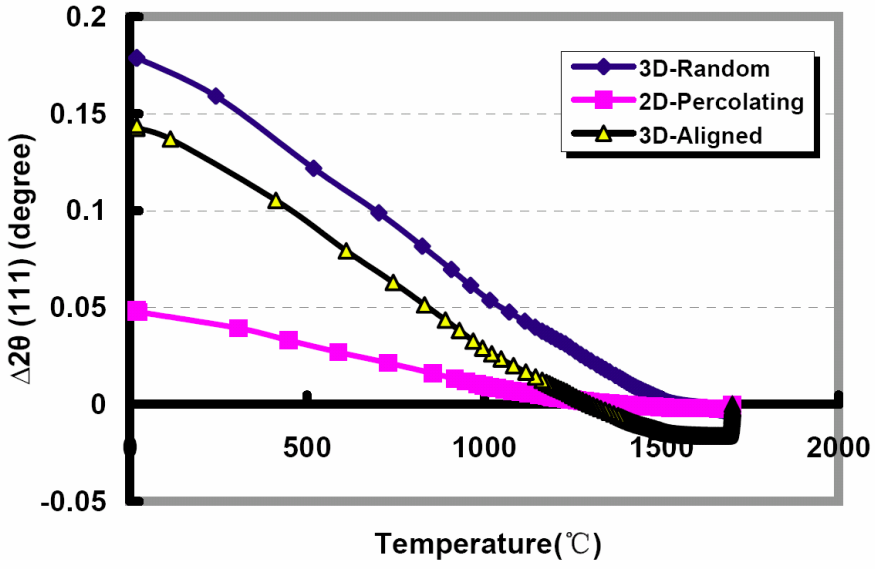

Figure 6.20 Peak-shift versus temperature after hot pressing for three kinds of whisker networks: 3D random, 2D percolating and 3D aligned unit cells, with λ=5, $\sigma_{applied}$ **= - 50MPa.**

The rapid increase of peak-width (Figure 6.19) at the beginning of cooling stage (1700℃ to 1500℃) suggests a dominance of creep deformation over thermal contraction due to the rapid creep strain rate at high temperature. Furthermore, for the 3D random and 2D percolating unit cells, thermal strain at the later stage of cooling dominates and enhances the extent of the stress distribution range. On the contrary, for the 3D aligned unit cell, after this rapid increasing period with peak value of 0.01173° around 1658℃, peak width decreases to a minimum value of 0.005907° around 1307℃ associated with a minimum total strain, and then increases with the further drop of the temperature to a final value of 0.05769°. This is because the whisker elongates first as a Poisson effect along the *z* direction (parallel to its axis) due to the compressive stress along the *y* direction (normal to its axis) and then contracts with the continue dropping of temperature. Still, the random and percolating geometries contribute mainly to peak-width (giving final values of 0.1365°and 0.1299° respectively).

Meanwhile, for three unit cells, peak positions shift to higher values indicating a compressive mean stress state due to the overall thermal contraction during cooling after hot pressing process. The random geometry still has the largest value of peak-shift (0.1786°) while the percolating geometry has the smallest value (0.04882°) similar to the case in section 6.3.1 due to different deformation mode. Same as before, the competing process is clearly demonstrated in the 3D aligned unit cell, the creep strain first opposes the thermal strain yielding a rapid leftward shifting up to -0.01615° around 1665℃(due to the Poisson effect as mentioned in the case of *FWHM*), followed by a period of plateau before reaching 1500℃. Then the thermal contraction dominates and increases the peak position rapidly to a final value of 0.1441° with a zero-shift around 1300℃ associated with the minimum total strain. Furthermore, a higher final value (closer to the one from the 3D random geometry) could be extrapolated if a compressive stress was applied along the whisker axis (*z* direction) for the 3D aligned geometry.

6.3.3. Effect of applied stress during cooling after creep

Same as in Section 6.2.3, three values of stress: 60MPa, 75MPa and 100MPa, are applied to the three whisker networks with aspect ratio of 5 in order to check the effect of the external stress during cooling after creep if the sample is crept to a strain of 0.005 before cooling. Figure 6.21 and 6.22 show the *FWHM* and peak-shift versus temperature respectively. The 2D percolating geometry still shows no dependence on the applied stress for both peak-width and -shift. For the non-percolating geometries, 3D random unit cell possesses the dependence of the peak width on the external stress during cooling while the 3D aligned one does not. A larger stress yields a smaller thermal contraction resulting in a smaller final *FWHM*. As for the case of the peak-shift, the two geometries behave in a contrary manner. The 3D random unit cell shows no dependence while the 3D aligned one does. It is obvious that the cooling stage after creep complicates the peak-width and -shift opposing the case observed in Section 6.2.3.

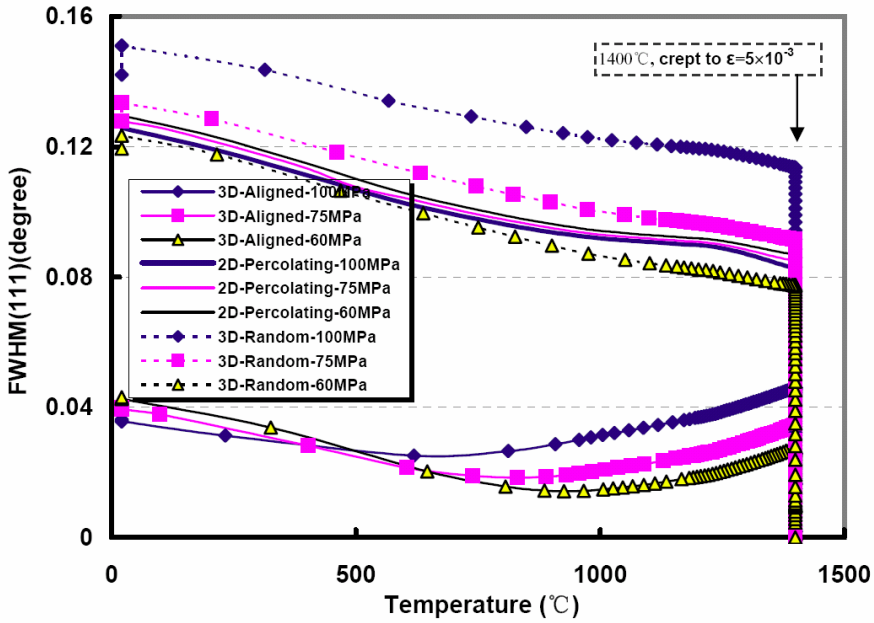

Figure 6.21 *FWHM* versus temperature under different applied stresses for 2D percolating, 3D aligned and 3D random unit cells, with λ=5, as they are deformed to a strain of 0.005 at 1400℃, then cooled to 20℃.

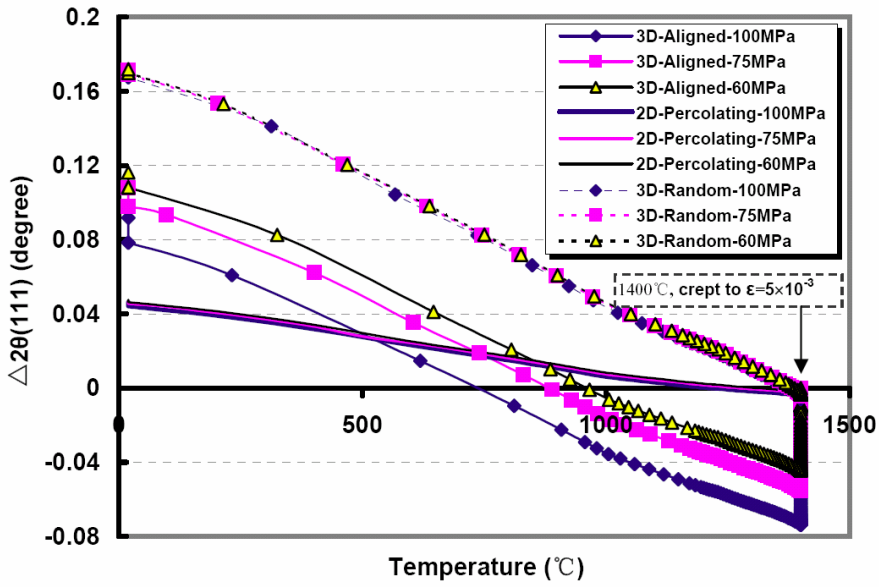

Figure 6.22 Peak-shift versus Temperature under different applied stresses for 2D percolating, 3D aligned and 3D random unit cells, with λ=5, as they are deformed to a strain of 0.005 at 1400℃, then cooled to 20℃

6.3.4. Effect of aspect ratio with thermal stress

6.3.4.1. 2D percolating geometry

During the cooling stage after creep, peak-width (Figure C-19 to C-21) and peak-shift (Figure C-22 to C-24) behave similarly for all aspect ratios under different applied stresses: (1) *FWHM* increases continually as temperature drops after creep; (2) peak position shift rightwards during the cooling stage from the leftward shifting during creep representing a compressive mean stress state due to thermal contraction.

Figures 6.23 and 6.24 show the peak-width and -shift versus aspect ratio for the 2D percolating geometry at four stages during deformation: elastic deformation (ED), creep deformation (CD), cooling under load (Cooling) and elastic unloading (EU). Generally, peak-width still decreases with the aspect ratio for the 2D percolating geometry and the saturation at

the stage of creep deformation is not that significant after being virtually cooled under load in air as shown in Figure 6.23. Furthermore, both creep deformation and cooling contribute mainly to the peak-width while the elastic deformation shows a trivial effect. Meanwhile, peak position shifts rightwards to a higher value for a bigger aspect ratio as shown in Figure 6.24 after cooling, for which the contribution of the cooling stage is dominant.

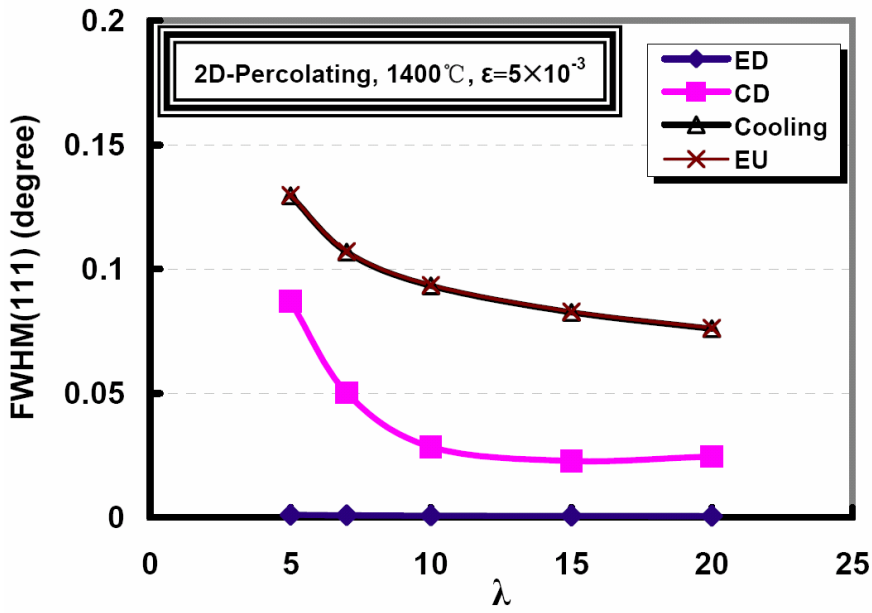

Figure 6.23 ***FWHM*** **versus aspect ratio for 2D percolating unit cells with λ=5, 7, 10, 15 and 20, deformed to a strain of 0.005 at 1400℃ then cooled to 20℃ with $\sigma_{applied}$ = 60MPa, ED: elastic deformation, CD: creep deformation, EU: elastic unloading.**

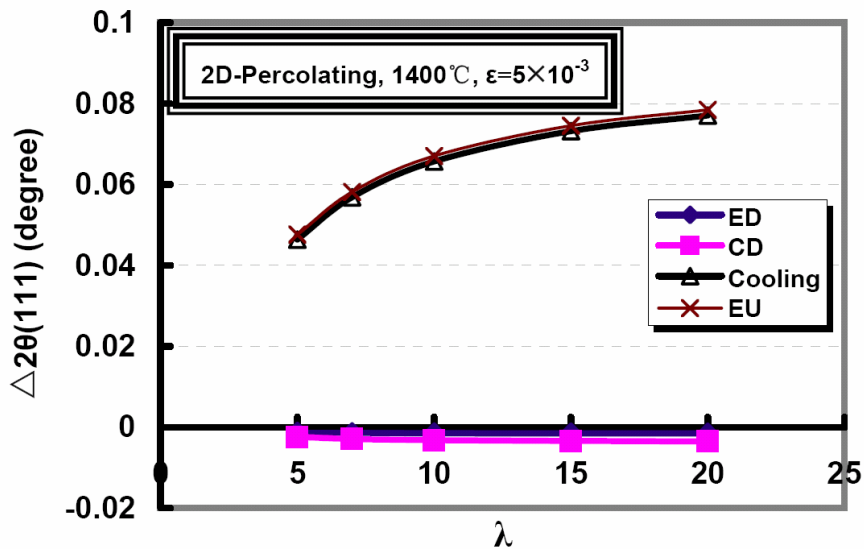

Figure 6.24 Peak-shift versus aspect ratio for 2D percolating unit cells with λ=5, 7, 10, 15 and 20, deformed to a strain of 0.005 at 1400℃ then cooled to 20℃ with $\sigma_{applied}$ = 60MPa, ED: elastic deformation, CD: creep deformation, EU: elastic unloading.

For the case of hot pressing, peak-width (Figure 6.25) and peak-shift (Figure 6.26) behave similarly for all aspect ratios as before based on the same deformation mode (bending) and competing strains (creep strain opposes thermal strain). Normally, peak-width still decreases with the aspect ratio for the 2D percolating geometry. Meanwhile, peak position shifts rightwards to a higher value for a bigger aspect ratio after cooling due to the dominant thermal contraction.

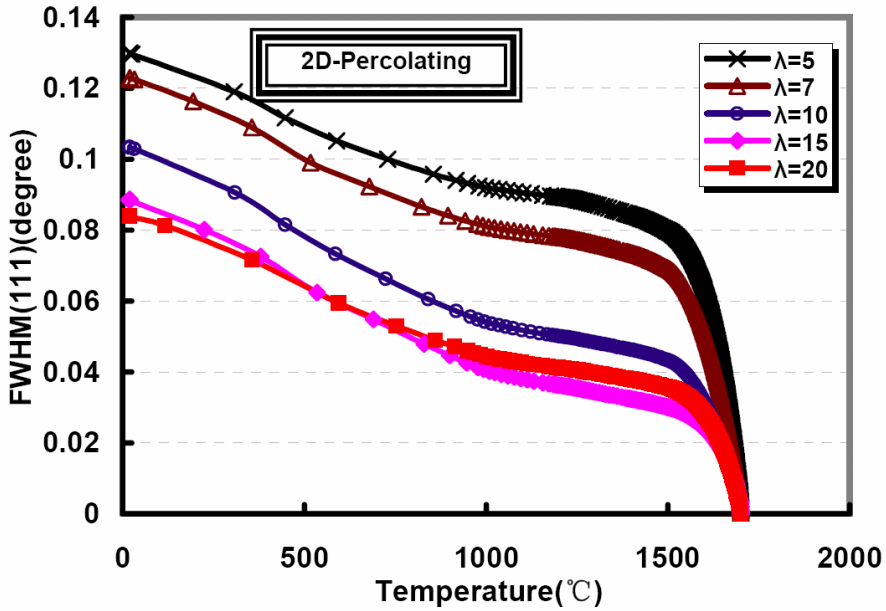

Figure 6.25 ***FWHM*** **versus temperature after hot pressing for 2D percolating unit cells with λ=5, 7, 10, 15 and 20,** $\sigma_{applied}$ **= - 50MPa.**

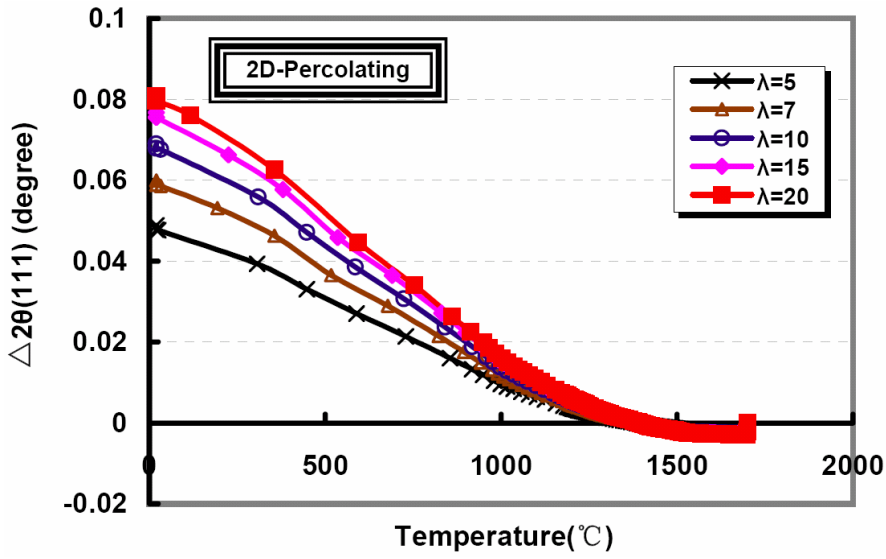

Figure 6.26 Peak-shift versus temperature after hot pressing for 2D percolating unit cells with λ=5, 7, 10, 15 and 20, $\sigma_{applied}$ **= - 50MPa.**

6.3.4.2. 3D aligned geometry

Same as before, for 3D aligned geometry peak-width (Figures C-25 to C-27) behaves similarly during cooling stage after creep for varied aspect ratios and applied stresses. However, some small differences are still observed. In general: (1) *FWHM* decreases first then increases again with the dropping temperature for all aspect ratios with $\sigma_{applied}$ =60MPa; for aspect ratios of 5, 7 and 10 with $\sigma_{applied}$ =75MPa; for aspect ratios of 5 and 7 with $\sigma_{applied}$ =100MPa; (2) monotonously decreases as temperature drops after creep for bigger aspect ratios and applied stresses: aspect ratios of 15 and 20 with $\sigma_{applied}$ =75MPa; for aspect ratio of 10, 15 and 20 with $\sigma_{applied}$ =100MPa.

As mentioned before, the whisker elongates along the *z* direction (parallel to its axis) during creep and then contracts with the continue dropping of temperature. Larger tensile stress shows a stronger effect of inhibiting the thermal contraction yielding a smoother change of peak-width during cooling for each aspect ratio (closer to the second case). Meanwhile, larger aspect ratio shows a stronger reinforcing effect yielding a smoother change of peak-width during cooling for varied applied stress. Therefore, unit cell with smaller aspect ratio contracts more and might overcome the effect of creep strain while the one with larger aspect ratio might not and results in a monotonous decrease as temperature drops. The extent is determined by the applied stress.

For the case of peak-shift, it behaves in a similar way for all aspect ratios and different applied stresses (Figures C-28 to C-30) during cooling stage after creep. In general, peak position shifts rightwards due to cooling from the leftward shifting due to creep deformation indicating a change of the mean stress state from tensile to compressive. Meanwhile, no significant dependence of the peak-shift on the aspect ratio was found after being virtually cooled under load in air and almost all aspect ratios combine into one line. However, a bigger applied stress affects the peak-shift more significantly and results in more scattered lines during cooling stage.

Figures 6.27 and 6.28 show the peak-width and -shift versus aspect ratio for the 3D aligned geometry at four stages during deformation: elastic deformation (ED), creep deformation (CD), cooling under load (Cooling) and elastic unloading (EU). Both creep deformation and cooling contribute mainly to the peak-width while the elastic deformation shows a trivial effect. Furthermore, an initial decrease then an increase with increasing aspect ratio of peak-width (purple line in Figure 6.27) is observed after cooling and the monotonous increasing trend with the aspect ratio after creep is no longer existed (black line in Figure 6.27). Meanwhile, peak position shifts rightwards after cooling from the leftward shifting after creep as shown in Figure 6.48. Still, both creep deformation and cooling affect mainly the peak-shift while the elastic deformation shows a somehow smaller contribution.

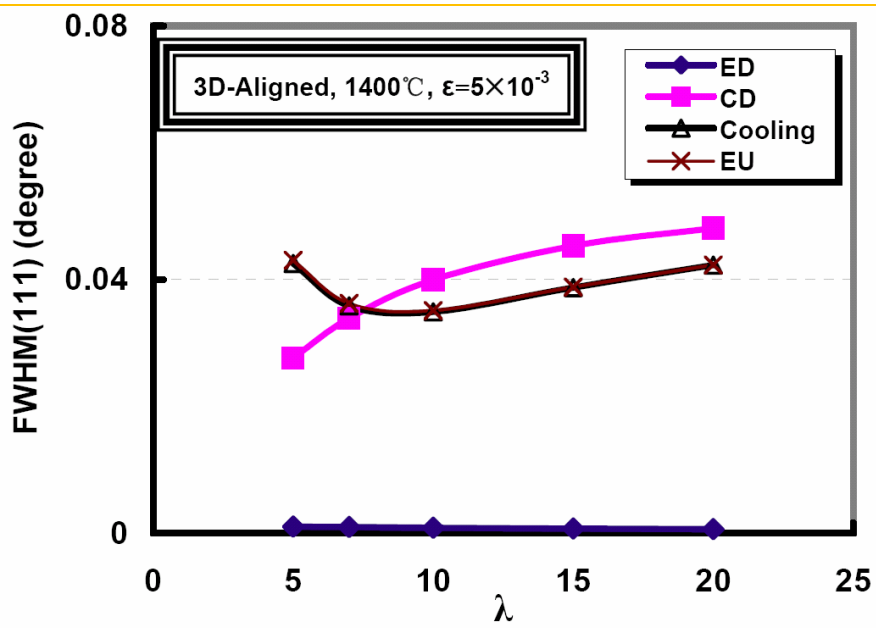

Figure 6.27 ***FWHM*** **versus aspect ratio for 3D aligned unit cells with λ=5, 7, 10, 15 and 20, deformed to a strain of 0.005 at 1400℃ then cooled to 20℃ with $\sigma_{applied}$ = 60MPa, ED: elastic deformation, CD: creep deformation, EU: elastic unloading.**

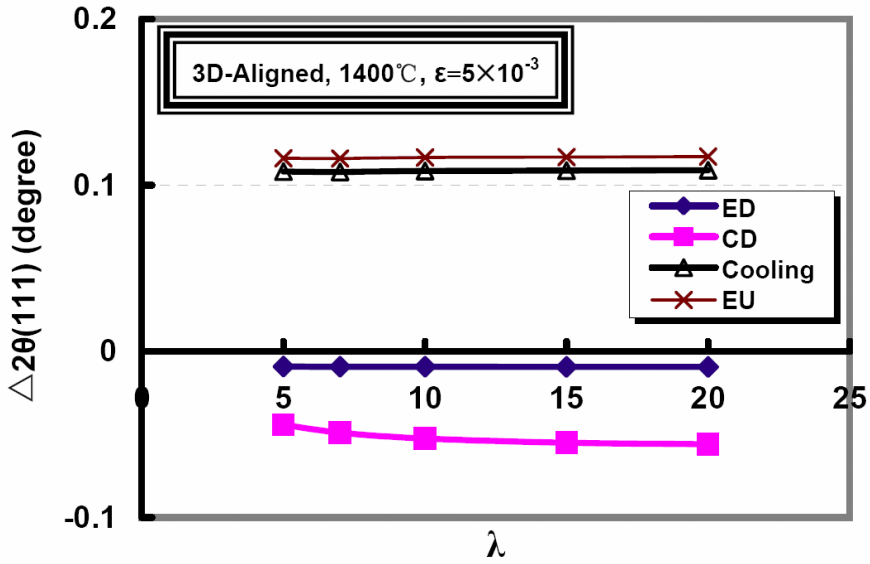

Figure 6.28 Peak-shift versus aspect ratio for 3D aligned unit cells with λ=5, 7, 10, 15 and 20, deformed to a strain of 0.005 at 1400℃ then cooled to 20℃ with $\sigma_{applied}$ = 60MPa, ED: elastic deformation, CD: creep deformation, EU: elastic unloading.

For the case of hot pressing, peak-width (Figure 6.29) and peak-shift (Figure 6.30) still behave similarly for all aspect ratios as before based on the same deformation mode (elongation or contraction) and competing strains (creep strain opposes thermal strain). Normally, smaller aspect ratio yields a larger peak-width for the 3D aligned geometry for the same reason mentioned above. Meanwhile, peak position also exhibit a strong effect of thermal stress instead of the aspect ratio during hot pressing while a larger aspect ratio does result in a larger rightward shift insignificantly.

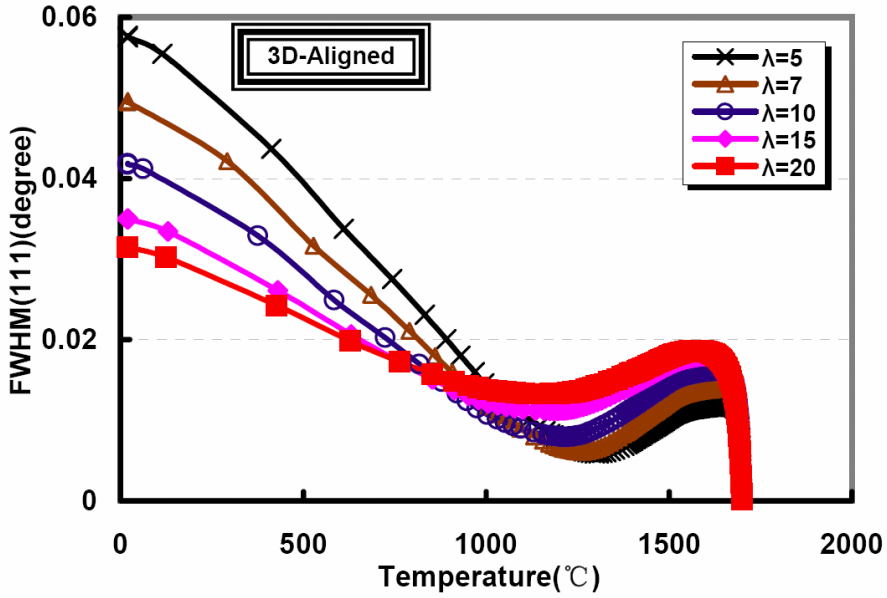

Figure 6.29 ***FWHM*** **versus temperature after hot pressing for 3D aligned unit cells with λ=5, 7, 10, 15 and 20,** $\sigma_{applied}$ **= - 50MPa.**

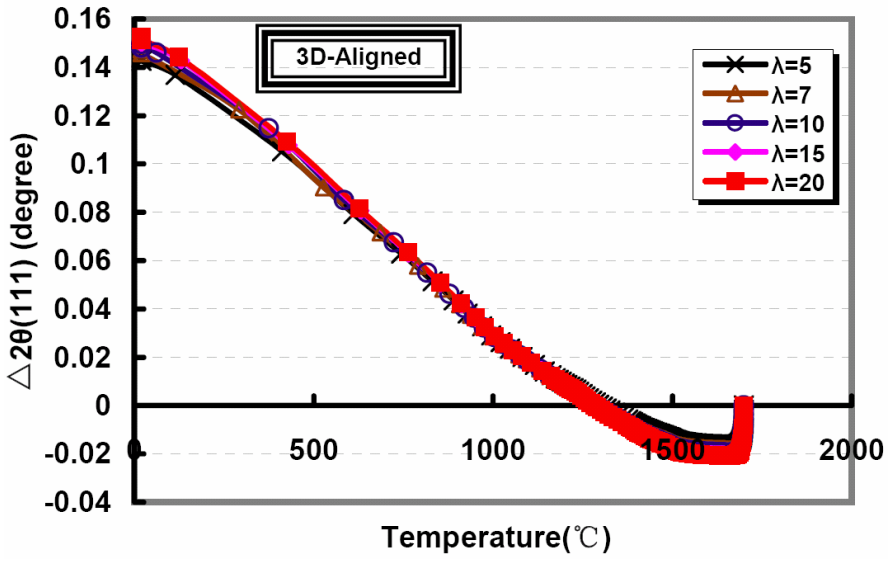

Figure 6.30 Peak-shift versus temperature after hot pressing for 3D aligned unit cells with λ=5, 7, 10, 15 and 20, $\sigma_{applied}$ **= - 50MPa.**

6.3.5. Net change of peak-width and -shift after creep

Figures 6.31, 6.32, 6.33 and 6.34 show the net change of peak-width and -shift by comparing the samples before and after creep with thermal effects in section 6.3 for 2D percolating and 3D aligned geometries: being cooled from 1700℃ to 20℃ under 50MPa compressive stress after hot pressing; being crept to a strain of 0.005 then cooled under load with 60MPa, 75MPa and 100MPa. The relationship between the peak-width and -shift with the deformation modes and aspect ratio studied in section 6.2 (i.e. Figure 6.12, 6.13, 6.14 and 6.15) are concealed by the thermal stress from the two cooling stages: i.e. the decreasing and saturation of the peak-width with increasing aspect ratio for the 2D percolating geometry (Figure 6.12), and the increasing of peak-width with increasing aspect ratio for the 3D aligned geometry (Figure 6.14). However, the non-dependence of peak-width change on the applied stress as well as the wavy dependence on the aspect ratio is observed for the 2D percolating geometry (Figure 6.31). Meanwhile, for the 3D aligned geometry the peak-width (Figure 6.33) still increases with the aspect ratio with varied applied stresses and behaves in a different way from Figure 6.14. Most importantly, both broadening and narrowing effect of the peak-width after creep are predicted here while in section 6.2 we summarized that creep deformation would inevitably introduce peak broadening from a initial stress free state. Furthermore, the net change of peak-shift (Figures 6.32 and 6.34) for both geometries decreases with the aspect ratios for varied applied stresses and exhibits a leftward shift as before (Figures 6.13 and 6.15).

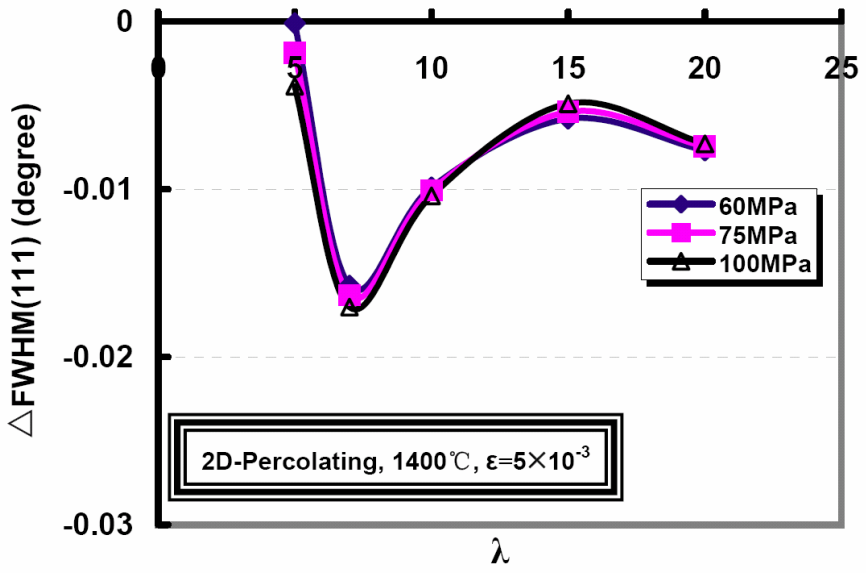

Figure 6.31 $\Delta FWHM$ **versus aspect ratio for 2D percolating unit cells with λ=5, 7, 10, 15 and 20, compared between samples before (hot pressed with** $\sigma_{applied}$ **= - 50MPa) and after creep (deformed to a strain of 0.005 at 1400℃ then cooled to 20℃ with** $\sigma_{applied}$ **=-60MPa, -75MPa and -100MPa).**

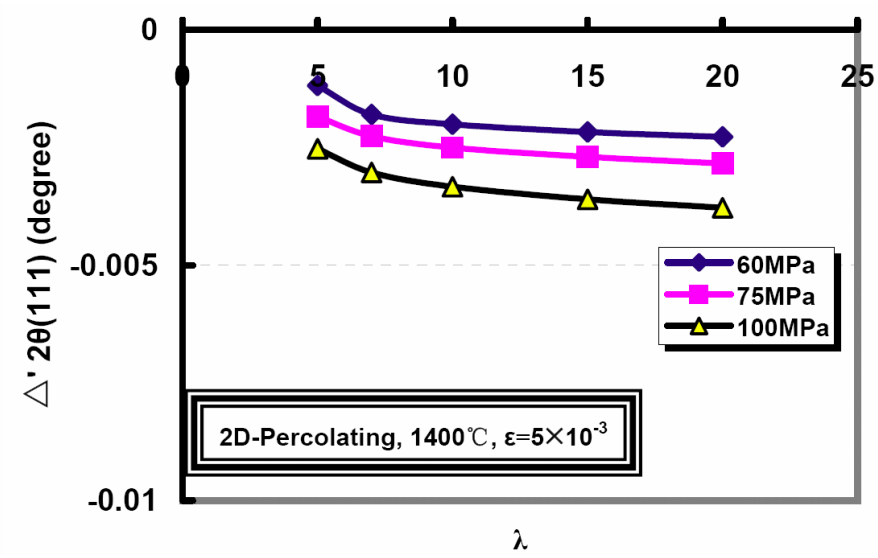

Figure 6.32 Peak-shift versus aspect ratio for 2D percolating unit cells with λ=5, 7, 10, 15 and 20, compared between samples before (hot pressed with $\sigma_{applied}$ **= - 50MPa) and after creep (deformed to a strain of 0.005 at 1400℃ then cooled to 20℃ with** $\sigma_{applied}$ **=-60MPa, -75MPa and -100MPa).**

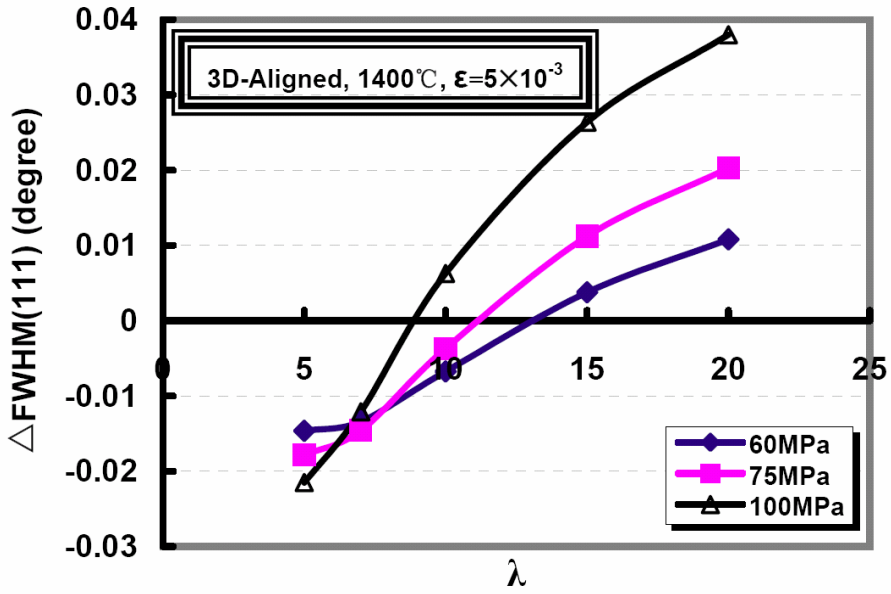

Figure 6.33 $\Delta FWHM$ **versus aspect ratio for 3D aligned unit cells with λ=5, 7, 10, 15 and 20, compared between samples before (hot pressed with** $\sigma_{applied}$ **= - 50MPa) and after creep (deformed to a strain of 0.005 at 1400℃ then cooled to 20℃ with** $\sigma_{applied}$ **=-60MPa, -75MPa and -100MPa).**

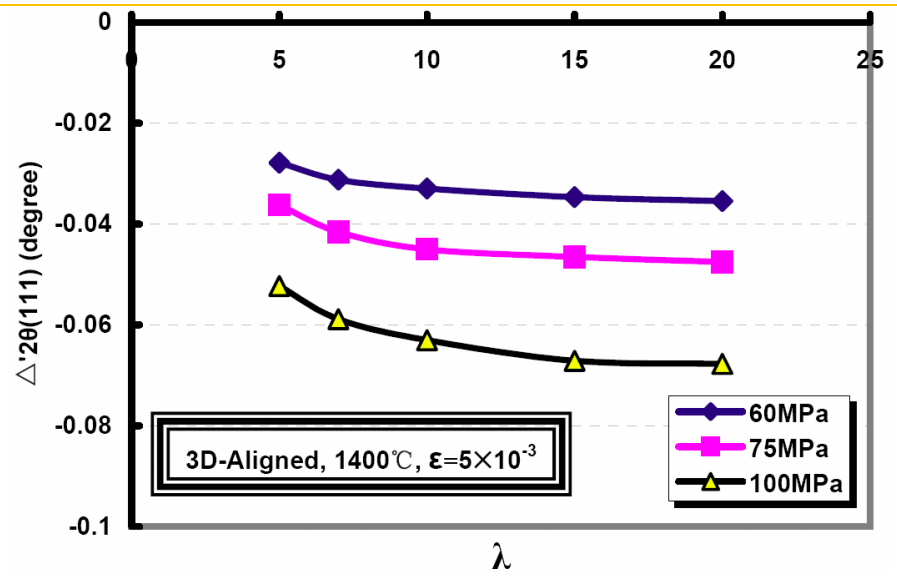

Figure 6.34 Peak-shift versus aspect ratio for 3D aligned unit cells with λ=5, 7, 10, 15 and 20, compared between samples before (hot pressed with $\sigma_{applied}$ **= - 50MPa) and after creep (deformed to a strain of 0.005 at 1400℃ then cooled to 20℃ with** $\sigma_{applied}$ **=-60MPa, -75MPa and -100MPa).**

6.4. Discussion

Information in section 6.3.5 points out the critical effect of the thermal stresses on the final peak-width change and position although extracting a systematic trend coupling the network deformation, load transfer and the thermal stress is not possible due to the complexity of the situation. Therefore, a general comparison between the virtual results and the experimental data is made below, which emphasizes the range of the results obtained in this work and from Quan's experiments.

Figure 6.35 (a) shows the peak-width predictions on the 2θ goniometric scale due to creep deformation from an initial stress-free state while the distribution range is different for different geometries as illustrated in Table 6.1. These values can be compared with the error range for neutron diffraction (±0.0067~±0.0132) according to Quan's (2004) data based on the E3 materials science diffractometer attached to the National Research Universal (NRU) reactor at Chalk River Laboratory (CRL). It would seem that the peak width changes predicted by the models are sufficiently large that they might be seen experimentally. In terms of peak-shifts, only the 3D aligned geometry might yield shifts big enough to be measured experimentally (Figure 6.35(b)), as illustrated in Table 6.1.

Table 6.1 FWHM and Peak-shift (Δ2θ) range for three geometries without thermal stress **

	2D percolating geometry	3D aligned geometry	3D random geometry
FWHM	0.02464° (60MPa, λ=20) ∫ 0.08698° (60MPa, λ=5)	0.02765° (60MPa, λ=5) ∫ 0.08023° (100MPa, λ=20)	0.07747° (60MPa, λ=5) ∫ 0.1135° (100MPa, λ=5)
Δ2θ	-0.002368° (60MPa, λ=5) ∫ -0.005952° (100MPa, λ=20)	-0.04423° (60MPa, λ=5) ∫ -0.09323° (100MPa, λ=20)	-0.00222° (60MPa, λ=5) ∫ -0.004761° (100MPa, λ=5)

**Based on virtual tests with λ=5, 7, 10, 15 and 20, $\sigma_{applied}$ = 60MPa, 75MPa and 100MPa, as they are deformed to a strain of 0.005 at 1400℃.

Together with the thermal effect, external stress yields net changes of the peak-width ($\Delta FWHM$ in Figure 6.35(c)) after creep in a broader range determined by the geometry and stress, as illustrated in Table 6.3. Peak position shifts (Figure 6.35(d)) to lower values for all virtual tests among which the 3D aligned geometry yields significant effect as before, as illustrated in Table 6.2.

Table 6.2 FWHM and Peak-shift (Δ2θ) range for three geometries with thermal stress **

	2D percolating geometry	3D aligned geometry	3D random geometry
FWHM	-0.0001104°(60MPa, λ=5) ∫ -0.01702°(100MPa, λ=7)	-0.021496°(100MPa, λ=5) ∫ 0.03798°(100MPa, λ=20)	-0.01706° (60MPa, λ=5) ∫ 0.005624°(100MPa, λ=5)
Δ2θ	-0.001182° (60MPa, λ=5) ∫ -0.003778° (100MPa, λ=20)	-0.027846° (60MPa, λ=5) ∫ -0.06771° (100MPa, λ=20)	-0.006712° (60MPa, λ=5) ∫ -0.007804°(100MPa, λ=5)

**Based on virtual tests with λ=5, 7, 10, 15 and 20, $\sigma_{applied}$ = 60MPa, 75MPa and 100MPa, as they are deformed to a strain of 0.005 at 1400℃, then cooled to 20℃.

Net changes of the peak-width and -shift obtained virtually cover the range of the data obtained from experiments and explain the apparent contradiction between theory and experimental results mentioned in the introduction as shown in Figure 6.35(e) and 6.35(f). Despite the deformation mode, peak broadening representing the non-uniform distributions of stress fields inside the whisker network embedded in the matrix comes from two sources: external stress or temperature change while the latter one makes the data intractable. Furthermore, the peak position is also dominated by the thermal stress.

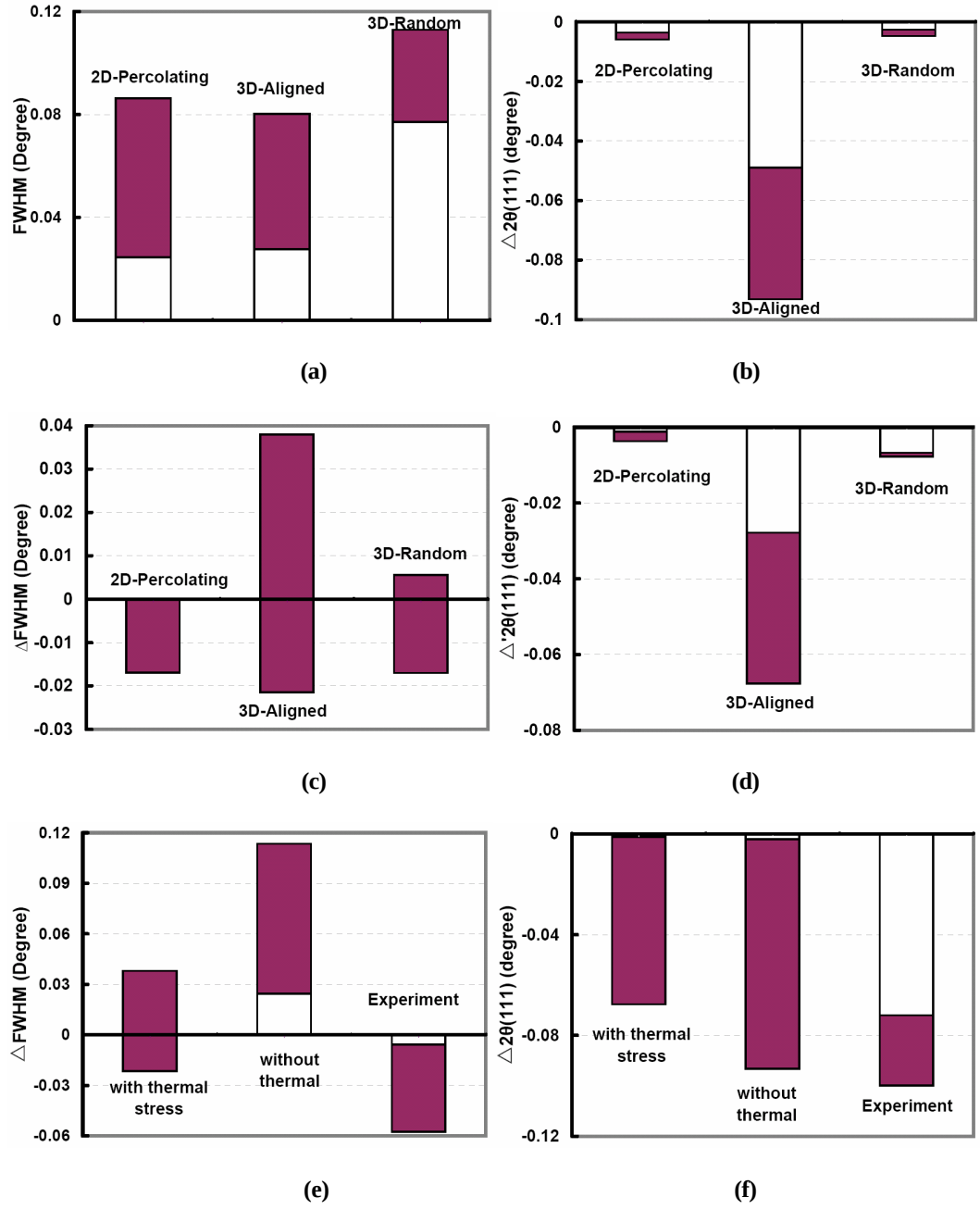

Figure 6.35 ***FWHM*** **and Peak-shift predictions (dark area) : (a) and (b) for three geometries without thermal stress, (c) and (d) for three geometries with thermal stress, (e) and (f) for all virtual tests with thermal stress, without thermal stress and experimental tests; virtual tests are with λ=5, 7, 10, 15 and 20,** $\sigma_{applied}$ **= 60MPa, 75MPa and 100MPa, as they are deformed to a strain of 0.005 at 1400℃, then cooled to 20℃ if thermal stress is considered.**

Therefore, it is not helpful to freeze the bending strain after creep by cooling the samples under load because this will introduce the complicated thermal stress and conceal the phenomenon of interest. Although the changes of peak-width and -shift obtained in this work seem detectable via neutron diffraction (i.e. error range between ±0.0067~±0.0132 from Quan's work), it should be used with caution even for cases without thermal stress since they are of the same order of magnitude, Moreover, some effects are still undetectable such as cases in Figure 6.35 (b) and (d). Furthermore, the whisker geometry in the experiments does not exactly match any of the virtual configurations studied, suggesting a more realistic microstructure of the Al_2O_3-SiC_w composite is needed for simulations in order to make a closer matching.

CHAPTER 7

SUMMARY AND FUTURE WORK

7.1. Summary

This work systematically studied the anelastic behavior and deformation mechanisms for Al_2O_3-SiC_w composites containing a percolating whisker network as well as explained the contradicting experimental neutron diffraction results in the former work (Quan, 2004). It provides a framework for performing virtual tests covering mechanical deformation and the corresponding characterization via diffraction in terms of peak width and position. Deformation mechanisms have been studied using micromechanical methods and characterized using the virtual diffraction developed in this work. Specifically, this work addressed and answered the following issues:

(1) **The origins of the anelastic creep recovery for Al_2O_3-SiC_w**:

It exists not only in composites but also in un-reinforced materials and arises from two sources: dislocation activities and plastic strain misfit. For SiC whisker containing alumina composites, the latter is the main mechanism due to the high formation energy and Peierls force of dislocations. In this work we have verified the critical importance of a percolating whisker network for the anelastic recovery based on the 3D multi-whisker random unit cell.

(2) **Deformation mechanisms of the percolating network during creep:**

We demonstrated that bending is the dominant mechanism over contact from an energy point of view during the creep deformation of a composite containing a well aligned percolating whisker network based on the 2D unit cell model.

(3) **Comparison between analytical and FEM results for anelasticity:**

Good qualitative agreement was found between our FEM simulations and the analytical model of Wilkinson and Pompe with regards to the maximum recoverable strain

and the characteristic relaxation time. Despite the deviations in absolute magnitude, the analytical model captures all the critical properties characterizing the deformation mechanisms or strain recovery. These include: the maximum recoverable strain is inversely proportional to the whisker's Young's modulus and proportional to the third power of the aspect ratio; the characteristic relaxation time is inversely proportional to the Young's modulus of the whisker and creep pre-exponent constant for the matrix, and proportional to the fourth power of the whisker aspect ratio. Plane stress condition has been demonstrated to more closely represent the real situation over plane strain condition since the matrix could flow out from the deformed region and a beam is more suitable to describe a whisker.

(4) **The effect of creep deformation and thermal stress on diffraction pattern:**

Peak-width (***FWHM***) is a measure of stress distribution with the elastic whisker while peak position represents the mean stress state. It has been shown that creep deformation inevitably yields non-uniform distributions of stress fields inside the whisker network embedded in the matrix and results in the peak broadening for a zero stress initial state despite the deformation mechanisms. Both bending (2D percolating geometry) and random (3D random geometry) modes contribute mainly to the peak width instead of the peak-shift with an order of magnitude difference, while elongation/contraction mode (3D aligned geometry) contributes almost equally. Increasing the aspect ratio decreases the peak-width to a limit for the bending mode and increases for the elongation mode. However, both modes showed more significant peak-shift for a bigger aspect ratio. The load transfer process has been verified via the partial and/or full saturation of the peak-width and -shift. Furthermore, the 2D percolating geometry demonstrates the independence of the peak width on the external stress due to percolating and the dominant bending mechanism, while the other two geometries show the dependence. However, all three geometries show the dependence of the peak-shift on the external stress.

We have further demonstrated that the thermal stress from the cooling stage following the creep deformation increased the scatter in the stress distribution inside resulting

in a continuing increase of peak width. This temperature change is so large that the final mean stress state became compressive despite the deformation modes. The effect of aspect ratio is not straightforward under the interaction of thermal stress and external stress for both bending and elongation/contraction modes. The cooling stage following the hot pressing process has been shown to broaden the peak-width despite the different geometries and yields a compressive residual stress as well. It has been found that this thermal stress concealed the observation of a peak broadening effect and shifted the peak to a lower position when compared with samples after and before creep. This explained the contradicting neutron diffraction data wherein both broadening and narrowing of peak width has been obtained. The neutron diffraction method is found to be not suitable for the characterization of deformation mechanisms due to the rather low angular resolution. That is, the error range is too large in comparison with scale of the effects due to creep and thermal effects, thus preventing a definitive determination of the processes at play.

7.2. Future work

In terms of experiments, it is essential to use an x-ray source with a small intrinsic peak width. It would also be wise to choose a system without such a large thermal expansion difference between two constituents. In situ experiments would enable more accurate tracking of the observed phenomena. It would be interesting to check the effects of percolating, applied stress together with the aspect ratio on diffraction patterns experimentally while a diffraction source with higher angular resolution than neutron diffraction should be used.

In terms of modeling, this work used three simplified geometries: percolating, random and aligned and obtained useful information such as the deformation mechanism inside a percolating geometry and the correlation between deformation and diffraction pattern. A 3D plane-random percolating geometry closer to the real microstructure is needed in future work to better understand the processes at play. This could be generated numerically using a random sequential adsorption algorithm or experimentally, for example by a TEM sectioning

method or xerography via synchrotron radiation source from real samples. Whiskers with non-circular cross section might be used to avoid the critical problem of element discretization based on the conclusion in this work that the contact contribution is insignificant for a percolating network in terms of energy. Based on the 3D plane-random percolating geometry, direct study of the effects of percolating, aspect ratio and experimental conditions on the anelastic behaviour could be carried out.

REFERENCES

A. Abuhasan, C. Balasingh, and P. K. Predecki, *J. Amer. Cer. Soc.*, **73** (8) 2474-84 (1990).

A. R. De Arellano-Lopez, F. L. Cumbrera, A. Dominguez-Rodriguez, K. C. Goretta and J. L. Routbort, *J. Am. Ceram. Soc.*, **73** [5] 1297-300 (1990).

A.R.De Arellano-Lopez, A. Dominguez-Rodriguez, K. C. Goretta, and J. L. Routbort, *J. Am. Ceram. Soc.*, **76** [6] 1425-32 (1993).

A.R.De Arellano-Lopez, A. Dominguez-Rodriguez, and J. L. Routbort, *Acta mater.*, **46** [18] 6361-73 (1998).

A. R. De Arellano-Lopez, J. J. Melendez-Martinez, A. Dominguez-Rodriguez, J. L. Roubort, H. T. Lin and P. F. Becher, *J. Am. Ceram. Soc.*, **84** [7] 1645-47 (2001).

R. M. Arons, J. K. Tien, *J. of Mat. Sci.*, **15,** 2046-58 (1980).

M.F.Ashby and R.A. Verrall, *Acta Metallurgica*, **21**, 149-63 (1973).

P. F. Becher, P. Angelini, W. H. Warwick, and T. N. Tiegs, *J. Am. Ceram. Soc.*, **73**[1] 91-6 (1990).

P. F. Becher, C. H. Hsueh, P. Angelini and T. N. Tiegs, *J. Am. Ceram. Soc.*, **71**[12] 1050-61(1988).

P. F. Becher and G. C. Wei, *J. Am. Ceram. Soc.*, **67** [12] C-267-C-269(1984).

J. Beddoes, W. Wallace, and L. Zhao, *Inter. Mater. Reviews*, **40** [5] 197-217 (1995).

W. Beere and I. G. Grossland, *Acta Metall.*, **30**, 91–9 (1987).

C. B. Blanchard, H. T. Lin and P. F. Becher, *J. Am. Ceram. Soc.*, **81** [6] 1429-36 (1998).

C. R. Blanchard, and R. A. Page, *J. Mater. Sci.*, **33,** 5037-47 (1998).

H. J. Böhm, " A Short Introduction to Basic Aspects of Continuum Micromechanics," CDL-FMD-Report 3, Vienna University of Technology, Vienna (Australia), 1998.

H.J. Böhm, *Adv. Eng. Mat.*, **6** [8] 626-33 (2004).

H.J. BÖhm, A. Eckschlager, W. Han, *Comput. Mater. Sci.*, 25 (2002) 42-53

J.T. Boyle, J. Spence, *Stress Analysis for Creep*, Butterworths, London (1983).

W.R. Cannon, T. G. Langdon, *J. Mater. Sci.*, **18,** 1-50 (1983).

R.M. Cannon, W.H. Rhodes, A.H. Heuer, *J. Am. Ceram. Soc.*, **63** [1-2] 46-53 (1980).

N. Chawla, K.K. Chawla, *J. Mater. Sci.*, **41,** 913-25 (2006).

Yet-Ming Chiang, D. Birnie III, and W. D. Kingery, *Physical Ceramics: Principles for Ceramics Science and Engineering*, pp. 245-51, John Wiley & Sons, Inc., New York, 1997.

A.H. Chokshi, J.R. Porter, *J. Am. Ceram. Soc.*, **68** [6] C-144-C-145 (1985).

R. L. Coble, *J. Appl. Phys.*, **34,** 1679-1682 (1963).

R.L. Coble, R. M. Cannon, "Current Paradigms in Powder Processing", pp151-70 in *Processing of Crystalline Ceramics*, *Mat. Sci. Res.* Vol. 11, H. Palmour III, R. F. Davis, and T. M. Hare, Eds., Plenum Press, New York, (1978)

Committee on Integrated Computational Materials Engineering, National Research Council, *Integrated Computational Materials Engineering: A Transformational Discipline for Improved Competitiveness and National Security*, The National Academy Press, Washington, D.C., 2008.

R. D. Cook, *Finite Element Modeling for Stress Analysis*, New York: John Wiley & Sons, Inc., 1995.

R. Courant, *Bull. Amer. Math. Soc.*, **49**, 1-23, (1943).

H.L. Cox, *J. Appl. Phys.*, **3,** 72-9 (1951).

Z. Y. Deng, J. L. Shi, Y. F. Zhang, T. R. Lai, and J. K. Guo, *J. Am. Ceram. Soc.*, **82** [4] 944-52 (1999).

T. L. Dragone and W. D. Nix, *Acta metal. Mater.*, **40** [10] 2781-91 (1992).

D. Duschlbauer, H. J. BÖhm and H. E. Pettermann, *J. Compos. Mater.*, **40** [24] 2217-34 (2006)

D. Eberly, ''Intersection of Cylinders''; http://www.geometrictools.com, 2008.

J. D. Eshelby, *Proc. Roy. Soc.*, **241**, 376-96, (1957)

H.E. Evans, B. Wilshire, *Creep of Metals and Alloys*, Inst. Metals, 1985

V. Favier, R. Dendievel, G. Canova, J. Y. Cavalle, and P. Gilormini, *Acta Mater.*, **45** [4]1557–65 (1997).

W. Flügge, *Viscoelasticity*, 1967, Blaisdell Publishing Co..

H. J. Frost, M. F. Ashby, *Deformation-Mechanism Maps, The Plasticity and Creep of Metals and Ceramics*, Oxford; Pergamon Press, New York,1982.

J. C. Gibeling and W. D. Nix, *Acta Metall.*, 29, 1796–84 (1981).

R.C. Gifkins, *Metall. Trans.*, **7A**, 1225-32 (1976).

R.C. Gifkins, *J. Mater. Sci.*, **13**, 1926-36 (1978).

Y. Goldberg, M. Levinshtein and S. Rumyantsev, "Silicon Carbide (SiC), Chapter 5," in *Properties of Advanced Semiconductor Materials: GaN, AlN, InN, BN, SiC, SiGe*, Editors, M. E. Levinshtein, S. L. Rumyantsev, M. S. Shur, John Wiley & Sons, Inc., New York, 2001.

R.S.Gordon, *J. Am. Ceram. Soc.*, **56** [3] 147-152 (1973).

D. M. Grannan, J. C. Garland, and D. B. Tanner, *Phys. Rev. lett.*, **46**, 375-8 (1981).

W. Z. Gu, J. R. Porter, and T. G. Langdon, *J. Am. Ceram. Soc.*, **77** [6] 1679-81 (1994).

W. Z. Gu, J. R. Porter, and T. G. Langdon, *Ceram. Eng. Sci. Proc.*, **16**[1] 242-52 (1995).

Z. Hashin and S. Shtrikman, *J. Mech. Phys. Solids*, **10**, 335-43 (1962).

Z. Hashin, *J. appl. Mech.*, **29**, 143-50 (1962).

J. Henderson and J. D. Sneddon, *Appl. Mater. Res.*, **4**, 148-67 (1965).

J. Henderson and J. D. Sneddon, *J. Mech. Eng. Sci.*, **10**, 24–35 (1968).

C. Herring, *J. Appl. Phys.*, **21,** 437-45 (1950).

A.H. Heuer, N.J. Tighe, R.M. Cannon, *J. Am. Ceram. Soc.*, **63** [1-2], 53-8 (1980).

R. Hill, *J. Mech. Phys. Solids*, **13**, 189-98 (1965).

R. Hill, *J. Mech. Phys. Solids*, **13**, 213-22 (1965).

J. W. Holmes, Y. H. Park and J. W. Jones, *J. Am. Ceram. Soc.*, **76** [5] 1281-93 (1993).

E. D. H. Hübner (Ed.), *Alumina Processing, Properties, and Applications*; pp. 1-317, Springer-Verlag, New York, 1984.

D. Hull and T. W. Clyne, *An Introduction to Composite Materials*, Cambridge University Press, Cambridge, UK, 1996.

K. L. Johnson, *Contact Mechanics*, Cambridge University Press, Cambridge, UK, 1985.

S. Kari, H. Berger, U. Gabbert, *Comput. Mater. Sci.*, **39,** 198–204 (2007).

A. Kelly and K. N. Street, *Proc. R. Soc. Lond.*, A.328, 283-93 (1972)

Kingery, W. D., Bowen, H.K. and Uhlmann, D.R., *Introduction to Ceramics*, John Wiley & Sons Inc., New York, 1976.

H. P. Klug, L. E. Alexander, *X-Ray Diffraction Procedures – For Polycrystalline and Amorphous Materials*, Second Edition, John Wiley&Sons, Inc., New York, 1974.

F. A. Kröger, "Experimental and Calculated Values of Defect Parameters and the Defect Structure of α-Al_2O_3," pp.100–18 in *Advances in Ceramics*, Vol.10, *Structure and Properties of MgO and Al_2O_3 Ceramics*, American Ceramic Society, Columbus, OH, 1984.

L. D. Landau, E. M. Lifshitz, *Theory of elasticity*, 3rd English ed., Pergamon Press, Oxford; New York:, 1986.

F. F. Lange, D. R. Clarke, B. I. Davis, *J. Mater. Sci.*, **15,** 611-5 (1980).

J. Lee and I. B. Cutler, *Am. Ceram. Soc. Bull.*, **54** [2] 195-8 (1975).

I. Levin, D. Brandon, *J. Am. Ceram. Soc.*, **81** [8] 1995-2012 (1998).

I.M. Lifshitz, *Soviet Physics JETP*, **17**, 909-20 (1963).

H. T. Lin, P. F. Becher, *J. Am. Ceram. Soc.*, **73** [5] 1378-81 (1990).

H. T. Lin, P. F. Becher, *J. Am. Ceram. Soc.*, **74** [8] 1886-93 (1991).

H. T. Lin, Kathleen B. Alexander, P. F. Becher, *J. Am. Ceram. Soc.*, **79** [6] 1530-6 (1996).

P. Lipetzky, S. R. Nutt and P. F. Becher, *Mat. Res. Soc. Symp. Proc.* **120**, 271-7 (1988).

G. J. Lloyd and R. J. McElroy, *Acta Metall.*, **22,** 339–48 (1974).

P. Lipetzky, S.R. Nutt, D. A. Koester, R. F. Davis, *J. Am. Ceram. Soc.*, **74** [6] 1240-7 (1991).

S. Majumdar, D. Kupperman, J. Sing, *J. Am. Ceram. Soc.*, 71 [10] 858-63 (1988)

S. Majumdar, D. Kupperman, *J. Am. Ceram. Soc.*, 72 [2] 312-3 (1989).

J. T. Marti, *Introduction to Sobolev Spaces and Finite Element Solution of Elliptic Boundary Value Problems*, New York: Academic Press, 1986.

D. McLean, *J. Mater. Sci.*, **7**, 98-104 (1972)

C. O'Meara, T. Suihkonen, T. Hansson, R. Warren, *Mater. Sci. and Eng.*, **A209,** 251-9 (1996).

M.L. Mehan, L.S. Schadler, *Composites Science and Technology*, **60,** 1013-26 (2000).

M. J. Mills, J. C. Gibeling and W. D. Nix, *Acta Metall.*, **34** [5] 915-25 (1986).

Y. Mishin, M. Asta and J. Li, *Acta Mater.*, **58** [4] 1117-51 (2010)

T. Mura, *Micromechanics of Defects in Solids*, 2nd Ed., pp.378, Martinis Nijhoff, The Netherland, 1987.

R.G. Munro, *J. Am. Ceram. Soc.*, **80** [8] 1919-28 (1997).

F.R.N. Nabarro, "Deformation of Crystals by the Motion of Single Ions," *Report of a Conference on Strength of Solids*, (London, England: The Physical Society, 1948), 75-90.

C.-W. Nan, *Prog. Mater. Sci.*, **37**, 1-116 (1993).

S. R. Nutt, *J. Am. Ceram. Soc.*, **67** [6] 428-31(1984).

S. R. Nutt, P. Lipetzky, P. F. Becher, *Mater. Sci. and Eng.*, **A126,** 165-172 (1990).

S. R. Nutt, P. Lipetzky, *Mater. Sci. Eng.*, **A166**, 199-209 (1993).

C. H. Park, Byoung-Ho Cheong, Keun-Ho Lee and K. J. Chang, *Physical Review B*, **49** [7] 4485-9 (1994)'

M. Pahutova, J. Cadek, and P. Rys, *Mater. Sci. Eng.*, **39**, 169–74 (1979).

V. K. Pecharsky, P. Y. Zavalij, *Fundamentals of Powder Diffraction and Structural Characterization of Materials*, Boston: Kluwer Academic Publishers, 2003.

J.J. Petrovic, J.V. Milewski, D. L. Rohr, F.D. Gac, *J. Mat. Sci.*, **20,** 1167-77 (1985).

J. P. Poirer, *Creep of Crystals: High-Temperature Deformation Processes in Metals, Ceramics and Minerals*, Cambridge University Press, Cambridge, UK, 1985.

J. R. Porter, *Mater. Sci. Eng.*, **A107** [1-2] 127-32 (1989).

P. K. Predecki, A. Abuhasan, and C.S. Barrett, "Residual Stress Determination in Al_2O_3 / SiC (Whisker) Composites by X-Ray Diffraction," pp. 231-43 in *Advances in X-Ray Analysis*, Vol. 31. Edited by C.S. Barrett, J.V. Gilfrich, R. Jenkins, J.C. Russ, J.W. Richardson, Jr., and P.K. Predecki. Plenum Press, New York, 1988.

N. Provatas and K. Elder, *PhaseField Methods in Materials Science and Engineering*, Wiley VCH, Germany, 2009.

G.-C. Quan, ‘‘Tensile Creep of SiC Whisker-Reinforced Alumina Composites’’; Ph.D. Thesis, McMaster University, 2004.

R. Raj, M. F. Ashby, *Metall. Trans.*, **2**, 1113-7 (1971).

L. S. Ramsdell, *Am. Mineral.*, **32**, 64 (1947).

J. C. Romero, R.J. Arsenault, R.F.Krause, *Mater. Sci. Eng.*, **A201**, 13-23 (1995).

R. P. Simon and S. B. Sinnott, *Science*, **325**, 1634-5 (2009).

M. Es-Souni, *Mater. Character.*, 45, 153–64 (2000).

A. R. Stokes, *Proc. Phys. Soc.* (London), **A61**, 382-91 (1948).

D. Stolle, *An Introduction to the Finite Element Method*, Custom Courseware, McMaster University, 2005.

A. H. Swan, M.V. Swain and G. L. Dunlop, *J. of Europ. Ceram. Soc.*, **10,** 317-26 (1992).

M. Taya and R. J. Arsenault, *Metal Matrix Composites: Thermomechanical Behavior*, Pergamon Press, Oxford, 1989.

T. N. Tiegs and P.F. Becher, *J. Am. Ceram. Soc.*, **70**[5] C-109-C-111(1987).

S. P. Timoshenko, J. N. Goodier, *Theory of Elasticity, Third Edition*, New York: McGraw-Hill; 1970.

R. I. Todd, B. Derby, in E. V. Barrera and I. Dutta (eds.), *Residual Stresses in Composites*, TMS, 147-60, (1993).

W. Voight, *Wied. Ann.*, **38**, 573-87 (1889)

C. M. Wang, J. N. Reddy, K. H. Lee, *Shear Deformable Beams and Plates: Relationship with Classical Solutions*, Elsevier Science, Oxford, UK, 2000.

B.E. Warren, *X-RAY Diffraction*, Dover Publications, Inc., New York, 1990.

C. M. Weisbrook, V. S. Gopalaratnam, A. D. Krawitz, *Mater. Sci. Eng.* A201, 134-42 (1995).

C. M. Weisbrook, *Analysis of Thermal Residual Stress in Tungsten Caribide-Nickel Composites using Neutron Diffraction and Finite Element Methods*. Ph.D. Thesis, University of Missouri-Columbia, Columbia, MO, 1995.

K. Wefers and C. Misra, "Oxides and Hydroxides or Aluminum," Alcoa Technical Paper No. 19, Alcoa Laboratories, Pittsburgh, PA, 1987.

D.S. Wilkinson, *J. Am. Ceram. Soc.*, 81 [2] 275-99 (1998)

D.S. Wilkinson and W .Pompe, *Acta Mater.*, **46** [4] 1357-69 (1998).

A. J. C. Wilson, *Proc. Phys. Soc.*, **81**, 41-6 (1963).

M. Wilson, M. Exner, Y.-M. Huang, and M. Finnis, *Phys. Rev. B: Condens. Matter*, **54** [22] 15683-9 (1996).

E. W. Wong, P. E. Sheehan, C. M. Lieber, *Science*, **277** [26] 1971-5 (1997).

D. A. Woodford, *J. Am. Ceram. Soc.*, **81** [9] 2327-32 (1998).

R. W. G. Wyckoff, *Crystal Structure*, Vol. **I,** 2nd ed.: *pp*.**111,** Interscience, New York**,** 1963.

W. C. Young, *Roark's Formulas for Stress and Strain*, McGraw-Hill Book Company, New York, 1989.

R. Zallen, *The Physics of Amorphous Solids*, John Wiley & Sons Inc., New York, 1983.

D. G. Zill and M. R. Cullen, *Advanced Engineering Mathematics, 2nd edition*, Jones and Bartlett Publishers Inc., Sudbury, MA, 2000.

Appendix A

The Analytical Model for 2D Percolating Geometry

This appendix illustrate the the analytical model used in chapter 5. It is based on the Wilkinson and Pompe model (1998) for the creep and anelastic recovery of whisker- and platelet- reinforced ceramics. In the 2D unit cell, as shown in Figure 5.8, whiskers are described as beams with rectangular cross section embedded in a creeping matrix. The Euler equation for the beam deformation is given as below

$$-E_w I \frac{\partial^4 u}{\partial x^4} = P + F\delta(x) \tag{A.1}$$

where ***P*** is the distributed load(force per unit length), $\delta(x)$ is the Dirac delta function, *F* is the point load, ***u*** is the displacement along the ***y*** direction and other parameters have the same meanings as in section 5.2.3. ***P*** is proportional to the stress exerted on the beam surface by the surrounding matrix and to ***W***, the depth along the ***z*** direction, the former of which could be related to the creep strain rate through the creep constitutive law as $\sigma = \frac{\dot{\varepsilon}}{C}$. The strain rate $\dot{\varepsilon}$ is equal to the displacement rate $\dot{u}$ divided by half of the unit cell height ***H*** since there are two three-point bending in one unit cell along the ***y*** direction. Furthermore, a factor of 2 is included accounting for the effects from two surfaces, top and bottom, due to the perfect interface bonding. Finally, for the 2D unit cell with length ***L*** (***ob***), Height ***H*** (***bc***) and depth ***W***, the governing equation for a bent whisker embedded in a creeping matrix is given

$$-E_w I \frac{\partial^4 u}{\partial x^4} = 2\frac{1}{C}\frac{W}{(H/2)}\dot{u}(x,t) + F\delta(x) \tag{A.2}$$

Calculation for characteristic relaxation time

Let $\boldsymbol{A}=\boldsymbol{E_w I}$, $\boldsymbol{B}=-2\frac{1}{C}\frac{W}{(H/2)}$ and rewrite equation (A.2) as

$$A\frac{\partial^4 u}{\partial x^4} = B\dot{u}(x,t) \tag{A.3}$$

Using the method of separation of variables, assuming,

$$\dot{u}(x,t) = u(x)u(t) \tag{A.4}$$

The boundary conditions for a symmetric bending beam simply supported for any time are given by

$$\left.\begin{aligned} &\frac{\partial u}{\partial x} = 0 && \text{at } \boldsymbol{x=0} \\ &u(x) = 0 && \text{at } \boldsymbol{x=\pm d} \end{aligned}\right\} \tag{A.5}$$

Substitute (A.4) into (A.3),

$$\frac{1}{u(x)}\frac{\partial^4 u(x)}{\partial x^4} = \frac{B}{A}\frac{1}{u(t)}\frac{\partial u(t)}{\partial t} == K_1 \tag{A.6}$$

where K_1 is the eigenvalue for the differential equation which is a series of constants. Solve the temporal part

$$\frac{\partial u(t)}{u(t)} = \frac{A}{B}K_1 \partial t \tag{A.7}$$

which has the standard solution of (Zill, *et al.*, 2000) [43]

$$u(t) = K_2 \exp(\frac{A}{B} K_1 t) \tag{A.8}$$

$$\text{with } \tau = -\frac{B}{AK_1} \tag{A.9}$$

The value of K_1 is needed to calculate τ, which can be determined via solving the spatial part

$$\frac{\partial^4 u(x)}{\partial x^4} = K_1 u(x) \tag{A.10}$$

The general solution for equation (A.10) is the form (Zill *et al.*, 2000)

$$u(x) = D_1 e^{\sqrt[4]{K_1}} + D_2 e^{\sqrt[4]{K_1}} + D_3 \cos\sqrt[4]{K_1} + D_4 \sin\sqrt[4]{K_1} \tag{A.11}$$

Place the boundary conditions (A.5) into (A.11), we get $D_1 = D_2 = D_4 = 0$, and the smallest value of K_1 is (which corresponding to the maximum relaxation time)

$$K_1 = \left(\frac{\pi}{2d}\right)^4 \tag{A.12}$$

Substitute (A.12) into (A.9), the characteristic relaxation time is given by

$$\tau_M = \frac{48(2d)^4}{E_w C \pi^4 (2r)^3 H} = \frac{12}{\pi^4} \frac{\lambda^4}{E_w C} \tag{A.13}$$

Calculation for maximum recovered strain

The maximum recovered strain is obtained by integrating the equation (A.1) directly when the load is fully carried by the beams:

$$\left.\begin{aligned} u_\infty(x) &= u_\infty^*\left[1-\frac{3}{2}\left(\frac{x}{d}\right)^2-\frac{1}{2}\left(\frac{x}{d}\right)^3\right] \qquad -d \le x \le 0 \\ u_\infty(x) &= u_\infty^*\left[1-\frac{3}{2}\left(\frac{x}{d}\right)^2+\frac{1}{2}\left(\frac{x}{d}\right)^3\right] \qquad 0 \le x \le d \end{aligned}\right\} \quad (A.14)$$

with $u_\infty^* = -\dfrac{F(2d)^3}{48E_wI}$ (A.14A)

which is the maximum displacement at ***x=0*** (middle of the beam). The maximum recovered strain is obtained via combining the load $F = \sigma WL$ and span $2d = \lambda \times 2r$ into (A.14A)

$$\varepsilon_M^* = \frac{u_\infty^*}{H/2} = \frac{L}{16r}\frac{\sigma\lambda^3}{E_w} \quad (A.15)$$

Appendix B

FEM Simulations for 2D Percolating Geometry with Plane Strain Conditions

Figure B-1 and Figure B-2 show the stress distribution of S_{11} and S_{22}, normal stress along the ***x*** and ***y*** direction respectively, at full loading of whisker network without any matrix based on plane strain conditions for aspect ratios of 5, 10 and 20. It is seen that the whiskers behave similarly to three-point loaded bending plates during deformation. One half of the plate is under tension and the other half is under compression. Maximum normal stress S_{11} occurs at the mid-span of the plate with positive and negative values corresponding to the tensile and compressive part respectively. Normal stress S_{22} is distributed near contact region with its maximum value located around the contact center, reflecting a contribution of the contact effect. Figure B-3 shows the von Mises equivalent stress distribution at full loading of the whisker network without a matrix based on plane strain conditions for aspect ratios of 5, 10 and 20. The maximum value of equivalent stress occurs beneath the contact surface where the shear stress is the largest during deformation. This is a typical stress distribution for a Hertzian contact problem with non-conforming contact surfaces (Johnson, 1985).

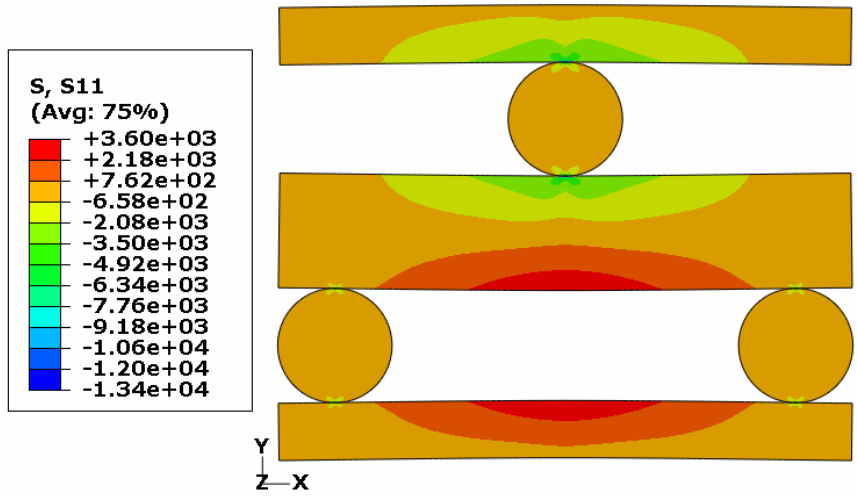

(a) λ= 5, Deformation scale factor 1, $\sigma_{applied}$ = -100MPa

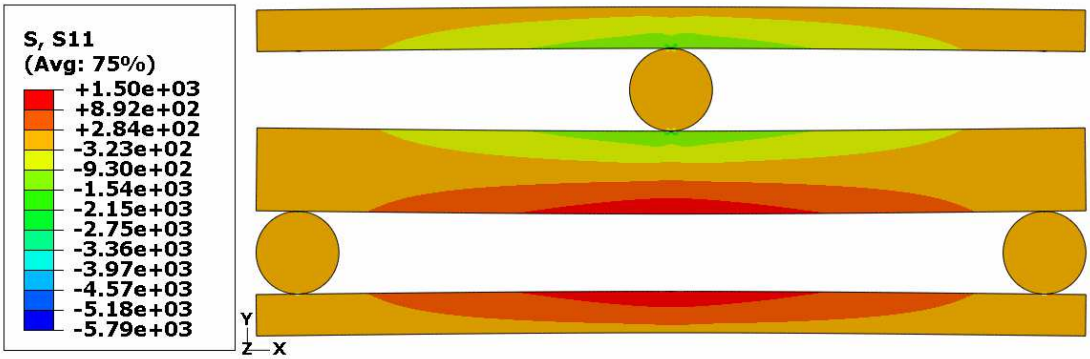

(b) λ= 10, Deformation scale factor 1, $\sigma_{applied}$ = -10MPa.

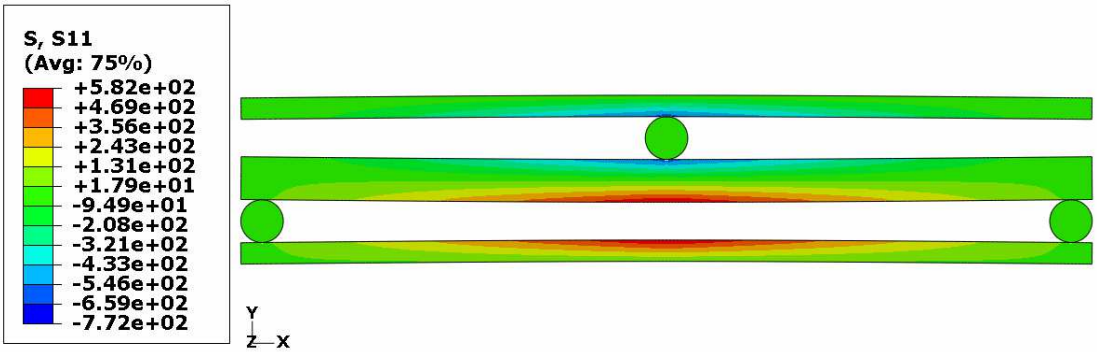

(c) λ= 20, Deformation scale factor 1, $\sigma_{applied}$ = -1MPa.

Figure B-1 S_{11} **distribution within whisker network without matrix for aspect ratio 5, 10 and 20 with plane strain condition.**

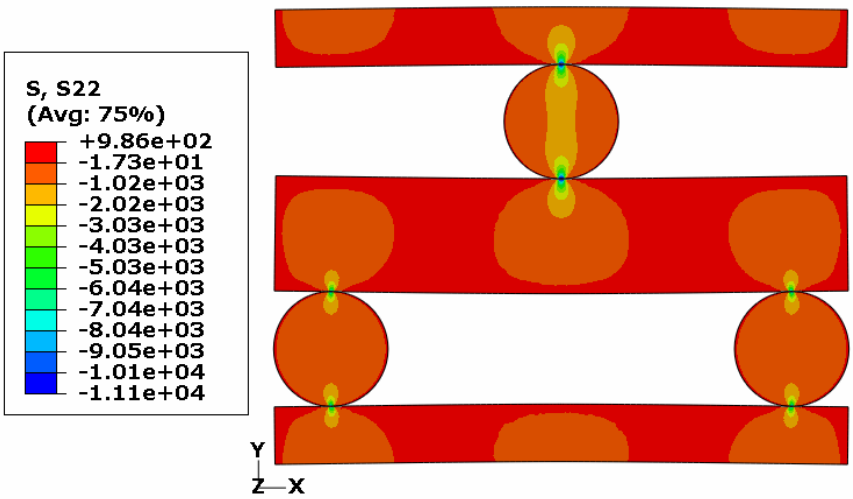

(a) λ= 5, Deformation scale factor 1, $\sigma_{applied}$ = -100MPa

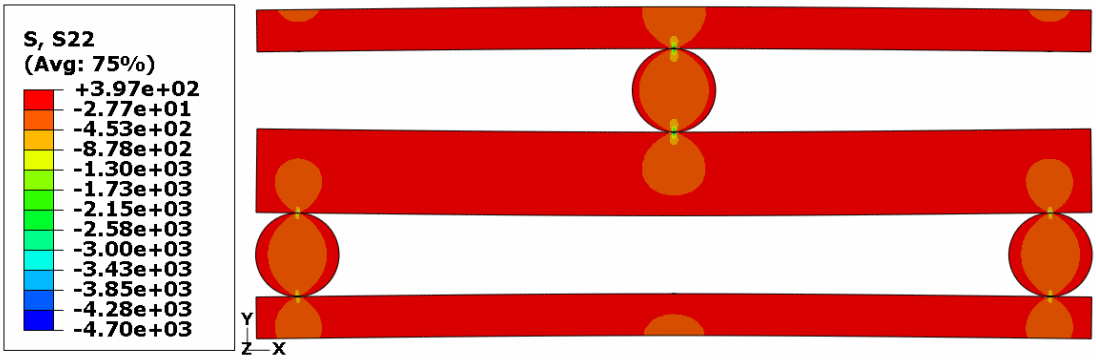

(b) λ= 10, Deformation scale factor 1, $\sigma_{applied}$ = -10MPa

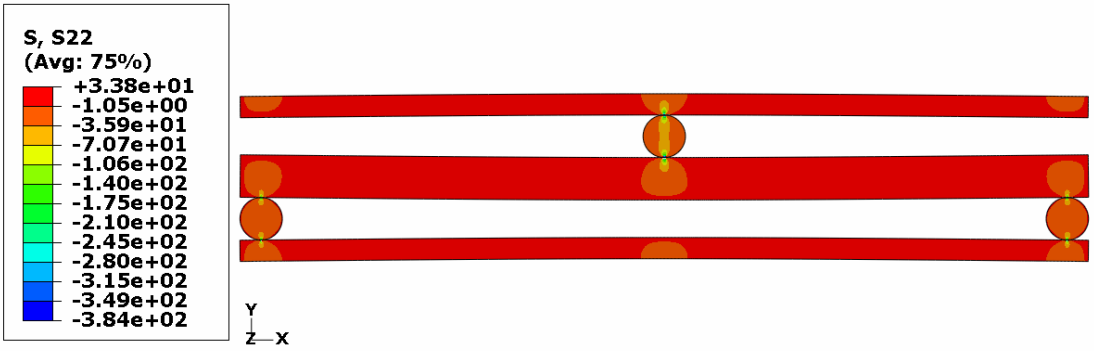

(c) λ= 20, Deformation scale factor 1, $\sigma_{applied}$ = -1MPa

Figure B-2 S_{22} **distribution within whisker network without matrix for aspect ratio 5, 10 and 20 with plane strain condition.**

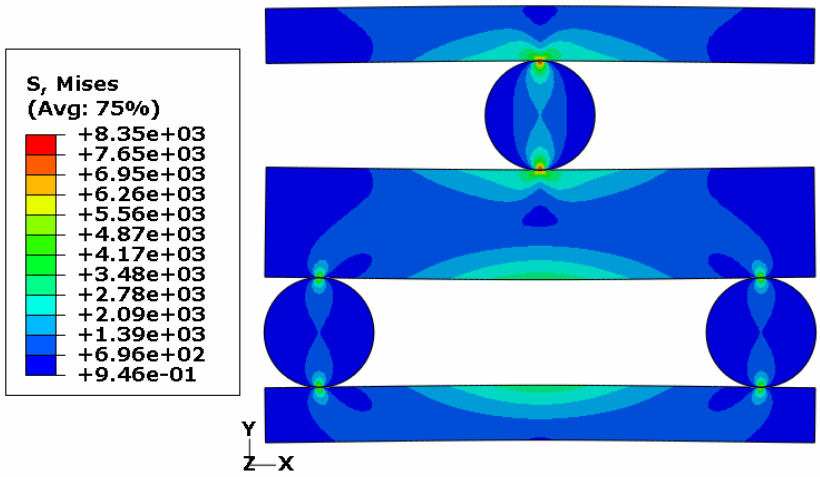

(a) λ= 5, Deformation scale factor 1, $\sigma_{applied}$ = -100MPa

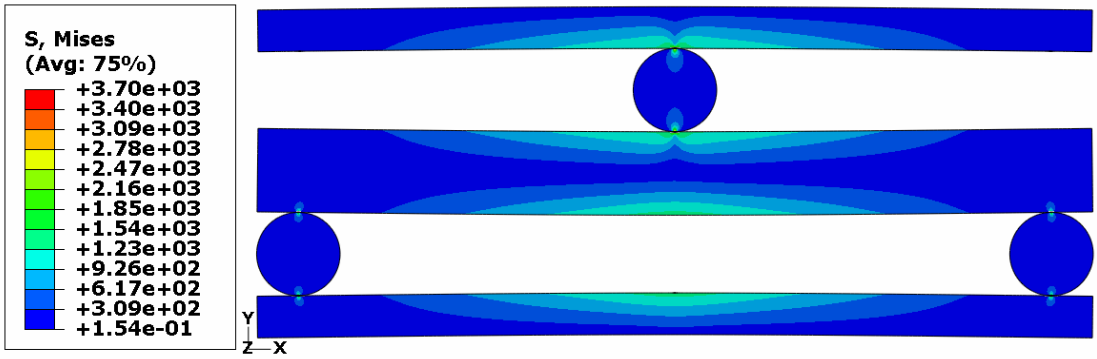

(b) λ= 10, Deformation scale factor 1, $\sigma_{applied}$ = -10MPa.

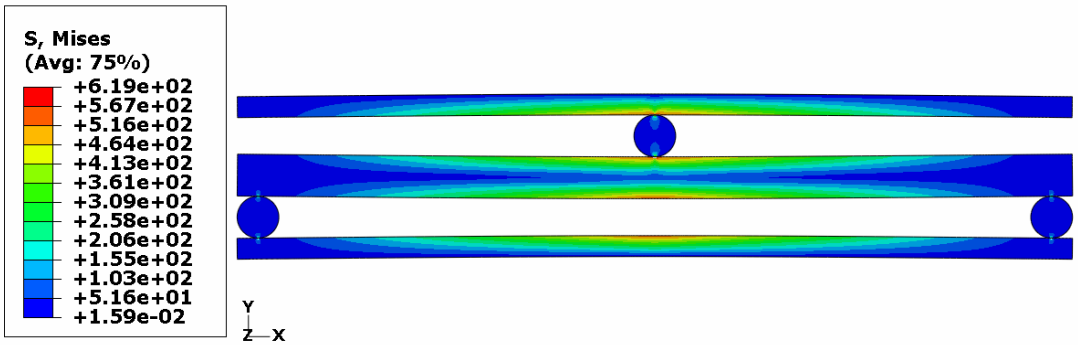

(c) λ= 20, Deformation scale factor 1, $\sigma_{applied}$ = -1MPa.

Figure B-3 Von Mises stress distribution within whisker network without matrix for aspect ratio 5, 10 and 20 with plane strain condition.

One thing important to mention is that the applied stresses specified in the Figures above are based on the 2D percolating unit cells with matrix present as shown in Figure 3.6, which should be increased by a factor of $\frac{L}{\lambda \times 2r}$ while applied here to the network without matrix (L is the length of unit cell with matrix in Figure 3.6 and $\lambda \times 2r$ is the length of unit cell without matrix here). Different stresses are applied to different aspect ratio in order to keep the strain within the order of 10^{-2}.

From simple plate theory (Cook and Young, 1985)

$$-D\frac{\partial^4 u}{\partial x^4} = q \qquad \text{(B-1)}$$

which share a close similarity with the equation (A-1). It is simple to obtain the strain for a 2D unit cell without a matrix based on the plane strain condition:

$$\varepsilon_M^* = \frac{L\sigma}{16r}\frac{\lambda^3}{E_w}(1-\nu^2) \qquad \text{(B-2)}$$

which is a version of equation A.15 obtained by increasing the E_w by $\frac{E_w}{(1-\nu^2)}$.

Table B-1 shows the maximum strain from FEM simulations and the analytical model prediction. It seems that the end effect is still significant since for aspect ratios of 10 and 20, data fitted with $\lambda - 1$ agree better with the FEM simulations. However, for aspect ratio of 5, it between the fitting with λ and $\lambda - 0.5$ suggesting that the situation is much more complicated due to the small aspect ratio.

Table B-1 FEM results and analytical model predictions (AM) for plane strain condition

Aspect ratio	FEM	AM		
		λ	$\lambda-0.5$	$\lambda-1$
5	1.24×10^{-2}	1.57×10^{-2}	1.14×10^{-2}	8.03×10^{-3}
10	1.77×10^{-2}	2.27×10^{-2}	1.94×10^{-2}	1.65×10^{-2}
20	2.98×10^{-2}	3.43×10^{-2}	3.18×10^{-2}	2.94×10^{-2}

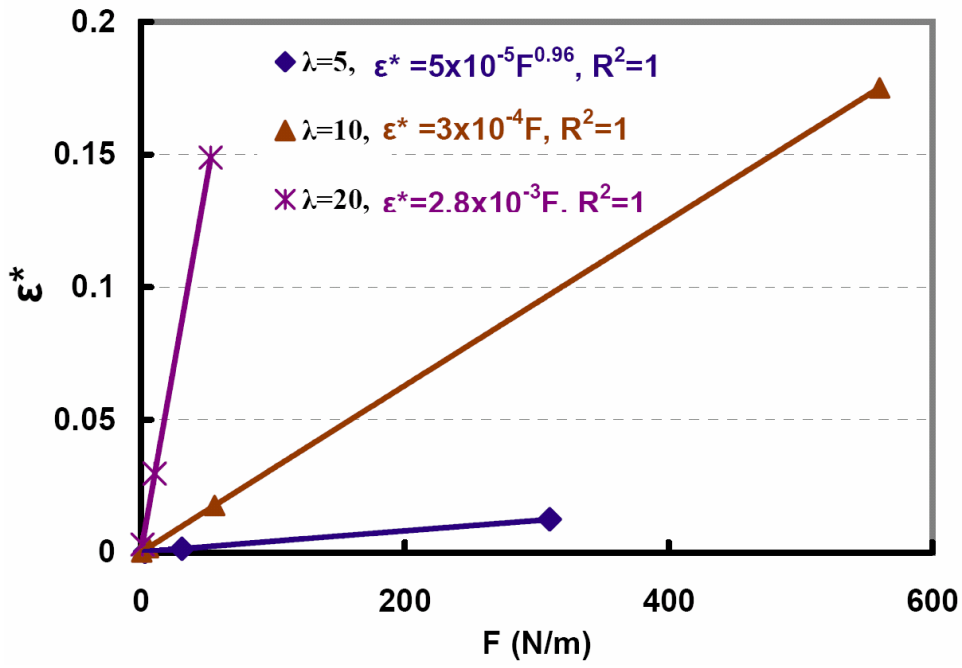

Figure B-4 Maximum strain versus load with the fitting equations, plane strain condition.

Figure B-4 shows the maximum strain versus load with the fitting equations from FEM simulations. It seems that the nonlinear load-deflection relationship is not significant except for aspect ratio of 5 which indicates that the plate theory is not applicable for short plate due to the effect of contact and shear deformation mentioned in section 5.4. All the data are

compared with the analytical model (equation B-2) in table B-2 while the data for aspect ratio of 10 and 20 are fitted using $\lambda - 1$, and λ is used for the aspect ratio of 5. Good agreement is obtained showing the validity of the analytical model for unit cells without a matrix based on the plane strain condition.

Table B-2 Maximum strain from FEM predictions (Figure B-4) and analytical model (AM) for 2D percolating whisker unit cells without matrix based on plane strain condition

Aspect ratio λ	FEM	AM
5	$\varepsilon^* = 5\times10^{-5}F^{0.96}$	$\varepsilon_M^* = 5.06\times10^{-5}F$
10	$\varepsilon^* = 3\times10^{-4}F$	$\varepsilon_M^* = 2.95\times10^{-4}F$
20	$\varepsilon^* = 2.8\times10^{-3}F$	$\varepsilon_M^* = 2.8\times10^{-3}F$

Appendix C

FEM Data for Chapter 6

This appendix summarizes supplemental figures of Chapter 6 for 2D percolating and 3D aligned unit cells with aspect ratios of 5, 7, 10, 15 and 20 which are deformed under stresses 60MPa, 75MPa and 100MPa with and without thermal stress.

(1) Figures C-1 to C-9 for section 6.2.3.1 (2D percolating unit cells)

Figures C-1, C-2 and C-3 show the creep strain versus time while Figures C-4 to C-9 show peak width and position versus creep strain for 2D percolating unit cells with varied aspect ratios under varied stresses. Larger stress yields the same value of creep strain in a quicker time for all aspect ratios. Although the unit cell with a bigger aspect ratio has a longer characteristic relaxation time τ (as demonstrated in chapter 5), it approaches the creep strain of 0.005 in a shorter time since it is more flexible (bigger maximum recoverable strain ε^*) provided the same condition. Peak width and position behave similarly for all aspect ratios: (1) *FWHM* increases with the creep strain; (2) peak position shifts to a lower value and saturates.

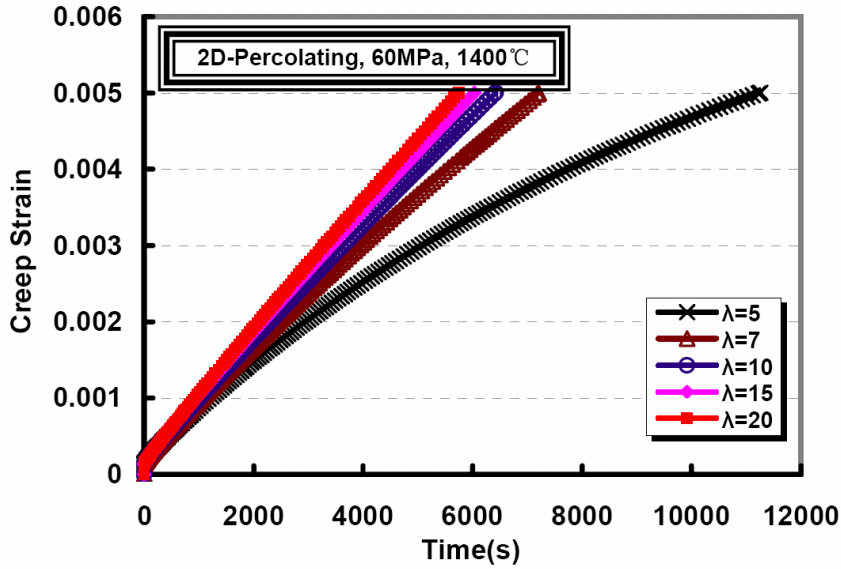

Figure C-1 Creep strain versus time for 2D percolating unit cells with λ=5, 7, 10, 15 and 20, T=1400℃, $\sigma_{applied}$ = -60MPa.

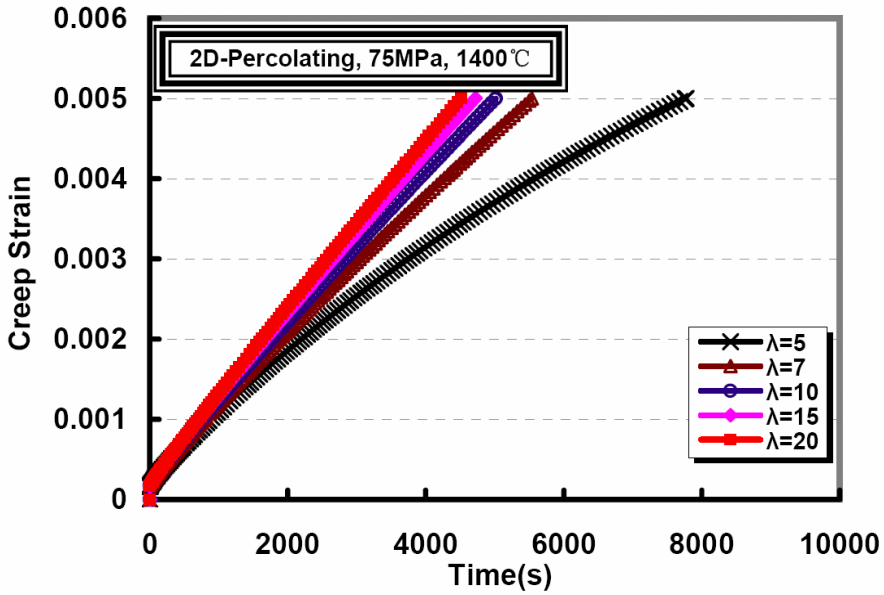

Figure C-2 Creep strain versus time for 2D percolating unit cells with λ=5, 7, 10, 15 and 20, T=1400℃, $\sigma_{applied}$ = -75MPa.

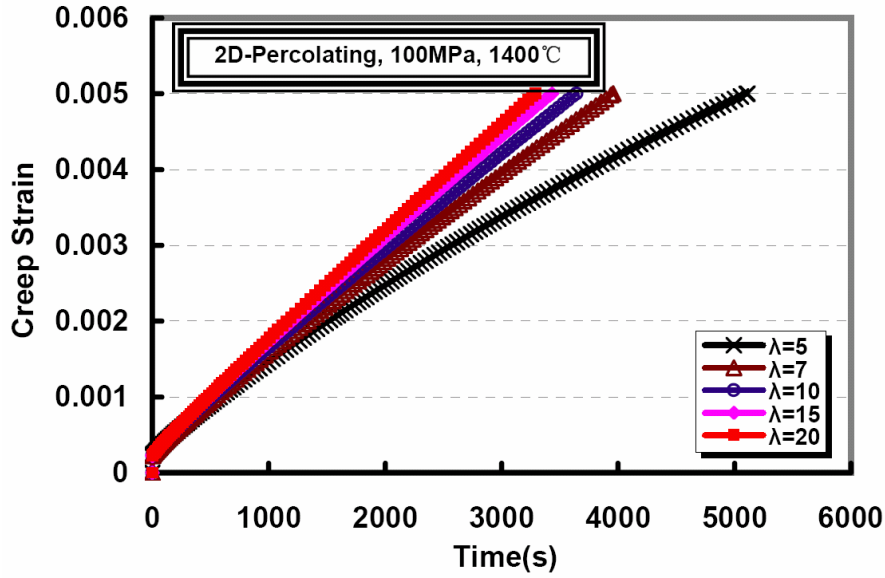

Figure C-3 Creep strain versus time for 2D percolating unit cells with λ=5, 7, 10, 15 and 20, T=1400℃, $\sigma_{applied}$ = -100MPa.

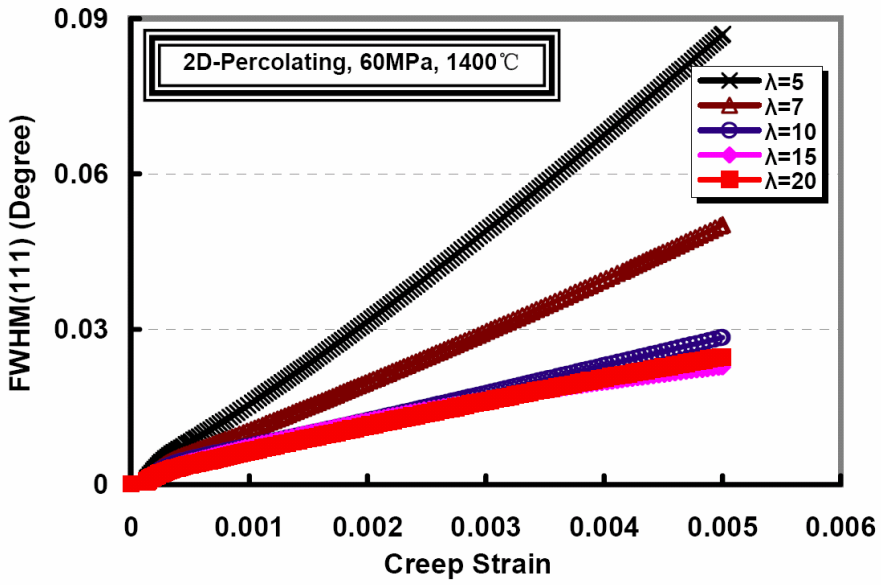

Figure C-4 ***FWHM*** **versus creep strain for 2D percolating unit cells with λ=5, 7, 10, 15 and 20, T=1400℃,** $\sigma_{applied}$ **= -60MPa.**

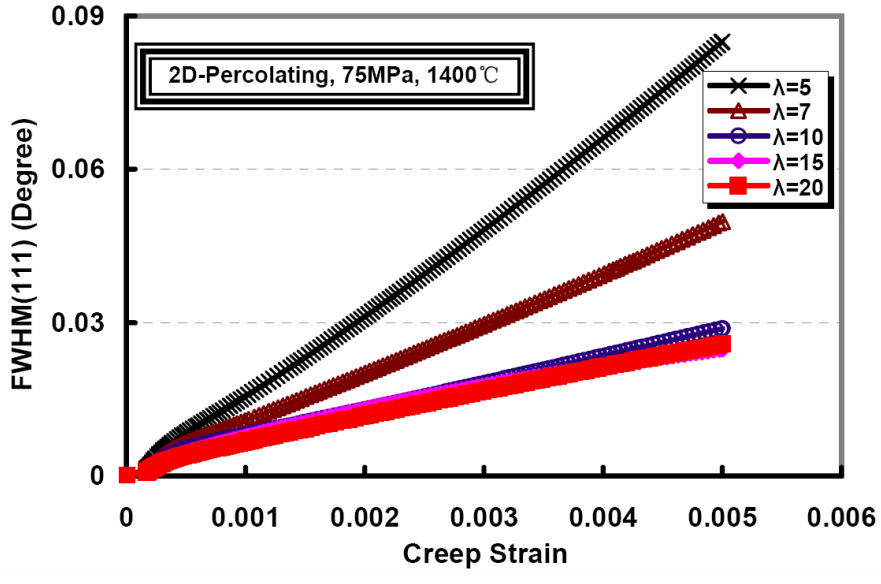

Figure C-5 ***FWHM*** **versus creep strain for 2D percolating unit cells with λ=5, 7, 10, 15 and 20, T=1400℃,** $\sigma_{applied}$ **= -75MPa.**

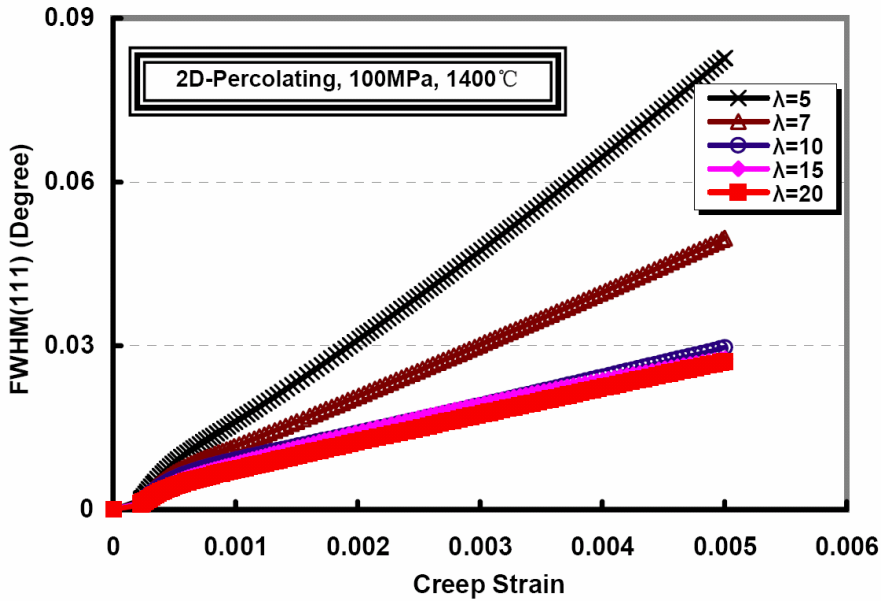

Figure C-6 ***FWHM*** **versus creep strain for 2D percolating unit cells with λ=5, 7, 10, 15 and 20, T=1400℃,** $\sigma_{applied}$ **= -100MPa.**

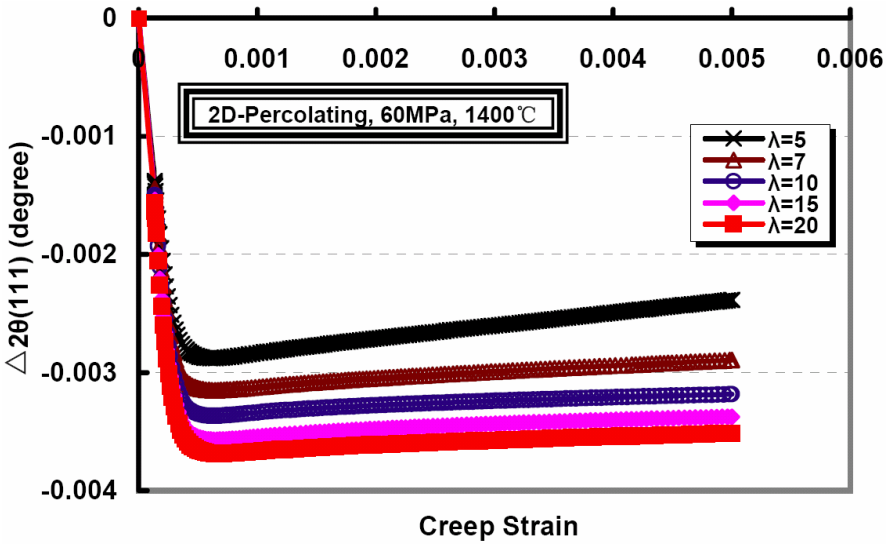

Figure C-7 Peak shift versus creep strain for 2D percolating unit cells with λ=5, 7, 10, 15 and 20, T=1400℃, $\sigma_{applied}$ **= -60MPa.**

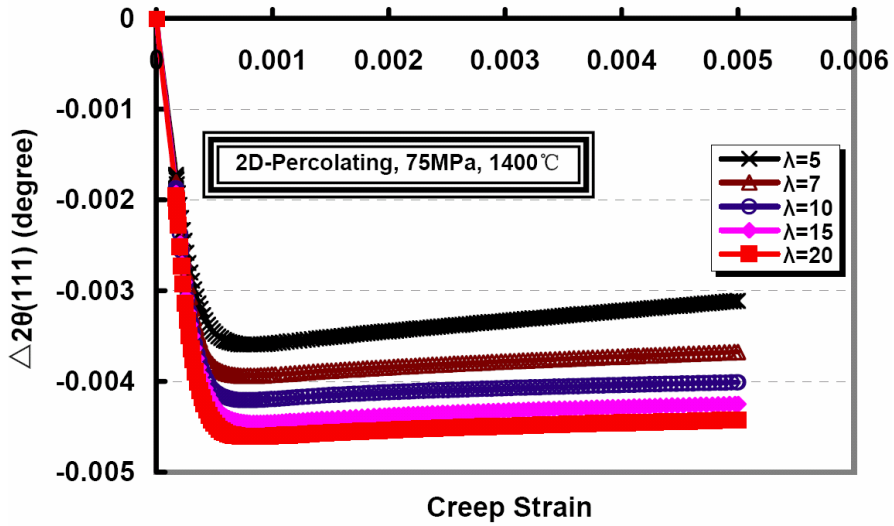

Figure C-8 Peak shift versus creep strain for 2D percolating unit cells with λ=5, 7, 10, 15 and 20, T=1400℃, $\sigma_{applied}$ = -75MPa.

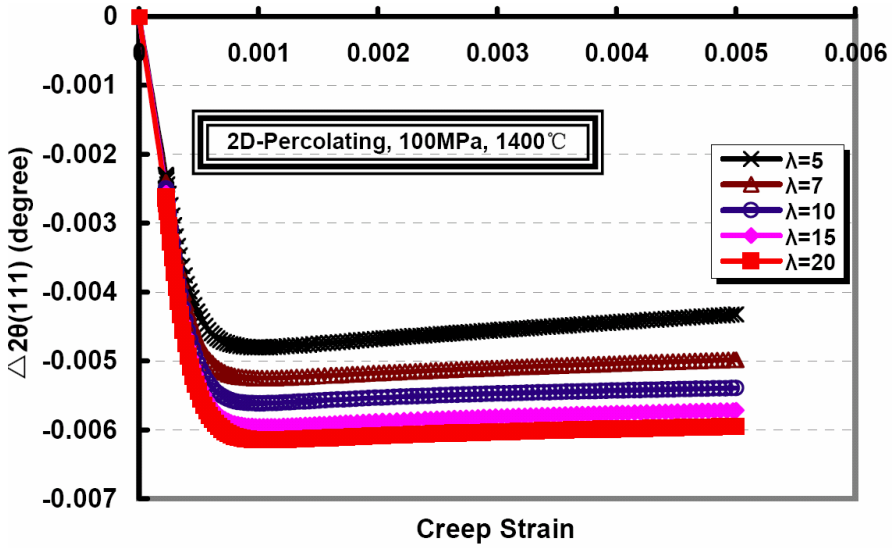

Figure C-9 Peak shift versus creep strain for 2D percolating unit cells with λ=5, 7, 10, 15 and 20, T=1400℃, $\sigma_{applied}$ = -100MPa.

(2) Figures C-10 to C-18 for section 6.2.3.2 (3D aligned unit cells)

Figures C-10, C-11 and C-12 show the creep strain versus time while Figures C-13 to C-18 show the peak width and position versus creep strain for 3D aligned unit cells with varied aspect ratios under varied stresses. Larger stress always yields the same value of creep strain in a quicker time for all aspect ratios. The unit cell with a larger aspect ratio has a more significant strain rate shifting and approaches the creep strain of 0.005 in a longer time if other conditions are fixed. This represents an increasing reinforcing effect of the larger aspect ratio and is consistent with the prediction based on the shear lag model (Cox, 1951 and Mclean, 1972). Peak width and peak-shift behave similarly for all aspect ratios under different external stresses: (1) *FWHM* increases with the creep strain and then saturates when the entire load is transferred to the whisker; (2) peak position shifts to a lower value and saturates when the entire load is transferred to the whisker.

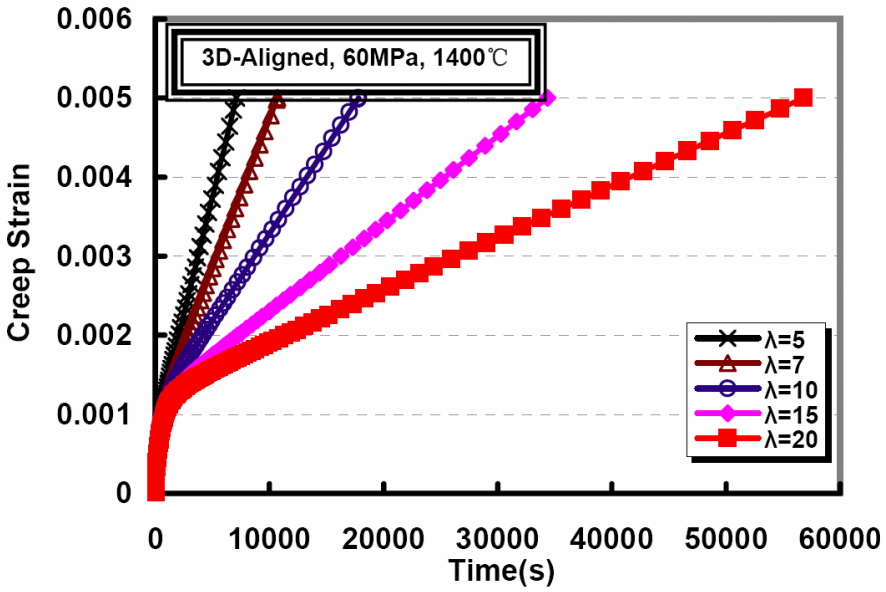

Figure C-10 Creep strain versus time for 3D aligned unit cells with λ=5, 7, 10, 15 and 20, T=1400℃, $\sigma_{applied}$ = 60MPa.

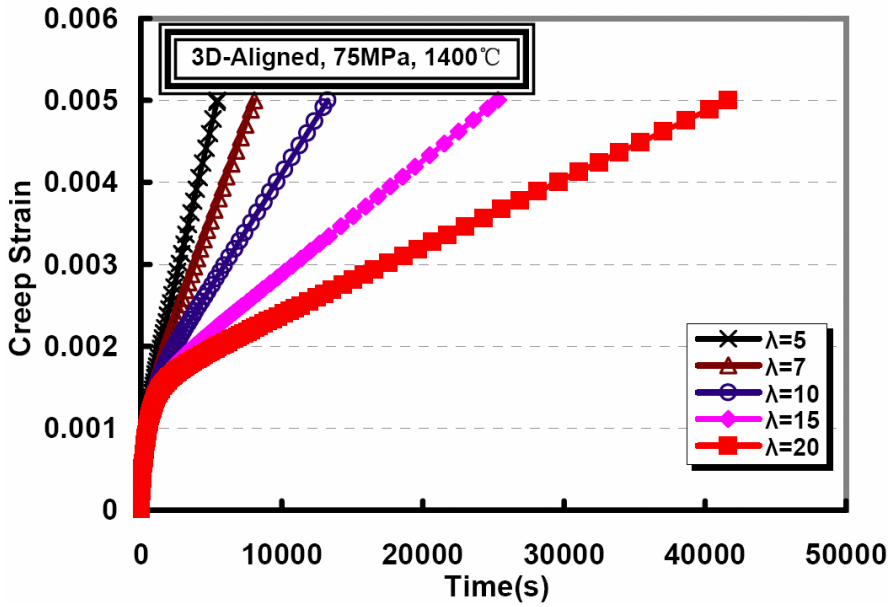

Figure C-11 Creep strain versus time for 3D aligned unit cells with λ=5, 7, 10, 15 and 20, T=1400℃, $\sigma_{applied}$ = 75MPa.

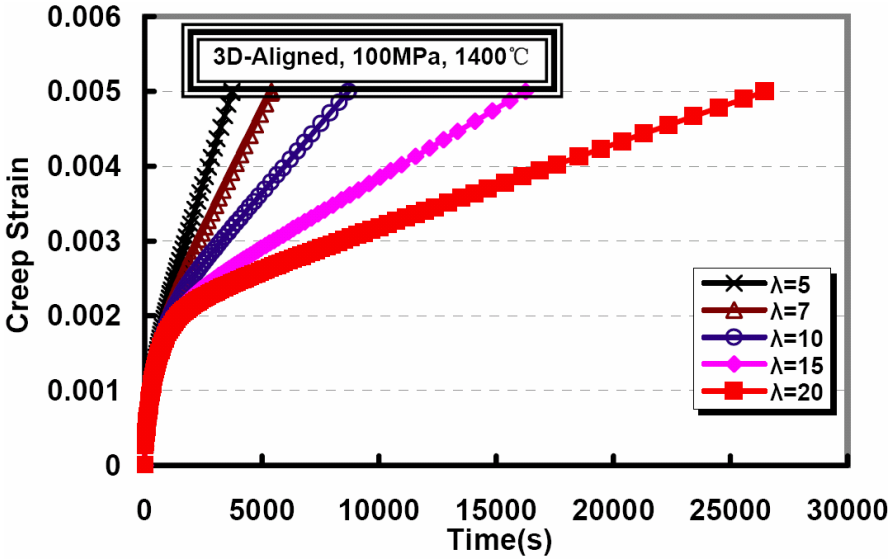

Figure C-12 Creep strain versus time for 3D aligned unit cells with λ=5, 7, 10, 15 and 20, T=1400℃, $\sigma_{applied}$ = 100MPa.

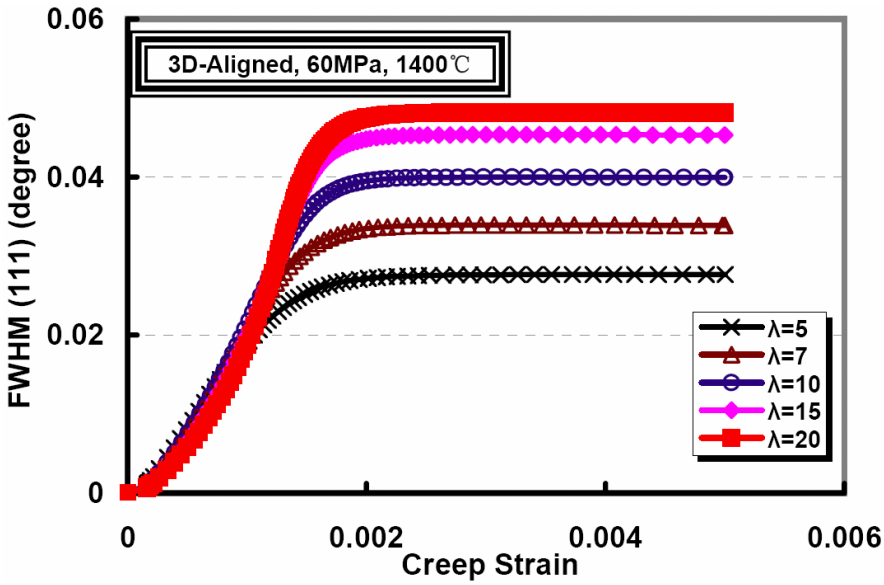

Figure C-13 ***FWHM*** **versus creep strain for 3D aligned unit cells with λ=5, 7, 10, 15 and 20, T=1400℃,** $\sigma_{applied}$ **= 60MPa.**

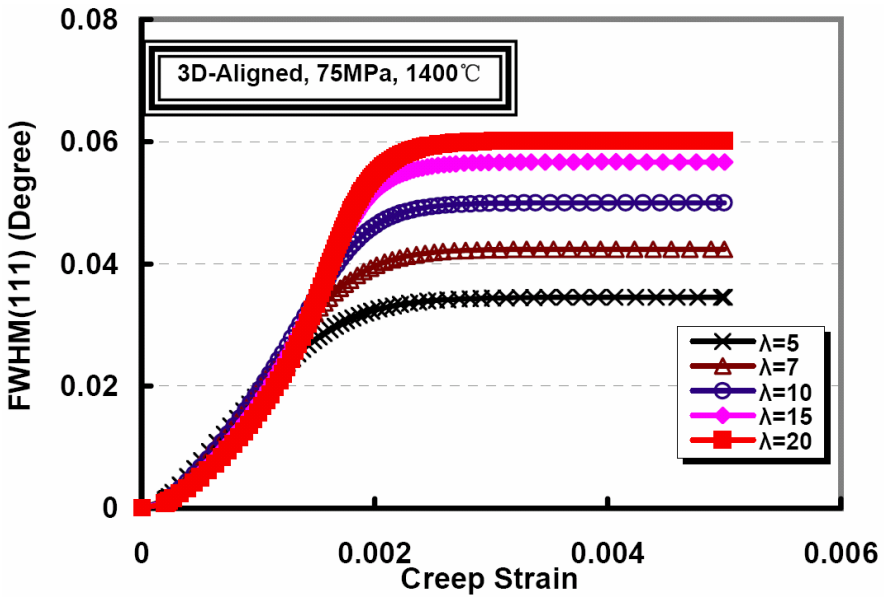

Figure C-14 ***FWHM*** **versus creep strain for 3D aligned unit cells with λ=5, 7, 10, 15 and 20, T=1400℃,** $\sigma_{applied}$ **= 75MPa.**

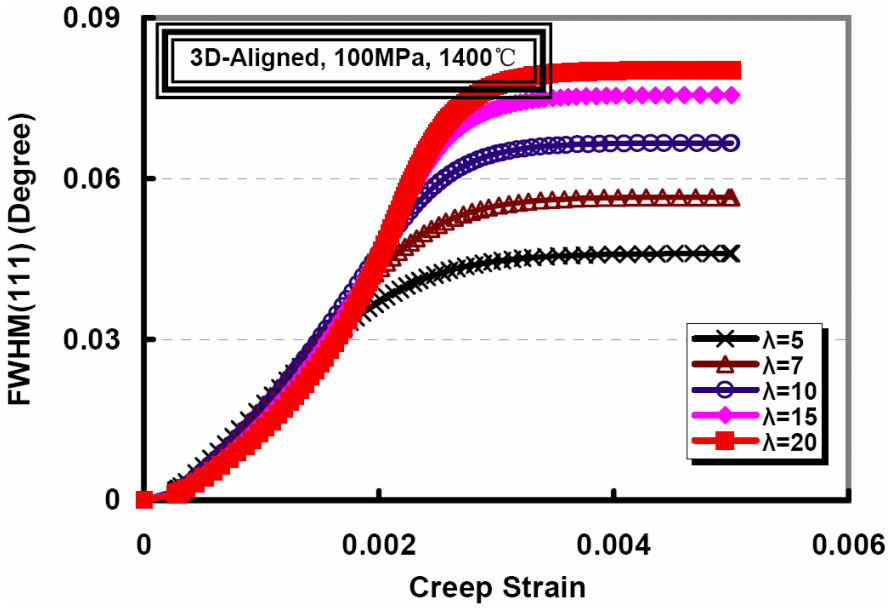

Figure C-15 ***FWHM*** **versus creep strain for 3D aligned unit cells with λ=5, 7, 10, 15 and 20, T=1400℃,** $\sigma_{applied}$ **= 100MPa.**

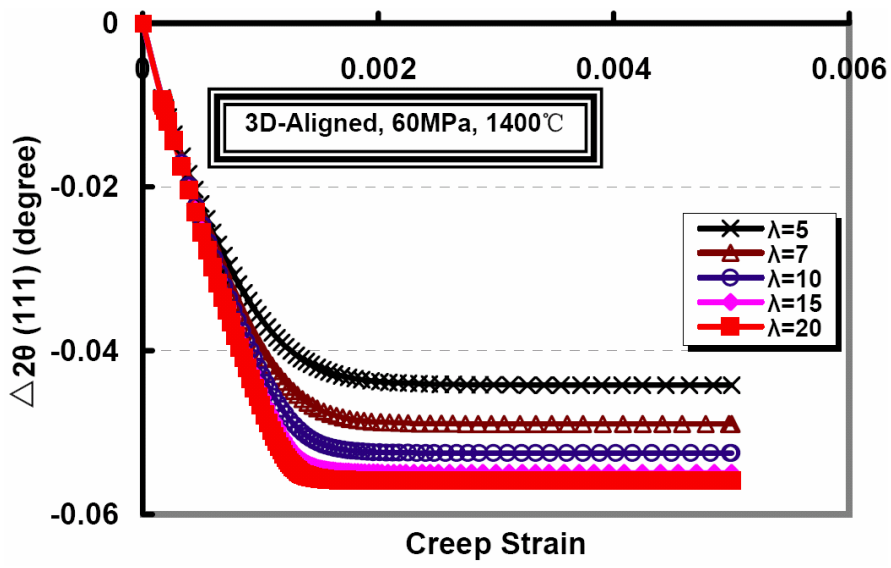

Figure C-16 Peak shift versus creep strain for 3D aligned unit cells with λ=5, 7, 10, 15 and 20, T=1400℃, $\sigma_{applied}$ **= 60MPa.**

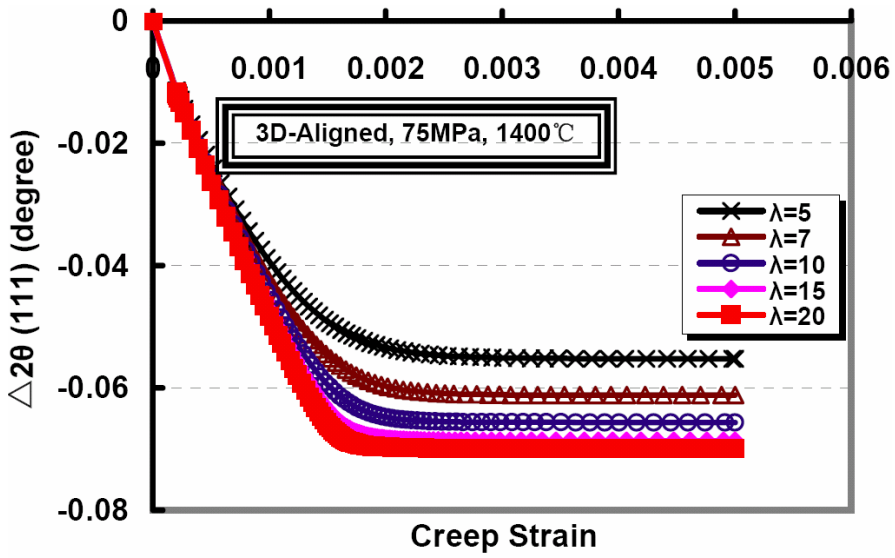

Figure C-17 Peak shift versus creep strain for 3D aligned unit cells with λ=5, 7, 10, 15 and 20, T=1400℃, $\sigma_{applied}$ = 75MPa.

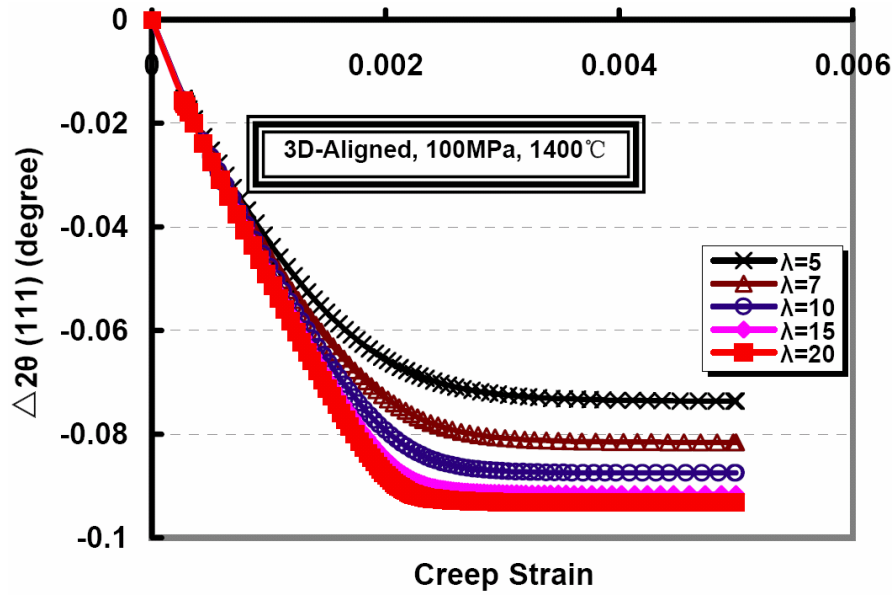

Figure C-18 Peak shift versus creep strain for 3D aligned unit cells with λ=5, 7, 10, 15 and 20, T=1400℃, $\sigma_{applied}$ = 100MPa.

(3) Figures C-19 to C-24 for section 6.3.4.1 (2D percolating unit cells)

Figures C-19, C-20 and C-21 show the peak width versus temperature while Figures C-22, C-23 and C-24 show the peak-shift versus temperature during the cooling stage after creep for 2D percolating unit cells with varied aspect ratios under varied stresses. They behave similarly for all aspect ratios under different applied stresses: (1) *FWHM* increases continually as temperature drops after creep; (2) peak position shift rightwards during the cooling stage from the leftward shifting during creep representing a compressive mean stress state due to thermal contraction.

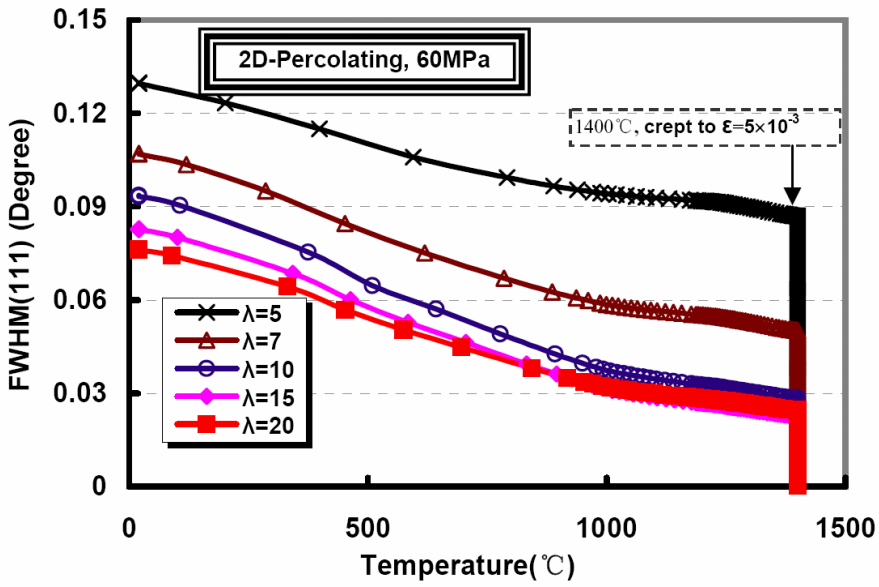

Figure C-19 *FWHM* versus temperature for 2D percolating unit cells with λ=5, 7, 10, 15 and 20, $\sigma_{applied}$ = -60MPa, as they are deformed to a strain of 0.005 at 1400℃, then cooled to 20℃.

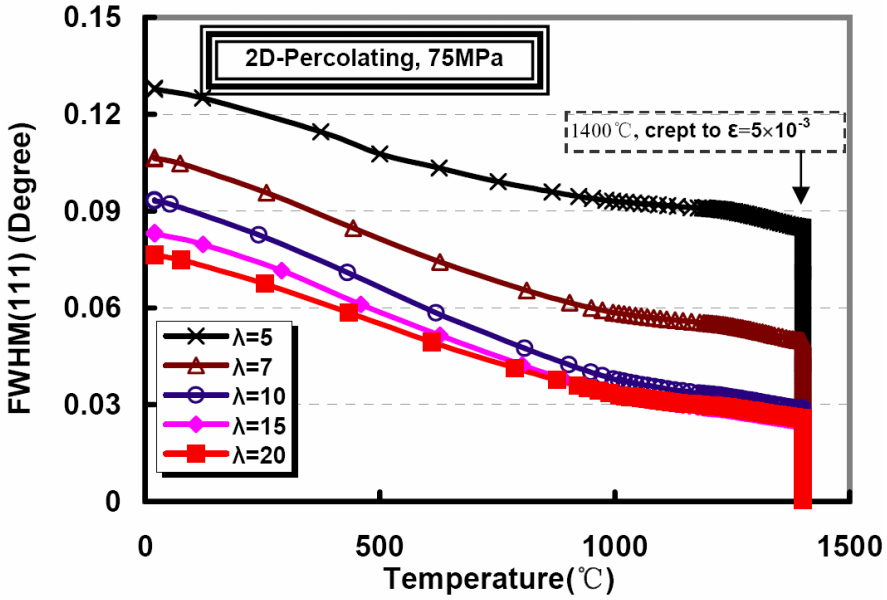

Figure C-20 ***FWHM*** **versus temperature for 2D percolating unit cells with λ=5, 7, 10, 15 and 20,** $\sigma_{applied}$ **= -75MPa, as they are deformed to a strain of 0.005 at 1400℃, then cooled to 20℃**

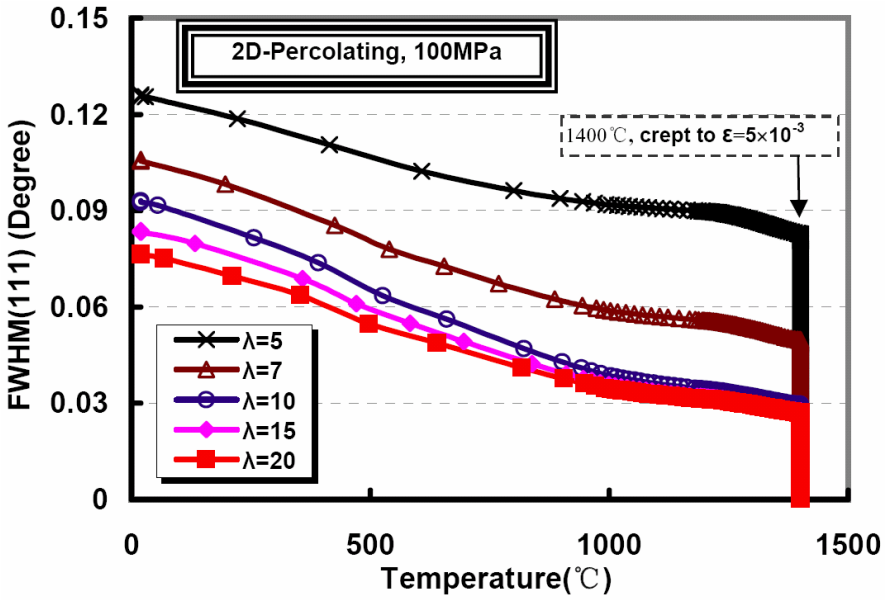

Figure C-21 ***FWHM*** **versus temperature for 2D percolating unit cells with λ=5, 7, 10, 15 and 20,** $\sigma_{applied}$ **= -100MPa, as they are deformed to a strain of 0.005 at 1400℃, then cooled to 20℃.**

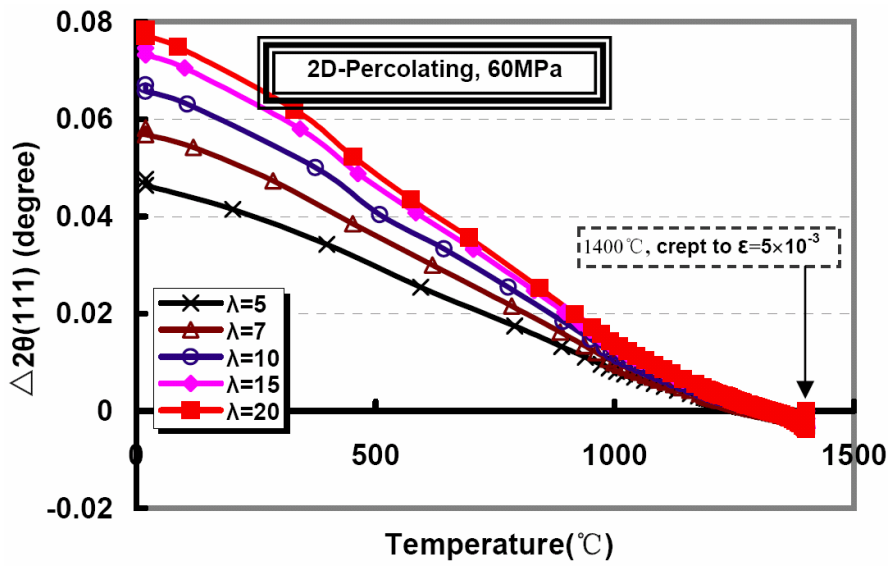

Figure C-22 Peak-shift versus temperature for 2D percolating unit cells with λ=5, 7, 10, 15 and 20, $\sigma_{applied}$ = -60MPa, as they are deformed to a strain of 0.005 at 1400℃, then cooled to 20℃.

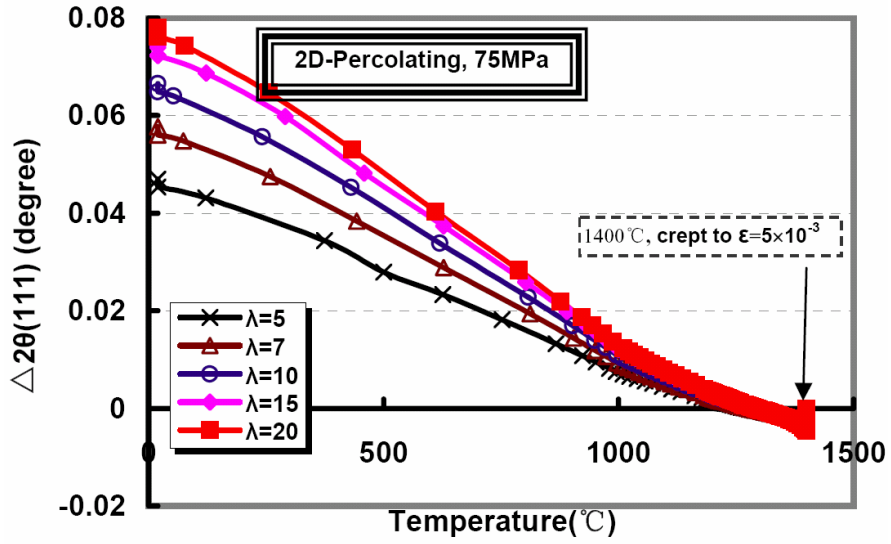

Figure C-23 Peak-shift versus temperature for 2D percolating unit cells with λ=5, 7, 10, 15 and 20, $\sigma_{applied}$ = -75MPa, as they are deformed to a strain of 0.005 at 1400℃, then cooled to 20℃.

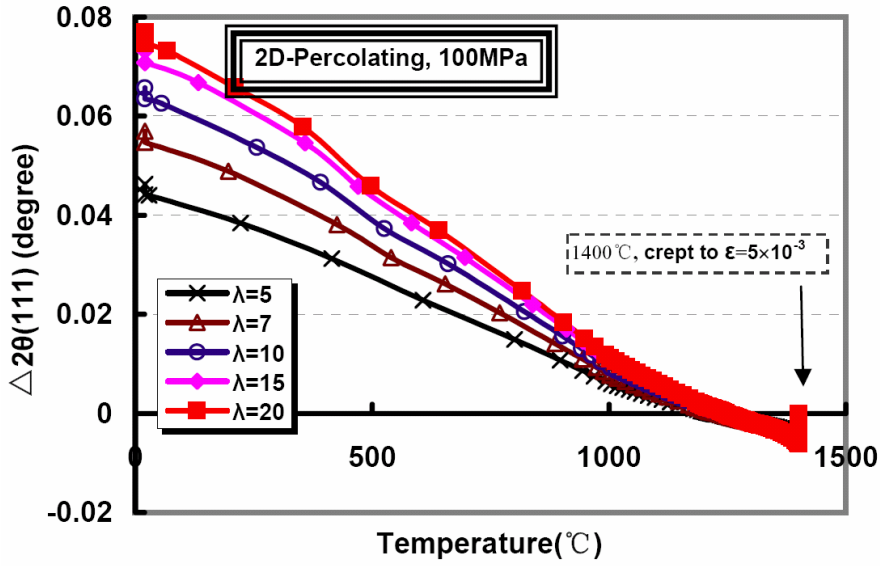

Figure C-24 Peak-shift versus temperature for 2D percolating unit cells with λ=5, 7, 10, 15 and 20, $\sigma_{applied}$ = -100MPa, as they are deformed to a strain of 0.005 at 1400℃ then cooled to 20℃.

(3) Figures C-25 to C-30 for section 6.3.4.2 (3D aligned unit cells)

Figures C-25, C-26 and C-27 show the peak width versus temperature while Figures C-28, C-29 and C-30 show the peak-shift versus temperature during the cooling stage after creep for 3D aligned unit cells with varied aspect ratios under varied stresses. Same as before, for 3D aligned geometry peak-width (Figures C-25 to C-27) behaves similarly during cooling stage after creep for varied aspect ratios and applied stresses. However, some small differences are still observed. In general: (1) *FWHM* decreases first then increases again with the dropping temperature for all aspect ratios with $\sigma_{applied}$ =60MPa; for aspect ratios of 5, 7 and 10 with $\sigma_{applied}$ =75MPa; for aspect ratios of 5 and 7 with $\sigma_{applied}$ =100MPa; (2) monotonously decreases as temperature drops after creep for bigger aspect ratios and applied stresses: aspect ratios of 15 and 20 with $\sigma_{applied}$ =75MPa; for aspect ratio of 10, 15 and 20 with $\sigma_{applied}$ =100MPa.

For the case of peak-shift, it behaves in a similar way for all aspect ratios and different applied stresses (Figures C-28 to C-30) during cooling stage after creep. In general, peak position shifts rightwards due to cooling from the leftward shifting due to creep deformation indicating a change of the mean stress state from tensile to compressive. Meanwhile, no significant dependence of the peak-shift on the aspect ratio was found after being virtually cooled under load in air and almost all aspect ratios combine into one line. However, a bigger applied stress affects the peak-shift more significantly and results in more scattered lines during cooling stage.

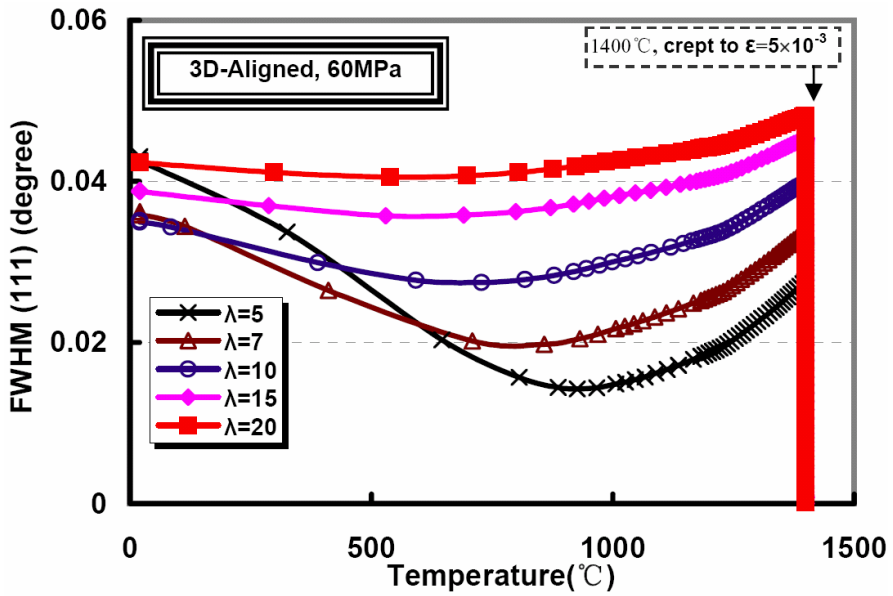

Figure C-25 ***FWHM*** **versus temperature for 3D aligned unit cells with λ=5, 7, 10, 15 and 20,** $\sigma_{applied}$ **=60MPa, as they are deformed to a strain of 0.005 at 1400℃, then cooled to 20℃.**

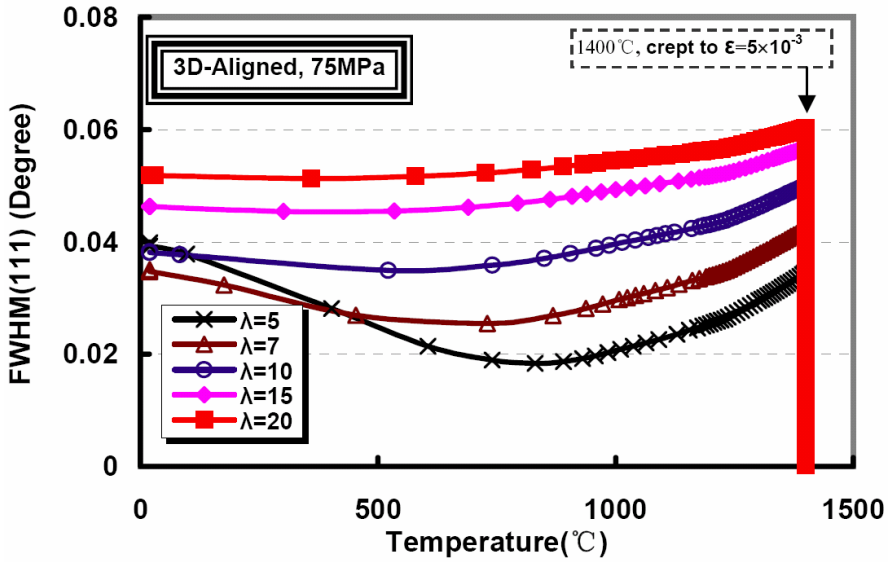

Figure C-26 ***FWHM*** **versus temperature for 3D aligned unit cells with λ=5, 7, 10, 15 and 20,** $\sigma_{applied}$ **= 75MPa, as they are deformed to a strain of 0.005 at 1400℃, then cooled to 20℃.**

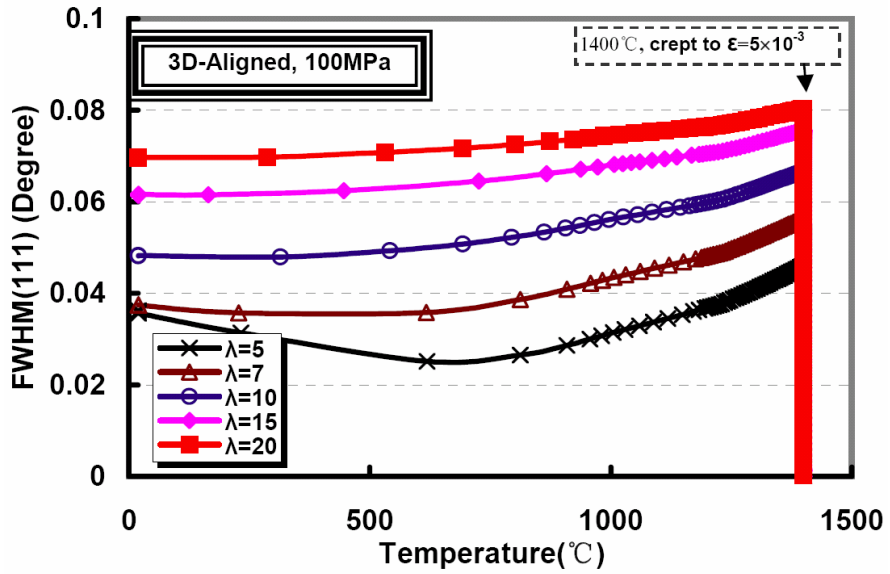

Figure C-27 ***FWHM*** **versus temperature for 3D aligned unit cells with λ=5, 7, 10, 15 and 20,** $\sigma_{applied}$ **= 100MPa, as they are deformed to a strain of 0.005 at 1400℃, then cooled to 20℃.**

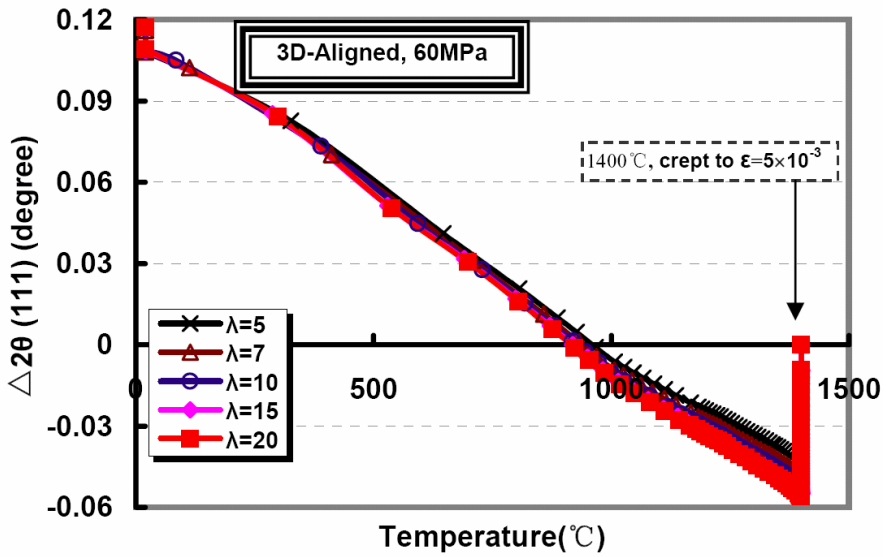

Figure C-28 Peak-shift versus temperature for 3D aligned unit cells with λ=5, 7, 10, 15 and 20, $\sigma_{applied}$ = 60MPa, as they are deformed to a strain of 0.005 at 1400℃, then cooled to 20℃.

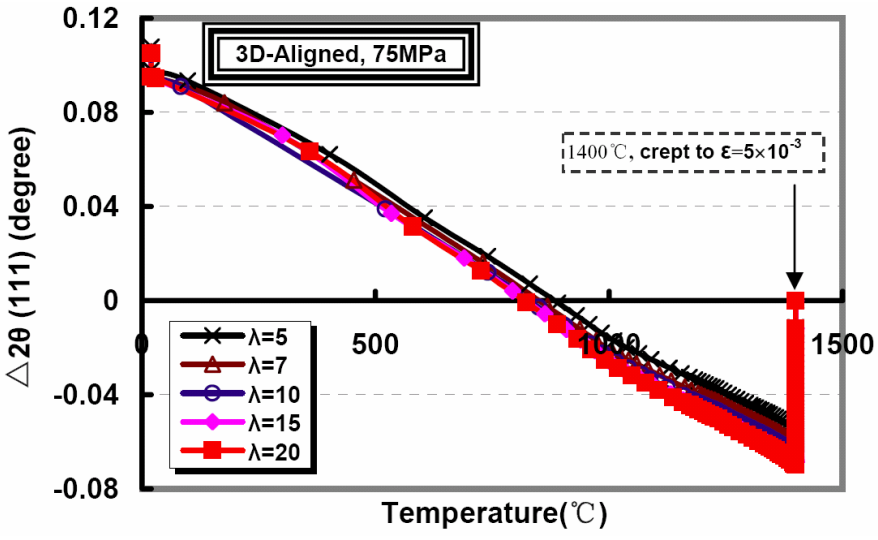

Figure C-29 Peak-shift versus temperature for 3D aligned unit cells with λ=5, 7, 10, 15 and 20, $\sigma_{applied}$ = 75MPa, as they are deformed to a strain of 0.005 at 1400℃, then cooled to 20℃.

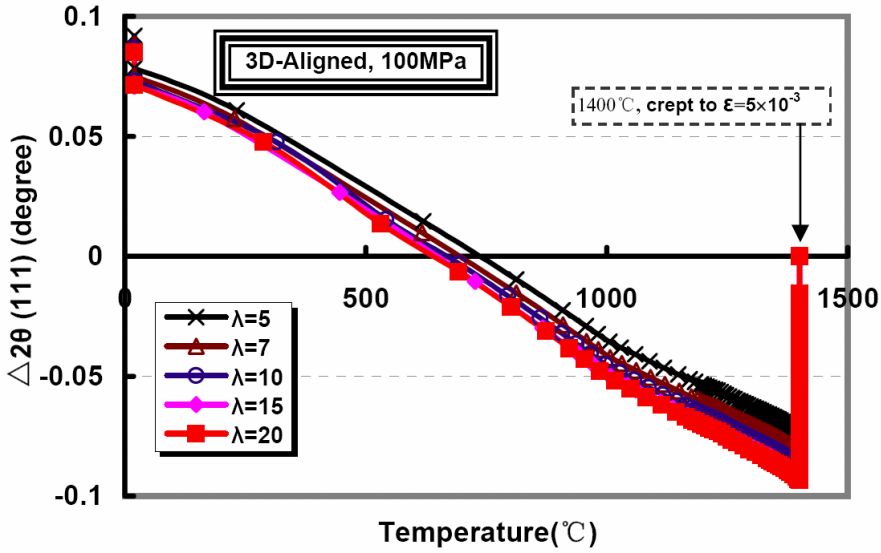

Figure C-30 Peak-shift versus temperature for 3D aligned unit cells with λ=5, 7, 10, 15 and 20, $\sigma_{applied}$ = 100MPa, as they are deformed to a strain of 0.005 at 1400℃, then cooled to 20℃.